Technical Report for the Design, Construction and Commissioning of The CALIFA Barrel: The R^{3}B CALorimeter for In Flight detection of γ rays and high energy charged pArticles

November 30, 2011

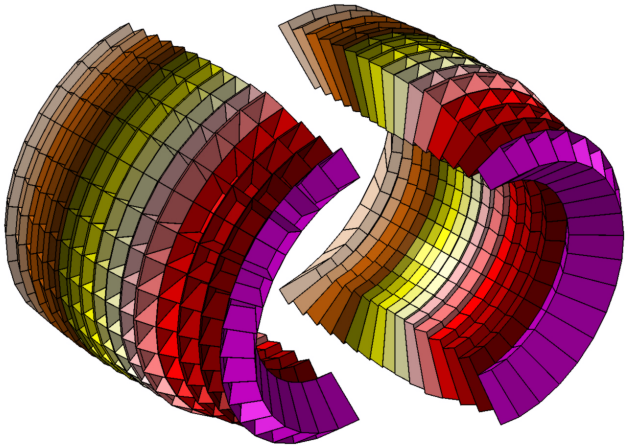

R^{3}B	Name	E-Mail
Project Leader/Spokesperson	Thomas Aumann	t.aumann@gsi.de
Deputy	Bjoern Jonson	bjn@fy.chalmers.se
Technical Coordinator	Roy Lemmon	roy.lemmon@stfc.ac.uk
Deputy	Olof Tengblad	olof@iem.cfmac.csic.es
Project Coordinator	Heiko Scheit	hscheit@ikp.tu-darmstadt.de
Contact Person at the FAIR site	Haik Simon	h.simon@gsi.de
CALIFA Convener	Dolores Cortina	d.cortina@usc.es
Deputy	Bo Jakobsson	bo.jakobsson@nuclear.lu.se

The R^3B Collaboration

Brazil

University of Sao Paulo: Alinka Lepine-Szily

Canada

Saint Mary's University Halifax: Rituparna Kanungo

TRIUMF Vancouver: Reiner Krücken

China

Institute of Modern Physics Lanzhou: Ruofu Chen, Songlin Li, Hushan Xu, Yu-Hu Zhang

Denmark

Arhus University: Dmitri Fedorov, Hans Fynbo, Aksel Jensen, Karsten Riisager

Finland

VTT: Simo Eränen, Juha Kalliopuska

France

CEA/DAM Bruyères-le-Châtel: Farouk Aksouh, Audrey Chatillon, Julien Taieb

CEA/DSM/IRFU Saclay: Alain Boudard, Diane Dore, Bernard Gastineau, Wolfram Korten, Philippe Legou, Sylvie Leray, Stefano Panebianco

GANIL: David Boilley, Wolfgang Mittig, Fanny Rejmund, Patricia Roussel-Chomaz, Herve Savajols, Christelle Schmitt

IPN Orsay: Bernard Genolini

Germany

EMMI and FIAS: Enrico Fiori, Bastian Löher, Deniz Savran

GSI Darmstadt: Yuliya Aksyutina, Denis Bertini, Konstanze Boretzky, Peter Egelhof, Hans Emling, Hans Feldmeier, Hans Geissel, Jürgen Gerl, Kathrin Goebel, Magdalena Górska, Jörg Hehner, Michael Heil, Jan Hoffmann, Günter Ickert, Aleksandra Kelic-Heil, Ivan Kojouharov, Nikolaus Kurz, Karl-Heinz Langanke, Yvonne Leifels, Thomas Neff, Chiara Nociforo, Maria Valentina Ricciardi, Dominic Rossi, Thomas Roth, Takehiko Saito, Karl-Heinz Schmidt, Haik Simon, Klaus Sümmerer, Wolfgang Trautmann, Helmut Weick, Martin Winkler

Helmholtz-Zentrum Dresden-Rossendorf: Daniel Bemmerer, Zoltan Elekes, Arnd Junghans, Mathias Kempe, Manfred Sobiella, Daniel Stach, Andreas Wagner, Jörn Wüstenfeld, Dmitry Yakorev

TU Darmstadt: Leyla Atar, Thomas Aumann, Timo Bloch, Christoph Caesar, Joachim Enders, Diego Gonzalez-Diaz, Marcel Heine, Matthias Holl, Alexander Ignatov, Oleg Kiselev, Dmytro Kresan, Thorsten Kröll, Alina Movsesyan, Manfred Mutterer, Valerii Panin, Stefanos Paschalis, Marina Petri, Norbert Pietralla, Achim Richter, Heiko Scheit, Mirko von Schmid, Linda Schnorrenberger, Philipp Schrock, Stefan Typel, Vasily Volkov, Felix Wamers

TU Dresden: Thomas Cowan, Marko Röder, Kai Zuber

TU Munich: Michael Bendel, Michael Böhmer, Thomas Faestermann, Roman Gernhäuser, Walter Henning, Reiner Krücken, Tudi Le Bleis, Olga Lepyoshkina, Max Winkel, Sonja Winkler

University of Cologne: Jannis Endres, Andreas Hennig, Vassili Maroussov, Lars Netterdon, Peter Reiter, Andreas Zilges

University of Frankfurt: Sebastian Altstadt, Olga Ershova, Christoph Langer, Christian Müntz, Ralf Plag, René Reifarth, Kerstin Sonnabend, Meiko Volknandt, Christine Wimmer

University of Gießen: Horst Lenske

Unversity of Mainz: Jens Volker Kratz

Hungary

ATOMKI: Margit Csatlós, Zoltán Elekes, Zsolt Fülöp, János Gulyás, Attila Krasznahorkay, László Stuhl, János Timár, Tamás Tornyi

University of Budapest: Ákos Horváth

India

AM University Aligarh: Rajeshwari Prasad, Manoj Kumar Sharma, Pushpendra Pal Singh

BARC Mumbai: S. Kailas, Kripamay Mahata, Aradhana Shrivastava

SINP Kolkata: Bijay Agrawal, Padmanava Basu, Pratap Bhattacharya, Sudeb Bhattacharya, Santosh Chakraborty, Sujib Chatterjee, Ushasi Datta Pramanik, Pradipta Kumar Das, Janaki Panja, Anisur Rahaman, Jayati Ra, Tinku Sinha

Tata Institute: Rudrajyoti Palit

Japan

RCNP Osaka: Isao Tanihata

Tokyo Institute of Technology: Takashi Nakamura

Norway

University of Bergen: Jan Vaagen

Poland

IFJ PAN Cracow: Bronislaw Czech, Stanislaw Kliczewski, Maria Kmiecik, Jerzy Lukasik, Adam Maj, Piotr Pawlowski, Miroslaw Zieblinski

University of Cracow: Reinhard Kulessa, Wladyslaw Walus

Portugal

LIP Coimbra: Alberto Blanco, Paulo Fonte, Luis Lopes, Rui F. Marques

University of Lisbon: Daniel Galaviz Redondo, Ana Henriques, Jorge Machado, Pamela Teubig, Paulo Velho

UTL Lisbon: Raquel Crespo

Romania

Horia Hulubei National Institute of Physics: Mihai Stanoiu

Institute of Space Sciences Bucharest: Madalin Cherciu, Maria Haiduc, Dumitru Hasegan, Mihai Potlog, Emil Stan

Russia

INR Moscow: Alexander Botvina

Ioffe PTI St. Petersburg: Yuri Tuboltsev, Elena Verbitskaya

IPPE Obninsk: Anatoly V. Ignatyuk

JINR Dubna: Irina Egorova, Sergey N. Ershov, Andrey Fomichev, Mikhail Golovkov, Alexander V. Gorshkov, Leonid Grigorenko, Sergey Krupko, Yulia Parfenova, Sergey Sidorchuk

PNPI Gatchina: Georgy Alkhazov, Vladimir Andreev, Andrey Fetisov, Victor Golovtsov, Anatolii Krivshich, Lev Uvarov, Vladimir Vikhrov, Sergey Volkov, Andrey Zhdanov

RRC Kurchatov Institute Moscow: Boris Danilin, Leonid Chulkov, Alexei Korsheninnikov, Eugenii Kuzmin, Aleksey Ogloblin

Saudi Arabia

National Center for Mathematics and Physics: Hamoud AlHarbi, Nasser AlKhomashi, Abdulrahman AlGhamdi, Abdulrahman Maghrabi

King Saud University: Khalid Kezzar, Safar AlGhamdi, Mohamed AlGarawi, Farouk Aksouh

Slovakia

Slovak Academy of Sciences: Martin Veselsky

Spain

IEM-CSIC Madrid: Maria José Garcia Borge, Eduardo Garrido, Enrique Nacher, Angel Perea, Guillermo Ribeiro, José Sanchez del Rio, Jorge Sanchez Rosado, Olof Tengblad

Universidad Complutense of Madrid: Samuel España, Luis M. Fraile, Jose Udias-Moinelo

Universidad de Santiago de Compostela: Héctor Alvarez-Pol, José Benlliure, Manuel Caamaño, Dolores Cortina-Gil, Ignacio Durán, Beatriz Fernández-Domínguez, Carlos Paradela

Universidad de Vigo: Enrique Casarejos

UPC Barcelona: Francisco Calviño

Sweden

Chalmers University: Christian Forssén, Johan Gill, Julius Hagdahl, Andreas Heinz, Håkan T. Johansson, Björn Jonson, Thomas Nilsson, Goran Nyman, Natalia Shulgina, Ronja Thies, Staffan Wranne, Mikhail Zhukov

KTH Stockholm: Bo Cederwall, Stanislav Tashenov

Lund University: Vladimir Avdeichikov, Joakim Cederkall, Douglas Di Julio, Pavel Golubev, Bo Jakobsson

Switzerland

CERN: Vladimir Eremin

The Netherlands

KVI: Nasser Kalantar, Ali Najafi, Catherine Rigollet, Branislav Streicher

University of Groningen: Jarno Van de Walle

United Kingdom

CCLRC Daresbury Laboratory: Patrick Coleman-Smith, Marc Labiche, Ian Lazarus, Roy Lemmon, Simon Letts, Vic Pucknell, John Simpson

University of Birmingham: Nick Ashwood, Matthew Barr, Martin Freer

University of Edinburgh: Tom Davinson, Phil Woods

University of Liverpool: Marielle Chartier, John Cresswell, Simon Gannon, Paul Nolan, Mark Norman, Janet Sampson, David Seddon, T. Stanios, Jonathan Taylor, John Thornhill, David Wells

University of Manchester: David Cullen, Sean Freeman

University of Surrey: Jim Al-Khalili, Carlo Barbieri, Wilton Catford, William Gelletly, Ron Johnson, Zsolt Podolyak, Patrick Regan, Arnau Rios, Edward Simpson, Paul Stevenson, Jeffrey Tostevin

University of York: Charles Barton

USA

Argonne National Laboratory: Jerry Nolen

EMMI/JINA: Justyna Marganiec

Michigan State University: Bradley Sherrill, Remco Zegers

Texas A&M University Commerce: Carlos Bertulani

Contents

Executive Summary

The R^3B (Reactions with Relativistic Radioactive Beams) experiment at FAIR will be the only facility worldwide providing the capability for kinematically complete measurements of reactions with relativistic heavy-ion beams up to around 1 AGeV, which provides sufficiently high resolution to enable a comprehensive experimental investigation of fundamental questions relating to nuclear-structure, astrophysics, and properties of bulk (isospin-asymmetric) nuclear matter. The experimental setup has been designed and will be built by the international R^3B collaboration on the basis of more than 20 years experience with the LAND reaction setup at GSI. The newly designed instrumentation therefore overcomes major limitations of the present setup. Main design goals following from the physics cases are the applicability of the experimental approach to 1 AGeV beams whilst maintaining high resolution, as well as the extension of the physics program.

The CALIFA (CALorimeter for the In Flight detection of γ rays and light charged pArticles) calorimeter surrounds the R^3B reaction target and is one of the key detectors of the R^3B experiment, accordingly optimised for the exacting requirements of the ambitious physics program proposed for the R^3B facility. The unprecedented requirements for proton and particle detection performance necessitated a dedicated simulation study accompanying an in-depth investigation encompassing the major modern developments in detector technology. CALIFA features a high photon detection efficiency and good energy resolution even for beam energies approaching 1 AGeV. This is in addition to the required calorimetric properties for detection of multiple γ cascades, and high efficiency for proton detection. CALIFA consists of two sections, a 'Forward EndCap' and a cylindrical 'Barrel' covering an angular range from 43.2 to 140.3 °. This Technical Design Report describes the technical details and the performance of the latter; the CALIFA Barrel.

The CALIFA Barrel is an integral part of the R^3B experimental setup, meeting the challenging demands imposed by the wide-ranging R^3B physics program; which requires both detection of low energy γ rays from single-particle excitations and high-energy γ rays associated with different collective modes, in addition to the detection of charged particles emitted from the reaction zone.

The detector will consist of 1952 crystals providing the angular resolution necessary to overcome limitations imposed by the Doppler broadening at high beam energies approaching 1 AGeV. The individual CsI crystals are read out by Avalanche Photo Diodes, orientated within a very compact geometry (an internal radius of 30 cm) that maximises the calorimetric properties. For some experiments, a silicon tracker an accompanying liquid hydrogen target will be positioned inside the detector. The design here proposed provides a photo-peak efficiency for 2 MeV photons emitted from a projectile with 700 AMeV in the angular range of the Barrel of 52 %, with a resolution of 5.5 %, and 39 % with 5 % in the case of 10 MeV photons. In addition, the invariant-mass analysis of high-lying states (e.g. Giant and Pygmy resonances) requires the calorimetric measurement of the γ sum energy in the case of cascade decays following neutron evaporation. On average, only few percent of the energy being lost in the passive material. In the case of quasi-free scattering

reactions, mid-energy range γ rays have to be detected with high resolution in coincidence with high-energy protons. The length of the crystals has been selected to ensure that protons arising from quasi-free knockout reactions are stopped within the scintillator for beam energies up to 700 AMeV. This corresponds to about 320 MeV protons in the most forward direction of the Barrel, necessitating 22 cm long CsI crystals for this polar angle.

This document summarises a large collaborative R&D effort performed over the past several years by a significant number of European Research Institutions and Universities. Different scintillation materials and readout concepts have been considered and investigated, including recent innovations in scintallator material development; for example, LaBr crystals. The optimum cost-effective solution has been determined, which is based on CsI crystals whose material properties provide a rather good energy resolution and the density required for high detection efficiency.

Prototype studies have demonstrated that Avalanche Photodiodes (APD) are very well suited when coupled with CsI(Tl) to meet the energy resolution specifications required by the R^3B physics program. Further advantages of APDs include an insensitivity to the fringe field of the superconducting dipole magnet GLAD, of which CALIFA is directly adjacent. Different prototype detectors have been tested extensively with both photons and high energy proton beams, as described in Chapter 3. The difficulty of temperature sensitivity of the APD readout has been overcome by support from a dedicated electronics system, as described in Chapter 5, and via the use of a stabilising cooling system. The electronics is adapted to the large dynamic range of light output necessitated by the diverse R^3B physics program. Both low-energy photons and a few-hundred MeV protons can be measured simultaneously. The presented solution features a fully-digital signal processing system providing flexibility, energy filtering, triggering, pileup rejection, calibration in addition to complex particle-identifications algorithms.

Extensive simulation studies have been performed, guiding the design to reach its final version. The granularity has been optimised in such a manner to ensure that the final resolution is not dominated by Doppler broadening, but close to the intrinsic resolution of the scintillation material.While aiding energy resolution an excessively high segmentation would be at the expense of calorimetric properties, consequently the optimum compromise between these factors has been determined. An in-depth investigation into the best suited mechanical design, including the housings of crystals and support structures, has additionally been undertaken for determination of the final design. The full system has been simulated for a number of realistic physics cases; demonstrating that the detector performance meets the R^3B physics program requirements, as reported in detail in Chapter 4. Details of the technical realisation, including mechanics, tests, calibrations, as well as the construction procedure are summarised in Chapters 6 to 11, with an accompanying detailed estimate of the investment cost for the construction in Chapter 12.

The project plan foresees start of construction for the Barrel section in 2012. An important milestone will be met with the operation of a 20% demonstrator detector for physics experiments in 2014 in Cave C at GSI, even at this stage profiting from the improved resolution for photon detection. The full detector is expected to be ready in the last quarter of 2015 and commissioned in 2016. The final detector will be moved after full commissioning and first production runs in Cave C to its final location at the R^3B hall at the FAIR site in 2017, being fully operational for physics experiments in 2018 when Super-FRS is expected to deliver the first beams at FAIR.

1. Introduction

Reaction experiments at relativistic energies have proven to be an essential tool for nuclear structure investigations. A large range of reaction channels are accessible and the intrinsic structure of the participant nuclei can be disentangled from the reaction mechanism. Furthermore, the possibility of using thick secondary targets in combination with efficient coverage utilising a wide range of detector enables an excellent match for experiments with the most exotic nuclear species. The acronym R^3B stands for Reactions with Relativistic Radioactive Beams. The R^3B experiment will be installed at the high-energy branch focal-plane of the Super-FRagment-Separator 'Super-FRS' at FAIR, the Facility for Antiproton and Ion Research, and will allow a wide experimental program on reactions between high-energy radioactive beam nuclei and stable target nuclei. In particular, the experimental set-up is capable to fully benefit from the Super-FRS [GWW+03] beams with characteristics inherent to the in-flight production method, and will thus have the ability to explore the 'isospin frontier', capitalising the most short-lived and exotic nuclear systems that can be produced at the facility.
The R^3B activity is incorporated into the NUSTAR (NUclear STructure, Astrophysics and Reactions) pillar of the FAIR experimental program. The design and construction of the R^3B facility is being pursued within the R^3B collaboration, a large international consortium comprising more than 200 scientists over 20 countries. The relevant physics cases and detailed conceptual layout of the experiment including its instrumental parts have been laid out in the Conceptual Design Report for FAIR [col01] in 2001 and at a more in-depth level in the R^3B Technical Proposal [AJ05] in 2005. Since then, an extensive R&D program has been pursued, leading to the final design of the different detection components. This report, describes in detail the technical design of the Barrel section of the calorimeter CALIFA (CALorimeter for In Flight detection of γ rays and high energy charged pArticles). The CALIFA detector system, surrounding the reaction target of the R^3B set-up, down-stream of the Super FRS, is a unique detector based on extremely performant CsI(Tl) scintillation crystals, large area avalanche photodiodes and a light mechanical structure that maximizes the calorimetric properties. It will serve as high resolution γ-ray spectrometer, high efficiency γ-ray calorimeter and also for the identification of high energy charged particles arising from the target. The device is extremely compact and highly segmented, subtending the angular region spanning the opening acceptance of the beam line and 140.3^{o}[1] The different detection units are supported by minimally interacting mechanical structure which maximizes the calorimetric properties of CALIFA. All these characteristics contribute towards CALIFA acting as a key instrument for the realization of the ambitious physics program of R^3B, enabling the investigation of nuclear reactions with an unprecedented precision.

The R^3B experiment will enable kinematically complete measurements of reactions with relativistic beams up to energies of approximately 1 AGeV. (The upper limit in energy is defined by the maximum magnetic rigidity of 20 Tm of the Super-FRS). The flexibility

[1] All the angles have the target position as origin.

of the detection systems within the setup allow the accommodation of experiments utilising different types of reactions and physics cases. An overview on the physics subjects to be investigated has been discussed in the Conceptual Design Report [col01]. The list of reactions to be considered for the R^3B experiment includes: elastic and quasi-elastic scattering, Coulomb excitation, knockout reactions, total-absorption and charge-exchange reactions, fission and spallation, fragmentation and multi-fragmentation. Due to the high intensity of exotic beams, R^3B experiments can address the burning questions of the nuclear many-body problem in new ways. Exotic clustering at the drip-lines, evolution of nuclear shells and single-particle structure far from the line of stability can be studied through single- or few-nucleon knockout reactions. One example of this is the determination of the halo nucleon wave function in momentum-space from knock-out reactions. These wave functions have so far been possible to study only for the lightest nuclei. The intensities of the Super-FRS beams will open up this field for heavier systems, and the vastly improved detection capabilities in conjunction with a liquid hydrogen target will permit using tools such as (p,2p)-, (p,pn)- and (p,pd)-reactions to study deeply bound states and also to study T=0, T=1 pairing competition in exotic nuclei. Further issues include exotic collective excitation modes and astrophysical S factors. High energies in combination with heavy targets permits determination of (n,γ) and (p,γ) cross sections through studies of Coulomb break-up using inverse reactions.
In the following Chapters (see Chapter 2 and Section 4.5), is discussed the different CALIFA working modes and a selection of particular physics cases for which the CALIFA detector with its demanding requirements must play an important role.
The advantages of utilizing high-energy beams are many-fold. Firstly, the production, separation, and identification of radioactive beams at high energies is very efficient due to the kinematic forward focusing and the possibility to use thick targets. Secondly, it also enables a clean separation of even heavy beams with masses A $\geq$ 200 due to the fact that ions are fully stripped, a prerequisite for the magnetic analysis of heavy ions. Similar arguments hold for the measurement of secondary reactions with these beams. R^3B will be the first experiment which will allow a kinematically complete measurement of peripheral reactions with such heavy ion beams, including the coincident detection and identification of the heavy residues in addition to neutrons and photons. Other advantages of the high beam energy are related to the reaction mechanisms, which become simpler, permitting reliable model description at higher beam energies. At high velocity, reactions can be accurately described by theory, nuclear-structure observables being less convoluted by reaction mechanism effects, and can thus be deduced more precisely.

This report does not describe the complete R^3B experimental setup with related instrumentation, but rather we would like to refer the reader to the R^3B Technical Proposal [AJ05]. However, to understand the context of CALIFA within the setup, we briefly mention the development and construction status of the main components of the R^3B setup, as shown in Fig. 1.1.

Key instruments besides CALIFA include the neutron detector NeuLAND, the silicon tracker R^3B-Si-TRACKER and the super-conducting large-acceptance dipole R^3B-GLAD. In addition, several charged-particle detectors are used for beam tracking, ΔE and time-of-flight measurements. The Technical Design Report corresponding to the NeuLAND detector has been recently submitted. NeuLAND Construction is foreseen to commence in 2012, roughly in parallel to CALIFA. The target recoil detector is being designed by a consortium of institutes from the UK under the leadership of STFC Daresbury Laboratory.

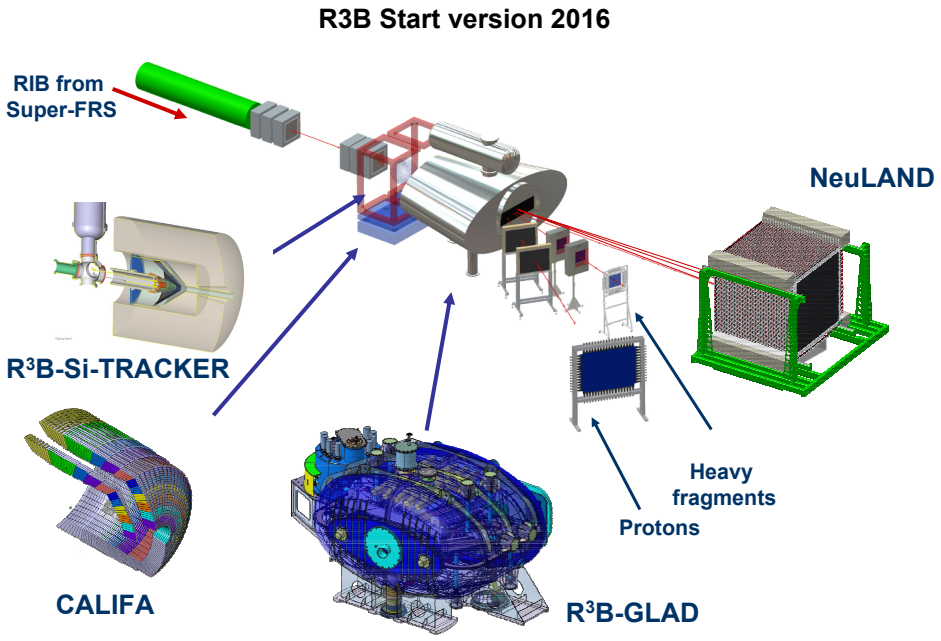

Figure 1.1.: *The complete R^3B detector set-up*

The funds for the R&D and the final construction are secured by the UK funding agencies and the complete detector will be available for experiments in 2015. The construction of the superconducting dipole magnet has already started at CEA Saclay and the cold mass including the superconducting coils have been already assembled. The completion and delivery of the device is foreseen for the end of 2012. The magnet will then be installed in Cave C at the present GSI facility.

The challenges of performing nuclear-structure and reaction experiments at relativistic beam velocities are related to the high magnetic rigidity of the ions and the demands on the overall resolution of the detection system. The experiment has to resolve excitation energies in the 100 keV domain populated in a reaction with, e.g., a ^{132}Sn beam (1 AGeV) with a momentum of 220 GeV/c. The precursor experiment of R^{3}B, the ALADIN-LAND [LAN] setup at GSI, on which the concept of R^{3}B is based, does not have these capabilities. Although very successful throughout the past 20 years, the main limitations of the present setup are the restricted magnetic rigidity, the limited resolution in momentum for fragments and neutrons, the reduced capability to detect multi-neutron events and lack of good resolution for γ-ray detection (mainly due to the Doppler broadening) and restricted calorimetric properties when dealing with energetic γ rays and particularly charged particles. CALIFA will represent a major improvement when compared with its direct precursor: the CrystalBall detector, offering technical solutions that overcome its predecessor's limitations. In particular, a substantial improvement in energy reconstruction of γ rays with energies ranging from 100 keV up to 30 MeV in laboratory frame and also a much better separation of the low energy background is achieved by the high granularity layout of the detector.

This document is the result of an extensive R&D program performed over the last five

years. It presents the technical choices for the CALIFA Barrel design and the inherent details associated with its construction. Though it concerns uniquely the Barrel description, on several occasions both the full CALIFA device or the Forward EndCap separately will be referred to for completeness. It should be noted that CALIFA Barrel will itself be an independent device, adapted for use in experiments as a stand-alone detector. The most challenging requirement on individual CALIFA detectors is the wide dynamic range to be covered, from low energy (<100 keV) γ rays to 300 MeV protons, combined with a high energy resolution (from 1% to 10% for the lower γ-ray energies). A typical R^3B experiment will investigate reactions induced by projectiles with energies up to 1 AGeV (nominal value 700 AMeV). This introduces significant Lorentz boost and Doppler broadening of the emitted γ rays. Thus, it is convenient to divide the search for the optimal detector material and geometry of CALIFA into a low-angle section, from the beam pipe aperture to 43.2^o, 'Forward EndCap' and a large-angle 'Barrel', from 43.2^o to 140.3^o . The device will be highly segmented ($\approx$ 3000 [2] individual crystals) with a unique shape and different angular aperture and length corresponding to different polar angle regions. These aspects are related to the main physics requirements and conceptual design guidelines, discussed in Chapter 2.

The characteristics of CALIFA demanded the selection of the most appropriate detector material and read-out devices presented in Chapter 3. The choice of Barrel detector scintillation material, CsI(Tl), is based on its large light output, rather good intrinsic resolution and capability of proton - γ-ray separation. Other important qualities are its simplicity to handle, low hygroscopy and relatively low price. The best choice for the CALIFA Barrel photosensor has been found with the use of Avalanche Photodiodes, which possess a perfect match to the CsI(Tl) spectral response. They are insensitive to the presence of magnetic fringe fields, and can cover large areas; providing an excellent physical coupling to the crystal surface exit. Additionally, APDs provide very good energy resolution for low energy γ rays [GAPB+08a], but have high demands on temperature and voltage stability.

The detailed response of the CALIFA Barrel has been extensively investigated by means of simulation codes, providing a quantification of the detector performances which has guided the design process; the results presented in Chapter 4, together with a detailed response of the system for selected physical cases.

The front-end electronics (FEE) and data acquisition (DAQ), summarised in Chapter 5, are designed mainly within the NuSTAR Synergy Group for Front-End-Electronics and Data Acquisition (SGFD) and always in close coordination with the CALIFA working group.

The mechanical support for CALIFA, presented in Chapter 6, is based on epoxy-carbon fibre boxes with an alveolar structure. This minimises the geometrical losses and introduce a natural modularisation of CALIFA.

Different radiation and safety issues are discussed in Chapter 7, whereas Chapter 8 summarises the different production, quality, assurance and acceptance tests foreseen for CALIFA Barrel components. Chapter 9 is devoted to the different procedures foreseen to ensure an accurate calibration of the detector.

Plans on specific infrastructure related issues and the detector installation procedure in its final location are presented in Chapter 10 and 11 respectively.

Explicit financial evaluation of the cost related with this detector, together with the collaboration engagement is presented in Chapter **??**. The expected time schedule in the construction of the CALIFA Barrel is described in detail in the working plan presented in Chapter 12.

[2] including the Forward EndCap

2. Physics requirements of CALIFA

CALIFA, the R^3B calorimeter, is an extremely versatile device that will play a key part in the realisation of full kinematics measurements. It will surround a central target and detect (normally in coincidence with other R^3B detectors) the emission of a wide energetic range of γ rays (from 100 keV to 30 MeV) and light-charged particles (for example, protons with energies up to 320 MeV) arising from reactions induced by relativistic radioactive beams impinging on to the R^3B target. The particular kinematics of high-energy reactions (strong Lorentz boost focusing and accompanying Doppler broadening and shift) has to a large extent determined the geometry of the detector, this detailed in Section 2.2. Prior to this is an overview of the requirements imposed by the research program that is planned for the R^3B campaign.

CALIFA will be used in many of the physical cases of the R^3B experiments, even though the required functionality will vary greatly from one case to another. Three different working conditions for CALIFA can be considered:

In some cases it will be used as a high-resolution spectrometer, being responsible for the detection of relatively low-energy γ rays (0.1 to 2 MeV), consequently with low multiplicity (2-3). The energy resolution will be in this case the most critical parameter of CALIFA. This value has been set to be of $\Delta E/E < 6\%$ (see Table 2.1 for a 1 MeV γ ray), which allows to distinguish most of the simple γ-ray cascades that come from the de-excitation of light exotic nuclei. A typical example of reactions that could benefit from this operational mode are knock-out reactions employing light, radioactive beams.

Another case will require CALIFA's employment as a γ-ray calorimeter, required for the detection of very energetic γ rays (up to 10 MeV) and associated to very fragmented decays (high-multiplicity events). In this case the key parameters will be the total γ-ray absorption (intrinsic photopeak efficiency), γ-ray sum energy and γ-ray multiplicities. A typical reaction that will profit from this operational mode is the investigations of pygmy- (or giant-) resonance decays.

The most challenging scenario corresponds to the use of CALIFA as an hybrid detector that has to provide simultaneously good calorimetric properties together with high-resolution. A typical example of a reaction channel that might require this performance is that of quasi-free scattering (i.e (p,2p),(p,pn)...). In this case, the detection of highly energetic light charged particles (protons up to 320 MeV) has to co-exist with the detection of the prompt γ ray de-excitation of the residual fragment, both processes measured with good energy resolution over a huge dynamic range.

At this stage it should be noted that the recoiling protons and also other light fragments are to be measured by CALIFA operating in coincidence with the Silicon Tracker system,

Intrinsic photopeak efficiency	40 % (at E_γ=15 MeV projectile frame)
γ-ray sum energy resolution $\Delta(E_{sum})/<E_{sum}>$	$<$ 10% for 5 γ rays of 3 MeV
γ-ray Energy resolution	5-6 % ΔE/E for 1 MeV γ rays
Calorimeter for high energy light charged particles(LCP)	Up to 320 MeV in Lab system
LCP energy resolution	$<$1% $\Delta E_p/E_p$ $\frac{\sqrt{(100MeV)}}{\sqrt{E}}$
proton-γ ray separation	for 1 to 30 MeV

Table 2.1.: *Nominal specifications of the R^3B calorimeter (β=0.82). These parameters are defined by the Physics program defined in the R^3B Technical Proposal [AJ05]*

which fulfils well the required angular precision. Losses due to elastic and inelastic scattering could be quite relevant in these cases.

The demanding requirements (summarised in Table 2.1), together with the required granularity to overcome the energy degradation due to the Doppler Broadening, for the 'Barrel' section seem achievable via the use of high performance CsI(Tl) crystals coupled to Large Area Avalanche Photo Diodes, such as the ones proposed in this document, Chapter 3. The improvement of the performances of the detector with better scintillation crystals in terms of intrinsic energy resolution or reduction of losses associated to scattering process of the light charged particles in the crystal are still in development and will be the subject of a complementary TDR document for the small-angle section 'Forward EndCap'.

2.1. Conceptual Design

The total CALIFA detector concept is based on detailed simulations of the typical experiments to be performed in R^3B (see Chapter 4). Here the interplay of intrinsic properties of the individual detector elements and the overall arrangement of the apparatus had to be optimised to individual requirements, while maintaining sufficient flexibility for the versatile program of R^3B.

However, the basic characteristics of CALIFA are to a large extent determined by the particular kinematics of reactions at relativistic energies. We introduce in the following section the key factors that have guided the calorimeter conceptual design [APBC+08].

- The shape and length of the crystals; to ensure a high total absorption efficiency
- The detector granularity, which is crucial to provide the necessary angular resolution for the reconstruction of the γ-ray energies in the projectile rest frame, 'PF'.

CALIFA detectors must combine high efficiency and good energy resolution for γ rays with relatively high stopping power for light charged particles. It must also be possible to perform signal summing for γ rays and protons in order to optimise the efficiency for CALIFA as a calorimeter. Taking these considerations into account means that special

attention is needed when selecting crystal material and geometry.

The high energy of the incoming beam and consequent Doppler shift and broadening of γ rays emitted in the reaction leads to different requirements on the detector system for different angles with respect to the beam axis. For example it is not necessary that the same type of scintillator material should be used for the large-angle part as for the small-angle part of CALIFA. Consequently, the system was divided into two parts, the large-angle part - the 'Barrel' - that is described in this TDR and the 'Forward EndCap', described in a forthcoming report.

Measuring the energy of γ rays emitted by sources moving with relativistic energies suffer from the Doppler effect. A perfect determination of the γ-ray energy emitted in the projectile rest frame (PF) requires a perfect measurement of both the laboratory energy and the emission polar angle with respect to the recoil fragments velocity. Even if the energies in the laboratory frame were perfectly determined, the inescapable uncertainty on the polar angle of emission would contribute to the PF γ-ray energy uncertainty. The calorimeter design is constrained by this contribution to the resolution.

For a γ ray emitted by a fast projectile, the Lorentz transformation boosts its laboratory energy to

$$E_\gamma^L = \frac{E_\gamma^{PF}}{\gamma} \frac{1}{1 - \beta \cos\theta} \tag{2.1}$$

where E_γ^{PF} is the energy of the γ ray in the PF, θ the emission polar angle, β the projectile velocity and $\gamma = 1/\sqrt{1-\beta^2}$.

Assuming that we know the polar angle of the emitted γ ray with an uncertainty $\Delta(\theta)$, then

$$\Delta^2(E_\gamma^{PF}) = \gamma^2 \beta^2 E_\gamma^L \sin^2\theta \; \Delta^2(\theta) \tag{2.2}$$

and

$$\frac{\Delta(E_\gamma^{PF})}{E_\gamma^{PF}} = \frac{\beta \sin\theta}{1 - \beta\cos\theta} \Delta(\theta) \tag{2.3}$$

If a constant relative resolution is required for the reconstruction of the γ-ray PF energy ($\Delta(E_\gamma^{PF})/E_\gamma^{PF} = k_1$), we obtain the expression

$$\Delta(\theta) = k_1 \frac{1 - \beta\cos\theta}{\beta \sin\theta} \tag{2.4}$$

which can be used to determine the calorimeter shape and the maximum angle covered by each crystal, as a function of their position in the calorimeter.

The Barrel crystal design has been determined based on the partition of the solid angle given by the previous expression for a constant relative resolution of $\Delta(E_\gamma^{PF})/E_\gamma^{PF} = k_1 \sim 5\%$ (Fig. 2.1). The red lines that appear in this picture correspond to the angular aperture of the different CALIFA Barrel crystals.

The design of CALIFA has thus particularly been guided by the γ ray emission from excited projectile remnants. Fig. 2.2 displays the section of the energy distribution that is detected

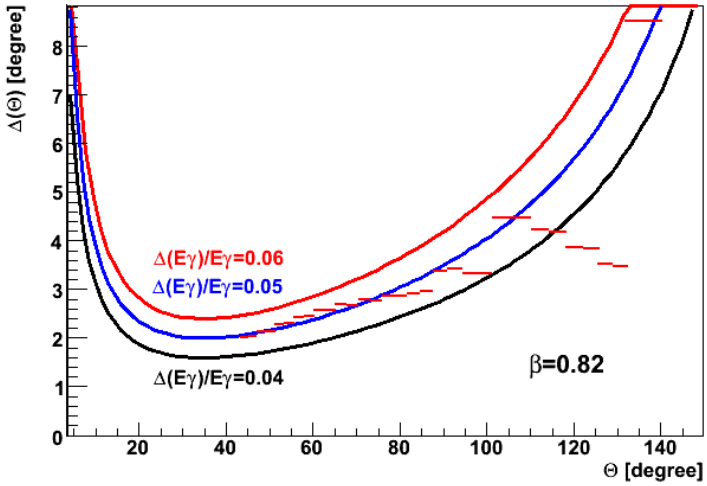

Figure 2.1.: *Graphic representation of the polar angular aperture needed as a function of the polar angle for a given projectile velocity (β=0.82). The coloured lines correspond to different values of k_1 (contribution to the energy resolution due to Doppler broadening) ranging form 4 to 6 %. CALIFA Barrel has been designed to have a k_1 value close to 5 % (each red line corresponds to the angular range covered by a crystal) representing an upper limit for geometrical energy resolution of the CsI(Tl) crystals used.*

in the various CALIFA regions when the remnant has an energy of 700 A MeV. In this representation, we distinguish the different regions.

- The Forward EndCap covering the region between beam pipe limit to 43.2° and concentrates 58.3% of the total γ rays emitted by a moving source at the nominal value of 0.82c. This region (particularly between 20-40°) is extremely complex because it concentrates a large fraction of the γ rays emitted and the Doppler shift boosts the energy to 1.5-2.5 times its value in the Center of Mass (CoM) frame.[1]
- The Barrel enclosing polar angles between 43.2 to 140.3° with 38.9% of γ rays emitted in this direction.
- The regions at polar angles below 7^o and above 140.3^o with only 3% of γ emitted in this directions are not covered by any scintillation crystals.

The election of the limit of approximately 43.2° between the Forward EndCap and Barrel section has been determined based on the following criteria: i) preserve the angular region at approximately 25° where the γ-ray angular distribution is at its maximum (see Fig. 2.2), ii) allow the detection of one proton in each section in the case of studies of (p,2p) reactions, and iii) avoid excessive tilting of the crystal position in the Barrel section with the intention of minimizing losses due to non-detection of Compton events. These losses arise as a consequence of an increased displacement of crystal face alignment, causing photons to scatter not into the adjacent crystal, but rather through the gap as a result of this

[1] Please note that what we propose here is only one of the studied options. As previously explained, the final design for this detector section is not yet complete.

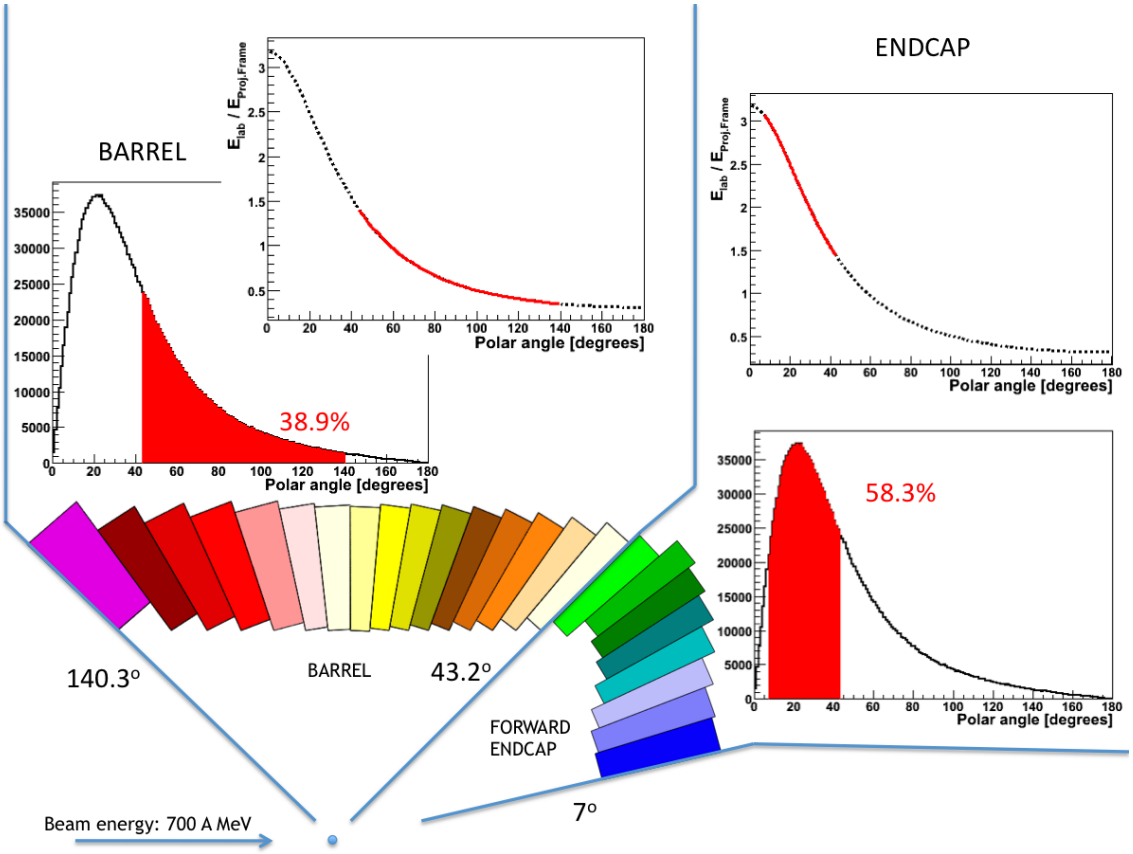

Figure 2.2.: *Schematic representation of the CALIFA detector profile. The portion of angular distribution of emitted γ rays covered by each CALIFA section and the corresponding Doppler shift is highlighted in this figure.*

displacement, which increases with increasing polar angle.

The election of about 140° in the backward angle coverage is justified as follows: i) the γ-ray angular distribution has a tiny contribution of events above this angle, ii) the aperture of the furthest backward angles facilitate detector cabling installation and access to the target area. It should be noted that although the percentage of γ rays emitted by the target is minimal at angles in excess of 140°, it is possible that a more significant loss in efficiency for this region could be due to the escape of pair-production photons from the EndCap. Work is currently ongoing to determine if the addition of an ancillary detector, termed the 'lid', is justifiable in cost:efficiency terms when recouping the loss of this fraction of 511 keV annihilation photons.

The internal CALIFA Barrel radius has been determined according to the compromise of: i) allowing the installation of the R^3B target and Silicon Tracker System ii) approaching the CsI(Tl) crystal towards the target to maximise the solid angle covered by each individual CsI(Tl) crystal.

Summarising, the necessity to identify high-energy protons and γ rays with good geometrical efficiency limits first of all the minimum thickness of detectors in the beam direction. The degradation of the energy resolution (for γ rays) and the maximum acceptable loss of

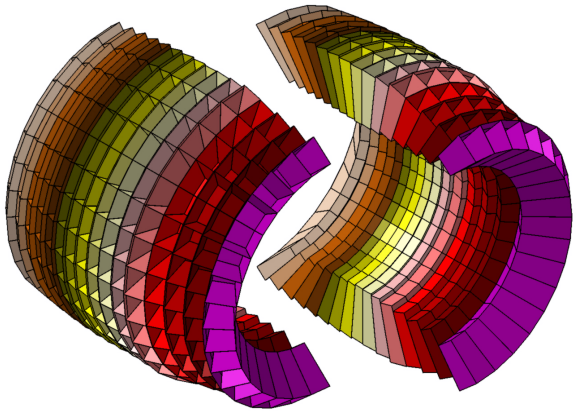

Figure 2.3.: *Artistic view of the CALIFA calorimeter. The inner radius of the Barrel is 30 cm. The main symmetry axis is placed along the beam direction and defines the origin for polar angles*

protons in inelastic reactions in the detector material conditions the choice of the maximum detector thickness. At the same time, an increase in the crystal length will also translate in the γ ray case to a degradation of the energy resolution, as a consequence of the ratio between the entrance crystal area and the length; very far from the ideal 1:1.

An artistic view[2] for the large-angle 'Barrel' section is shown in Fig. 2.3. This design version comprises a total of 1952 detection units (crystals + LAAPD) with 11 different geometries (see Table 2.2).

2.2. Detector shape and granularity

Accounting for the aforementioned criteria, the optimum design for the CALIFA Barrel has been determined to be frustum-shaped crystals (see the technical drawings in Fig. 2.4 corresponding to Type I crystals) arranged in a cylindrical pattern around the beam line. The longer axis of the frustum-shaped crystals is directed towards the target.

The design features include:

- Use of a minimum set of different crystal shapes, which simplifies construction and reduces costs.
- Reduction of the empty space and material (wrapping and support structures) within the active volume.
- Reduction of γ rays escaping through the spaces between crystals, by slightly tilting the crystal axis with respect to the polar angle.

[2]This figure does not represent crystals, but rather alveoli. Each alveolus contains 4 individual wrapped crystals, except for the furthermost backward angle ring, containing a single crystal

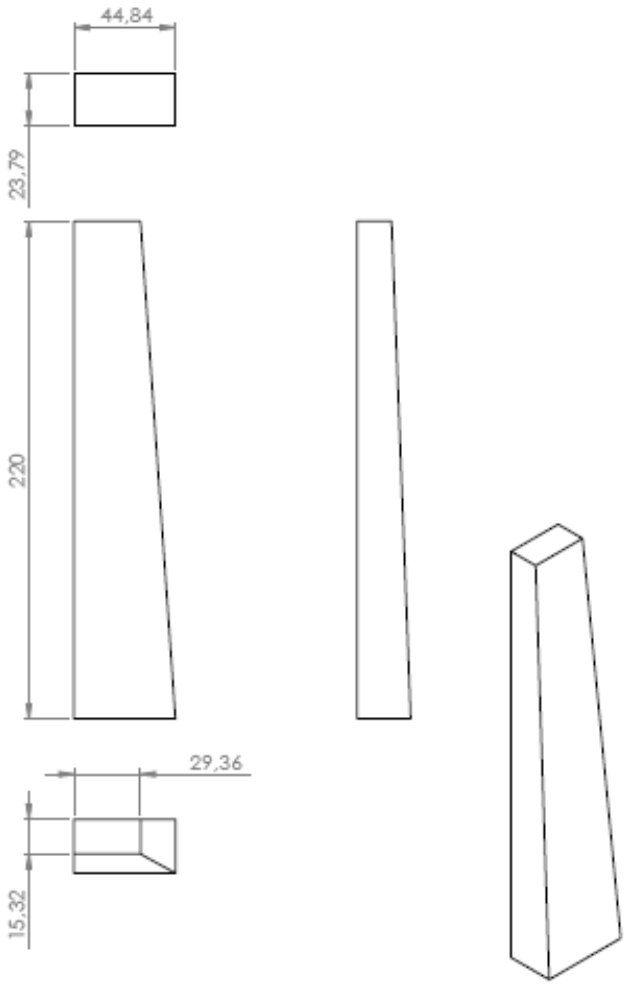

Figure 2.4.: *Technical drawing corresponding to a typical CALIFA frustum crystal located at 45º polar angle. (Distances in mm)*

Table 2.2 summarises the bulk properties of the CALIFA Barrel in terms of total number of crystals and different geometries corresponding to six crystal types associated to six angular sectors. The crystals are arranged in carbon fibre alveoli. Those associated to the first five forward angular sections are filled with four crystals corresponding to two different geometries that are mirror images. The last alveolus, covering the most backward angles, is filled with a single crystal. The average weight of the full systems is approximately 6tm, being about 4.3 tm of the associated weight of the mechanical structure and close to 1.3 tm of the CsI(Tl) weight.

The length of the crystals should be selected according to the detection efficiency required at the energy corresponding to each angular region; shorter for the larger polar angles where the Lorentz boost reduces the energy of the γ rays, and longer[3] for the forward polar angles. Conversely to efficiency, the crystal length adversely affects the energy resolution and consequently should be kept as short as possible. The optimum length has been determined according to the results of a dedicated simulation package (Chapter 4) and also regarding kinematical criteria. In Table 2.3 we present, as an example, the energy of

[3]In case similar material is used.

Inner radius	30 cm
Numb. of crystals	1952
Diff. crystal geometries	11
Av. crystal volume (CsI(Tl))	$\approx$ 285.000 cm^3
Av. crystal weight (CsI(Tl))	$\approx$ 1300 kg
Full operation system weight	$\approx$ 6100 kg

Table 2.2.: *Bulk properties of the 'Barrel' section*

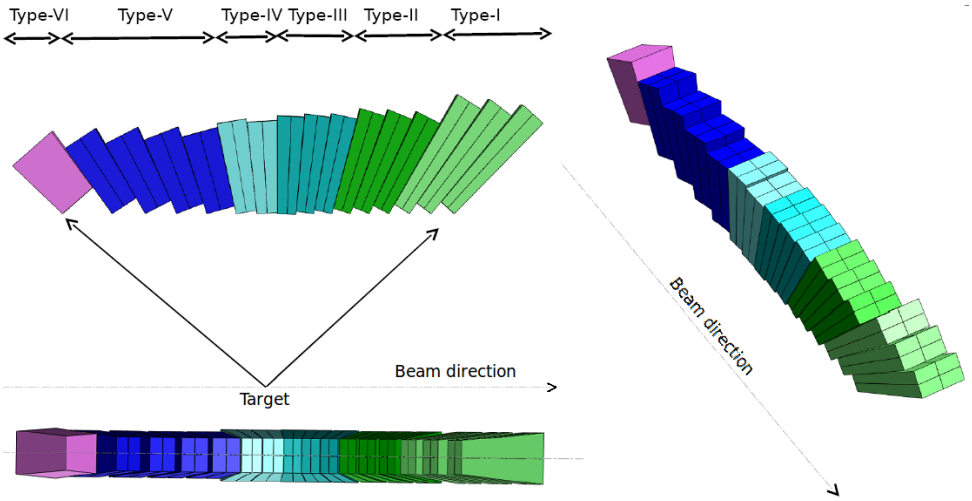

Figure 2.5.: *Different artistic views of CALIFA Barrel crystals geometry*

protons emitted after a (p,2p) QFS reaction induced by projectiles at 700 A MeV in the angular region corresponding to the furthermost forward angles of the CALIFA Barrel. The range evaluation for those energetic protons fixed the length of the crystals; for the region which covers the most forward angles of CALIFA Barrel this value was determined to be 220mm. Fig. 2.5 shows different perspectives of CALIFA Barrel crystal profiles distributed in the six aforementioned angular sectors.

The dependence between crystal length and energy resolution degradation is particularly important for the case of long crystals; accordingly this has been studied experimentally, the values kept in such way that the requirements defined in Table 2.2 are preserved.

θ (°)	E$_p$ (MeV)	p range(mm) in CsI(Tl)
43	319	220
45	295	196
47	271	171

Table 2.3.: *Kinematics of protons emerging from the QFS (p,2p) reactions induced by relativistic projectiles (700 A MeV) together with the corresponding p range on CsI(Tl).*

type	polar angle coverage °	azim. base mm	polar base mm	polar o. angle °	azim. o. angle °	height mm	weight kg	number of rings	number of pieces
I	43.2 - 55.5	29.36	15.32	92.20	94.02	220.0	0.73	3	384
II	55.5 - 70.4	29.39	15.34	92.27	94.90	180.0	0.58	3	384
III	70.4 - 87.6	29.25	15.35	92.39	95.48	170.0	0.55	3	384
IV	87.6 - 101.2	29.37	17.85	92.92	95.50	160.0	0.60	2	256
V	101.2 - 132.6	29.37	24.80	92.74	94.54	140.0	0.63	4	512
VI	132.6 - 140.35	67.77	69.69	95.00	94.54 - 93.90	120.0	3.14	1	32

Table 2.4.: List of the design parameters of CALIFA Barrel crystals. Types I to V have prismatic shapes, with a rectangular base, one edge extended at a 90° angle, and the other edges with two different opening angles in azimuthal and polar directions. Each type is cut in two mirrored symmetric shapes. In that way, four pieces of each type, with the two shapes paired, form a prismatic shape growing in both polar and azimuthal directions, as for the alveoli. Type VI crystals fill a single alveolus.

Table 2.4 summarises the final characteristics for the CALIFA Barrel crystals.

Incorporation of the numerous design parameters detailed throughout this Chapter result in the construction of CALIFA being an extremely challenging task. In order to successfully accomplish this, it was agreed by the R^3B collaboration to schedule the following different construction stages. The first is intended to be the construction of a detector Demonstrator that comprises a significant fraction of the ultimate number of detection units (up to 576) to be employed in the CALIFA array, corresponding to approximately 20% of the final detector. The construction of this device is scheduled to commence in the first quarter of 2012. It has a modular structure comprised of (up to 8) different units named Petals. A Petal is a set of 9x2 carbon fibre alveoli, each alveoli holding four different crystals (72 in total) covering the furthest forward angles of the CALIFA Barrel (Type I in Fig 2.5).

The CALIFA Demonstrator (see Fig. 6.18), in addition to performing as a real test bench for the construction of the full CALIFA, will be used in Cave C as part of an intensive physics program, commencing in 2013, in conjunction with the new GLAD magnet and the Neuland Demonstrator. The determination of this dedicated physical measurement campaign will be regulated by the R^3B collaboration, with plans for a call for proposals in 2012.

3. Detectors and Readout Devices

This Chapter presents the research and test program for detectors and readout devices that the Calorimeter Working Group (CWG) of R^3B undertook (2006-2011) in order to define the properties of the detectors for the large-angle part of CALIFA. The Technical Proposal (TP) [AJ05], describes CALIFA as one of the major tools of the R^3B program at FAIR, which must act both as spectrometer and calorimeter with capacity to register and measure precisely energies of γ rays and protons and even heavier nuclear fragments. It will also operate together with a silicon tracking system, that determines the trajectory of charged particles emitted from the interaction point.

3.1. Crystals for the Barrel

The most important decision for the calorimeter is the selection of the most appropriate scintillation materials. Table 3.1 presents potential scintillating materials for the CALIFA Barrel. The given resolutions and material constants are taken from the literature. Other high quality materials, some currently under development, such us SrI_2,CYGAG(Cl) or LYSO, were ruled out due to individual arguments pertaining to mechanical stability, light output, internal radioactivity or price, but primarily the issue of mid-term availability of larger quantities.

The standard detector, for which the γ-ray energy resolution at 662 keV is presented in Table 3.1, was read out by a Photonis XP5300B Photomultiplier Tube (PMT) with a photo-cathode with a maximum Quantum Efficiency (QE) of 20% (λ = 500 nm) and an active area larger than the back end surface of the crystal. The TP requires a resolution of $\Delta E/E \approx 5$ % (FWHM) at 1 MeV γ-ray energy, which had not been achieved for any CsI(Tl) detector at the time.

The $LaBr_3$(Ce) and $LaCl_3$(Ce) crystals, exhibit the best energy resolution and are therefore good candidates for the Forward EndCap ($\theta < 43^\circ$). Due to the large quantities and

Material	CsI(Tl)	$LaBr_3$(Ce)	$LaCl_3$(Ce)	NaI(Tl)
Density (g/cm^3)	4.51	5.29	3.86	3.67
Light Output (photons/MeV)	52k	63k	49k	39k
$\Delta E/E$ (% at 662 keV, PMT)	6	3	3.5	7
Sensitivity peak (nm)	550	380	350/430	310/415
Decay constant (ns)	700/3300	25	25/213	620/230
Hygroscopic	Slightly	Yes	Yes	Yes
Radiation Length (cm)	1.86	1.881	2.813	2.59

Table 3.1.: Main properties of different scintillator materials

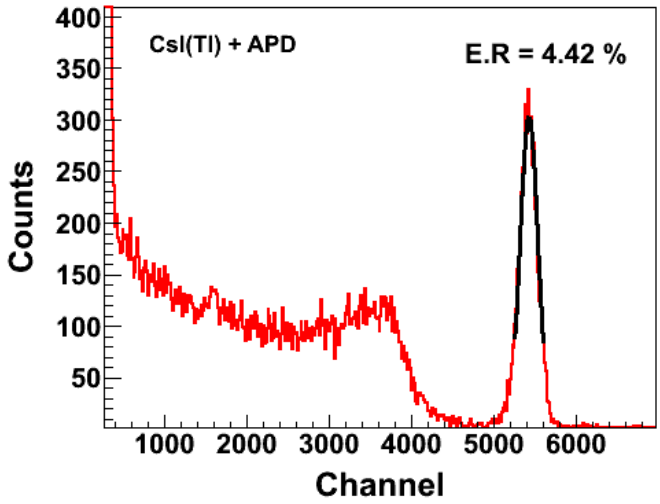

Figure 3.1.: Example of the best energy resolution achieved for 1cm^3 CsI(Tl)coupled to a S8664-1010 Avalanche Photo Diode (APD) [GAPB+08a]

the shaping of the crystals needed for the Barrel, it would be difficult to use these new materials. Aside from the price, at the moment the manufacturer (St. Gobain) mounts these crystals only in rather massive cans, which will not allow for the high segmentation necessary to function as R^{3}B calorimeter.

NaI(Tl) exhibits a similar energy resolution to CsI(Tl) whereas CsI(Tl) has higher density. NaI(Tl) is cheaper, but it is strongly hygroscopic and therefore requires extra housing. The experience with CsI(Tl) is that no special precaution is needed in this respect; although long-time storage in humidity controlled environment is recommended.

The γ-ray energy resolution of the CsI(Tl) detector was re-evaluated during the R&D phase, this time coupled to Avalanche Photodiodes (APD), yielding significant improvement. Fig.3.1 shows an example of the γ-ray energy resolution obtained for a 1cm^3 CsI(Tl) crystal coupled to a well matched Avalanche PhotoDiode (APD), the S8664-1010 from Hamamatsu. The resolution obtained with a ^{137}Cs source is 4.42 % [GAPB+08a] (ΔE/E). This excellent result initially motivated the choice of CsI(Tl) as the scintillator material for the CALIFA Barrel. Further details concerning the resolution for detectors of CALIFA Barrel geometry are discussed in the following sections. Due to its two decay time constants, CsI(Tl) also provides a good proton - γ ray and neutron - γ ray separation using pulse shape analysis (see Chapter 5). This additional feature will allow for a better background suppression especially in the intermediate energy region.

Five producers of CsI(Tl) crystals were identified. Detectors of CALIFA Barrel type were delivered by four of these companies for preliminary tests. All producers proved to be able to deliver functional crystals of the requested geometry, however some differences in quality were observed. Several batches of CsI(Tl) crystals, containing approximately 100 samples, were tested using γ-ray sources with both PMTs and APDs as readout devices. These crystals were supplied by Amcrys-h Ltd, Kharkov, Ukraine; St.Gobain Crystals, Nemours, France; IMP, Lanzhou, China; Scionix, The Netherlands.

In conclusion, CsI(Tl) provides good intrinsic energy resolution and has a sufficiently high effective charge. Furthermore, it is weakly hygroscopic, reasonably cheap and easy to manufacture with several producers available. The final selection of CsI(Tl) as detector material for the Barrel was made based on these arguments.
We present in the next subsections a summary of the research program performed that has defined our final certification and quality requirements for the crystals presented in Chapter 8.

3.1.1. Light Collection Uniformity

Long crystals with mirror polished facets exhibit light output non-uniformity when irradiated at different positions along the main axis. The effect is caused by light attenuation and optical focusing. Light attenuation yields a decrease in light output with increasing distance to the photosensor, conversely to the effect of optical focusing [BGGR+94]. For CALIFA crystals the optical focusing effect prevails. For crystals with uniform dopant concentration and surfaces with mirror reflectivity, this results in an exponential drop in light output along the main axis as the distance to the photosensor becomes smaller. Starting from such a dependence, lapping can be applied in order to achieve a uniform light output.

Crystals differ in light output uniformity significantly depending on the manufacturer, but also between samples from the same manufacturer. Variations in light output, ΔLO $\simeq$3-7% have typically been measured. Consequently, to exploit maximum performance, each element of the calorimeter will need individual surface treatment.

The effect of non-uniformity in light output on the proton spectrum can be illustrated by a model calculation. For protons the light response in a CsI(Tl) crystal can be expressed as:

$$L(E) = a \cdot E^b \tag{3.1}$$

with b $\simeq$1.0. If one assumes a linear decrease in light output, ΔLO, along the crystal length, the light response, $L(E)$, for the path of an incoming proton of energy E, can be obtained by stepwise integration to give a relation between ΔLO and the corresponding change in $L(E)$, [DAC+09, AJN+01]. The resulting relation can, as a percentage, be approximated by:

$$\Delta L(E) = 0.36 \cdot \Delta LO. \tag{3.2}$$

Fig. 3.2 shows an example for this calculation where protons are detected in a crystal with a 5 % and 10 % change in light output along the crystal axis. This gives rise to a variation in the energy determination of 1.8 % and 3.6 %, respectively. This effect is particularly important when gain-corrected summing of signals is used.

This effect will be even more important for high-energy γ rays, where interaction points can be distributed over the entire crystal volume.

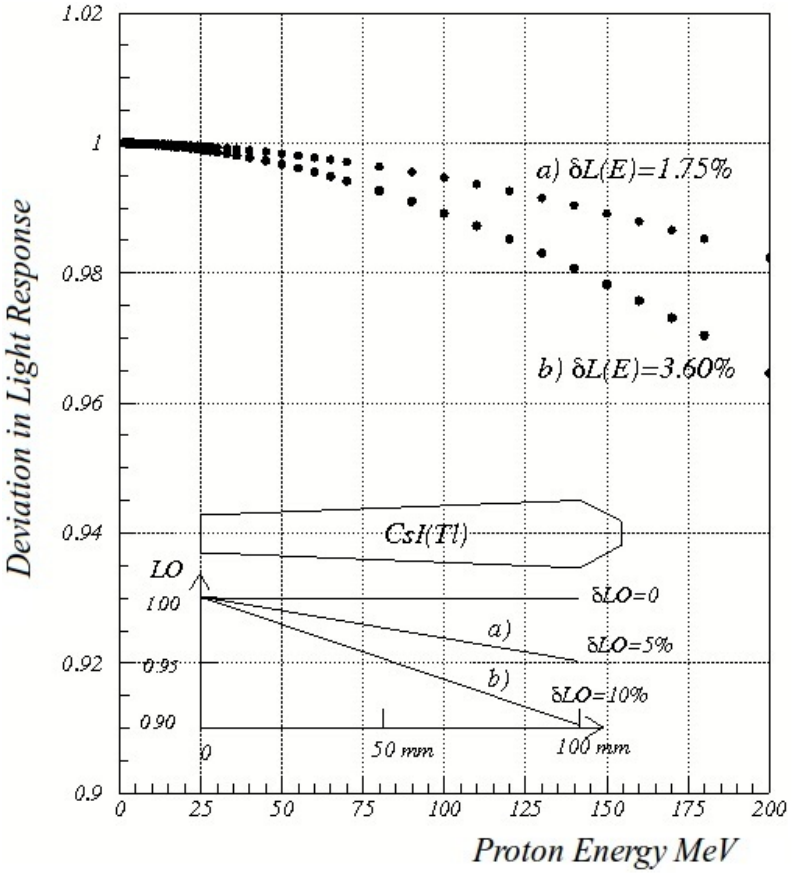

Figure 3.2.: The calculated deviation of the light response for protons with a given energy for the case of a linear non-uniformity in the light output along the crystal length, ΔLO=5% (a) and 10% (b).

Uniformity adjustment

Methods to obtain a more uniform light output based on changing the reflectivity of the crystal surfaces have been introduced in earlier work [BRQ05, Gra08, The02, Zhu94]. These methods result in a uniformity within ±2%. For the CALIFA project a specific lapping method has been investigated.

The crystals used in this work had an initial deviation in light output, $\Delta LO \leq 8\%$, over a length of 100 mm. Lapping was applied to the rear half of the crystal surface using Al_2O_3 powder with 10 μm grain size. The starting point for the lapping depends on the ΔLO value. Even for a significantly non-uniform start value, a uniformity better than 1% could be obtained after lapping (see Fig.3.3).[1]

Crystals can suffer from radiation damage during in-beam operation. In a CsI(Tl) crystal radiation damage leads to the formation of colour centres that reduce light transmission, which results in a decrease in the photon yield which in turn can lead to light uniformity

[1] The implementation of this careful lapping procedure will be very expensive and is in principle not foreseen for each of the CALIFA Barrel crystals.

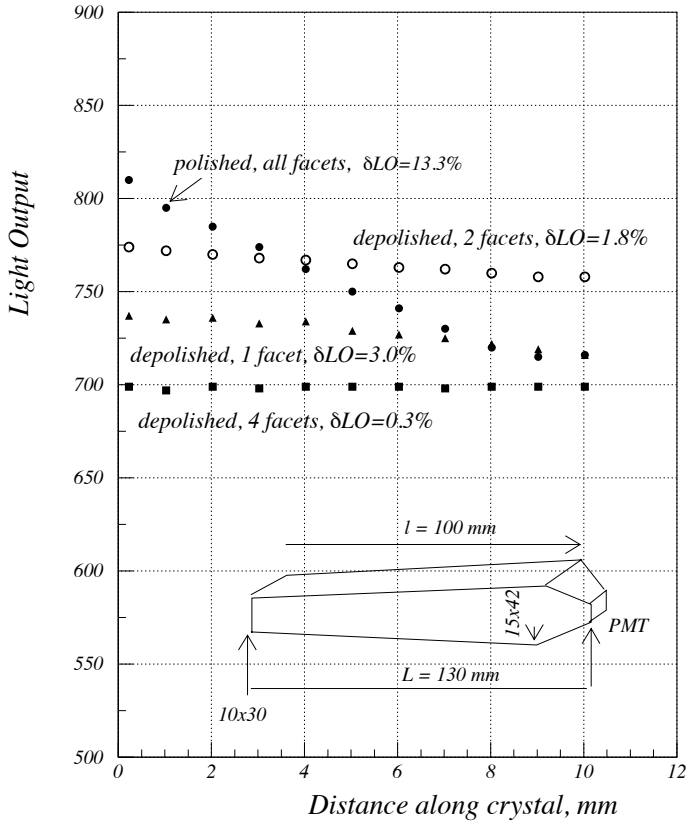

Figure 3.3.: De-polishing effect on the light output along a 100 mm CsI(Tl) crystal. Filled circles are data obtained for a crystal polished by the supplier. The other points show the influence of the de-polishing of the facets.

deterioration [DGI+00]. Changes in light yield and degradation in light output uniformity are not expected over time due to the short running periods and low radiation level of the experiment.

3.1.2. Wrapping

The absolute light yield from a crystal depends on wrapping material and wrapping technique. A basic requirement is that the wrapping is thin, but maintains good reflectivity. A number of different reflective materials, including a new material, ESR - Enhanced Specular Reflector - produced by the 3M Company [3M] were tested during this work.

Thermal heating of the wrapped element at 80°C for 30 min, was applied to make a tight wrapping between crystal and ESR foil. The ESR foil is partially transparent to light at viewing angles -40° to +40°. Each crystal individually wrapped in a single layer of ESR reduces the light cross-talk already to non measurable levels and provides good light collection.

ESR film has been used in other recent projects [BBB+04, SAB+07]. The conclusion drawn from the tests presented here is to use ESR film for the detectors of the CALIFA Barrel.

3.1.3. Crystal Ageing

CsI(Tl) crystals are slightly hygroscopic and particularly polished or lapped surfaces may react differently to moisture and thus affect the light output along the crystal length. To study this effect, two crystals differing by length and lapping were tested for ageing effects. The two crystals were kept at normal laboratory conditions for a period of 6 months and measurements were made 1 h, 1 day, 1 month and 6 months after lapping.

A 200 mm long crystal, which had an initial non-uniformity of ∼7.4%, was lapped over the full length of two facets and a non-uniformity of 1.1 % was obtained. The difference in light output uniformity between tests over the six month period was negligible. The second crystal of 100 mm length had an initial non-uniformity in light output of ∼ 3.5%. It was lapped over the rear quarter of the length and a non-uniformity of 1.5% was reached. A small change in uniformity, 0.6 % after six months, was observed in this case

Cold dry air could be used to keep the humidity in the calorimeter below 10% [DGI+00]. Such air flow may also serve to stabilise the temperature of the CsI(Tl) elements within 1 °C. Another approach to stabilise humidity is to circulate nitrogen through the full volume of the spectrometer. A stability of 1 ± 0.5 % has been reported using this method [The02]. For CALIFA a combination of methods will be employed.

3.2. Readout Devices for the Barrel

The requirements for the CALIFA detectors include impermeability to the magnetic fringe field of the R^3B GLAD magnet, where fields up to 30 mT occur. In order to accurately record both low energy γ rays and high energy protons (≈300 MeV) they must also cover a large dynamic range. These criteria come in addition to other important photosensor characteristics such as QE, time response, linearity and stability to temperature and voltage variations. The selection of a readout device for CALIFA is therefore not straightforward and several readout devices (i.e: PMT, PD, SiPM and APDs) have been investigated in laboratory and accelerator tests. The detailed description of the results from measurements performed with Photomultipliers (PMTs) and Photodiodes (PDs) are presented in Appendix B.

Standard PDs can be used as readout device for detection of protons and high-energy γ rays, but high noise levels make it difficult to achieve a satisfactory threshold and energy resolution from low energy γ rays. PMTs can be shielded for moderate magnetic fringe fields, but inclusion of μ-metal shields would require a different packing geometry and a rather complex support structure. The fringe field of the GLAD magnet strongly depends on the precision of the coil geometry and might easily exceed the typical limit of 20 mT for thin shields. First real measurements of this field cannot be performed before the installation in 2013, so it would be a high risk to use PMTs, especially for the forward region of the Barrel in very close proximity to the magnet. Additionally the QE of PMT's is significantly lower compared to silicon, which is only partly compensated for by a larger active area. SiPM were also investigated. Current modules still have two major disadvantages. Firstly, the typical pixelisation does not allow for a QE greater than 30% due to the ratio of active

Photosensor type	APD S8664-55	APD S8664-1010
Active area (mm^2)	5×5	10×10
C (pF)	80	270
QE (560 nm,%)	80	85
I_d (25^o, nA)	2-5	10-50
Gain	40-50	40-50
Gain vs. V (1/M*dM/dV,%)	3.3^a	2.0^b
Gain vs. T (1/M*dM/dT,%)	-2.2^a	-4.5^b

Table 3.2.: Summary of tested APDs.

[a] - measured by CMS
[b] - R^3B/CALIFA measurements taken over a large T range.

to total area. Secondly the number of pixels is insufficient to cover the large dynamical range needed for CALIFA.

The conclusion drawn from the tests performed is that APDs are the preferred solution for CALIFA Barrel Photosensors. This is due to their insensitivity to magnetic field, their high QE, their relatively high gain and the recent development of APDs with large sensitive areas. APDs exhibit gain variations that depend on voltage and temperature. However, these variations can be compensated as detailed in Chapter 5).

The APD combines the properties of the PIN PD and the PMT. It has a QE between 75-80% in the CsI(Tl) emission spectrum, an internal gain of 40-50 and a linear light response in the 400-800 nm region. Basic properties for APDs are presented in Table 3.2. Fig. 3.4 shows different Hamamatsu APDs from the S8664 series used within this work. The commonly used APD S8664-55 is the result of R&D carried out by the CMS Collaboration and Hamamatsu Co. This APD has found wide application in calorimeters for high-energy physics [ABI+05, BBL+09] and its characteristics are well studied. The model, S8664-1010 [Ham], has been developed by the PANDA-Hamamatsu collaboration and was rigorously investigated within this work since their performance is well suited to the CALIFA requirements.

Additional tests with prototypes developed by PANDA [Wil] with an active area of 7x7 mm^2 (S8664-77) were also performed.

In the following sections we present different aspects of APD functionality that have been studied. The results were used to define the final certification and quality requirements that are presented in Chapter 8.

3.2.1. Dark Current and Noise

The Hamamatsu S8664-1010 APD has a nominal gain M=50, in the voltage range 380 - 450 V, at +25 ^{0}C. Higher gains than M=50 can be reached; however, beyond this value the stability of the gain drops and the rise in excess noise becomes crucial for the energy resolution. More than fifty S8664-1010 samples with a specified gain of M=50 at T=23 ^{0}C were tested in this work. The dark currents for the APDs in the batch, given at their

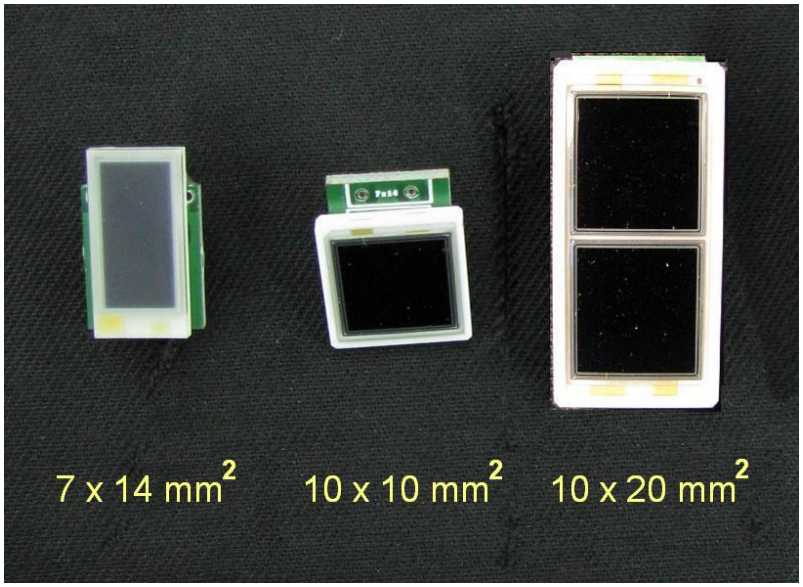

Figure 3.4.: Hamamatsu APDs from S8664 series tested within this work

respective nominal voltage, V_{nom}, ranged from 10 to 50 nA, with an average dark current of ∼30 nA when no special requirements were asked of the manufacturer. The dark current was ∼18 nA, with very small spread, when low I_d selection (maximum 20 nA) was requested. The I_d selection is important, since the spread in current influences the spread in APD electronic noise and therefore affects the energy resolution.

3.2.2. Temperature Dependence

The APD gain, dark current and the electronic noise of the APD/preamplifier depends on temperature [A+a, Gas10]. The effect has been explored for APDs working at the nominal bias voltage V_{nom} (see Fig. 3.5). The gain–temperature dependence is displayed in Fig. 3.5 and was measured to be $(-2.8)\%/°C$ in the range 22-24 °C. This value compares well to the $(-2.5)\%/°C$ given by Hamamatsu [IKY+05]. A larger variation $(-4.82\pm0.15)\%/°C$, at V_{nom} (see Fig. 3.6) was measured when the temperature range was extended to 0–25°C.

The current dependence on temperature can be expressed as:

$$I_{db} \simeq aT^2 exp(-E_t/k_bT), \tag{3.3}$$

where k_b is Boltzmann's constant, E_t is the activation energy for silicon, 1.15 eV, and T is the absolute temperature. APD noise also increases with increasing temperature. The noise can be described by a $\sqrt{I_{db}\tau}$ dependence with a multiplication factor dependent on temperature. This dependence is more pronounced at higher bias voltage. Here It is important to notice that the gain-temperature dependence is also more pronounced at higher bias voltage.

In conclusion, for APDs at room temperature, a temperature variation of 1°C typically gives rise to a 2-3% change in pulse height. A system to avoid pulse height fluctuation due

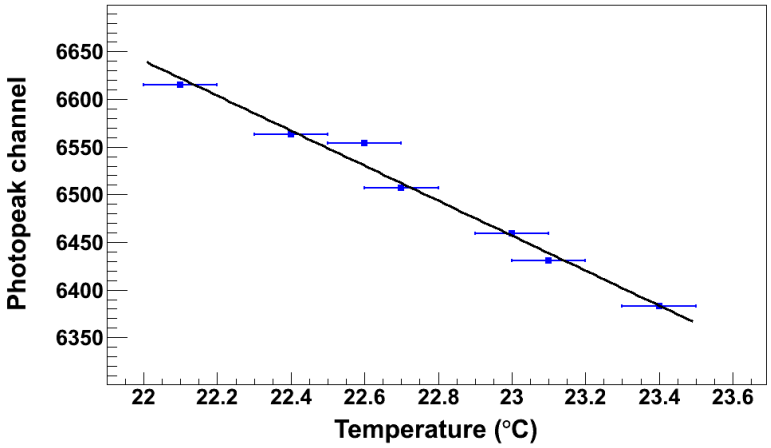

Figure 3.5.: Measured Gain-Temperature dependence for a Hamamatsu S8664-1010 APD.

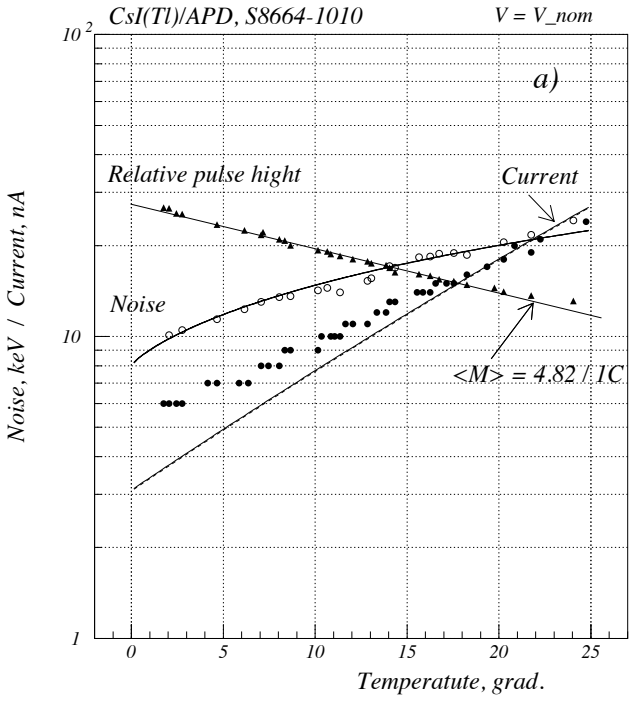

Figure 3.6.: Temperature dependence of the APD gain, current and electronic noise. Data were taken at V_{nom} and gain M=50 and T=23 ^{0}C. Current (dash-dotted line) calculations by Eq. 3.3.

to variations in temperature, at a level better than 1°C, is necessary to avoid degradation of resolution. In the case of the CALIFA Barrel, a solution has been found by compensating with reverse voltage variations. An alternative would be the continuous monitoring of the temperature at the APD level, enabling subsequent off-line corrections. These capabilities are implemented in the preamplification stage, the MSCF-16 amplifier is specifically developed for this purpose (see Section 5.3.4). As any such corrections should be kept to a minimum, the temperature variation will be minimized using twin cooling systems of air and dry nitrogen. (see Section 6.2.2).

3.2.3. Voltage Dependence

A compromise between high signal gain, noise and signal stability under change of temperature and bias voltage is important when optimising the energy resolution for scintillator/APD elements. The energy resolution of the CsI(Tl)/APD detector for a 662 keV γ ray as a function of the bias voltage (values around the V_{nom}) is presented in Fig. 3.7. The resolution shows a minimum at a voltage a few Volts lower than V_{nom}. This value defines the working voltage which must be determined in order to exploit maximum system performance.

Close to the nominal voltage both dark current and gain are sharply rising functions [MSKB02]. Gain and noise are therefore sensitive to bias voltage stability. Consequently the use of a slightly lower bias voltage leads to a more stable gain–voltage behaviour. The gradient of the signal output was measured to be typically dM/dV= 2.05±0.2%.

Summarising, there are two ways to maintain gain stability:

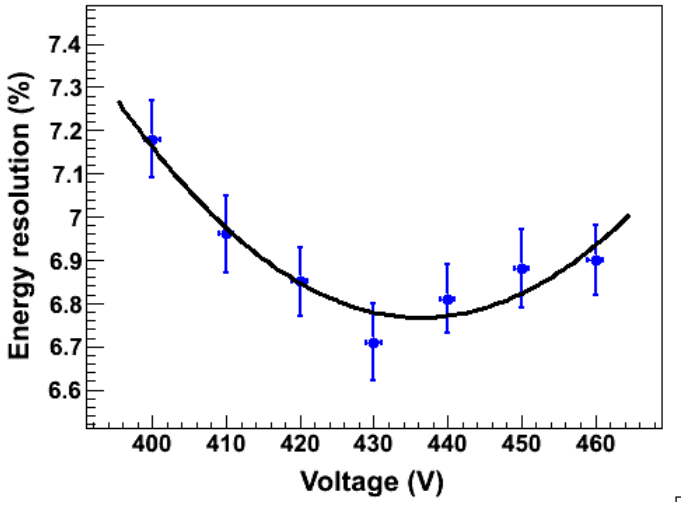

Figure 3.7.: Voltage dependence of the energy resolution achieved for along CsI(Tl) crystal connected to a Hamamatsu S8664-1010 APD. The minimum in this curve corresponds to the optimal working Bias Voltage. This value needs to be determined for each unit.

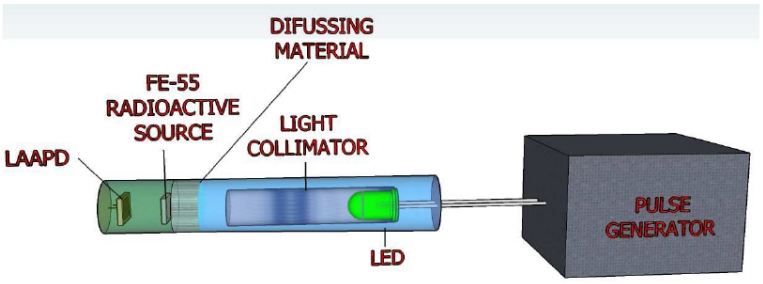

Figure 3.8.: Experimental setup for comparing different APD series/samples. The use of a radioactive ^{55}Fe source allows to calibrate the LED light yield as a function of the number of electron-holes created.

1. To apply an accurate gain-monitoring system which allows to correct for gain changes in the off-line data analysis [ACD+06].

2. To apply an APD bias voltage slightly lower than the nominal voltage. Typically, a voltage change relative to V_{nom} of about -5V is proposed in [MSKB02]. This latter method will be used for the CALIFA Barrel.

We have implemented a method (see [GAPB+08a] to determine the optimal voltage for each APD sample. The light-pulse resolution is defined as the FWHM of the LED pulse (in ADC channel units) divided by the channel number of the peak centroid. The optimal APD bias voltage is achieved when the light-pulse resolution is minimal, in a similar way as presented for the energy resolution and the complete CsI(Tl) and APD system in Fig. 3.7. The setup shown in Fig. 3.8 was used to measure the dependence of the light-pulse resolution on the APD bias voltage. The APD dark current was also measured at the bias voltage that gave the optimum light-pulse resolution. The APD bias voltage was obtained from the power supply value corrected by the voltage drop in the bias resistor network. The APD dark current was read out from the power supply (Iseg NHQ 225M) with a precision of 1 nA.

Fig. 3.9 (left) shows the light-pulse resolution as a function of the number of electron-hole pairs for the 10×10 mm^2 APD. From this plot, the APD contribution to the energy resolution can be deduced. The behaviour of the light-pulse resolution seems mainly to be due to the statistical variation given by the number of created electron-hole pairs (Ne-h) with an asymptotic value below 0.12%. This number was attributed to the electronic noise generated throughout the entire electronic chain.

Fig. 3.9 (right) shows a comparison of the light-pulse resolution as a function of the shaping time in the spectroscopy amplifier for three different APD sizes investigated. This figure compares the 10×10, 7×14 and a single channel of the 10×20 mm^2 APDs. For a 6 μs shaping time in the spectroscopy amplifier, the 10×10 mm^2 APDs had a light-pulse resolution of ≈0.6%. The 7×14 mm^2 APDs resolution was well above 0.7%, and the single-channel resolution for the 10×20 mm^2 APD was ≈0.65%. These values were obtained for light yields corresponding to around 7.10^5 Ne-h in Fig. 3.9 (right), where the statistical fluctuations in the APD are small. The saturation level here is mainly dominated by the detector leakage current, as previously discussed.

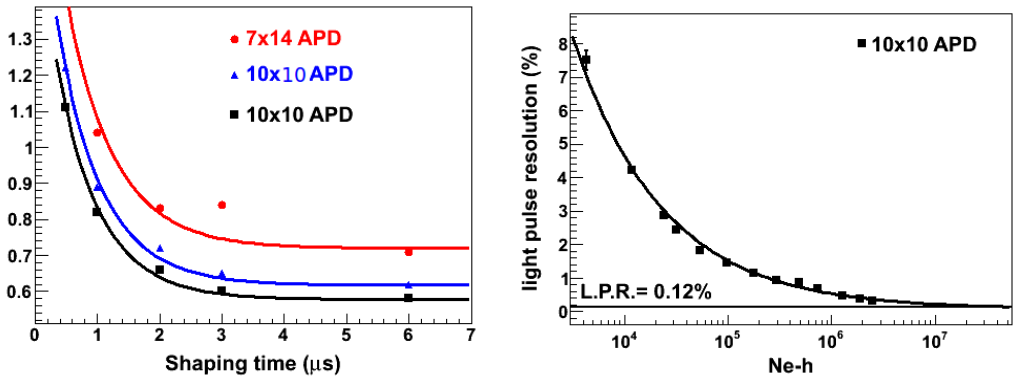

Figure 3.9.: Left: Light-pulse resolution versus shaping time for different APD sizes. Right: Light-pulse resolution versus Ne-h for a 10x10 mm^2 APD.

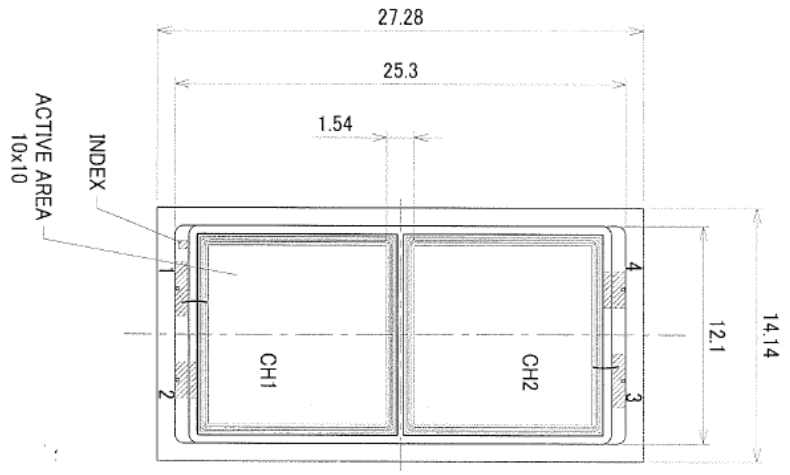

Figure 3.10.: Schematic of a 10x20 mm Hamamatsu double APD.

3.2.4. Development of Double APD-S8664-SPC1010 (2CH)

Based on the excellent results obtained with APD-S8664-1010, a joint venture with Hamamatsu, to develop a device with two APDs of this type in a common ceramic frame, was initiated. The objective was to retain the performance of the APD-S8664-1010 while increasing light collection by increasing the sensitive area. The design of the device is shown in Figs. 3.4 and 3.10. It minimises the dead zone between the two APDs. The two APDs, to be mounted in the same frame, were selected to have a deviation in nominal voltage of less than 5 V. Each individual APD was also selected to have $I_d < 25$ nA. Planarity of the detector is another important issue since it directly translates into a difference in the light collected by each unit.

The same voltage, given by the average of each individual working voltage, was applied to the twin APDs in the common frame. The charge signal from the twin APD unit was

added and treated as a single output. The experimental setup described in Fig. 3.8 was used to characterise the response of more than 50 APD-S8664-SPC1010 (2CH) units. The result of this characterisation was a 15% improvement in the intrinsic resolution of the system. Measurements undertaken using the setup described in Section 3.2.3 gave an average intrinsic resolution of 1.8 % for the S8664-1010 case, whereas a value of 1.5 % (with σ of 0.08) was observed for the S8664-SPC1010 (2CH) units.[2]

With regard to the optimum choice of LAAPD, an investigation of the performance of a single APD-S8664-1010 unit compared to a S8664-SPC1010 (2CH) unit revealed a 50% higher light collection efficiency for the S8664-SPC1010 (2CH) units, with a negligible contribution from crystal and wrapping properties.

This increase results in two main advantages;

Firstly, the significantly larger fraction of collected light with double APD sensors leads to a linear increase of the signal amplitudes in the detectors. The preamplifiers are designed to cope with the very large capacities and the increase of leakage current affects only the larger filter times. Therefore a larger value of energy deposited enables a significant reduction of trigger thresholds especially in cases of external noise sources which can play a more important role in larger systems. This does not only allow accurate measurement to extend to a lower energy range, but also is essential for the calorimetric properties where the collection of low energy residues from scattered γ rays enables an important improvement in the total energy recorded.

Secondly, an important factor is the improvement on final energy resolution. A direct comparison of the energy resolution of CALIFA Barrel elements for γ rays from ^{137}Cs and ^{60}Co have been investigated for two cases: a) readout with a single APD-S8664-1010 unit, and b) readout by S8664-SPC1010 (2CH) unit. The DAQ system used in both cases is the same and allows the direct comparison of the obtained results leading, in the case of S8664-SPC1010 (2CH), to an improvement of approximately 15 % (depending on the primary γ-ray energy).

Finally, a larger readout area is expected reduce the effetct of nonlinearity in the crystal as less reflections are used on average to collect the light.

These are the main arguments to equip the CALIFA Barrel with one Hamamatsu S8664-SPC1010(2CH) sensor per crystal. For a wider comparison, we report in Section 3.4 on measurements of the energy resolution for Hamamatsu APDs of the same series S8664-1010 and S8664-55 [3].

3.2.5. Radiation Damage

For CALIFA the parts most sensitive to radiation damage will be the APDs photosensors. Two components of the APD current can be distinguished; a surface current, I_{ds}, and a bulk current, I_{db}. The noise contribution from I_{ds} is reduced by the APD gain factor. The bulk current is more important because it is affected by the excess noise factor [HLN+95]. For APDs radiation effects consists of surface damage, caused mainly by γ rays, which

[2] 40 samples were measured.
[3] with active sensor areas of 10x10 and 5x5 mm^2 respectively

increases the surface current and deteriorate the APD QE, and neutron damage which causes defects in the silicon bulk and thereby increases the bulk dark current and noise. It has been shown [BFL+94] that the increase of dark current, I_d, under irradiation may be expressed as

$$I_d = \alpha \cdot V \cdot \Phi, \tag{3.4}$$

where V is the volume of the APD and $\alpha \simeq (8-10) \cdot 10^{-8}$ nA/cm for a flux Φ of ≈ 1 MeV neutrons. Taking the effective thickness of the APD as 7-10 μm and using a maximum dark current increase of 20-30 nA one can estimate the acceptable flux of 1 MeV neutrons for the CALIFA setup to be (2-3)$\cdot 10^{11}$ neutrons/cm^2. With an average estimated flux $\Phi = 5 \cdot 10^{10}$ neutrons/year of high energy neutrons (see Chapter 7) over the entire outer surface of the Barrel, there should be no influence of radiation damage from neutrons observable over a decade.

It is worth mentioning here that the APD devices have a higher radiation hardness than conventional photodiodes. The reason is the difference in the effective thickness; 7-10 μm for APDs and 200-300 μm for photodiodes. Neutron-induced radiation tests for photodiodes with regards to this work have also been performed[A+b].

In addition the radiation hardness of LAAPDs to medium energy protons was investigated. During a test experiment at the Maier-Leibnitz laboratory in Garching, Germany the influence of radiation damage caused by 24 MeV protons on the dark current of an Hamamatsu S8664-1010 LAAPD was analysed.

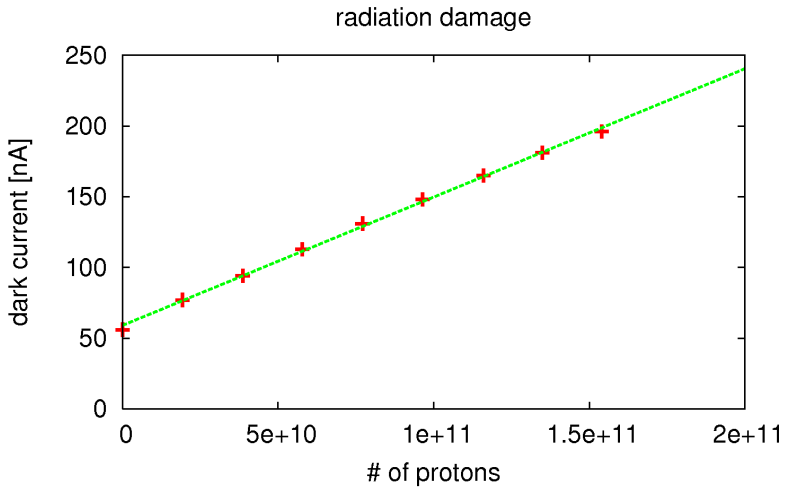

Figure 3.11.: Effect of radiation damage caused by 24 MeV protons on the dark current of an Hamamatsu S8664-1010 LAAPD. In the region up to 200 nA the dark current is proportional to the number of impinging protons.

In this test an LAAPD with an initial dark current of 56 nA was used. The assumed linear behaviour of the dark current with proton dose was observed (see Fig. 3.11). The bulk leakage current increased by about 1 nA per 10^9 protons incident upon the detector, which limits the operation to about 10^{10} protons/cm^2. This number is again several orders of

magnitude higher than the expected number of protons at the outer surface of the CALIFA Barrel per year.

These estimates lead to the conclusion that radiation damages caused by protons and neutrons is not a detrimental factor over the lifetime of the LAAPDs.

3.3. Resolution

Different prototypes have been used for energy resolution tests with standard radioactive sources and also under realistic experimental conditions (see Appendix A). We report in the following sections the main results obtained and differentiate the response to γ rays and light charged particles (protons). We restrict the presentation to those prototypes formed by CsI(Tl) crystals and read out by LAAPDs.

3.3.1. Energy resolution with γ rays

The first step consisted in determining the energy resolution with standard radioactive sources.

- A set of 15 CsI(Tl) crystals formed by two truncated rectangular pyramids was employed as a demonstrator. The crystals had a front area of 10×30 mm^2, a back area of 15×42 mm^2 and a length of 130 mm.[4] The light guide structure was an extension of the crystal itself. The rear facet of the crystal is 10×10 mm^2, matching the active size of the S8664-1010 APD. It allowed a collection of 44-51% of the primary light on the APD. This number is almost three times as high as the geometrical factor (the ratio of active areas of the CsI and APD). Crystals with a size of the rear facet of 10×20 mm^2 and 15×15 mm^2 were also tested using the same type of APD. By covering the extra surface with ESR film similar light collection and energy resolution was obtained under γ-ray testing.
  Each crystal was adjusted for light output uniformity to a level better than 0.7%, achieved following the lapping procedure described in Section 3.1.1.
  The measurement was done at an APD dark current I_d= 12 nA at T = 23^{0}C. The energy resolution of the elements for γ rays from ^{207}Bi, ^{137}Cs and ^{60}Co are presented in Fig. 3.12 [Aea].

  The spread in the light output from crystal to crystal in one batch is significant, but it has little influence over the final energy resolution.

- In total 32 longer crystals, designed for a prototype array, were also tested with radioactive sources. The crystals were formed by a truncated rectangular pyramids. The crystals had a front area of 14.7×29.3 mm^2, a back area of 21×41.3 mm^2 and are 190 mm long.[5] The rear facet of each crystal was coupled to an APD-S8664-SPC1010 (2CH) readout device detailed in Section 3.2.4. Each crystal was adjusted for light output uniformity to a level better than 4%, achieved after lapping performed by the manufacturer.

[4] This geometry corresponds to crystals located at polar angles of 90^0 in CALIFA Barrel.
[5] This geometry corresponds to crystals located at polar angles of 50° in CALIFA Barrel.

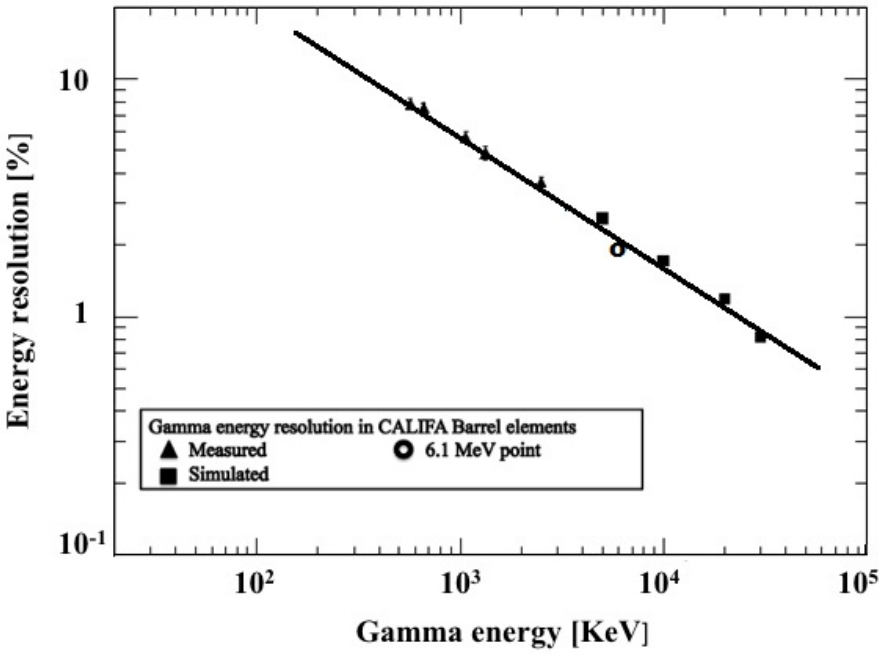

Figure 3.12.: γ-ray energy resolution for 130 mm long CALIFA detector read out by a Hamamatsu S8664-1010 APD. Experimental data from standard radioactive γ-ray sources are combined with the simulated response at higher γ-ray energies validated with a measurement point at 6.1 MeV

The measurement were taken at an APD dark current value of I_d= 20 nA at T = 23 ^{0}C.

The energy resolution obtained with both demonstrator systems are within the specifications of the CALIFA Barrel, namely ΔE/E $<$ 6% for 1 MeV γ rays (see Table 2.1).

The second step consisted in probing the energy resolution under the response to high energy γ rays. Those tests were performed in different European installations described in Appendix A.

In a complementary measurement to the test of the first detector array above (130 mm long detectors), 6.13 MeV γ rays were produced in the ^{19}F(p,$\alpha\gamma$)^{16}O reaction at the Lund University microbeam facility. Also the low energy γ rays produced by sources were remeasured under the same conditions, i.e. with detectors that all have a light output inhomogeneity $<$ 1%, cooling of detector and APD to + 3° C. Fig. 3.12 shows these results together with simulated resolution at higher energies (see section 4.3). It could be noticed that the measured resolution at 6.1 MeV falls rather below than above the simulated value.

- The first systematic test was done at CMAM with 6.1, 5.6 and 5.1 MeV γ rays corresponding to the de-excitation of ^{16}O first excited state and the associated single and double escape peaks. The prototype studied was a set of 16[6] CsI(Tl) crystals formed by two truncated rectangular pyramids. The crystals had a front area of 10×30 mm^2, a back area of 15×42 mm^2 and a 130 mm length. The light guide structure was once more an extension of the crystal itself. This time, the rear facet

[6]the prototype had 16 crystals, but only 6 were operative

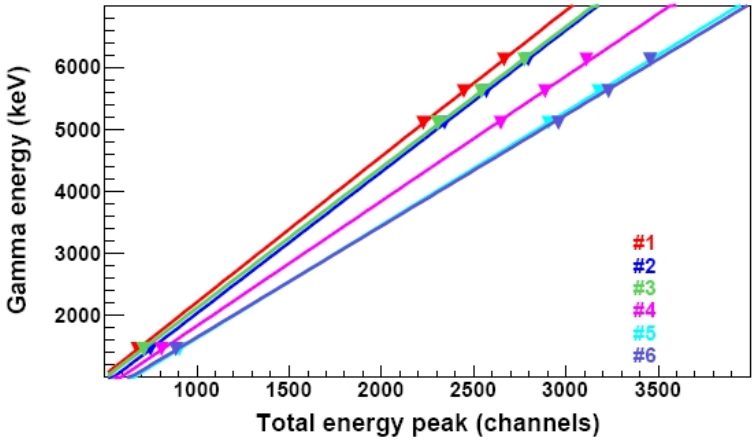

Figure 3.13.: Linearity of 6 CsI(Tl) crystals readout by APDs [Gas10].

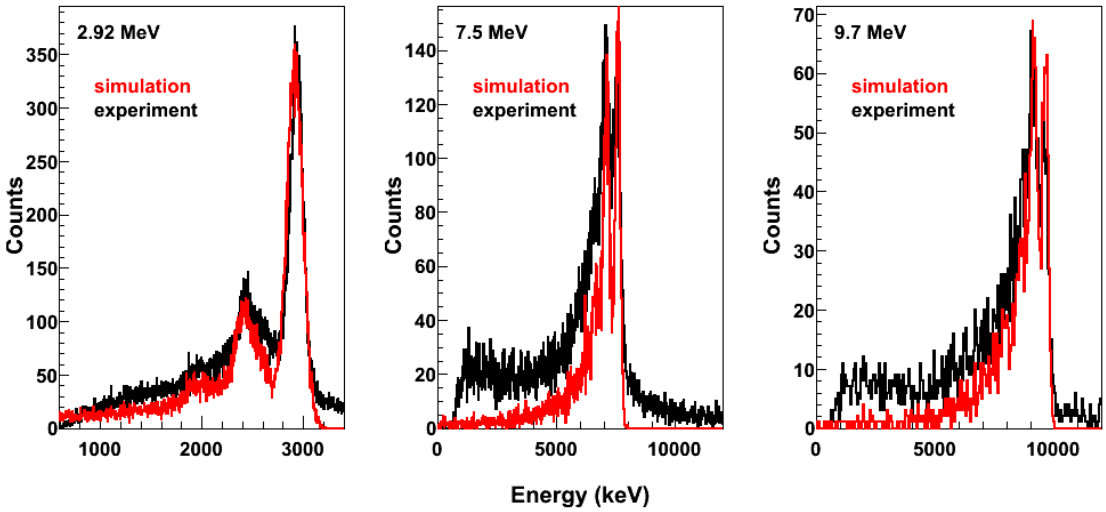

Figure 3.14.: Comparison of simulation and experimental values for the three tagged γ-ray energies [Gas10].

of the crystal was 10×10 mm^2 to match the active size of the S8664-1010 APD or 10×20 mm^2 to match the APD-S8664-SPC1010 (2CH). This experiment yielded energy resolutions of 3.4, 3.1 and 2.8% for the 5.1, 5.6 and 6.1 MeV γ rays respectively. Particularly interesting in this experiment is the observation of a linear γ-ray response for the CALIFA Barrel modules, shown in Fig. 3.13.

- The same 16 batch of CsI(Tl) coupled to S8664-1010 and S8664-SPC1010(2CH) APDs was exposed to higher energy tagged γ rays of 3.0, 6.3 and 9.3 MeV in the NEPTUN facility. As the main output of this test, we include a validation of the linear γ-ray response for the CALIFA Barrel modules up to energies approaching 10 MeV. This data also enabled the investigation of add-back performances and reconstruction procedures for CALIFA, illustrated in Fig. 3.14 (see Chapter 4 for details).

- The most recent prototype testing was performed at the Maier Leibnitz Labora-

tory of Technische Universität München, with 32 19 cm long crystals matched to fit S8664-SPC1010(2CH) APDs. During the experiment the prototype was exposed to high energy γ rays scattering throughout adjacent crystals, for example the 4.44 and 15.11 MeV γ rays released during the de-excitation of the 2^+ and 1^+ proton-excited states of ^{12}C. Energy resolution across a range of energy was measured, with values taken both from stationary source calibrations (511 keV, 1274 keV from ^{22}Na), γ rays emitted from an proton–activated carbon target (4.4 MeV and associated escape peaks). Measurements were performed with a MSCF-16 preamplifier with time constants set specifically for use with CsI(Tl) crystals and including an active gain variation with temperature correction (see Chapter 5), followed by a standard peak-sensing ADC.

The most important conclusions drawn from this work will be that the CALIFA Barrel detection modules used are within the specifications of the CALIFA Barrel, namely ΔE/E $< 6\%$ for 1 MeV γ rays (see Table 2.1).

3.3.2. Energy resolution with protons

The detector response to medium and high energy protons was tested in two different experiments in Uppsala and Munich (see Appendix A) at 180 MeV and 20 MeV respectively.

Fig. 3.15 shows a spectrum of scattered protons from the latter experiment. The measured width of the elastic scattered protons at around 20 MeV was found to be only 248 keV (1.2%). Furthermore, this width can be explained by the range straggling of the protons in the target and the limited angular resolution of about $\Delta\theta \approx 2^\circ$ in the setup. Thus that width serves only as an upper limit and the intrinsic resolution of the detector may indeed be better. The protons are stopped after 2-3 mm within the CsI(Tl) and interact only locally. So the effect of non uniform light collection is strongly reduced in this case and explains the good performance of the crystals in this measurement. A statistical extrapolation of this result down to 1 MeV would just correspond to the expected resolution of 5%.

For the higher energy protons measured in Uppsala the crystals showed energy resolutions between 0.8 and 1.1 % in this case, not dominated by the photon statistics.

3.4. Detector assembling

3.4.1. APD Mounting and Light Collection

In an ideal case the active area of the photosensor matches the geometrical size of the scintillator. The best energy resolution for the CsI(Tl)/PD structure [SGNB05] or CsI(Tl)/APD structure [GAPB+08b] have been obtained with a crystal of $10\times10\times10$ mm^3 and photosensor with active area of 10×10 mm^2. In most applications this is not the case. The ratio of the active area of the photosensor to the end surface of the crystal (the geometrical factor, GF) is usually smaller than one, thus the end surface is not fully covered by the photosensor. The influence on the light collection when adding a reflector (ESR in our case) was therefore investigated. The main conclusion was that a proper covering with

Table 3.3.: Collected light and effect of light guides.

Crystal type	$APD-1010/GF$	$APD-55/GF$
20×20-100-23×23 mm^3 (no light guide)	51%/18.9%	20.9%/4.7%
10×30-130-15×42 mm^3) (light guide, 10×10 mm^2)	44%/16%	18%/3.9%

ESR reflector of the rear surface of the crystal, not covered by the APD, increases the collected light by a factor of almost three and minimises the effect on energy resolution.

The effect of having a crystal light guide was also explored. Table 3.3 gives the test results for two different geometries for the CALIFA elements (with and without light guide) and also for two different geometries of the APDs themselves.

Two important consequences follow from the measurement. First, that the ratio of the active areas of the two tested APDs is 4/1, but the ratio of light collected by the APDs is $\simeq$2/1. Second, that the collected light is approximately 3-4 times higher when the ESR

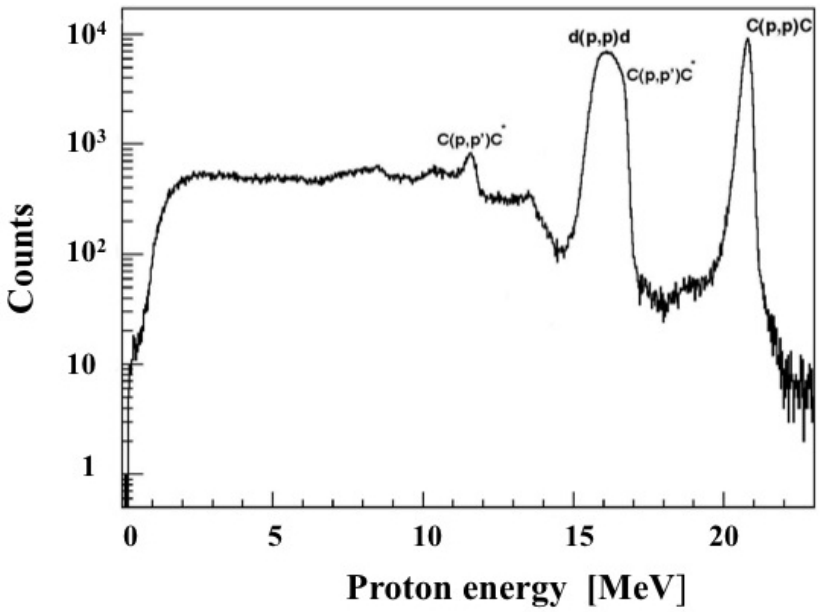

Figure 3.15.: Calibrated proton spectrum measured by scattering of 24 MeV protons on a deuterated PE target ($d = 70\frac{mg}{cm^2}$). A 15 cm long CsI(Tl) crystal was placed at a scattering angle of 45°, wrapped with one layer of the *3M Vikuiti Enhanced Specular Reflector* foil and read out by an *Large Area Avalanche Photo Diode* (LAAPD). The spectrum was acquired using the digital signal processing firmware, described in Section 5.5. The elastic and inelastic scattering reactions with the target can be observed as indicated on the figure. The FWHM resolution of the elastic scattering peak is mainly limited by the energy loss straggling within the target and had values of 317 keV (1,5 %)

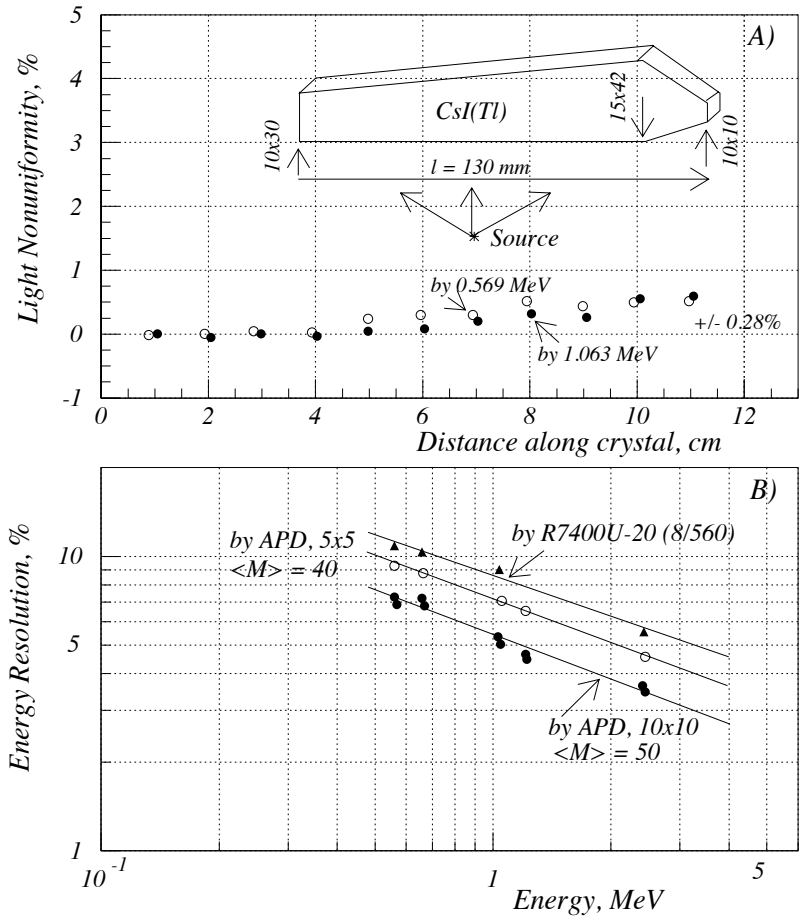

Figure 3.16.: Structure of the CALIFA CsI(Tl) element and the energy resolution measured by photosensors presented in Tables PCT1, PMT1.

foil is applied, but depends on the ratio of the active area of the photosensor to the rear surface area of the crystal. The dependence is different than what follows from simple geometrical considerations.

The effect of collected light on the energy resolution of the CsI(Tl)/APD detector for the APD-1010 and APD-55 is presented in Fig. 3.16. An increase in the APD active area of a factor of four results in an improvement of the energy resolution of the CALIFA element of 7.2%/5.2%=1.4 ($\approx$ 60% improvement).

3.4.2. Optical Coupling

Heat cycles may cause a degradation of the mechanical and optical contact between the photosensor (APD) and crystal surface when using hard optical glue. The basic requirement for the couplant is to create a soft, flexible bond with strong adhesion. Tests of heating and cooling cycles within the temperature range for CALIFA operation need to be made to measure the mechanical stability of the crystal to APD contact and potential changes in light yield.

Some of the tests presented in the previous Chapters utilise an optical grease as a couplant as it allows to dismount the crystal from the APD without damaging the APD surface. For permanent bonds the use of optical cement is recommended. The results reported for the different prototypes glued the crystals and APDs with Scionix RTV 811 [RTV] optical cement. This compound is an epoxy adhesive in a 10:1 mass ratio that has so far provided good results in terms of stability (12 months).

Elastic silicon glue, SE777, has been chosen in previous work [DGI+00] because of its fast curing time, stability against thermal cycling and almost 100% transparency. It is a colourless single component glue is easy to employ. After three years of detector operation no changes in crystal to PD coupling was reported. For coupling CsI(Tl) to PD in the GLAST calorimeter, DowCorning DC93-500 was chosen [BBB+04] as a best case among 10 tested couplants.

A bond process qualification plan will be established to study stability of the optical bond against thermal cycling before the final selection is made. No specific difficulties are expected during this process in view of previous work done on coupling CsI(Tl) to readout devices.

4. Simulations

The response of the detector crystals and the features and reconstruction capabilities of the CALIFA detector should be obtained from the meticulous analysis of a complete, detailed and precise simulation. This section describes the work performed to answer such relevant questions as the expected efficiency, resolution and reconstruction capabilities for different physical cases of interest for the whole calorimeter.

The first section provides an outline of the simulation framework employed; the R^3BRoot code, as well as a description of the CALIFA implementation. Event generators establish the initial point for the simulation of important physical cases, as well as providing the source of different particles for the evaluation of the detector. Following this section, the study, evaluation and optimization of algorithms for the reconstruction of γ rays and protons is presented. These algorithms have been used for the evaluation of the response of CALIFA under varying distributions of γ rays and light charged particles, relating to the study of several physical cases of interest.

4.1. Introduction to the simulation

This section contains the description of the R3BRoot code, the geometry of the CALIFA crystals and Barrel, the physical response to the passing of particles and the description of the event generations required for the evaluation of the detector.

4.1.1. The R3BRoot code

The R3BRoot code [Ber09] is an instance of the FAIRRoot framework developed for the description, simulation and data analysis of the R^3B setup and experiments.

The FAIRRoot framework [BMTKU08] is fully based on the ROOT system. The user can create simulated data and/or perform analysis within the same framework. Moreover, Geant3 and Geant4 transport engines are supported; however the user code that creates simulated data does not depend on a particular Monte Carlo engine. The framework delivers base classes which enable the users to construct their detectors and/or analysis tasks in a simple way [BMTKU08]. The FAIRRoot base library provides:

- A common data structure for simulation and analysis based on ROOT Trees.
- A common geometry description based on the ROOT Geometry Modeller.
- An interface to different Monte Carlo engines using the ROOT Virtual Monte Carlo package.
- Detectors base class handling initialization, geometry construction, hit processing (stepping action), etc.

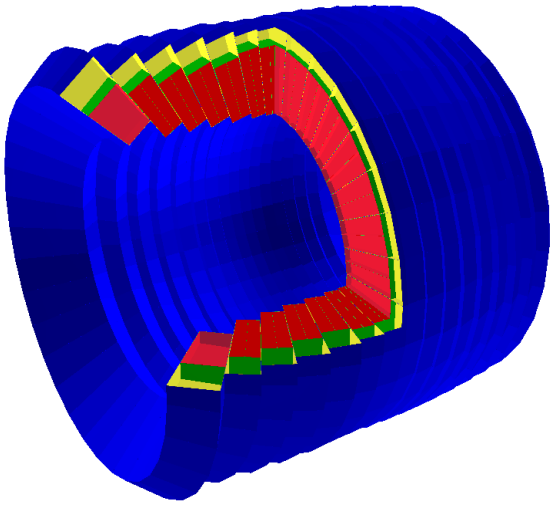

Figure 4.1.: A view of the CALIFA Barrel crystals in the R3BRoot event viewer.

- Geometry input readers supporting ASCII, ROOT and STEP (CAD) formats.
- A generic track propagation based on Geane [IMN].
- A generic event display based on Eve and Geane.
- A Runtime database for geometry and parameters handling.
- A Fast simulation base services based on Virtual Monte Carlo [BCHM] and the ROOT Tasks library.
- ROOT macro commands for steering the simulation and the analysis.
- ROOT macro commands for configuring the different Monte Carlo engines.
- A SVN repository to support code development and management.
- CMake [BY-] employed as a build system.
- CDash and CTest [BY-] are used for Code Quality Assessment.
- Grid computing using the Alien Grid Middleware from the Alice Experiment.

The R3BRoot code derives from the general classes of FAIRRoot and contains the geometrical and physical description of the detectors of the R^3B setup, magnetic field maps, event generators for the reactions of interest within its physics program and analysis and event visualization tools. It expands the framework behaviour by adding a dedicated physics list for low energy neutrons, γ-ray interactions and nuclear fragment transport while supporting a database connectivity to handle multiple experimental setup.

4.1.2. CALIFA description in R3BRoot

The CALIFA detector is comprehensively detailed inside the R3BRoot simulation and data analysis code, both geometrically and physically. The geometrical description of the CALIFA detector includes:

- The detailed volume of CsI crystals, modelled following the precise workshop drawings.
- The wrapping covering the crystals, with variable thickness for testing the influence on the event reconstruction.
- The carbon fibre alveoli that provide a support structure for the crystals.
- All relevant elements or detectors relating to the passage of matter between the production vertex and the calorimeter elements, including a vacuum container, the inner silicon tracker detectors and the target itself.

The full energy deposited in each crystal by all particles in each event is added and stored. The response of the detector is expected to be proportional to the total energy deposited. Effects exist that cause a deviation from this behaviour, such as non linearity in the light output-energy correlation and/or the non-uniformity due to the dependence in the interaction position. This last effect has been taken into account by introducing a variable step-function, smearing the detector response.

Two different data structures have been developed to account for the expected response of the crystals and the calorimeter. Firstly, for each crystal where energy has been deposited, a *CrystalHit* structure is filled, containing the total energy, the time of the first interaction in the crystal and the crystal identifier. Following the analysis of the event topology, a second data structure *CaloHit*, is filled containing the "clusters" or groups of CrystalHits which are expected to correspond to the same particle track crossing the detector. Section 4.2 deals with the algorithms used in this analysis and the results obtained.

4.1.3. Event generators

The evaluation of the performance of the CALIFA Barrel under different physics scenarios requires the construction of appropriate event generators, described within this section. Several event generators have been developed, ranging from trivial γ ray and particle distributions for testing the characteristics of the detector, to complex experimental events, to evaluate the reconstruction capabilities. In particular, we have focused our efforts in two different cases of great interest for the R^3B community where the CALIFA Barrel plays an important role: an example of nuclear spectroscopy and a typical giant-dipole resonance.

(Trivial) γ and particle distribution generator: a flexible code producing distributions of γ rays or charged particles is integrated within the R3BRoot event generators. The generator allows the selection of the particle type, angular emission (both in polar and azimuthal angles or angular region), the momentum (or momentum range), multiplicity and position of the emitted particles. Additional functions allow the generation of a flat distribution on the cosine of the polar angle for an isotropic angular emission, the random location of the vertex inside a volume which simulates an interaction within the target and the addition of the Lorentz boost for γ rays, with selectable projectile velocity.

This trivial generator has been used for the study of the core characteristics of the CALIFA Barrel detector described in this work.

Nuclear Spectroscopy and Giant/Pygmy Resonances: For these two cases a γ-ray cascade generator has been built. The input for the generator is an ascii text file in which the user can set the speed of the projectile (β for the Lorentz boost), its uncertainty due to the thickness of the target, and the main characteristics of the de-excitation pattern. This latter point is comprised of the position of a Giant Resonance, a Pygmy Resonance if applicable, their respective widths, the probability to populate each of the resonances in the reaction (i.e. cross section), the position of all the other levels (there is no limit on the number of levels), the probability to populate each level in the reaction, and finally, a branching ratio matrix which connects all the different levels and the resonances.

Fig. 4.2 shows an example of level scheme, branching ratios and population distribution that one might generate. The level at 9.5 MeV is not a narrow level but a broad resonance as one can see in the left spectrum (population) of the figure.

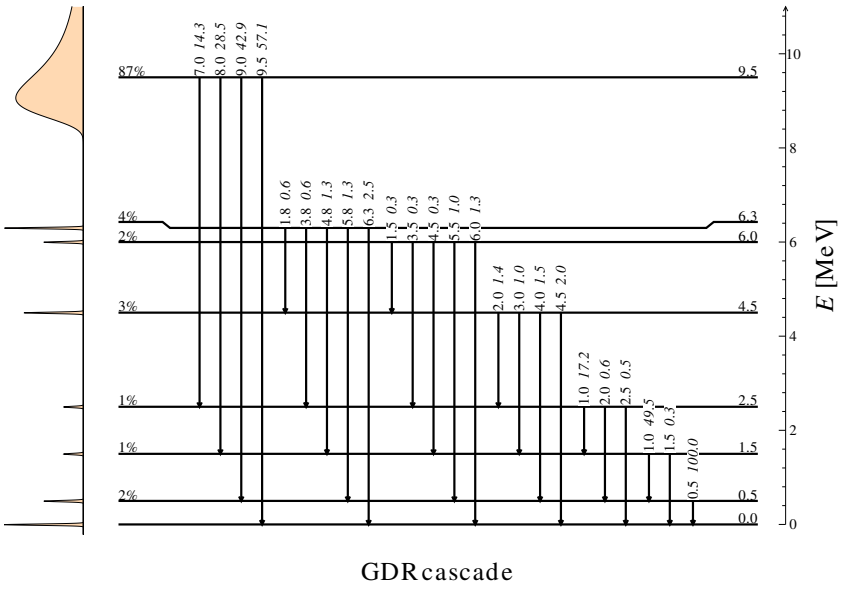

Figure 4.2.: Example of a generated decay scheme of a Giant Resonance. The level energy, in MeV, is written on the right side of the level while the population probability, in percent, on the left side. For the transitions, the energy and the branching ratio (normalized to the strongest transition) are shown. The left graph represents the population probability of the different levels in the final nucleus.

The output of the event generator, which is in fact the input for the simulations, can be seen in Fig. 4.3. In the top panel (a) of the figure the γ-ray spectrum in the projectile frame (PF) is shown. These γ rays are emitted isotropicaly in the PF frame . The lower panel (b) is the same γ-ray spectrum once the Lorentz boost is applied (β=0.5 in this case),

therefore in the Laboratory frame (Lab). We can appreciate how, in the Lab frame (lower panel), each energy peak of the upper panel is spread between a minimum and maximum level (depending on the angle of emission). This is the reason why the final spectrum is a continuum that shows steps instead of peaks. The emission of the γ rays in the Lab frame is not isotropic anymore but pushed forward by the Lorentz boost. In the particular case shown here, γ-ray cascades of multiplicity up to five have been generated.

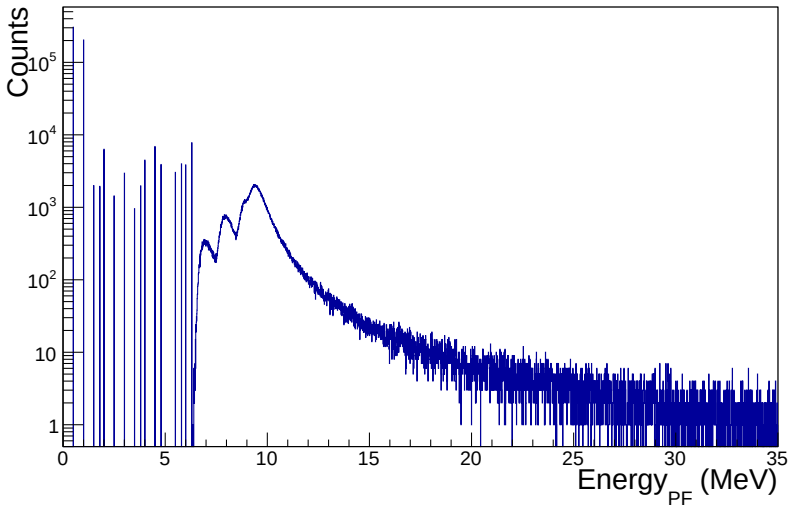

(a)

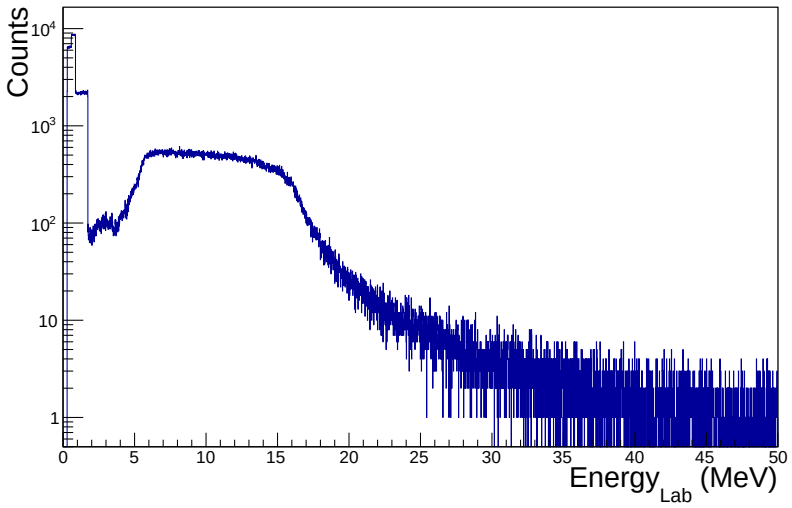

(b)

Figure 4.3.: a) γ-ray energy spectrum in the Projectile Frame (PF), corresponding to the decay represented in Fig. 4.2. b) The same γ-ray energy spectrum but in the Laboratory frame.

The γ-ray cascade generator can be used to generate events with low multiplicity and low energy γ rays instead of Giant Resonances simply by setting the probability to populate the resonance equal to zero and defining a very simple level scheme containing a few low energy levels. A Pigmy resonance can also be included besides the Giant Resonance as will be shown in Sec. 4.5.

Other event generators are available for specific reactions of interest. In particular, a kinematical Quasi Free Scattering (QFS) code based upon the Goldhaber model [Gol74], where the energy of the projectile nucleus is shared between the scattered protons in a way that is determined by their scattering angle, and hence the binding energy or internal momentum of the proton removed from the nucleus. The QFS of ^{12}C [^{12}C(p,2p)^{11}B] has been studied in this way, merging the proton distributions with Doppler boosted γ ray events emitted from the ^{11}B excited states decay.

4.2. Event reconstruction

Depending on the reaction under study, one or more particles are expected to be detected simultaneously by CALIFA. In addition, low-energy background produced via bremsstrahlung in the target or other mechanisms will contribute to the detected hits in a reaction. Thus, the development of intelligent reconstruction algorithms for both γ-rays and protons becomes mandatory in order to maximize the detection efficiency and resolution, the reconstruction of the single incident particles and the identification of possible contributions towards the low-energy background.

In the following, we present the steps towards obtaining efficient and robust algorithms, which mainly focus on the reconstruction of the correct energy of the detected photons. Beside the description of the algorithms we will provide benchmark tests to judge on the properties and quality of the reconstruction.

The most basic approach to an algorithm for the reconstruction of the γ-ray energy consists in summing up the energy of all the crystals in a selected angular region.
Two different approaches were adopted when considering the angular region for add-back purposes: a circular window, with just one parameter $\Delta\vartheta$ defining the solid angle covered by the window; and a square one, with two parameters ($\Delta\theta$ and $\Delta\phi$) defining the angular region considered. For one simulated event, as first cluster center the hit with the highest energy is chosen. All hits falling into the angular region around this center as defined by the two approaches is assigned to this cluster. After this procedure the crystal with the highest energy of the remaining hits is chosen as the next cluster center and the procedure is repeated until all hits above threshold (50 keV) have been assigned to a cluster. Each cluster corresponds to one identified incoming photon and the incoming angle is assigned by the angle of the cluster center. The performances of the two different definitions for the angular window were found to produce very similar results.

Simulations were performed considering photons of several energies (ranging from 0.1, to 10 MeV in the nuclear rest frame) under conditions equivalent to those expected in R^{3}B, emitted from a source at rest or moving at a velocity $\beta = 0.82$. The emission angles was varied isotropically in CALIFA's barrel solid angle. When only one γ-ray of energy E_γ per event was simulated, the efficiency was calculated as the number of hits in the photopeak (integration intervals $E_\gamma \pm 2\sigma$ where σ is given by the simulation parameters in the $\beta = 0$ case and by fit of the photopeak in the $\beta = 0.82$) normalized on the total number of γ-rays emitted into the solid angle covered by CALIFA's barrel. I.e., the calculated efficiency considers the intrinsic efficiency of the barrel and does not consider the geometric acceptance. A physical end cap (version 7.17) was present in the simulations, due to its importance in the event reconstruction, but no primary γ-rays were emitted in its direction.

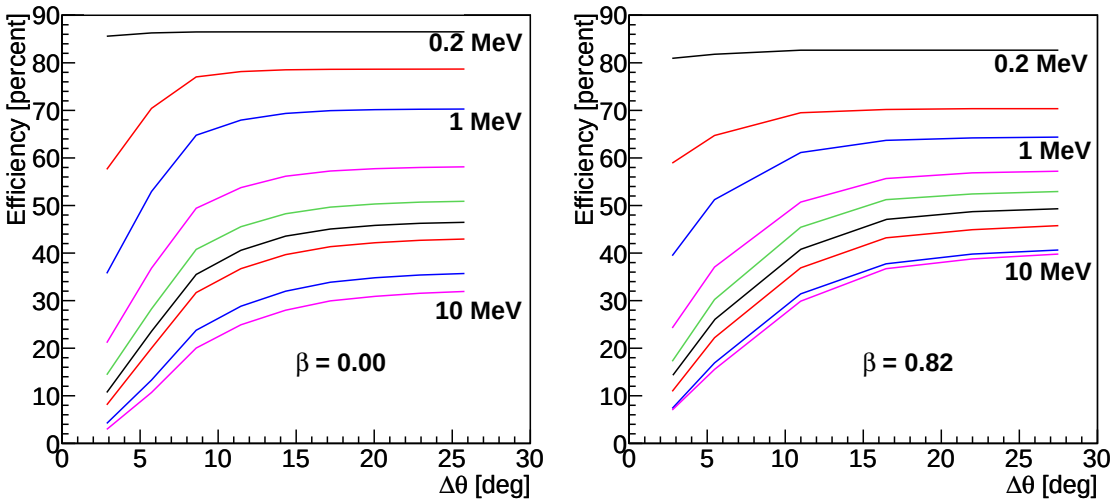

Figure 4.4.: Dependence of the efficiency of the clustering algorithm on the solid angle for add-back for various energies (from top to bottom: 0.2, 0.5, 1, 2, 3, 4, 5, 8, 10 MeV). Left plot: the source emitting the photons was at rest, i.e. $\beta = 0.00$; right plot: the velocity of the source was set to $\beta = 0.82$. Only one photon was simulated for each event.

In order to evaluate the performance of the reconstruction algorithms, the angular parameter was varied, analyzing the cases of a source at rest and moving at $\beta = 0.82$. The results of simulations with multiplicity one are shown in Fig. 4.4, respectively, where the obtained photopeak efficiency is presented as a function of the angular parameter.

From both figures we observed that, independent of the velocity of the source emitting the γ-rays, there is a certain angular window for which the algorithm saturates. This angular region shows a clear dependence on the energy of the photons, implying that the selection of a fixed angular parameter, not taking into account the energy detected in the crystal, might not be the most efficient way of reconstructing the energy of the events. The implementation of the energy dependence of the angular reconstruction parameter is an on-going work at this stage, which will improve the overall efficiency of the algorithm.

In the next step the performance of these algorithms has been studied considering events with multiplicity larger than one. In these simulations the source was always at rest (i.e. no Lorentz boost). In the reconstruction each identified cluster was assigned to one detected photon of the corresponding energy. The efficiency was again calculated as the integral of the photopeak corresponding to E_γ normalized to the total number of γ-rays emitted in the barrel direction. Hence, these numbers do not reflect the probability to detect an event with both correct multiplicity and energy, but to measure correctly the energy of one of the γ-rays emitted in the event. To get an estimation of the probability to reconstruct the event with the correct multiplicity these values should be raised to the power of the multiplicity. Fig. 4.5 shows the efficiency as a function of the clustering window size for different γ-ray energies (from top to bottom: 0.2, 0.5, 1, 2, 3, 4, 5, 8, 10 MeV). The simulation has been performed with the condition of having three γ-rays per event emitted in the direction of the barrel. The end cap was present due to its importance in the event reconstruction, i.e. secondary photons scattered into the end cap were also considered for the add-back procedure. The angular window, as parameter for the clusterization algorithm, can be

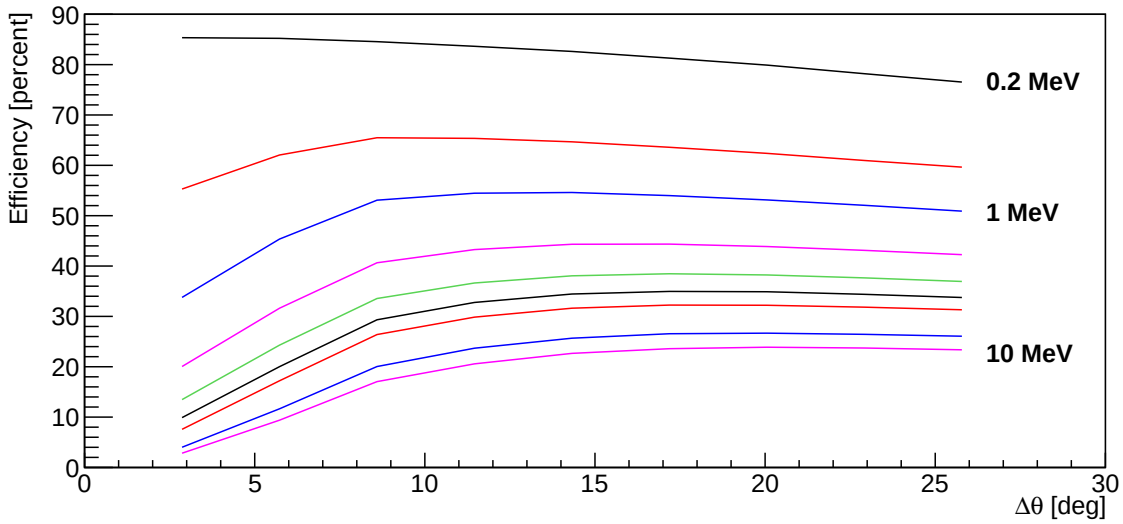

Figure 4.5.: Efficiency of multiplicity three events as a function of the clustering window size for different γ-ray energies (from top to bottom: 0.2, 0.5, 1, 2, 3, 4, 5, 8, 10 MeV). The simulation has been performed with three γ-rays emitted in the barrel direction per event.

optimized according to the detected γ-ray energy: A too small angular window is not able to collect all the crystal hits stemming from a single γ-ray, while a too wide window is leading to a mixing of crystal hits coming from different γ-rays. Both effects result in a lower photo-peak efficiency. For different energies, the maximum efficiency is attained at different values, pointing out possible dependencies that would help to improve the performance of the algorithm.

The shape of the efficiency curve for a given photon energy has been also studied for various multiplicities. Fig. 4.6 presents this dependence for the simulation of photons of 1 MeV with multiplicities ranging from 1 to 7. The efficiency is defined as the previous case, i.e. representing the efficiency of detecting one γ-ray with the correct energy. For this reason the efficiency is not dropping with the power of the multiplicity as the number of simulated γ-rays per event increases. In this way the effect of the decrease of photo-peak efficiency due to intermixing of hits stemming from different photons becomes more obvious and is directly represented by the loss of efficiency for higher multiplicities. The saturation effect that is observed for multiplicity one is due to the reaching of the maximum spread of the interactions in the scintillating material. For higher multiplicities this effect is combined with the mixing of crystal hits stemming from separate γ-rays which leads to an erroneous determination of the initial γ-ray energy. This effect is enhanced at higher multiplicities.

The performed studies also show the limited capability of the considered simple reconstruction algorithm. Thus, on going work will focus on the development of additional characteristics to the tracking so that it will be possible to improve the performance of CALIFA in the reconstruction of the correct energy of more than one photon entering the detector.

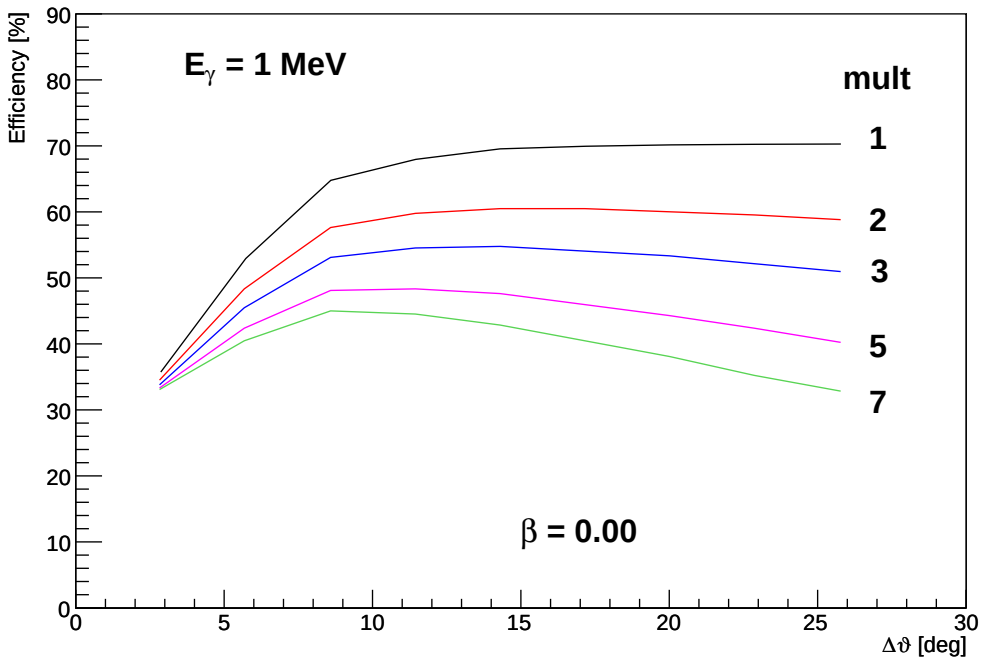

Figure 4.6.: Efficiency versus cluster window size for different multiplicities of the simulated event (from top to bottom: multiplicity 1, 2, 3, 5, 7) and a γ-ray energy of 1 MeV.

4.3. Response to γ rays

Within this section the response of the CALIFA Barrel to γ rays emitted from a fast projectile will be reviewed. Both the Barrel alone and the combination of the Barrel and a preliminary design of the CALIFA EndCap, using the same technology as the Barrel part, will be studied and reported[1].

Simulations of the γ ray response have been performed with the following parameters and constraints:

- The R3BRoot analysis framework interfaces with the Geant4 tracking engine, using electromagnetic standard physics.
- A plastic target (CH_2) of 1 cm radius and 0.1 mm length. The multilayer silicon tracker detector has been also included.
- γ rays have been emitted isotropically from a cubic box with $\pm$2 mm length for each axis around the origin. A Lorentz boost with β=0.82, corresponding to a projectile energy of 700 A MeV has been applied to the emitted γ rays. As a result, the energy distribution is flat, varying between approximately 0.4 and 3 times the original energy, the angular distribution peaking at a polar angle of approximately 20°.
- The crystal intrinsic non-uniformity has been included by simulating a 1% maximum random deviation from the original energy deposited in the scintillator material.

[1] CALIFA Barrel 7.07 (with EndCap 7.17 when an EndCap design was requested) was used, with 300 μm carbon fibre alveoli and 300 μm wrapping thickness.

- A Gaussian smearing of 4%, 5% and 6% at the energy of 1 MeV, scaling with the square root of the energy, has been used to represent the experimental resolution. 'Perfect' detectors have additionally been simulated to account for the geometrical contribution to the total resolution.

After the γ rays have been tracked and their energy deposited in the crystals, a reconstruction algorithm, as described in the previous section, provides the candidate γ rays from the energy deposited in a set of crystals or clusters. The reconstruction method is detailed below:

- Crystals in an angular window around largest energies are selected (a cluster); the 'double window' algorithm has been employed for the following plots, using both an optimized window size of approx. 15°, according to the results of the previous sections and also a simple summation of the energy for the full calorimeter for comparative purposes.
- Sums the cluster crystals energy deposition if exceeding energy threshold (20, 50 and 100 keV); if no comment is added to the figure or the caption, 50 keV is the default threshold considered in all plots.
- Takes the polar angle for correction from crystal in the cluster with the largest energy, assumed first hit.

A few parameters have been varied within the study to account for the response of the calorimeter under different conditions or working modes:

- The energy threshold for each individual crystal.
- The experimental resolution varying from 4%, 5% and 6% at 1 MeV, scaled with the square root of the energy. This is close to the values measured in the laboratory tests.
- The multiplicity of the emitted γ rays. The initial plots are made for multiplicity one, to reflect only the basic detection properties of the individual calorimeter crystals and their geometrical coverage. Following this, the capabilities of detecting emission multiplicities larger than one have been analysed.

The CALIFA Barrel and the complete calorimeter has been tested using γ rays emitted with energies between 200 keV and 15 MeV in the projectile frame. The upper pad of Fig. 4.7 shows the dependence with the projectile frame energy of the mean number of crystals with signal above threshold for the separate Barrel (dashed blue line) and EndCap (dotted red line) sections respectively. This number is obtained dividing the number of crystals with signal above threshold by the total number of emitted γ rays in the geometrical acceptance of each element. In black, the mean number of crystals for the whole calorimeter is quoted, evaluated with the total number of emitted γ rays (open markers) or the total number of γ rays in the calorimeter geometrical aperture (filled markers). The lower pad shows the number of clusters obtained after the reconstruction algorithm is applied, separately for the Barrel and EndCap regions. Again, the total number of clusters is divided by the total number of emitted γ rays in the geometrical acceptance of each element for the displayed results.

The number of crystal hits is only around one for the lower energies accessible to the calorimeter detectors. At energies around 1 MeV the mean number of crystals with signal is already above two, with the crystal-fold (the number of crystals with signal) in the

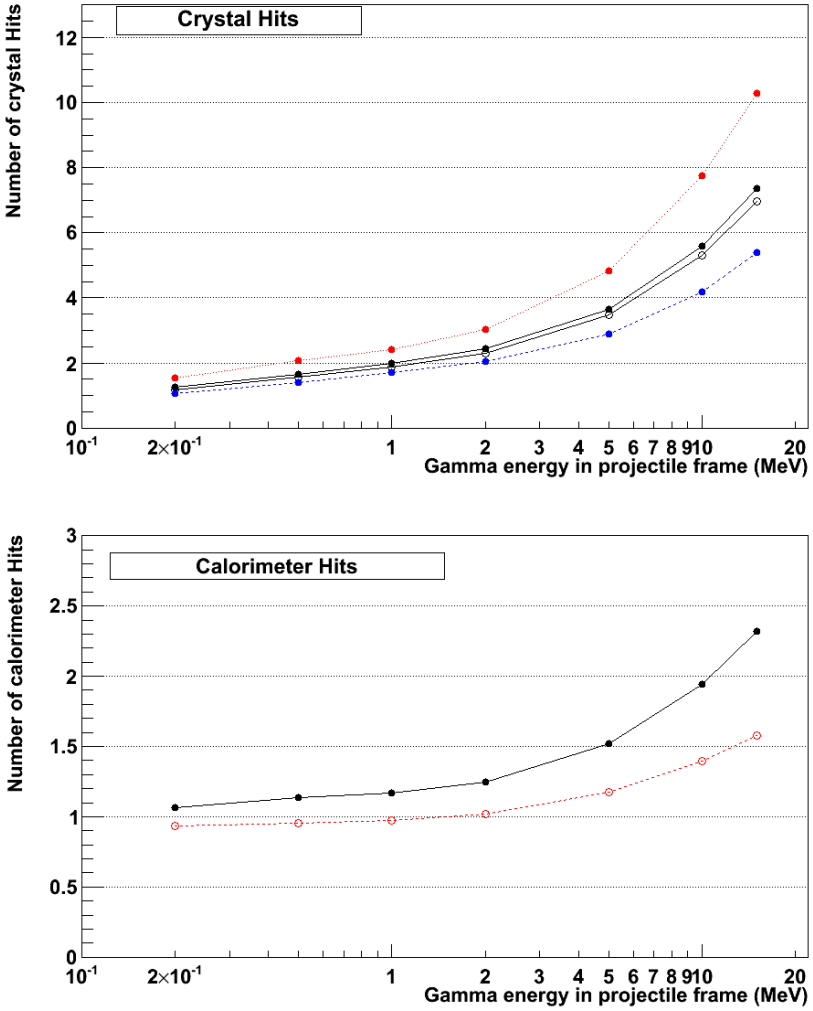

Figure 4.7.: Upper pad: dependence of the mean number of crystals with signal with the emitted γ ray energy in projectile frame. Results are displayed separately for the Barrel (dashed blue line) and the EndCap (dotted red line), while those in black continuous lines, obtained for the complete CALIFA, are evaluated with respect to the total number of emitted γ rays (open markers) or the total number in the calorimeter geometrical aperture (filled markers). Lower pad: dependence of the mean number of clusters with the emitted γ ray energy in projectile frame.

EndCap region much larger than in the Barrel, due to the characteristics of the Lorentz boost. The mean number of hits increases at high energy, reaching values above 4 for projectile frame energies of 10 MeV in the Barrel region, and close to 8 in the EndCap volume. Nevertheless, the crystal-fold distribution is quite broad, with a significant number of events depositing energy over three or four crystals at 1 MeV, while at 10 MeV events with crystal-fold above 10 are still quite probable (around 10% of the events).

The lower pad of Fig. 4.7 displays the dependence of the mean number of clusters with the emitted γ ray energy in projectile frame. The mean number of clusters in the Barrel are displayed in red open markers, while black filled markers are used for clusters in the

EndCap. The mean cluster-fold is around one at low energy. This number is slightly below one for the Barrel, due to the inefficiency factors (γ rays lost in the inactive volume or stopped in the matter before the active volume). At high energy, the mean cluster-fold is well above one, indicating that the algorithm with an optimized window is not able to collect in a single cluster all the relevant crystals with energy for each event, which could be located quite far away due to the different processes (mainly Compton and pair production). This is also the reason why, for the EndCap and at the lowest energies tested, the number is slightly above one; the probability of reconstructing two clusters from a single γ ray. In this case a large angle Compton is the most probable reason for a double cluster. Fig. 4.7 displays mean values, while the complete cluster-fold distribution shows a non-negligible probability of two clusters at low energy and, for the highest energy tested, 5% of events spanning more than five clusters.

4.3.1. Energy resolution

Energy resolution is one of the most relevant parameters to evaluate the capabilities of CALIFA within the R^3B Physics program. To a large extent, the energy resolution is given by the scintillator and the readout properties. However, the particular characteristics of the γ ray kinematics make calorimeter design and granularity important elements in the resolution assessment.

The following section defines the energy resolution as the FWHM obtained from the sigma of a Gaussian function fit to the photopeak (full γ ray energy reconstructed), as a percentage of the emitted γ ray energy. This definition provides results quite appropriate at low and intermediate energy, but progressively at higher energies there will be a deviation of the individual γ ray full energy peak reconstruction from a Gaussian shape, with an increase of a lower energy tail of the peak.

The top pad of Fig. 4.8 shows the dependence of the resolution on the emitted γ ray energy in the projectile frame. Different curves (black circles) correspond to different values of the crystals energy resolution: from the top to the bottom results for an experimental resolution of 6, 5 and 4% at 1 MeV (scaling with the square root of the energy) are displayed, while the lower curve (open markers) corresponds to ideal detectors, where the sole contribution to the resolution is the Lorentz broadening. The additional set of blue square markers represent the case where a sum over all crystals was employed, while the black circles use a reduced angular window optimized in the previous section to cope with multiplicities larger than one. They differ only at high energy, for 5 MeV and above, where the resolution is better when all of the crystals energy is added. This difference indicates that for the most energetic γ rays part of the energy could escape to large distances from the initial interaction point, complicating the reconstruction of clusters. Selecting a larger angular window would include this portion of the energy, conversely decreasing the efficiency for events with larger multiplicity.

At low energies the energy resolution is dominated by the intrinsic crystal resolution. At larger energies, above 2 MeV in the projectile frame, the granularity of the detector dominates, with the Lorentz broadening becoming the larger contribution to the energy resolution as the energy increases. This is easily deduced from the small difference between the filled markers and the open ones, where the detectors are taken as ideal and the only contribution to the resolution comes from the Lorentz broadening. It is worth noting

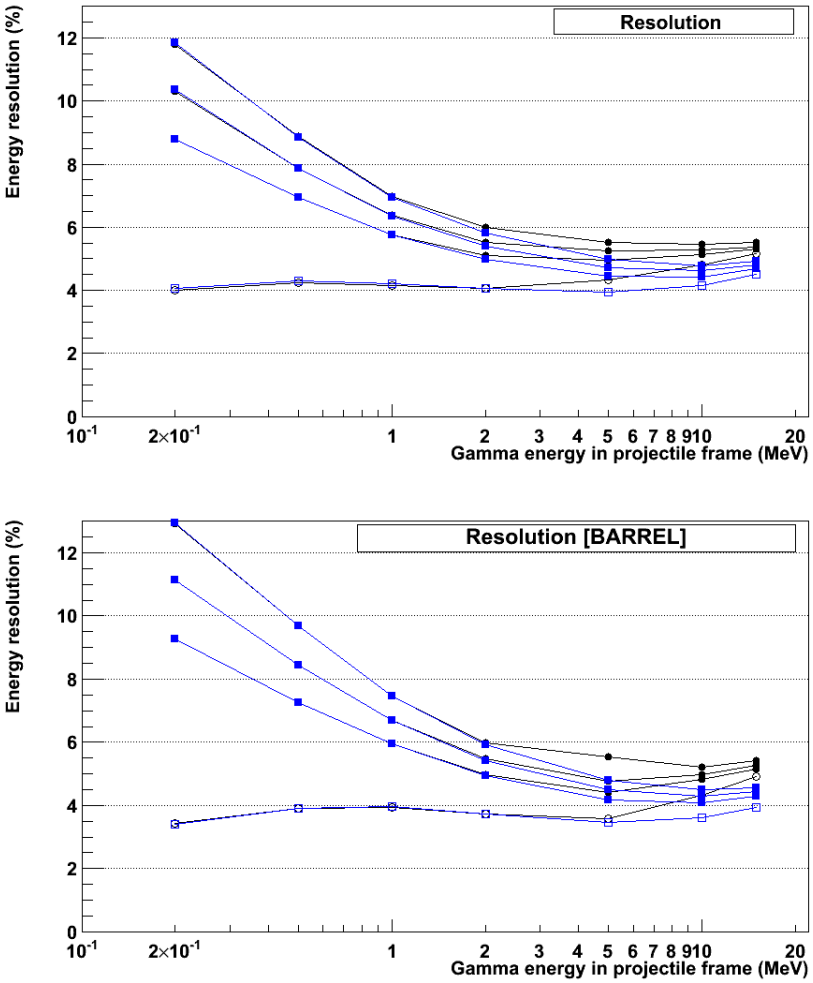

Figure 4.8.: Upper pad: dependence of the resolution with the emitted γ ray energy in the projectile frame. From the top to the bottom, in black circles, results for intrinsic resolution of 6, 5 and 4% at 1 MeV, (scaling with the square root of the energy) are displayed. The lower curve (open markers) corresponds to ideal detectors. The blue squares represents the same set of curves with addback in all the calorimeter crystals. Lower pad: dependence of the resolution with the emitted γ ray energy in projectile frame for the Barrel. The meaning of the different markers is the same than in the top pad.

that the granularity has been chosen to reduce the geometrical contribution to the energy resolution to approximately 4%.

It is important to remember that the energies quoted in the abscissa in Fig. 4.8 (and others in this section) correspond to energy emitted in the projectile frame. In the laboratory frame, the high beam energy causes a single energy to vary from 3 to 0.7 times the projectile frame energy over the range of the polar angles covered by the Calorimeter. The laboratory frame energies at the Barrel region being smaller than in the EndCap, resulting in a different set of curves for the efficiency and the resolution.

The lower pad of Fig. 4.8 shows the set of curves representing the resolution with respect

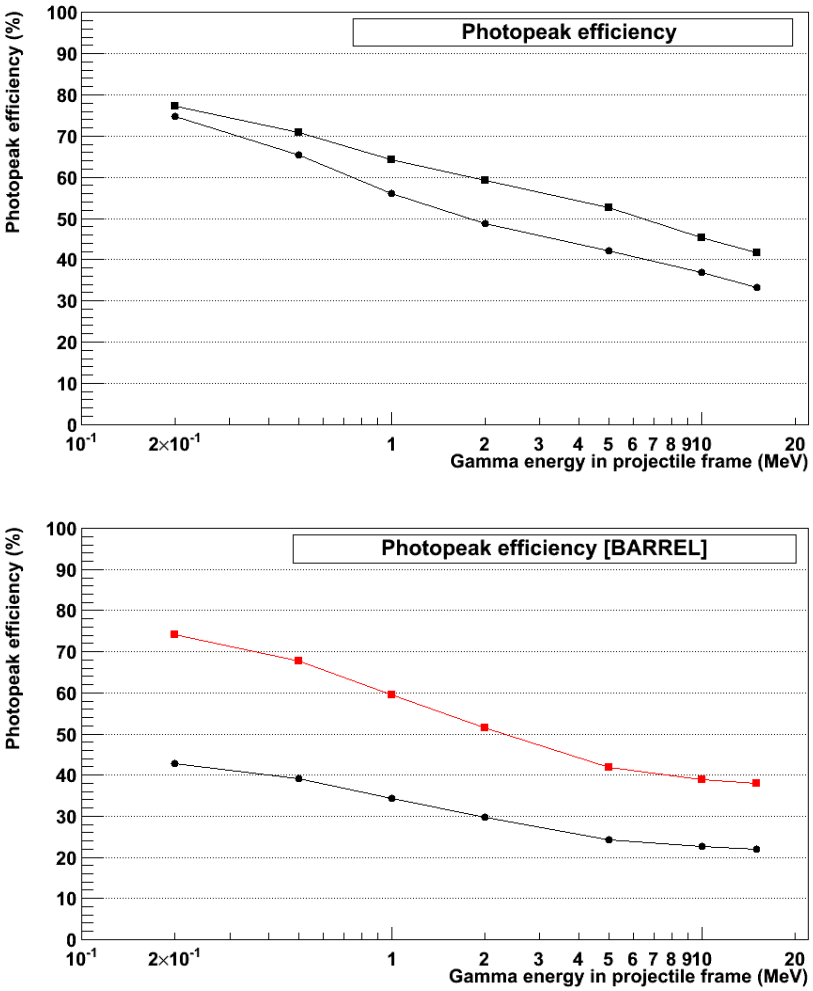

Figure 4.9.: Upper pad: dependence of the photopeak efficiency with the emitted projectile frame γ ray energy. The circle markers represent the results for an optimized angular window in the reconstruction algorithm, while square markers stand for the sum of the energy in all crystals. Lower pad: dependence of the photopeak efficiency with the emitted projectile frame γ ray energy for the Barrel. The red square markers represents the photopeak efficiency normalized to the number of γ rays emitted in the CALIFA Barrel geometrical acceptance, while the black circles correspond to the total emitted γ rays, independently of their direction.

to the projectile frame γ ray energies, for the Barrel region alone. Only γ rays entering in the geometrical acceptance of the Barrel have been considered for the evaluation of the Barrel properties. The meaning of the different curves and markers correspond to that in the top pad. The resolution at low energy is slightly worse than in the full setup, while at large energies the resolution improves. Both effects are caused by the Lorentz boost in the polar angles covered by the Barrel; as these angles are larger, the γ ray energies are lower, decreasing even in some cases from the original energy in the projectile frame.

4.3.2. Efficiency

The efficiency of the CALIFA barrel to the detection of γ rays has been one of the key requirements and a huge effort has been devoted to improve it in the calorimeter concept and design. This subsection involves a detailed evaluation of the results for the detection of a single γ ray and for events of larger multiplicity. The photopeak or full absorption efficiency is the key parameter in this evaluation. It is defined as the ratio between the number of events which are reconstructed with their complete energy and the total number of emitted events. The definition depends on what 'complete energy events' are considered. In this section, the events included within a window in the interval $[-2\sigma, 2\sigma]$ of the Gaussian function fit of the photopeak have been taken. This criteria is quite conservative, discarding entries in the tails of the peak which could be considered as well reconstructed, in order to avoid the inclusion of tails in the low energy region of the photopeak for the largest energies, where the photopeak shape diverge from a Gaussian distribution.

Efficiency for multiplicity one events

The top pad of Fig. 4.9 represents the photopeak efficiency for the entire calorimeter. The total absorption or photopeak efficiency could be specified dividing the detected events under the photopeak by the total number of emitted γ rays, independently of their direction (geometrically uncorrected) or dividing only for the amount of γ rays that are emitted in the geometrical acceptance of the part of the detector in consideration (geometrically corrected). The data shown in the figure corresponds to the last definition. The difference between the two cases amounts to $\sim 5\%$, due to particles lost in the parts not covered by the calorimeter elements (beam line pipe, backward angles aperture). The two data sets shown in the top pad of Fig. 4.9 correspond again to the results for different settings of the angular window in the Hit Finder algorithm: a sum over all crystals in the case of the square markers, and an optimized angular window represented by circles. At low energy both algorithm parameters return a similar result, while in the high energy region, above projectile frame energies of 1 MeV, the efficiency drops to around 10% when the addback is limited to a set of crystals and not to the full calorimeter, indicating that part of the energy is deposited in crystals which could be quite far away, as previously concluded from the mean number of clusters in the previous section.

The efficiency at low energies takes values between 70 and 80%, and is continuously dropping at larger energies, but it is worth mentioning that still at the largest projectile frame γ ray energies tested the total calorimeter efficiency remains quite high. Direct comparison with other devices is complex because CALIFA has been designed for the particular kinematics of the particle emission from fast projectiles at approximately the velocity of the beam. The capability to correct for the Doppler broadening makes CALIFA a unique instrument for the analysis of the reactions in the R^3B setup.

The efficiency of the Barrel section is shown in the lower pad of Fig. 4.9. Here, both the geometrically uncorrected (black circle markers) and the corrected (red square markers) photopeak efficiencies are shown; the first curve indicates the efficiency combining intrinsic and acceptance effects, while the second is corrected by the geometrical acceptance of the Barrel. In both cases the algorithm uses a reduced angular window optimized in the previous section to cope with multiplicities larger than one. There is an additional important point when discussing the efficiency: where is the undetected energy deposited? Part of the Compton scattered or the backscattering γ rays could escape the detector through the backward angles aperture, not covered by crystals. Another part, mainly at

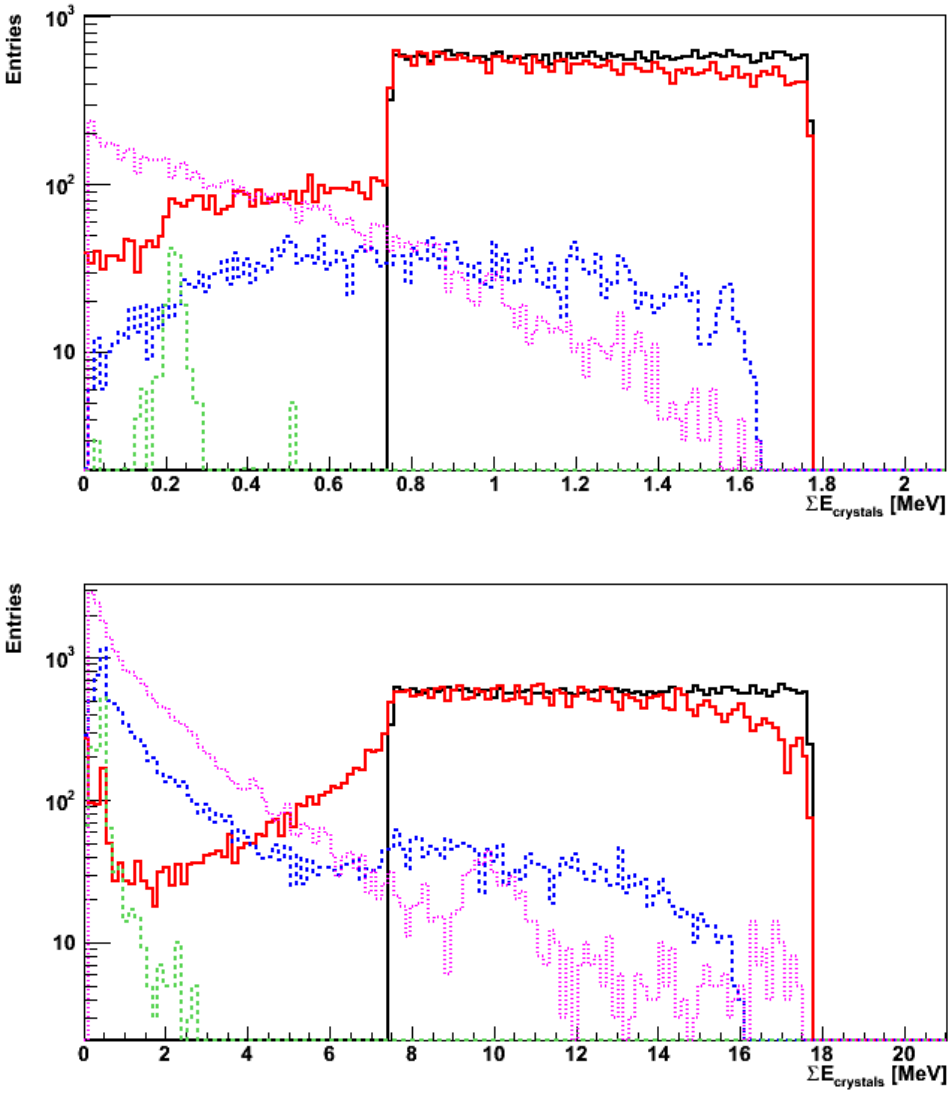

Figure 4.10.: Upper pad: energy spectra in the different regions and escaping zones for emitted γ rays of 1 MeV in projectile frame. The dark top line corresponds to the emitted energy spectra, the red line is the sum energy spectra in the crystals and below, in blue and green dashed line, the energy which escape beyond the Barrel outer surface and though the backward angle aperture are displayed, respectively. The dotted magenta line corresponds to the energy spectra absorbed by the passive matter. Lower pad: energy spectra in the different regions and escaping zones for emitted γ rays of 10 MeV in projectile frame. The meaning of the different lines corresponds to those in the top pad.

the highest energies, could escape after passing though the detector Barrel crystals. A specific simulation for testing where the energy escapes has been performed, measuring the number of events and the energy spectra i) in the crystals, ii) in the backward region not covered by the crystals, iii) around the Barrel section and iv) in the passive material (in this case, the wrapping and carbon fibre alveoli).

To perform a realistic evaluation, the simulation considers γ rays emitted at different

	Percentage of events with energy deposited in (or escaping through)			
Energy	crystals (Barrel + EndCap)	passive matter	barrel outer surface	backwards angle aperture
0.2 MeV	99.2% + 1.2%	7.4%	0.4 %	0.3 %
0.5 MeV	98.6% + 3.0%	12.0%	2.2%	0.4%
1 MeV	96.5% + 4.0%	15.3%	7.6%	0.4%
2 MeV	93.7% + 5.4%	23.1%	14.6%	0.7%
5 MeV	92.9% + 9.7%	34.1%	18.7%	1.7%
10 MeV	94.8% + 16.3%	50.9%	23.4%	3.0%
15 MeV	96.1% + 21.3%	63.7%	30.0%	3.9%
	Percentage of energy deposited in (or escaping through)			
Energy	crystals (Barrel + EndCap)	passive matter	barrel outer surface	backwards angle aperture
0.2 MeV	97.1%	2.3%	0.4%	0.1%
0.5 MeV	93.9%	4.0%	1.8%	0.1%
1 MeV	88.6%	6.0%	5.0%	0.1%
2 MeV	83.6%	8.2%	7.7%	0.1%
5 MeV	84.0%	8.0%	7.6%	0.1%
10 MeV	84.4%	8.5%	6.5%	0.1%
15 MeV	85.6%	8.0%	6.0%	0.1%

Table 4.1.: Percentage of events (upper table) and of the emitted energy (lower table) deposited in the CALIFA crystals, in the passive matter, escaping after passing through the Barrel region and escaping through the backwards angles aperture. The energy in the first column corresponds to the emitted projectile frame γ ray energies. See the text for further explanation.

energies in the projectile frame and, therefore, the energies on the Barrel vary with the polar angle. The angular range of the emitted particles have been selected to lie in the geometrical aperture of the Barrel section. Fig. 4.10 shows the energy spectra absorbed in the calorimeter elements, when γ rays of 1 MeV (upper pad) and 10 MeV (lower pad) in the projectile frame are emitted, again boosted at a velocity $\beta = 0.82$. The energy spectra corresponds to detection of γ rays at laboratory energies and, therefore, the spectra is motivated by the kinematics of the Lorentz boost; this result is evident in the emitted γ-rays spectra (upper black line), with a flat energy distribution ranging from 0.7 to 1.8 times the projectile frame energy. Immediately below, the next histogram (red line) corresponds to the energy spectra in the crystals, that is, to the detected energy. Below, in blue and green dashed line, the energy which escape beyond the Barrel outer surface and though backward angle aperture are displayed, respectively. The last histogram, in dotted magenta line, corresponds to the energy spectra which is not detected in any of the previous elements, that is, energy absorbed by the inactive matter between the emission point and the end of the γ-ray life.

Table 4.1 contains the percentage of events (upper table) and the percentage of the total energy (lower table) deposited in the CALIFA crystals, the passive matter, dispersed in the backwards angle aperture and traversing through the crystals to escape behind the Barrel volume. The percentage of events with energy deposited in the crystal is divided in two parts: events in the Barrel crystals and a small contribution of events in the EndCap crystals, arising from scattered γ rays, despite the fact that the angular range of the emitted particles have been selected to lie in the geometrical aperture of the Barrel section. Note that the percentage of events sums more than 100% due to the possibility of losing part of

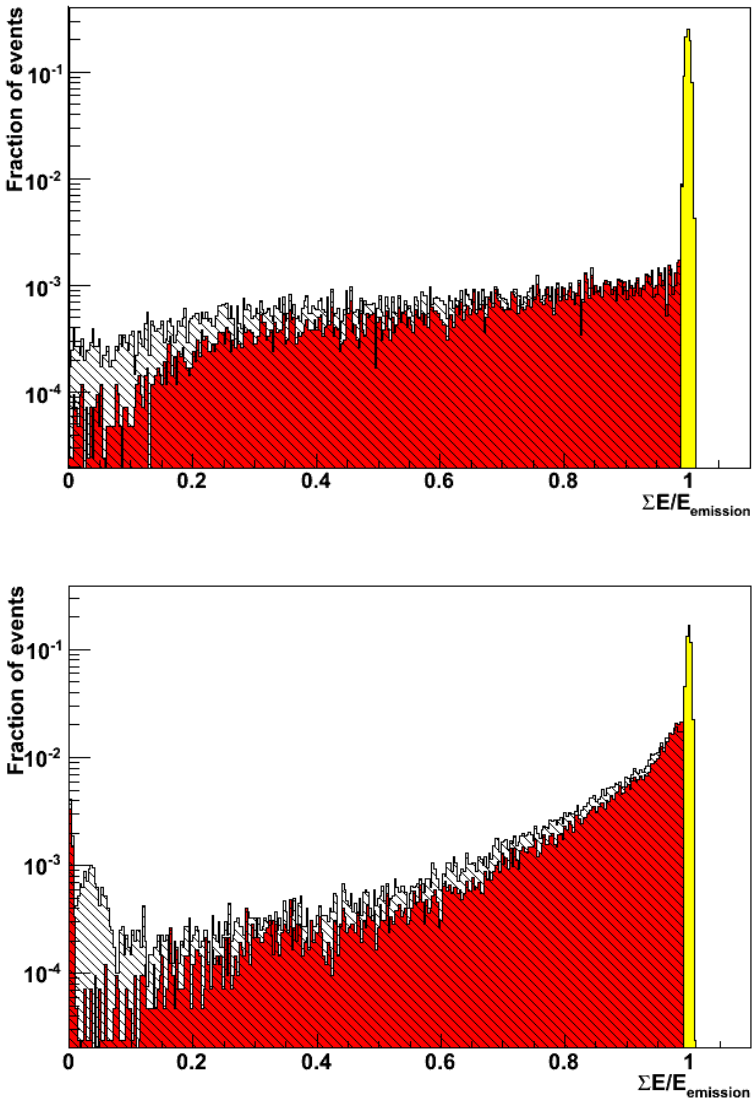

Figure 4.11.: Upper pad: fraction of events depositing energy in the calorimeter crystals (black pattern) and in the crystals and the escaping surfaces (red filled area and yellow peak for the full reconstructed events), for emitted γ rays of 1 MeV in projectile frame. The integral of the red filled area corresponds to the events with energy lost in the passive matter. The abscissa represents the ratio of the detected energy to the emitted laboratory energies. Lower pad: same ratio for emitted γ rays of 10 MeV in projectile frame. See the text for further explanation.

the energy in two or more different elements.

The percentage of energy (lower table in Table 4.1) is calculated from the integral of each energy spectra, normalized to the total energy emitted. The sum of the contributions in the different elements is 100%, once the escape through the forward beam pipe hole, of the order of 0.3%, is computed.

In the backward region (green dashed line in Fig. 4.10), the spectra is dominated by the

Compton (at low emission energies) and $e^+ - e^-$ annihilation γ rays, with the 511 keV peak visible in the left side of the spectra (at high emission energies). Only a small fraction (below 4% even at the higher energies) of the events lost part of their energy in this region, with a total energy percentage of less than 0.1%. Around the Barrel section (blue dashed line), the energy spectra spreads till the higher energies, representing partial escapes as the polar angle decreases and, therefore, the γ ray energy increases. The events with some energy lost in the direction upstream of the Barrel accounts from 8% till 30% of the total events, but the energy portion escaping is in the order of 7%.

It is important to evaluate the amount of energy stopped by the passive material and, therefore, undetected. The passive matter considered in this simulation comprehends the crystals wrapping and the carbon fibre alveoli supporting the crystals. The number of events depositing part of the total energy in this passive material could be obtained from the analysis of Fig 4.11, which displays the fraction of events depositing energy in the calorimeter crystals in a black patterned histogram and in the crystals plus the escaping surface (behind the barrel crystals and in the backward angles aperture) in the red filled histogram. The upper pad displays the event fraction for emitted γ rays of 1 MeV in projectile frame, while the lower pad for 10 MeV in projectile frame. The abscissa represents the ratio of the detected energy to the emitted laboratory energies, facilitating the identification of the full reconstructed events, in yellow. From the integral of the red filled histogram, it is possible to obtain the percentage of events with some energy lost in the passive matter, as quoted in the third column of the upper table 4.1. The total energy lost in the passive material could be obtained from the integral of its energy spectra, shown in dotted magenta line in Fig 4.10, and specified in the third column of the lower table 4.1. The impressively low amount of energy deposited in the passive matter confirms the minimum incidence of the support structures and crystal wrapping in the γ ray detection, despite the high granularity of the detector.

Efficiency for events with multiplicity above one

Up to this point all results have been obtained emitting a single γ ray per event. CALIFA should also work in many experiments as an efficient calorimeter, obtaining the individual energy for each emitted γ ray in events with multiplicity above one. To check the efficiency of the CALIFA complete calorimeter under these conditions, several γ rays of a given energy have been simultaneously emitted isotropically within the Barrel geometrical aperture. The Hit Finder algorithm works to reconstruct the individual γ rays, and their energy is summed to get the calorimetric properties of the detector.

An example of the outcome of this procedure, for multiplicity three, is shown in the lower pad of Fig. 4.12, where the peak at 3 MeV corresponds to the complete reconstruction and sum of the energies of three γ rays of 1 MeV each one, while the small peak at 2 MeV represents events where only two γ rays are reconstructed and the other does not deposit any energy. Other possibilities, such as the case that one of the particles is not completely reconstructed, or more than three clusters are found by the algorithm, return an incorrect sum energy, and therefore will contribute to the background observed in the figure.

It is important to note that to obtain any calorimetric property it is mandatory to find the individual γ ray energies and polar angles of each γ ray emitted. Adding the energies deposited in the crystals without the proper identification of the individual γ rays will not work due to the required transformation to the projectile frame, which requires both the energy and the angle. The angular window in the reconstruction algorithm has been optimized to work with events of moderate multiplicity, as shown in the previous section.

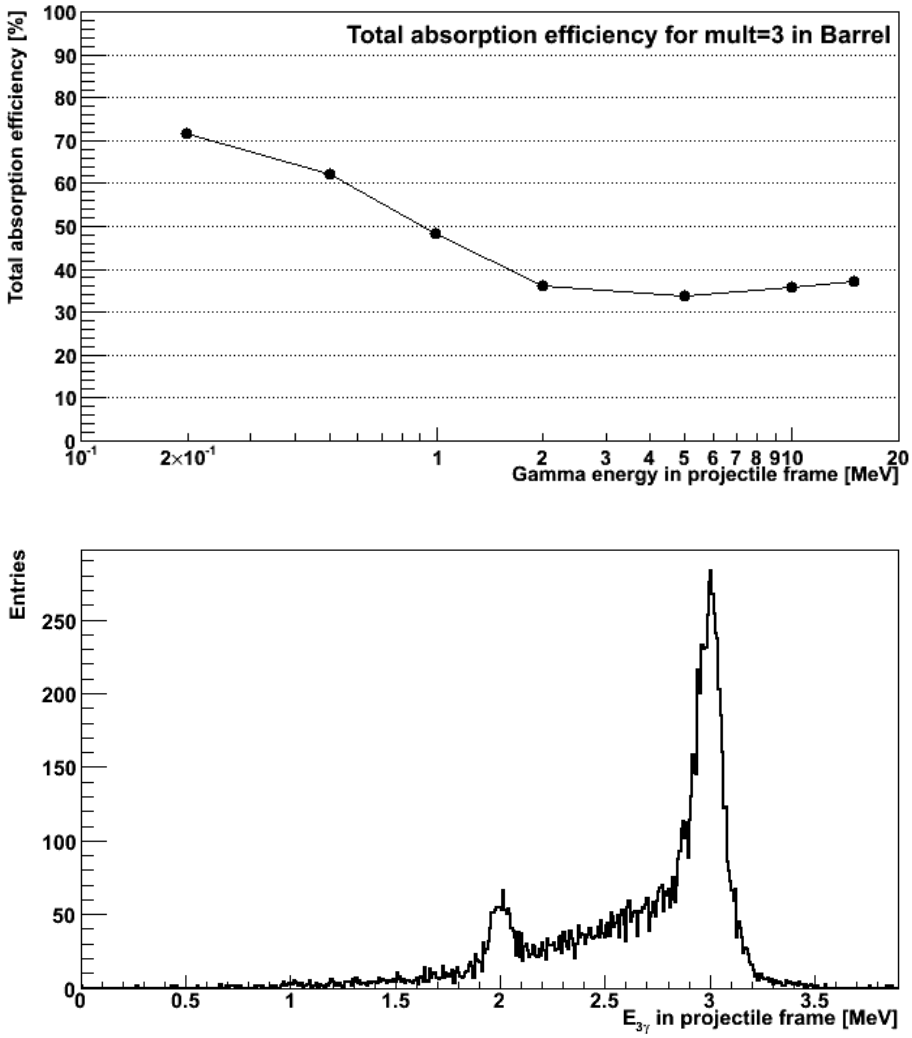

Figure 4.12.: Upper pad: total energy reconstruction efficiency with respect to the emitted projectile frame γ ray energy in multiplicity three events in the Barrel. The energy of the peak where the efficiency is evaluated corresponds to three times the energy in the abscissa. Lower pad: energy spectra of the reconstructed events with multiplicity three (that is, three γ rays emitted with 1 MeV each one) in the Barrel.

This does not prevent the use of more sophisticated algorithms that could improve the performance of the calorimeter after a proper investigation.

The upper pad of Fig. 4.12 displays the total absorption efficiency in the reconstruction of the events of multiplicity three, where the three γ rays are emitted with the same energy, that shown in the plot abscissa. The curve represents the efficiency results for the correct three-fold cluster detection with the proper sum energy. Note that for the typical spectroscopic energies below or around 1 MeV, the efficiency reconstructing the full event cascade is quite high, close to 50% for multiplicity three events.

Fig. 4.13 shows the results when events with multiplicity five are considered, on condition that three of these γ rays enter in the geometrical acceptance of the Barrel (as the previous

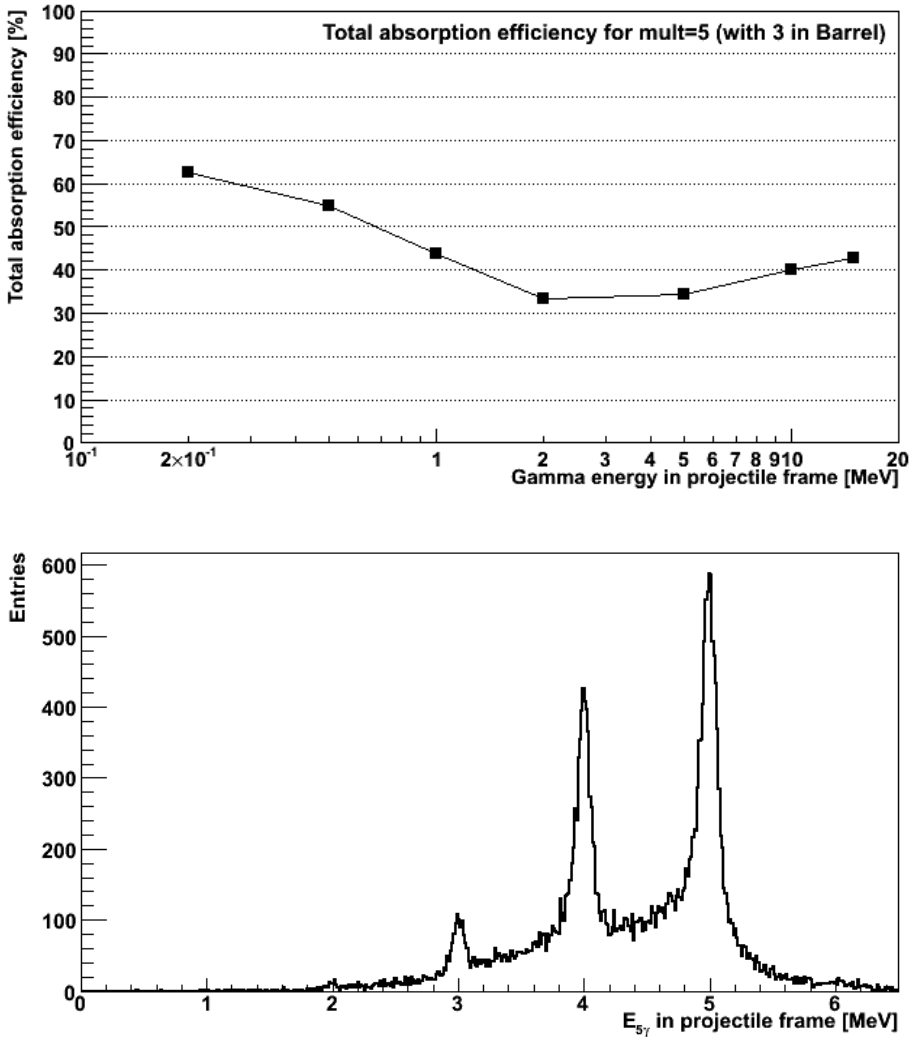

Figure 4.13.: Upper pad: total energy reconstruction efficiency with respect to the emitted projectile frame γ ray energy in multiplicity five events, provided than three γ rays enters in the geometrical aperture of the Barrel. The energy of the peak where the efficiency is evaluated corresponds to five times the energy in the abscissa. Lower pad: energy spectra of the reconstructed events with multiplicity five (that is, five γ rays emitted with 1 MeV each one, with three emitted in the Barrel).

case) while the other two are isotropically distributed and Doppler boosted (outside the Barrel geometrical acceptance). The γ rays entering into the EndCap region are considered as fully detected. As before, the black curve in the upper pad represents the efficiency when all the five γ rays have been properly recorded and therefore the total energy is centred in the proper energy value, being the abscissa the projectile frame energy of each emitted γ ray (and not the sum energy). The lower pad displays the obtained spectra.

In this case the entries below the peaks at a sum energy of 4 MeV and 3 MeV are larger, reflecting the probability of escaping of the γ rays emitted isotropically outside the Barrel, in the backward angles aperture or in the forward beam pipe aperture. Irrespective of this,

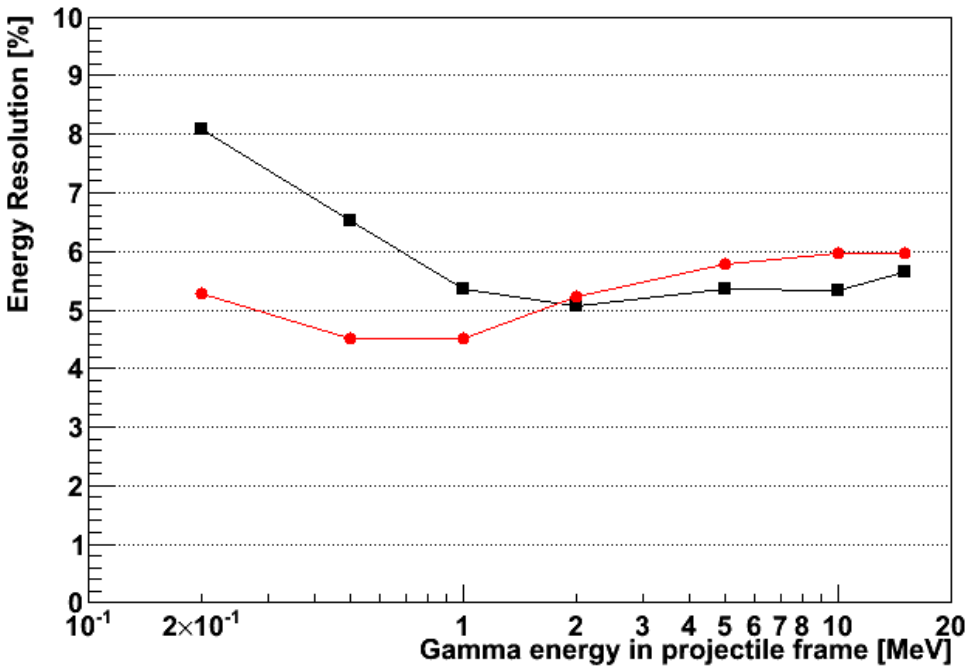

Figure 4.14.: Resolution of the total energy reconstruction peaks with respect to the emitted projectile frame γ ray energy, for multiplicities larger than one. The black squares correspond to multiplicity three events in Barrel and the red circles to multiplicity five, provided three γ rays enter in the Barrel geometrical acceptance.

the efficiency reconstructing the full event cascade remains quite high.

Note that the efficiency could be improved by identifying and adding the energy of separate clusters with 511 keV that are erroneously taken as an independent γ ray emitted from the target region. This is even more important in the EndCap region where the energy and so the cluster-fold, is larger than the Barrel region. The results evident from the observation of the lower pad in Fig. 4.7, where the cluster-fold for events of multiplicity one is larger than one at high energies, and even larger in the EndCap than in the Barrel, as expected from the Lorentz boost. The present algorithm does not perform this correction, therefore decreasing the estimation of the efficiency that the calorimeter could achieve.

4.3.3. Energy resolution as a calorimeter

From the previous analysis it is possible to obtain the energy resolution of the sum of the clusters which delivers the complete event energy in the calorimeter. The resolution is defined as in the previous section detailing spectroscopic energy resolution: it is the peak FWHM, calculated from the sigma of a Gaussian function fit to the sum peak, as a percentage of the emitted γ ray energy. The evaluation of the resolution has been performed for the peak resulting from the sum of the clusters when, apparently, all the γ rays have been properly recorded and therefore the total energy is centred on the proper value ($n \times E_\gamma$).

These curves are shown in Fig. 4.14, where the energy resolution for the total absorption peak is shown. The black squares correspond to the resolution results for the correct three-fold cluster detection peak, with the proper sum energy, while the red circles correspond to the energy resolution in multiplicity five events, provided three γ rays enter in the Barrel geometrical acceptance. The energy in the abscissa corresponds to the energy (in the projectile frame) of each γ ray emitted (and not the sum energy).

The resolution obtained in the sum peak is comparable to the corresponding resolution for the equivalent single γ ray energy, that is, the resolution for three or five times the abscissa energy in the Fig 4.8. Only for cases with high energy in all the γ rays composing the high multiplicity event (above 25 MeV of total energy in multiplicity five events), the reconstruction presents a lower resolution which is still fulfils the specifications.

4.4. Response to light charged particles

4.4.1. Efficiency

The response function of the calorimeter to light charged particles, in particular protons, is of great interest if one plans to carry out reactions such as quasi-free scattering of protons explained in Section 4.5. In reactions such as ^{12}C(p,2p)^{11}B, the two protons of the final state end up moving at $\sim$80° with respect to the one another and with energies ranging from $\sim$50 to $\sim$350 MeV.

In this section we have calculated the total absorption intrinsic efficiency of the CALIFA barrel for monoenergetic protons. In this context, intrinsic refers to the fact that we have considered only protons emitted within the angular coverage of the Barrel. In fact, for the highest energies we have focused on the most forward angles as they are of special importance for the (p,2p) reactions we are interested in. Due to the particular kinematics of these reactions we know that, in most of the cases, we will have one proton in the direction of the forward endcap and the other, with energy within the range 260 to 320 MeV heading towards the most forward rings of the barrel (see Table 2.3). With the aim of testing the performance of the barrel in this situation we have generated monoenergetic protons of energies between 50 MeV and 200 MeV emitted isotropically within the angular acceptance of the Barrel, and monoenergetic protons of energies between 260 MeV and 320 MeV emitted in the most forward angles covered by the barrel, i.e. between 43.5 and 48.5°. The energy deposited in the crystals has been collected and added up. As in the case of the γ-ray simulations described in Sec. 4.3, the energy resolution has been adjusted to 5% at 1.0 MeV.

Fig. 4.15 shows two panels. In the top panel one can see the energy spectrum for protons of 260 MeV. The low energy tail of the peak is mainly due the energy lost by the protons in the wrapping at the entrance window or between crystals. A correction has been applied to the spectrum by identifying events of multiplicity two and three (number of crystals fired) and adding an average energy loss due to the wrapping. This is why the tail is small in comparison to what we see in the figures of the next section. However, this correction can be highly improved by taking into account the energy deposited in each crystal to calculate more accurately the energy lost in the wrapping. There is still work going on in this matter.

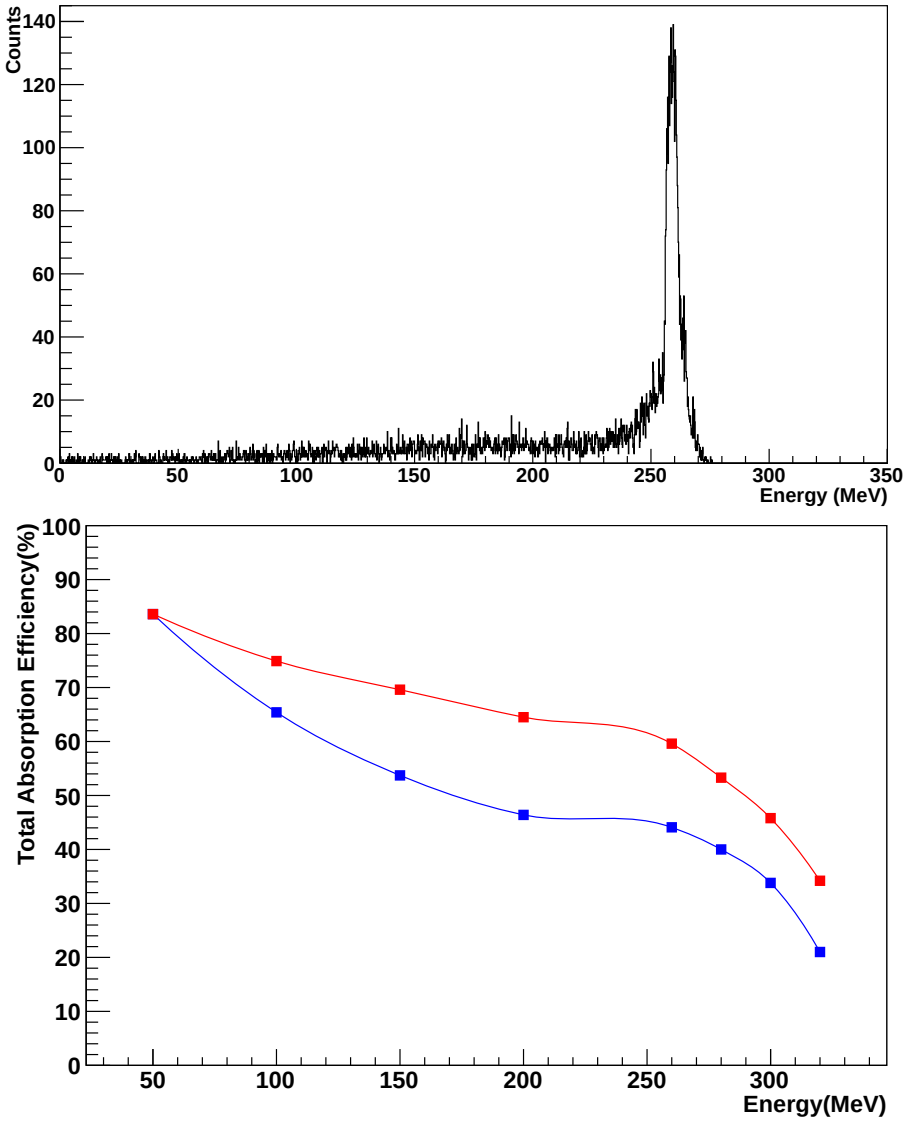

Figure 4.15.: Upper pad: Energy spectrum of protons of 260 MeV corrected attending to multiplicity (see text). Lower pad: intrinsic Total Absorption Efficiency of the CALIFA barrel. Blue: Integrating the area below the peak (mean +/- two sigmas). Red: Integrating the area below the peak from 90% of the nominal energy.

The bottom panel of Fig. 4.15 shows the Total Absorption Efficiency of the barrel for protons as a function of the energy. We see two different graphs because we have calculated the efficiency attending to two different criteria. The blue curve represents the efficiency calculated by integrating the area below the total absorption peak from the mean value plus/minus two sigmas. The red curve represents the efficiency calculated by integrating the peak from the point at 90% of the nominal energy. The former definition applies more to spectroscopic applications in which the energy resolution is the most important parameter, whereas the latter applies more to calorimetric purposes in which the efficiency is the most important parameter and we just need to be sure that we have measured at least 90% of the energy of the incoming proton. In fact, when the algorithm to correct the

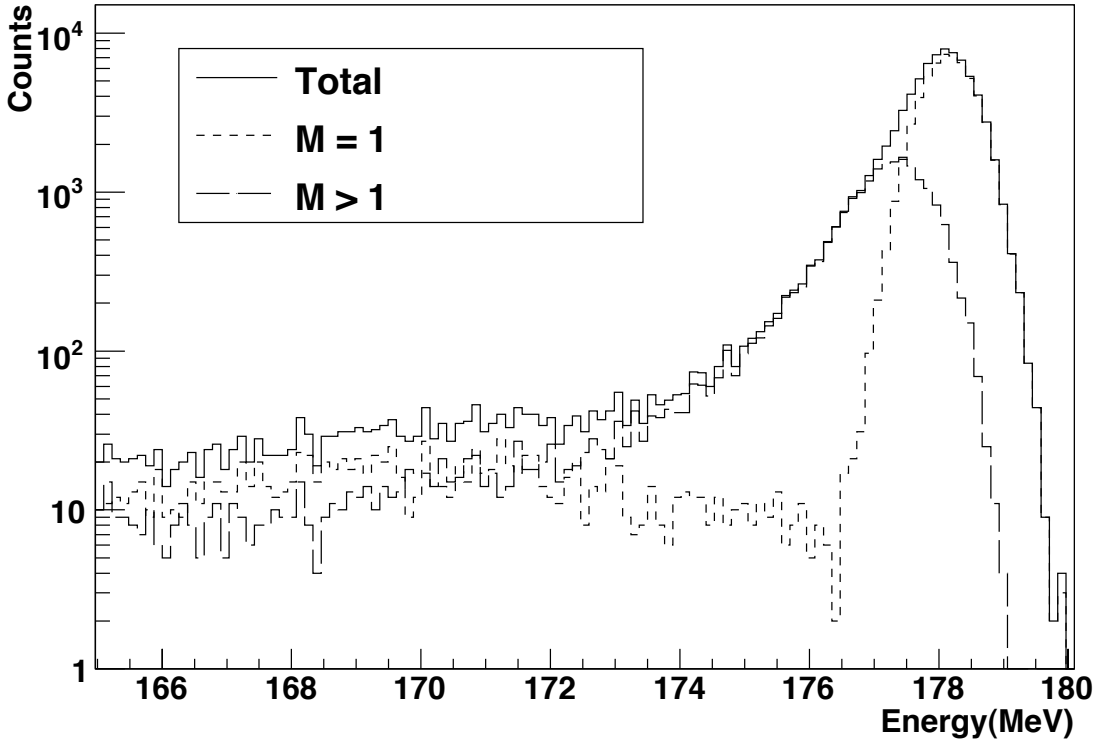

Figure 4.16.: Simulation spectrum using the binary cascade model. The two curves represent different multiplicity events. The impact area covers the full surface of the central element. Only events in the central three crystals are considered.

proton energy attending to the multiplicity is optimized, the blue points should be higher and both efficiency curves represented in Fig. 4.15 should be very similar.

4.4.2. Effect of the wrapping

Simulations have been performed with a prototype geometry. Mylar ($C_5H_4O_2$) was used as the reflective foil and pure CsI crystal as the detector material. In addition a gap between the CsI crystals was introduced, with a value of ∼0.4 mm.

GEANT4 includes two different physics lists for modeling hadronic cascades [FIW04, BG71]. Both were investigated in the simulations. Little or no difference was found between results of these two models. Detailed descriptions of both physics lists can be found in the GEANT4 user documentation [AAA+03]. The statistical broadening of the full energy peak is included by sampling the energy of the source particle from a Gaussian distribution with a width such that the experimentally measured FWHM is approximately reproduced.

The spectra calculated using the binary cascade model, including gain corrected summing for a uniformly irradiated central crystal, is shown in Fig. 4.16.

A similar structure as observed in the experiment is clearly visible in the simulated spectrum. Analysis of the simulated events shows that the missing energy can be attributed to protons traversing the material between elements. This effect was further confirmed by adding the energy lost in the foils to the energy deposited in the detector material. An

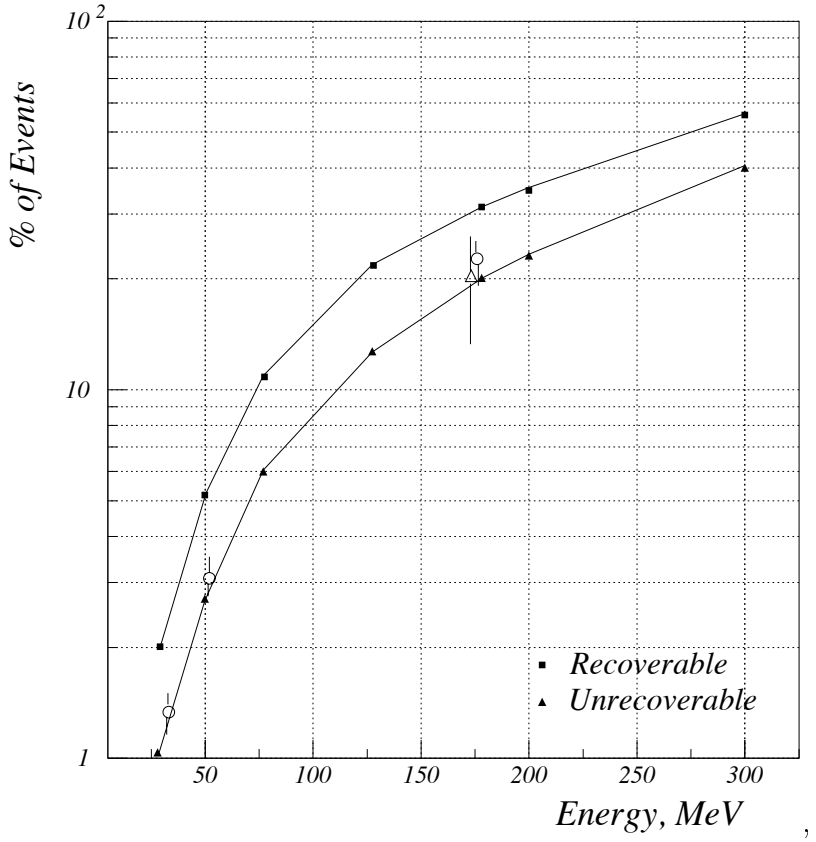

Figure 4.17.: The percentage of lost events which can be recovered by ideal add back (filled squares) and those lost to inelastic process (filled triangles), calculated for a crystal of the CALIFA geometry. Open circles - data from , open triangle - this work. The line is drawn to guide the eye through calculated points.

important issue is also the maximum number of events that can be recovered using add back. This number is limited by inelastic processes. We have estimated this effect using an ideal add back scenario.

Fig. 4.17 shows the results of these calculations. The number of events lost to inelastic processes was estimated from those falling outside of the full energy peak for an infinite detector block surrounding the target position. Subtracting the number of M=1 events that fall outside of the full energy peak for the central crystal in the simulated prototype from this number yields the ideal add back factor. As an example, at an energy of 180 MeV the simulations predict that 21% of the events are lost to inelastic processes leading to a maximum full energy peak efficiency of 79%. Of these events 32% are due to add back. The experimental value for irradiation through a single pixel close to the midpoint of the array is also given for comparison in the figure. One can note the excellent agreement between experiment and simulation. It was also deduced that an additional uncertainty of $\sim$7% is due to protons scattering out of the back or front surfaces of the crystal.

At low energies the fraction of inelastic events is small. However, at higher energies, e.g. 300 MeV, no protons deposit their full energy in a single crystal. In this case 60% of the events can be recovered by add back. However, as the multiplicity of the event increases the add back procedure will include more and more crystals. In order to improve the spectrum presented in Fig. 4.16, simulations were also performed using different foil thicknesses. The

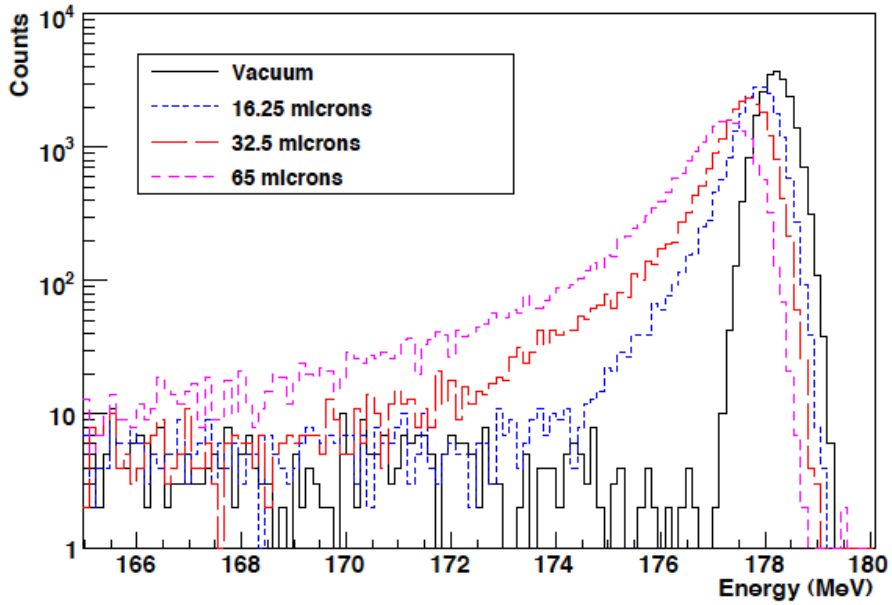

Figure 4.18.: Proton energy spectrum for M = 2 events and different ESR reflective film thickness. The impact area covers the full surface of the central element. Only events in the central three crystals are considered.

results are shown in Fig. 4.18. For protons totally absorbed in the central crystal, i.e. for M=1 events, the full energy peak is symmetric.

Although the FWHM is reduced for thinner foils the M = 2 add back peak remains asymmetric with a tail spanning a range of several MeV. One can conclude that the excellent energy resolution obtained for each individual crystal using the methods described are counteracted by this effect. An important factor is to determine to what extent a reduced foil thickness will influence the light collection properties of the single detector elements.

4.5. Simulation of selected Physical cases

4.5.1. CALIFA as a high resolution spectrometer: ^{22}O nuclear spectroscopy

In this subsection the spectroscopy of ^{22}O case is studied. We have selected the known knockout case of ^{23}O where we require CALIFA to act as spectrometer detecting relatively low-energy γ rays with low γ-ray multiplicity. This case exemplifies the performance of CALIFA as a high resolution spectrometer.

The ^{23}O nucleus, with a neutron separation energy of 2.7 MeV, lies very close to the dripline and has no bound excited states below 4 MeV [SAD+04]. In the nuclide chart, it is surrounded by ^{22}O (A-1 core-fragment), with a first excited 2^+ level at 3.17 MeV and ^{24}O (dripline) with no bound states [SAD+04]. Both neighbours seem to be double magic nuclei, indicating a persistence of the proton-magic number at Z=8 and (sub-)shell closures at N=14 and N=16. First experiments focusing on this nucleus yielded contradictory results concerning spin and parity assignment for the ground state of ^{23}O [SCO+00, KCI+02],

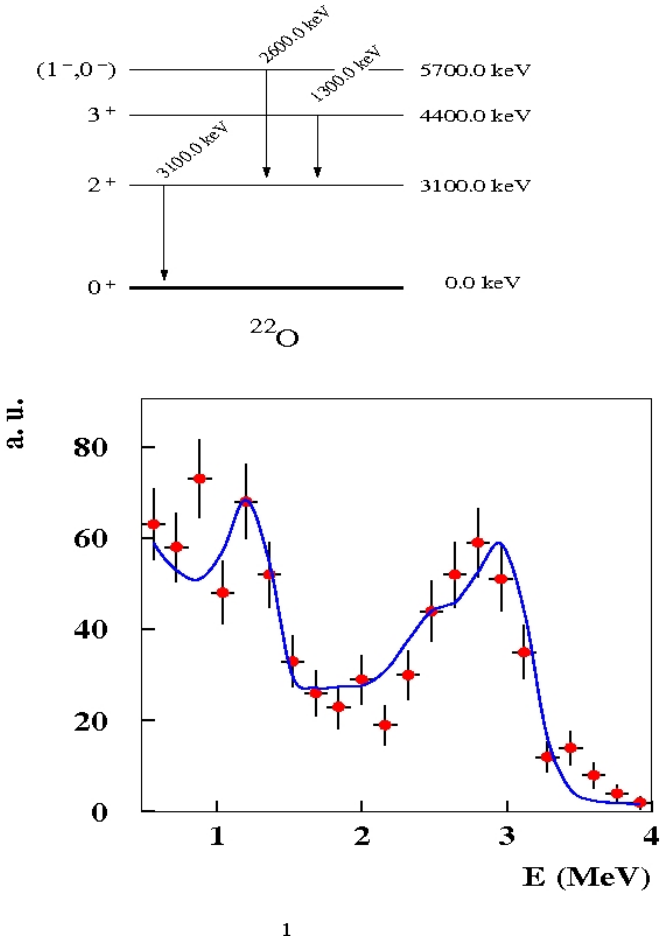

1

Figure 4.19.: Spectrum of γ rays in coincidence with ^{22}O fragments after one-neutron removal from ^{23}O in a carbon target. The spectrum shown here has been obtained from the measured γ-ray spectrum after Doppler correction. The experimental spectrum (dots) is compared with the result of a GEANT3 simulation (blue lines) adopting the level scheme shown above.

which motivated a deeper investigation of this nucleus by using the neutron-knockout technique at relativistic energies (939 MeV/nucleon) at the FRS-GSI [CGFVA+04].

This experiment allowed the measurement of the core-fragment momentum distribution and γ rays in coincidence, performed with a very basic array of 32 NaI(Tl)[2]. Fig. 4.19 shows the energy spectrum of γ rays recorded in coincidence with the ^{22}O fragments. This γ-ray spectrum was used to determine the exclusive cross section for different final core-fragment states. The broad peak observed at higher energy is assumed to be due to the 3.2 MeV and the 2.6 MeV transitions that the NaI(Tl) detectors could not resolve. The exclusive momentum distributions were extracted assuming that all ^{22}O excited levels decay through the first excited state at 3.2 MeV. This peak was, therefore, used to gate the longitudinal momentum distribution in order to obtain the exclusive momentum distribution of the ^{22}O ground state that finally enabled a conclusion that the ground-state spin of ^{23}O is $I^{\pi} = 1/2^{+}$, which brought the experimental controversy to an end.

[2]Hexagons of 5 cm side and 20 cm thickness place 80 cm behind the knock-out target in a wall configuration.

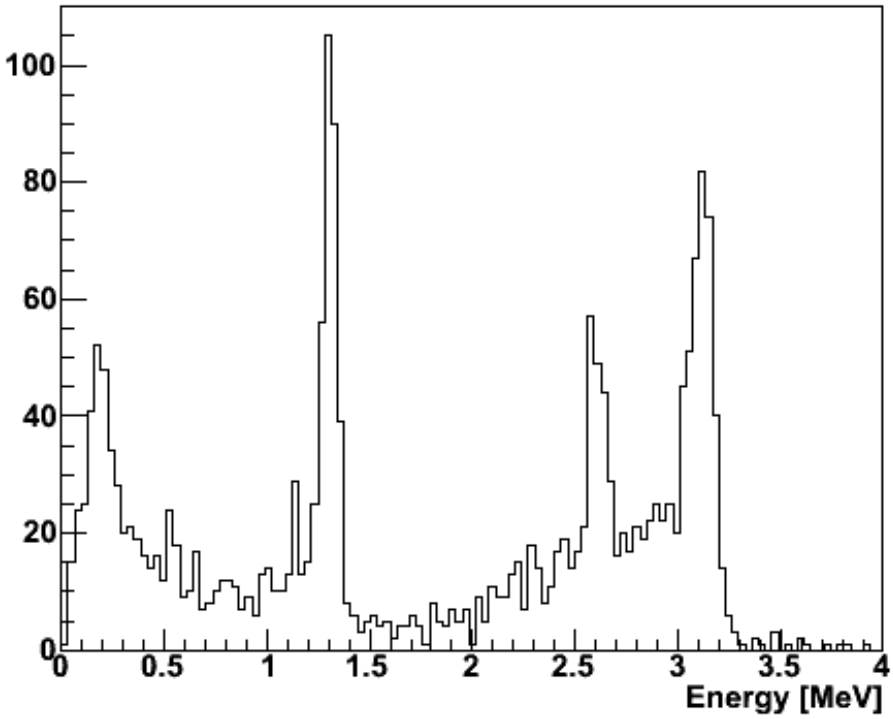

Figure 4.20.: Energy spectrum in CALIFA, after the analysis and Doppler correction of γ rays emitted according to the level scheme shown in the previous figure. See the text for further explanation.

In order to demonstrate the resolution of the CALIFA Barrel in a spectroscopic experiment, the level scheme shown in Fig. 4.19 has been introduced in the CALIFA-R3BRoot simulation. The total number of entries in the simulation has been selected to obtain a similar number of total entries than in the experimental spectra, while the population of the different schemes has been adjusted to the experimental values, without particular attention to the efficiency problems of the original experimental setup at high γ-ray energies. Also there is no attempt to reproduce any background or noise distribution over the simulated data; the experimental conditions were quite clear due to the time windows which allow the separation of different contributions from the target interaction in the γ-ray detectors. The result of the simulation is shown in Fig. 4.20. The two γ rays at 2.6 and 3.1 MeV are now perfectly separated, with energy resolutions of $\sim$5%, while the peak at 1.3 MeV presents a resolution of $\sim$8%.

To illustrate the high efficiency and resolution of CALIFA, additionally to the previous experimental results, we are going to compare with the simulation performed with the MINIBALL setup [EPT+01]. Prompt γ rays emitted by the reaction products could be detected with the eight triple-cluster detectors of the Miniball γ-ray spectrometer. For this simulation the detectors were arranged in a similar fashion to a recent experiment in the Fragment Separator FRS at GSI [MGK+09]: a ring with an average distance of 26.4cm between the front face of the detector and the centre of the target and at an average azimuthal angle of 40^o with respect to the beam axis. The absolute photopeak efficiency in the laboratory frame was determined, at that moment, to be 3.1% at 344.3 keV and 1.5% at 1332 keV. Using the 6-fold segmentation of the MINIBALL HPGe crystals for the Doppler correction of the γ-rays, a resolution of $\sim$40 keV (FWHM) at a projectile

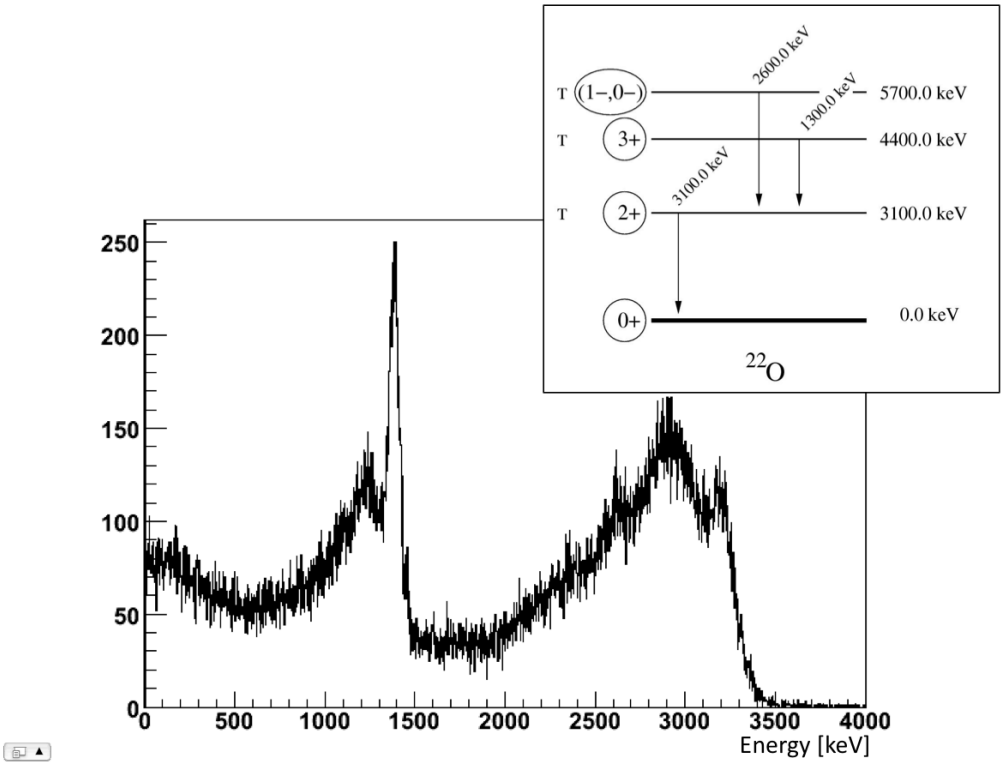

Figure 4.21.: Energy spectrum obtained from the analysis of events in MINIBALL according to the level scheme shown in the insert, after the proper analysis and Doppler correction. See the text for further explanation.

frame γ-ray energy of about 580 keV was achieved for the relativistic velocities of the reaction products of $\beta \sim 0.7$. This resolution was limited by the solid angle of the detector segments.

Both the simulation of the MINIBALL setup and the CALIFA-R3BRoot were performed using the same input, based on the previous level scheme shown in Fig. 4.19, with the same filling factors, including a flat background (which is not Lorentz boosted) between 0 and 5 MeV. The same number of events has been sent to both setups, with a Lorentz boost corresponding to a velocity of the projectile of $\beta = 0.82$ and the proper digitization and appropriate reconstruction algorithms, respectively. In the case of MINIBALL, an accurate position reconstruction within the HPGe crystals is assumed. For CALIFA, the algorithm is the same as already explained in previous sections.

Fig. 4.21 shows the energy spectra reconstructed in MINIBALL. The high resolution system suffers from different effects, reducing its capability to determine the characteristics of the spectrum. Firstly, the low efficiency at high energies reduces strongly the intensity of the 3.1 and 2.6 MeV peaks. Secondly, the high probability of escape of the γ rays scattered after a Compton process, mainly those produced in the forward direction, is evident in the large number of entries in an structure similar to the Compton edge[3]. Thirdly, the effect of the partial reconstruction of the γ ray energy and the limited angular resolution reduces significantly the resolution, making a broad distribution of the structures at high energy.

[3]After the Lorentz boost correction, typical spectroscopic features (Compton edge, double and single escape peaks) are smeared out and not easily identified in a simple energy spectrum.

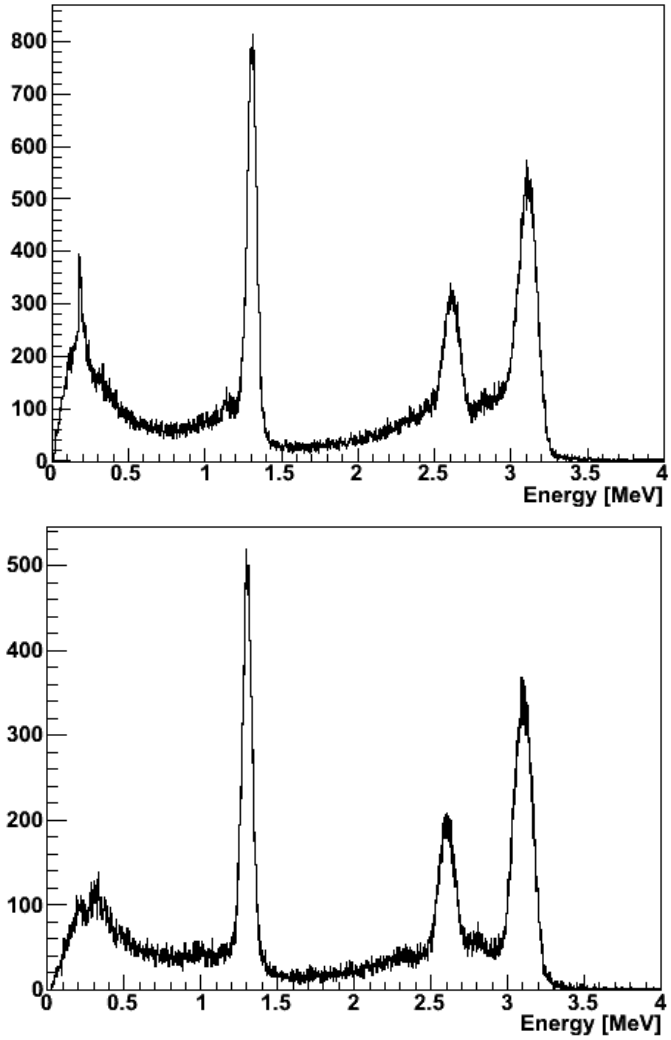

Figure 4.22.: Energy spectrum of γ rays after Doppler correction, obtained in the full CALIFA (top pad) and the CALIFA Barrel (lower pad) from the analysis of events according to the level scheme shown in the previous figure. See the text for further explanation

The reconstruction of the same physical process with identical statistics, is shown in Fig. 4.22 for the whole CALIFA setup (top pad) and for the CALIFA Barrel alone (upper pad). The number of events emitted from the target is the same as in the case of the MINIBALL setup. The three simulated transitions are perfectly separated, with an energy resolution similar to the numbers quoted before for the CALIFA detector with lower statistics. The resolution and the number of events with full energy recorded, due to the large photopeak efficiency, makes very favourable the relation between the peaks and the background and the transitions identification. Using the Barrel alone, the spectroscopic resolution and separation are not damaged, despite a reduction in the total statistics. It is even notable how the Compton edge-like structures are reduced due to the low number of events with part of the energy lost at these moderate energies. This is even more clear from the comparison between the upper pad (whole CALIFA) and the lower (only Barrel): in this later case, the energies reaching the Barrel are lower than in the EndCap and therefore the spectroscopic properties of the Barrel alone are favourable at intermediate energies.

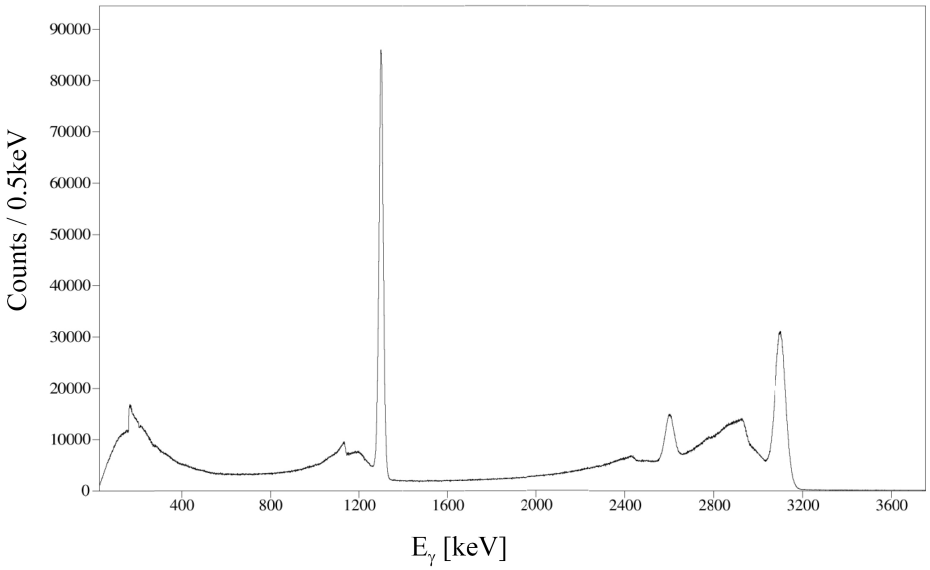

Figure 4.23.: Simulated energy spectrum of γ rays after Doppler correction reconstructed by the forward quarter of the γ-ray tracking array AGATA (courtesy: E. Farnea, INFN Padova). See the text for further explanation.

For comparison, in Fig. 4.23 we present the simulated response expected for a dedicated state-of-the-art spectrometer based on Ge detectors, hence a specialized array not intended for the use neither as calorimeter nor for the detection of protons. In the simulation, the use of the forward 1π quarter of AGATA consisting of 15 triple clusters, hence 45 capsules, has been assumed. The standard settings for position resolution from the pulse shape analysis and packing of interaction points, both 5 mm, have been applied. An amount of $5 \cdot 10^7$ events in total at an velocity of $\beta = 0.83$ with an isotopic emission in the rest frame of the emitting nucleus has been simulated. The data set contains a mixture of multiplicity $M = 1$ and $M = 2$ events modelling the experimentally observed intensities of the γ-ray transitions correctly. Effects arising from the extended beam spot and the velocity spread are neglected in this schematic approach. The achieved energy resolution at 3100 keV in the laboratory system is 50 keV (FWHM), hence 1.6%. The full energy efficiency at this energy is 5.8%. Although in forward direction the Doppler broadening is more important, the obtained energy resolution, as expected, is better because of the better position resolution for the first interaction point obtained by the γ ray tracking technique as well as the better intrinsic resolution of Ge detectors. However, it is also evident that for this and similar physics physics cases the energy resolution obtained with CALIFA is entirely sufficient. Already the full energy efficiency of the CALIFA barrel of around 25% at 3 MeV (lower panel of Fig. 4.9), as also expected, is by far superior compared to AGATA. The difference is even more drastic if the forward focusing due to the Lorentz boost is taken into account, preferring in the laboratory system the angles where the AGATA detectors are placed. The larger efficiency will enable experiments with more exotic beams at lower intensities or reactions with lower cross sections. In conclusion, CALIFA as a multi-purpose instrument is fulfils the necessary requirements for highly adequate use as a spectrometer in most cases.

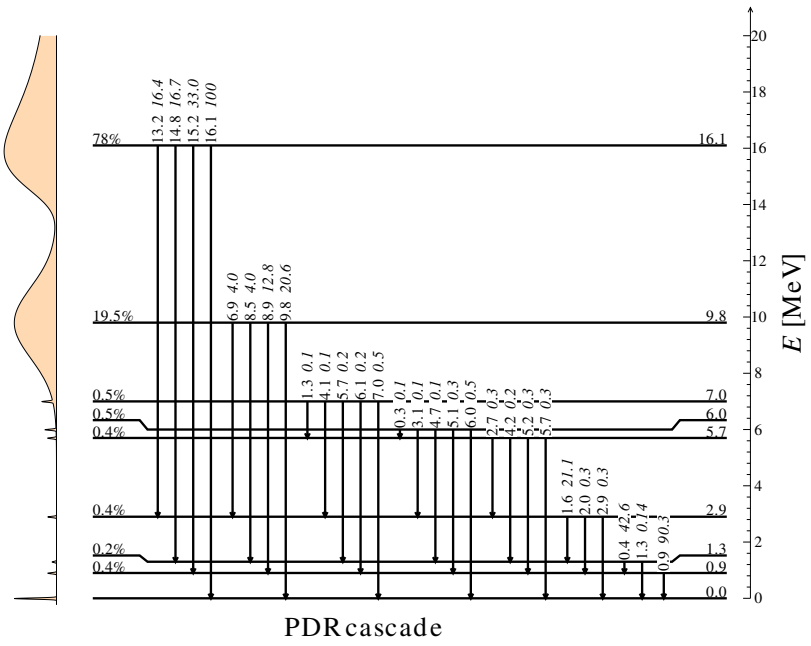

Figure 4.24.: Simulated level scheme for the pygmy dipole resonance physics case. The giant resonance at 16.1 MeV is combined with a pygmy resonance at 9.6 MeV, following the case of ^{132}Sn [AKF+05]. Only photon decays were allowed, i.e. no particles were emitted in the decay. The preferred decay channel is from the GDR directly to the ground state, which produces events with only one high-energy γ ray emitted. The decay from the first excited state, fed from the higher levels, to the ground state produces a strong low energy transition in relation to multiplicity two or three events.

4.5.2. CALIFA as an event calorimeter

In calorimetric mode the main task of CALIFA is focused on the correct determination of the total γ-ray energy emitted in a single event, while the energies of the individual γ-ray energies are of less interest.

Within this subsection two physics cases are distinguished depending on the expected number of γ rays per event.

CALIFA as a low-multiplicity event calorimeter: To demonstrate the calorimetric capabilities of CALIFA in a physics case with low γ-ray multiplicity per event we have used as input for the simulation the GDR event generator (see section 4.1.3) adapted to the ^{132}Sn case, where a high energy (15.1 MeV) giant dipole resonance (GDR) is combined with a lower energy (9.6 MeV) pygmy dipole resonance (PDR), as it has been observed in experiments at the present LAND setup [AKF+05]. In Fig. 4.24 the simulated level scheme is presented.

The relative strengths of the PDR and the GDR coulomb excitation cross sections have been set to mimic the experimental results but only photon decay was allowed. In addition a series of six discrete levels are included at lower energy. Their total excitation probability

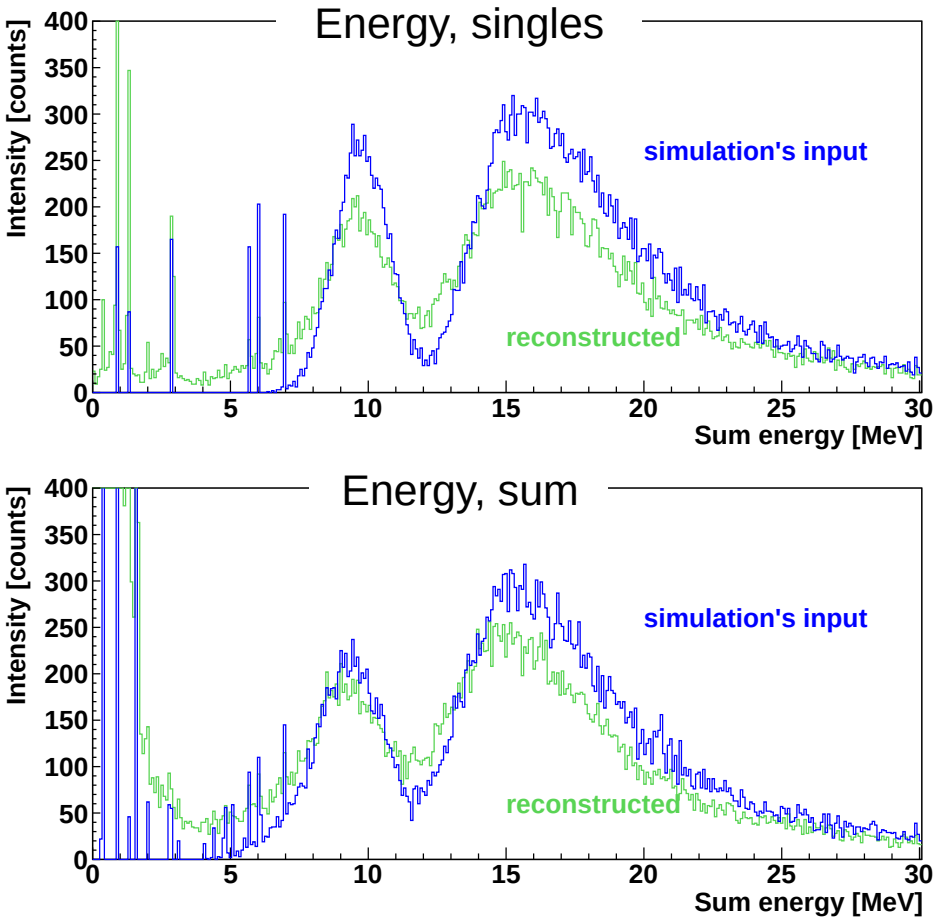

Figure 4.25.: Energy spectrum of the singles γ rays (top) and sum energy per event (bottom). In both cases the spectrum as used as an input for the simulation (in blue) is shown together with the reconstructed one (in green). The calorimetric sum spectrum is the total energy deposited in the calorimeter event by event. A 'perfect' EndCap is assumed - the γ rays emitted in its direction are analysed without experimental uncertainties. The double resonance structure is well represented.

(the probability of being populated as first level) is 2.5% compared to the higher energy region. In this simulation the favourite decay channel of the giant and pygmy resonance is chosen to be the decay directly to the ground state, i.e. the probability to decay in a cascade via low-lying excited states is quite low compared to a single transition. The average multiplicity of the decay is thus low, with 60% of the events having multiplicity one. The probability of having an event with multiplicity two, three and four is 20%, 10% and 10%, respectively.

The excitation probability as produced in the event generator is shown in Fig. 4.25 in blue. The GDR at 16.1 MeV and PDR at 9.6 MeV are shown together with the discrete levels at lower energy. The events are generated according to this excitation probability. The energy in the nuclear frame of the single γ rays is reconstructed from the data collected by the calorimeter, i.e. energy depositions in the single crystals. In order to exclude the effect of the EndCap from the performances of CALIFA's barrel, the γ rays emitted in its direction are analysed without experimental uncertainties, i.e. they are ideally reconstructed. In 86%

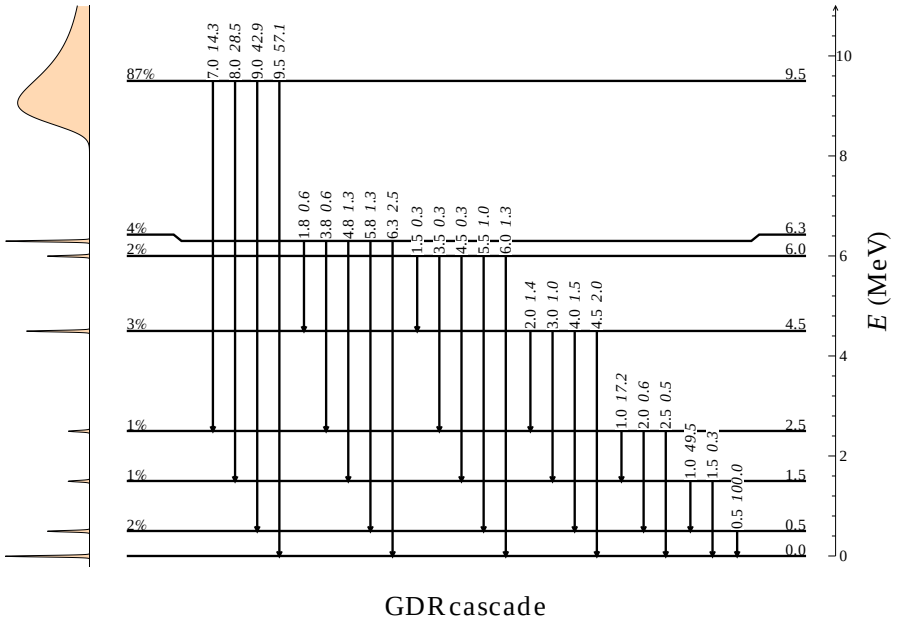

Figure 4.26.: Simulated level scheme for the giant dipole resonance physics case. The giant resonance at 10 MeV is combined to several discrete levels. Only photon decays were allowed, i.e. no particles were emitted in the decay. The different decay chains produce events with high-multiplicity, with about five γ rays emitted in each event.

of the events the barrel contributed to the detection of the emitted γ rays and only these events were taken into account in the analysis. In the analysis the clustering algorithm as described in sec.4.2 is used to determine photon energy and angle in order to perform the proper Doppler correction. The reconstructed photon energies are summed for every event, to determine the total excitation energy. The result is presented in Fig. 4.25 in green. The difference between the blue spectrum and the green one thus describes the detector response of CALIFA for this particular case.

In the reconstructed spectrum the PDR and GDR are reproduced and well separated. The distortion compared to the original input is mainly due to two effects: i) due to their high energy, the γ ray can escape the calorimeter without depositing its whole energy and ii) in case of multiplicity higher than one, one of the γ rays can escape the calorimeter. However, the realistic reproduction of the original features of the input distribution shows the excellent capabilities of CALIFA to act as a calorimeter in PDR studies.

CALIFA as high multiplicity, high-energy event calorimeter: As an expansion of the results presented for a calorimetric study with low multiplicity and the combination of a high energy GDR and a low energy PDR, a hypothetical population of a Giant Dipole Resonance located at 10 MeV combined with a strong population of several isolated resonances in a nucleus has been simulated. Such an example would test the performance of CALIFA under extreme conditions.

Several levels between 0.5 and 7.5 MeV were simulated, together with the resonance at 10 MeV. The simulated level scheme is presented in Fig. 4.26. The γ rays were emitted from a source moving at $\beta = 0.7$. The average multiplicity in this study was about 5,

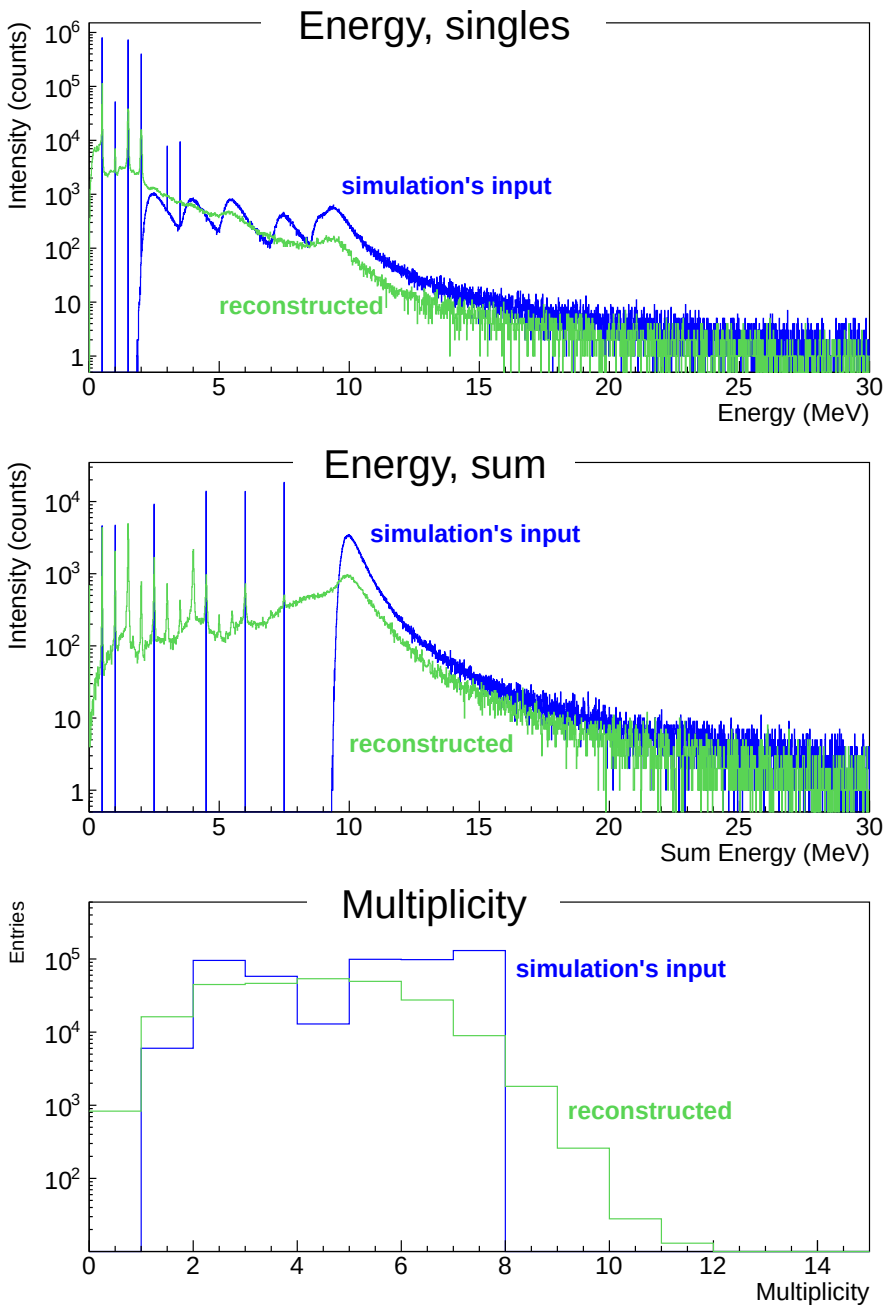

Figure 4.27.: Singles γ-ray spectrum (top), calorimetric sum spectrum, i.e., sum energy of all the clusters per event (centre), and event multiplicity (bottom). In all cases, the input for the simulation (in blue) is shown together with the result from the reconstruction (in green). The average multiplicity per event was 4.8 . The calorimetric sum spectrum is the total energy deposited in the calorimeter event by event. A 'perfect' EndCap is assumed - the γ rays emitted in its direction are analysed without experimental uncertainties. Both the GDR and individual resonances are correctly reproduced.

following the condition of simulating a high multiplicity case to test the performance of CALIFA. The simulated singles γ-ray spectrum, total energy sum of the γ-ray cascades,

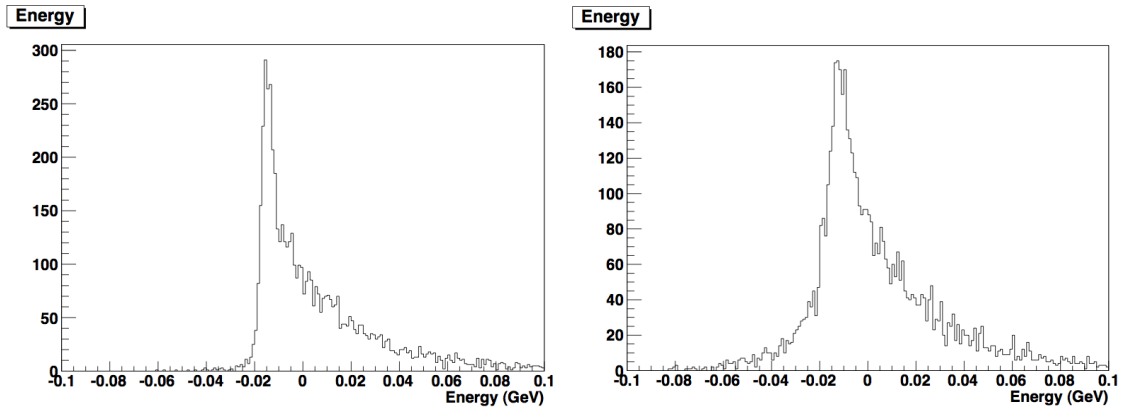

Figure 4.28.: Reconstructed Q value spectrum for ^{12}C(p,2p)^{11}B at 400 A MeV. In the left pad the ^{11}B is in the ground state, while in the right pad it is excited to 5 MeV.

and multiplicity spectra are shown in blue in Fig. 4.27.

Regarding the reconstruction of the events, a 'perfect' EndCap was again assumed. Under this high multiplicity conditions, there was over 99% probability of interacting with CALIFA's barrel, and all those events are considered in the analysis. Similar to the previous case, the clustering algorithm as described in sec. 4.2 was used to determine the photon energy and angle, and thus to perform a proper Doppler correction.

The results are presented by the green curves in Fig. 4.27. The top diagram shows the reconstructed individual γ-ray energies, which means, a histogram of the energy reconstructed by each individual cluster; the sum energy of all clusters per event is shown at the centre of the figure and represents the energy of the full γ-ray cascade rather than individual γ-ray energies. Finally, at the bottom panel, the reconstructed event multiplicity is presented. As it can be observed from the E_{sum} spectrum, both the position and the shape of the GDR can be satisfactory reproduced, while still having a great capability of resolving individual resonances. There are several additional peaks in the sum spectrum, which can be interpreted as events for which one low energy γ ray escaped through the holes of the calorimeter.

The current case demonstrates the already previously demonstrated capabilities of CALIFA as a γ-ray spectrometer and as a calorimeter can also be combined, providing excellent results in its performance.

4.5.3. CALIFA as a combined calorimeter-spectrometer: ^{12}C Quasi Free Scattering

In this subsection the reconstruction of a Quasi Free Scattering (QFS) archetypical case is presented. The reaction considered here is the quasi-free reaction (p,2p) induced by a ^{12}C beam at 400 MeV/A on a proton target, with a Q-value of -15.95 MeV. For this kind of experiment where a proton is scattered out of the incoming nucleus by the proton target, the main role of CALIFA[4] is to detect the energy of the two protons plus the

[4]Note that CALIFA Barrel version 7.07 and EndCap 7.17 was used for this simulation.

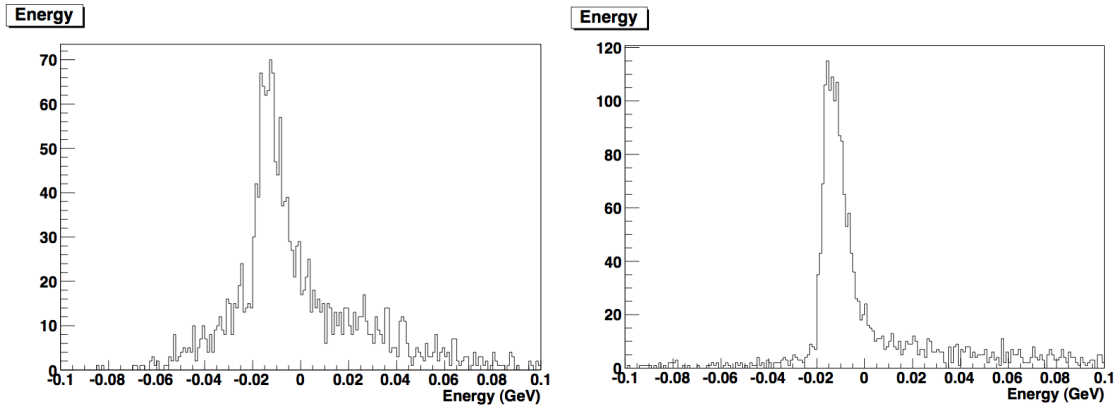

Figure 4.29.: Reconstructed Q value spectrum for ^{12}C(p,2p)^{11}B at 400 A MeV, with ^{11}B populated in the 5 MeV excited states. In the left pad, only the barrel of CALIFA was considered, while in the right pad an ideal EndCap has been added. Note that for this simulation, the barrel with 22 cm long crystals between 43 and 55° was considered.

eventual γ rays from the de-excitation of the recoiling heavy fragments, in a similar manner aforementioned in the ^{23}O knockout. Although the position of the protons detected in CALIFA is also an important piece of information in the event reconstruction algorithm, a precise measurement of the polar angles of the two protons is provided from a three-layer multi-strip silicon tracker placed in-between the target and CALIFA.

For the simulations discussed here, a 7 cm diameter and 6 cm long liquid hydrogen target contained within a thin Mylar envelope was considered together with a beam spot of 3 cm diameter. The position of the reaction was chosen randomly within the volume defined by the beam spot and the target length. A 60 MeV/c internal momentum for the proton scattered out the ^{12}C nucleus was considered in the event generator discussed in section 4.1.3. The simulations were run for 10.000 events in each case.

From the beam energy and the measurement of the angle and energy of the two protons, the Q-value distribution of the reaction can be reconstructed and analysed. Two different cases have been considered: the reaction product ^{11}B in the ground state and in an excited state of 5 MeV; hence with the γ-ray decay detected. The result is shown in Fig. 4.28. The left pad of the figure shows the case where ^{11}B lies in the ground state. The resolution was calculated to be 2.8 MeV and efficiency$\equiv$70% for detecting two protons. The right pad shows the case of the 5 MeV excited state and the effect on the Q-value distribution as a result of the presence of γ rays. Fig. 4.29 shows the same Q-value distribution for the 5 MeV excited state of ^{11}B considering the case of an ideal EndCap for CALIFA (right pad) and no end-cap at all (left pad). The absence of the perfect EndCap reduces only slightly the efficiency and resolution. One should note however that at higher beam energy, more events with one of the proton emitted at very forward angles are expected. The presence of the CALIFA EndCap becomes thus particularly important to maintain a good efficiency at high beam energy.

5. Electronics and Data acquisition

5.1. Overview and Concept

Modern techniques of digital data acquisition have been found to be a major step forward in the next generation of detectors in nuclear physics. Concepts based on digital pulse shape analysis (PSA) have triggered a major development effort in related fields. Certain advantages such as flexible trigger concepts, high rate capability and pile-up reduction, larger dynamic range and highly integrated concepts of data reduction already in the frontends maximise the information stemming from the detector response. Nevertheless, analogue signal conditioning is still an issue. Inexpensive materials such as CsI(Tl) or NaI(Tl) have a reasonably high light output, but their spectroscopic resolution is typically limited both by their intrinsic light output (∼40 photons/keV for NaI(Tl)) and intrinsic non-linearity. This is due to the fact that the light generation process depends on the ionisation density the interaction generates in the cascade until it is absorbed. This property not only influences the total amount of light generated but also the population of states generating the light. Velocity and charge dependence of the electronic energy loss was already used in some experiments like the INDRA detector to separate particles and γ rays. However, the analogue methods have a quite limited resolving power and flexibility at low energies. Recent investigations preparing this TDR [Ben10] have shown that the proton γ ray separation could be strongly improved by using numerical signal de-convolution. It is expected that neutron-γ ray separation will be possible in the same way and also that the energies of particles not fully absorbed in the active medium may be reconstructed.

Digital data acquisition also allows the coverage of a large dynamic range from one hundred keV to several hundred MeV in a very elegant fashion. Standard energy filters are quite well understood and their performance already allows a gain of 2-4 bits via oversampling the measured value in the linear range of the preamplifier at reasonable integration times. The high amplitudes will be covered by the so-called *time above threshold (TOT)* method which could be nicely calibrated in the overlap region of both methods. One important fact in digital DAQ is that the amount of data has to be reduced as much as possible to the frontend electronics to limit the data sizes and computing power needed for the final analysis. Consequently, all the algorithms described have to be reduced and simplified to run on a compact and low power Field Programmable Gate Array (FPGA) based hardware situated close to the detector. This requires a custom hardware electronics design for this application and optimised firmware all tested on small scale prototypes as described below.

The readout concept of the CALIFA barrel is basically divided in three independent layers described in the following section in more detail. The frontend electronics mounted directly at the detector is optimised for low noise and low power consumption to allow for a minimum of cooling infrastructure and good mechanical access to the detector. To minimize the cabling effort and costs it also contains individual channel high voltage using a serial single line slow control bus. Individual channel analogue differential signals are

transported via standard 100 Ohms shielded twisted pair cables of 5 metre length to the digitiser modules located on the movable support structure of the detector. These modules also perform full signal processing as described below and provide buffer memory for an asynchronous data collection. In the final layer the data collection uses only a few optical fibres and a trigger bus system connected to two computers, one for each side of the detector. All prototypes of this modern DAQ electronic based on the Multi-Branch System (MBS) [KE10] and the GOSIP protocol[1] have been used in the CALIFA test experiments described in section A, For compatibility with the existing triggered R3B DAQ and for all the ongoing developments, tests and experiments it is an essential advantage to use a system compatible with forthcoming developments from the FAIR DAQ group. In particular with regards to a future migration towards a more general timestamp based triggerless DAQ, a close collaboration with the NUSTAR DAQ group will provide a smooth transition and significant synergies for both sides.

5.2. Detector Signal

After being hit by any particle, the scintillation light of the CsI(Tl) light emission $L(t)$ shows the following pulse shape:

$$L(t) = \frac{N_f}{\tau_f} \exp\left(-\frac{t}{\tau_f}\right) + \frac{N_s}{\tau_s} \exp\left(-\frac{t}{\tau_s}\right) - \frac{N_r}{\tau_r} \exp\left(-\frac{t}{\tau_r}\right) \tag{5.1}$$

τ_f and τ_s are the decay time constants of a fast and a slow scintillation component, respectively. The time constants are in the order of $\tau_f \approx 600 - 800$ ns, $\tau_s \approx 3.0 - 3.5$ μs. τ_r is the time constant of a fast rise time in the order of $\tau_r \approx 20 - 30$ ns which may be neglected in the following discussion ($\tau_r \ll \tau_f, \tau_s$).

Due to quenching effects, the differential light yield $\frac{dL}{dE}$ as well as the total light $L(E)$ depend on the incident particle type. In order to apply correct energy calibrations it is therefore necessary to identify the particles. Not only the light yield but also the ratio of the components' amplitudes N_f and N_s is dependent on the incident particle type. For a given energy, the discrete values of N_f and N_s are characteristic of the particle type. By determining these amplitudes, the particle is identified [SJW58, GM62].

The APDs, which are connected to the CsI(Tl), convert the scintillation pulse into a photo current. When neglecting the drift time of the charge carriers within the APD $t_{drift} \approx 30\text{ns} \ll \tau_f, \tau_f$ [Kno10] and the light collection time, the photo current is directly proportional to the scintillation function: $I(t) \propto L(t)$.

5.3. Preamplification

The use of Large Area Avalanche Photodiodes was chosen due to the large light output of CsI(Tl) and the operation in the stray magnetic field of the GLAD magnet. Operated at a gain of around 50, this device needs special low noise preamplifiers optimised for their large capacities. High voltage also has to be adjusted individually for each channel and a temperature compensation is needed for a stable operation. This development successfully

[1] Both being developed by the FAIR DAQ group.

performed in collaboration with a local company (Mesytec GmbH & Co. KG[2]) together with its results and tests are described in this section. Based on an existing preamplifier unit MPR-16 [Mes11] from Mesytec, a special charge-sensitive preamplifier MPRB-16 adopted to the high capacities of LAAPDs and contributing a small amount of electronic noise was developed during the preparatory work for this TDR.
It contains 16 channels with individual voltage adjustments in one housing and one temperature sensor for all 16 channels.
Due to many different parameters that have to be set, the preamplifier will also provide remote control access.
Within the design concept (see 10) it is foreseen to position it adjacent to the detector to reduce noise contributions. Therefore the power consumption and heat production had to be minimised.

5.3.1. Basics

Within this charge-sensitive preamplifier the photo current (see Section5.2) of the LAAPD will be convolved with an exponential decay:

$$U(t) = \int_0^t \left(\frac{N_f}{\tau_f} \exp\left(-\frac{t'}{\tau_f}\right) + \frac{N_s}{\tau_s} \exp\left(-\frac{t'}{\tau_s}\right) \right) \exp\left(-\frac{t-t'}{\tau_{RC}}\right) dt' \tag{5.2}$$

where τ_f and τ_s are the two different time constants (fast and slow) of light emission in CsI(Tl) and τ_{RC} is the decay time constant of the preamplifier. The bandwidth limit of the MPRB-16 (about 30 MHz) is neglected in this consideration.

5.3.2. Three operational modes

To cope with the large dynamic range and the strongly varying requirements of different experiments (see Appendix A) from low energetic γ-rays up to 300 MeV particles, the preamplifier is equipped with two different gain modes. A high gain mode for γ energies up to 30 MeV and low gain mode up to 300 MeV.
This allows to run the calorimeter in three different operational modes:

Spectroscopic mode

In spectroscopic mode high resolution and high sensitivity are needed.
Therefore the preamplifier runs in high gain mode. γ-rays up to 30 MeV and also low energy particles can be detected.

[2] http://www.mesytec.com

Calorimetric mode

In calorimetric mode a large dynamic range is needed to detect light recoil fragments and high energetic γ-rays. Due to the decrease of resolution and increase of the trigger threshold with increasing range γ-rays with small energies will be lost. This mode is only optional for high-multiplicity experiments where individual interactions can barely be separated.

Hybrid mode

For experiments where low energetic γ-rays as well as high energy recoil fragments need to be measured with good resolution, a high sensitivity combined with a large range is necessary. In the hybrid mode the preamplifier runs in high gain. All energies up to 30MeV are determined with peak sensing after the deconvolution (see [GG93, GGL94]). For high energy particles above 30 MeV the energy will be determined by the so called *time over threshold (TOT)* method. Therefore the FPGA recognises when the input signal exceeds a certain threshold and counts the time until it returns below (see 5.3.5). Due to the exponential decay of the preamplifier signals also for signals beyond the dynamic range, the contribution to the relative resolution could be kept far better than 1% independent from energies E $>$ 10 MeV.
This will be the standard mode of operation for the CALIFA detector.

5.3.3. Integrated high-voltage supply

Highly limited space close to the detector necessitates integration of the bias voltage generators into the preamplifier. Due to remote control access the high voltage can be set in steps of 100 mV up to 600 V individually for each channel with a stability of 50 ppm.
Beside the remote controllability of the high voltage, there is also a push button to ramp all set voltages of the preamplifier module.

5.3.4. Temperature dependent gain stabilisation

The gain stability of an LAAPD is an important requirement for the usage in high resolution scintillation detectors. Variations due to changing external conditions reduce the available energy resolution strongly. The most important influences are variations in temperature and reverse voltage.

The gain dependence on the temperature can be explained by the drift of charge carriers through the LAAPD. Mainly the electrons contribute to the drift current. On their way through the silicon they interact with phonons and lose energy. With increasing temperature T the number of phonons increase and therefore also the probability of electron - phonon interactions increase [MCS+02],[IKY+03],[KSI+06]. This leads to a decreasing gain G (see Fig. 5.1, a). Assuming a linear dependence leads to

$$\frac{1}{G}\frac{dG}{dT} = -2.95\frac{\%}{^{\circ}C} \tag{5.3}$$

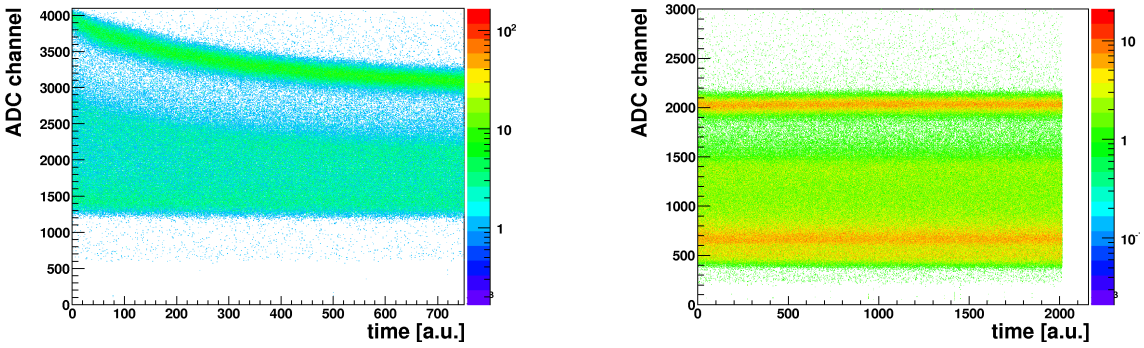

(a) (b)

Figure 5.1.: (a) Gain gradient due to continuous heating of the LAAPD from 11.3°C to 22.7°C: spectrum of a ^{137}Cs source measured with a CsI(Tl)-crystal and read out by an Hamamatsu S8664-1010 LAAPD. (b) Same as (a) but in the range of 6°C to 24°C with a temperature regulation.

With increasing reverse voltage U and therefore increasing band bending at the pn junction the kinetic energy of the drifting charge carriers increase in addition to the internal gain. Measurements have shown

$$\frac{1}{G}\frac{dG}{dU} = 2.5\frac{\%}{V}. \tag{5.4}$$

So by varying the reverse voltage U dependent on the temperature T with a stabilisation slope of

$$\frac{dU}{dT} = 1.18\frac{V}{°C} \tag{5.5}$$

the gain can be stabilised.

The MPRB-16 will provide a common linear temperature stabilisation for all 16 channels. That stabilisation is realised in an analog way to a very high precision below 0.1°C. In comparison, the slow-control temperature measurement can only be precise to 0.2°C in the best case.

5.3.5. Energy determination via Time-Over-Threshold measurements

In Hybrid Mode (see 5.3.2) the energy of high energy particles that exceed the range by far will be determined by the so called *time over threshold (TOT)* method. Therefore the FPGA recognises when the input signal (Fig. 5.2, red) exceeds a certain threshold (Fig. 5.2, green) and counts the time Δt until it returns below.

It is necessary that the decay of the preamplifier signal is fully exponential, including high signals which exceed range limits. This guarantees a constant relative resolution of better than 1% for energies over 10 MeV.

$$\frac{\Delta E}{E} = \frac{\Delta t}{\tau} = const \tag{5.6}$$

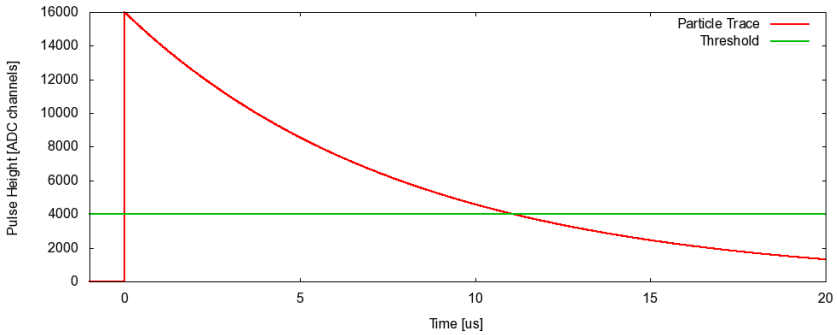

Figure 5.2.: Basic concept of Time-Over-Threshold measurements with an ideal signal trace (red): The time when the input signal exceeds a certain threshold (green) to the point in time, until it returns below, is measured.

For an ideal exponential input signal the dependence on the energy is logarithmic:

$$\Delta t = \tau \left[ln\, E - ln\, Thr \right] \tag{5.7}$$

where Thr is the threshold value and τ the preamplifier decay time constant.

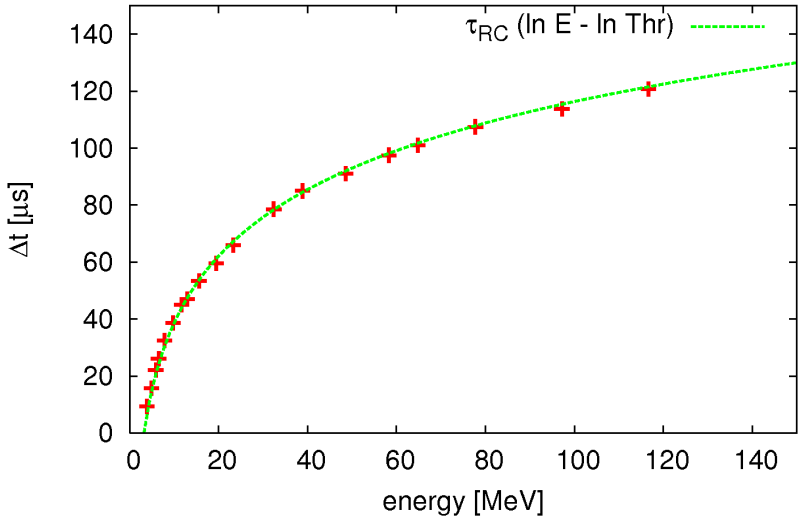

Figure 5.3.: In the energy range up to 120 MeV the logarithmic dependence of Δt on the energy can be clearly seen.

Pulser measurements up to an energy of 120 MeV confirm the logarithmic behaviour also for real preamplifier signals (Fig. 5.3). Larger signals could not be tested due to the 12 V limit of the pulser.

5.4. Digitiser

In order to provide high modularity and flexibility of the readout system easy adjustable to different experimental requirements, the whole readout and pulse processing system is

implemented digitally. In such systems most of the work goes into the hardware programming and not into the electronics development. Using a modern portable language like VHDL this allows easy upgrades of the functionality, additionally allowing an easy change of the hardware for future upgrades. Also individual parts of the algorithm could be ported in other detectors and readout systems in FAIR as the hardware can be changed without changing the firmware and vice versa.

5.4.1. Hardware

The Front End Electronics cards (FEE) of CALIFA feature a fast sampling ADC to digitise the preamplifier's signal and a Field Programmable Gate Array (FPGA), a programmable logic device, to perform the signal processing on the digital data stream from the ADC. The signal processing firmware (see Section5.5) was and will be implemented and tested on the following devices:

HADES RICH ADC module First implementations have been developed for the ADC module of the HADES RICH detector. It features two 12 bit, 40 MHz fast sampling ADCs with 8 input channels each and a *Lattice ECP2M 100* FPGA with 100k look up tables (LUTs). The ECP2M series features, amongst others, dedicated multiplier and memory cells. A micro controller on board connected to the FPGA enables complicated computations. The TRBnet protocol, which uses a optical fibre network with star topology, is used for slow control and event readout [MBKP10].

FEBEX 2 Since TRBnet is not designed for the usage with MBS, the *Gigabit Optical Serial Interface Protocol* (GOSIP) will be used for CALIFA. In contrast to TRBnet, GOSIP uses a ring or chain topology. The *Front End Board with optical link Extension, version 2* (FEBEX 2) served as a basis for the first implementations using GOSIP. A 12 bit ADC with eight input channels operated at 60 MHz conversion rate digitises the preamplifier's signal and feeds it to the *Lattice ECP2M 50* FPGA with 48k LUTs[3] [Hof11a].

CALIFA Front End As the logic resources of the ECP2M 50 are not sufficient for CALIFA's signal processing, the development of a dedicated FEE was started for CALIFA. It will be built on top of the existing FEBEX 3. It features two 14 bit ADCs with 8 input channels each, operated at 50 MHz conversion rate. The *Lattice ECP3 150* FPGA with 149k LUTs provides sufficient logic and memory resources. A great feature of FEBEX 3 [Hof11b] is the PCI express connector with which all Front Ends are assembled in a crate with a common optical fibre connection. First tests have been successfully done in the GSI electronics department.

5.4.2. Analog Preprocessing

Unlike the preamplifier, the FEE are not placed close to the detector but at a distance of about 3 – 5 m. This is essential due to heat production of about 500mW per channel (see 10) and to avoid induction of electronic noise to the preamplifier or the LAAPDs by the FEE.

[3] Look-Up Tables.

As already mentioned in section 5.3.4, the LAAPDs' gain strongly depends on the operational temperature. Temperature fluctuations or gradients as produced by the FEE would impair the energy resolution and particle identification capabilities of the detector.

To minimize the induction of noise, the preamplifiers' outputs are connected to the FEE using differential signalling over shielded, twisted pair cables. Nevertheless, on the input stage of the FEE, the signal has to be processed by a low pass filter to reduce white noise and, even more important, avoid aliasing effects. While digitizing the signal, it will be translated into a discrete time domain. Disturbances with frequencies above the Nyquist frequency

$$f_{Nyquist} = \frac{1}{2} f_{ADC} \tag{5.8}$$

(where f_{ADC} is sampling frequency of the ADC) will lead to aliasing in the digitized signal [Smi03]. An anti aliasing filter will therefore be placed at the input buffer amplifier at the FEBEX3 ADC.

5.5. Digital Signal Processing

A complex digital signal processing firmware is implemented on the FEE FPGA. It's written in VHDL (Very High Speed Integrated Circuit Hardware Description Language) and can thus be easily maintained, modified or changed. Its primary goal is to detect events and extract all information of interest in real-time. For each event, only this information is sent to the MBS readout. No particle traces need to be acquired; reducing both the network load and the storage size. This enables higher event rates that can be handled by the detector.

An overview of the implemented digital signal processing firmware is given in figure 5.4 and will be explained in detail in the following sections. The firmware is based on the Moving Window Deconvolution (MWD) [GGL94] and the Reconstructive Particle Identification (RPID) [Ben10].

To minimize dead-times, the complete firmware is continuously running within the ADC sampling clock domain. Each incoming data sample is directly processed. It is however not possible to perform the full process within a single clock cycle. The technique of pipelining is used to ensure that the processing rate equals the ADC sampling rate. With this techniques it is furthermore possible to accept new events while the previous event is still being processed.

5.5.1. FPGA Implementation

As the algorithms to be implemented on the FPGA are very complicated and thus need many logic and memory resources which are limited by the FPGA, some challenges arise when implementing particular filters. The following methods have been used to fit to the available resources.

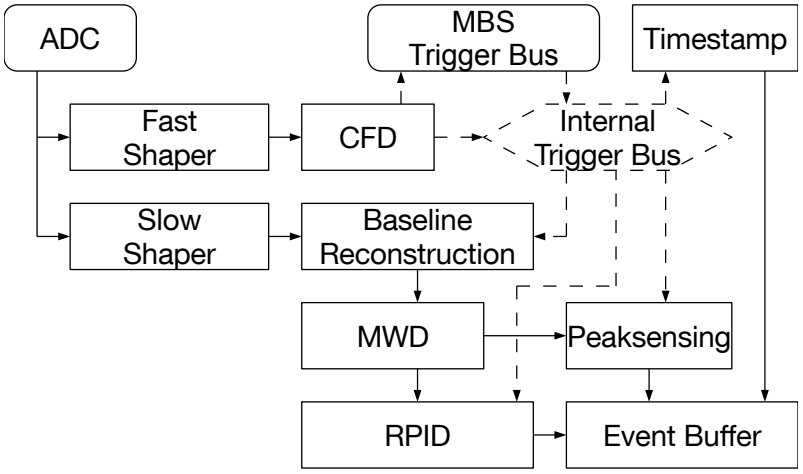

Figure 5.4.: Digital signal processing firmware implemented in the FPGA on the FEE. Please refer to the text for a detailed description.

Division and Multiplication Both division and multiplication are non-trivial operations which need a lot of logic resources when implemented using general purpose logic cells. To cope with that, the utilized Lattice ECP3 FPGA features dedicated DSP (Digital Signal Processing) cells that can be used for signed or unsigned integer multiplications. Every filter which needs to perform multiplications makes use of one of those DSP cells. General purpose logic cells are thus saved and are available for the filter logic.

Divisions in contrast can not be performed. Though it is in general possible to implement divisions on an FPGA, the benefit of implementing a division does not compensate for the hardware effort. Wherever possible, divisions are replaced by bit-shift operations. This allows divisions by powers of two. If a division by a number that is not a power of two is replaced by such a bitshift operation, the result is scaled by a constant factor. This is not an issue, since the energy and particle identification information need to be calibrated anyhow.

Memory Nearly every processing step requires a delay line. These delay lines are implemented as First In First Out (FIFO) ringbuffers which use dedicated dual port, random access memory (RAM) cells. Each RAM cell can store 18 kbit of data, organized in 1024 addresses of 18 bit data width. Within one clock cycle, one data word can be written to and read from arbitrary addresses at once.

Floating Point Operations The whole signal processing is implemented using integer logic. The FPGA does not feature floating point support. Nevertheless it is of course possible to implement floating point operations. But again, these are very resource intensive operations. That amount of resources is not available.

Because the dedicated DSP and memory cells feature 18 bit inputs/outputs, all operations are implemented using 18 bit integer arithmetic. After multiplying two 18 bit numbers, or summing up several numbers, the result exceeds 18 bit and has to be shifted to the right to again fit into 18 bit. In order not to lose significance by rounding errors, the user can choose not to scale down the results providing they don't exceed the 18 bit range.

Interlacing In general, the complete processing firmware has to be implemented on the FPGA once per input channel. The maximum number of processable input channels is constrained by the FPGA's resources.

To increase that count, interlacing can be used. The processing clock frequency is increased to an integer multiple of the ADC sampling frequency ($n \times f_{ADC}$). Within each clock cycle, the data sample of another input channel is processed by one and the same logic. After n clock cycles, the next data sample of the first input channel is processed and so on.

The amount of logic cells needed is strongly reduced. With interlacing, the limiting factors for the count of input channels are the memory space and the maximum clock frequency.

5.5.2. Operation Modes

The signal processing firmware features three operation modes: Free running (self triggered), externally triggered, internally triggered with external validation.

Free Running In this mode, all FEE modules are independent. The internally generated local trigger (see section 5.5.3) is directly fed to the internal trigger bus and optionally to a trigger bus controlling the data collection. New events are acquired on each pulse on the internal trigger bus. Multiple events may be acquired before being read out at once by the MBS readout.

Externally Triggered Trigger signals from the MBS trigger bus are directly fed to the internal trigger bus. With every trigger pulse, a new event is acquired and immediately read by MBS. This leads to two implications: Firstly, the whole detector (or dedicated parts) is triggered synchronously and read at once. Secondly, all input channels will be read without the need for the internal discriminator to pass a certain threshold.

Validated The internally generated trigger signals are delayed by a constant time. On every coincidence between the delayed, internal and external trigger signals from the MBS trigger bus, a trigger pulse is fed to the internal trigger bus. In this configuration, all channels of the whole detector (or dedicated parts) are read at once, as long as the internal discriminators pass their thresholds. The internal trigger signal is used to reconstruct the exact timing of the event.

Both in externally triggered mode and validated mode, the external trigger source can either be an external detector or CALIFA itself (see section 5.6 for trigger signals generated by CALIFA).

5.5.3. Local Trigger Generation

The data stream from the ADC is split and fed into a fast and a slow shaper. Both shapers use a moving average unit (MA) [Smi03, ch 15] which is a digital lowpass filter to reduce the bandwidth and increase the signal to noise ratio of the incoming data stream. For the fast shaper, shaping times in the order of 100 ns – 300 ns are used to keep a reasonable time resolution. The shaped data stream is used by a Constant Fraction Discriminator (CFD) to generate fast trigger signals. Whenever the internal CFD value passes a certain

threshold, a trigger pulse is issued. As denoted above, the generated trigger signals can either be fed into the MBS trigger bus or directly into the internal trigger bus.

These trigger signals serve as a basis for most higher level trigger signals generated by CALIFA and are therefore termed the *Local Trigger*. Please refer to section 5.6 for more information about CALIFA's high level triggers.

5.5.4. Energy Determination

To cope with varying requirements, three algorithms are implemented to determine the energy of an event: One using the full processing chain as outlined in figure 5.4 for high energy resolution, time over threshold for particle traces exceeding the ADC input range and finally slope extrapolation as a fast energy approximation for trigger generation.

Full Processing Chain

Slow Shaper Initially, the ADC data stream is processed by the slow shaper. To achieve a good energy resolution, the slow shaper uses shaping times in the order of 2 – 5 μs to eliminate high frequency noise.

Baseline Reconstruction The shaped data stream is passed to the baseline reconstruction to compensate for a potentially floating baseline value. The baseline reconstruction uses a modified MA to calculate the current baseline value and subtract it from the incoming data stream:

$$\Sigma_n^{BL} = \begin{cases} \Sigma_{n-1}^{BL} + D_n - BL_{n-1} & \text{if } \overline{G}, \\ \Sigma_{n-1}^{BL} & \text{if } G \end{cases} \tag{5.9}$$

$$BL_n = \frac{1}{L}\Sigma_n^{BL} \tag{5.10}$$

$$Q_n = D_n - BL_n \tag{5.11}$$

where Σ_n^{BL} denotes the moving baseline sum after the n-th data sample, D_n the incoming data samples, BL_n the baseline values, L the window size of the baseline reconstruction (i.e. the shaping time) and Q_n the baseline corrected data samples. The condition G is true within an active trigger gate, while $\overline{G}$ is true outside trigger gates, i.e. no event signal is present.

Since there is no division implemented on the FPGA, L has to be a power of two: $L = 2^n, n \in \mathbb{N}$

Moving Window Deconvolution At this point, the data stream is still a convolution of the charge signal with the preamplifier's exponential decay (see equation (5.2)). This leads to two major problems: Firstly, the signal has a rather long exponential tail which leads to a signal distortion in the case of pile up events. The measurement of the energy and the particle identification will fail. Secondly, a ballistic deficit in pulse height is induced by the preamplifier. This will lead to a reduced energy resolution.

To cope with these issues, the shaped and baseline corrected data stream is processed by the MWD [GGL94] which deconvolves the preamplifier's exponential decay and delivers the integrated charge function:

$$Q_n = D_n - D_{n-L} + \frac{1}{\tau_{RC}} \sum_{k=n-L}^{n-1} D_k \tag{5.12}$$

where again D_n are the shaped and baseline corrected data samples, L the window size of the MWD, τ_{RC} the preamplifier's time constant and Q_n the signal's integrated charge within D_{n-L} – D_n:

$$Q(t) = N_f \left((1 - \exp\left(-\frac{t}{\tau_f}\right)\right) + N_s \left(1 - \exp\left(-\frac{t}{\tau_s}\right)\right) \tag{5.13}$$

The MWD shortens the events' signals and thus suppresses pileup effects. The minimum time difference between two events without pileup effects is reduced to the window size L which is in the order of 9 μs – 18 μs. The eligible event rate adds up to about 55 kHz – 110 kHz.

In this case, the division by τ_{RC} can not be replaced by a bitshift operation, because the MWD won't reproduce the integrated charge function if τ_{RC} is not properly set. Instead, equation (5.12) is multiplied by τ_{RC}:

$$\widehat{Q_n} \equiv Q_n \cdot \tau_{RC} = \tau_{RC} \cdot (D_n - D_{n-L}) + \sum_{k=n-L}^{n-1} D_k \tag{5.14}$$

Indeed, the resulting $\widehat{Q_n}$ is scaled by τ_{RC}, but the energy measured by the Peak Sensing has to be calibrated in any case.

Peak Sensing To finally measure the energy of an event, the signal is first processed by another MA instance with a time constant in the order of 100 ns (and thus creating a two pass MA). A register, which is reset to zero on every trigger signal, stores the maximum signal amplitude. At the end of a trigger gate, this maximum value is stored to the event buffer.

Time Over Threshold

If the incoming analogue signal exceeds the ADC voltage range, the above explained processing chain can't be used to determine the energy of an event. Instead, the time over threshold method explained in section 5.3.2 is used.

Slope Extrapolation

CALIFA has to be able to deliver sum energy triggers within 1 μs. However, it takes about 10 μs to collect 99% of the event charge. Thus with a simple peak sensing (even without the full processing chain) that requirement obviously can not be met.

However, the rise time of the signal is nearly independent of the total energy, so in first approximation the slope of the rising edge is proportional to the final energy and can be used as an early approximation. This approximation is used for energy sum trigger decisions as explained in section 5.6.

5.5.5. Particle Identification

Since the differential light yield $\frac{dL}{dE}$ of the CsI(Tl) scintillators depends on the type of irradiation (see Section5.2), unique energy calibrations have to applied for the different particle types. Thus, the incident particles need to be identified. To identify the particles, the *Reconstructive Particle Identification* (RPID) algorithm is used. The idea is to analytically reconstruct the scintillation components N_f and N_s from the luminescence signal (eq. 5.1) [Ben10].

Starting point of the RPID is the integrated charge function as obtained by the MWD (equation (5.13)). In the first step, this signal is being differentiated. For that, the signal is integrated in two windows. These integrals are then subtracted:

$$I_i = \sum_{k=i-L}^{i} Q_k - \sum_{k=i-L-G}^{i-G} Q_k \tag{5.15}$$

Q_k is the deconvolved input signal, I_i the differentiated output, L the integration time and G the gap between the two integrals. For calculating the integrals again an MA filter is used.

After this differentiation, the signal has got the shape of the original luminescence signal:

$$I(t) = \frac{N_f}{\tau_f} \exp\left(-\frac{t}{\tau_f}\right) + \frac{N_s}{\tau_s} \exp\left(-\frac{t}{\tau_s}\right) \tag{5.16}$$

Next, the signal is multiplied by $\exp\left(\frac{t}{\tau_s}\right)$, leading to a pure exponential with constant baseline:

$$\begin{aligned} J(t) &= I(t) \cdot \exp\left(\frac{t}{\tau_s}\right) \\ &= \frac{N_f}{\tau_f} \exp\left(-\frac{t}{\tau_{sf}}\right) + \frac{N_s}{\tau_s} \\ \text{with } \tau_{sf} &= \frac{\tau_s \tau_f}{\tau_s - \tau_f} \end{aligned} \tag{5.17}$$

As the exponential can not be computed by the FPGA, the values of $e^{\frac{t}{\tau_{sf}}} \equiv \exp_t$ are stored as a look up table within a memory cell. Each value is stored in a pseudo floating point

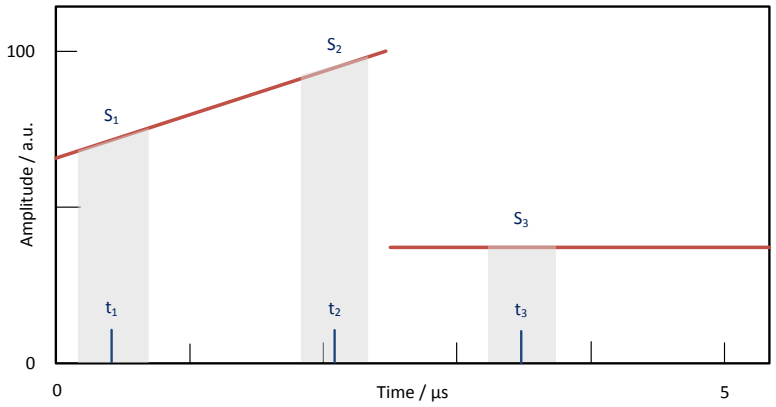

Figure 5.5.: Time windows of the RPID algorithm.

structure.

$$\begin{aligned} \exp_t &= M_t \cdot 2^{-E_t} \\ M_t &\in \mathbb{N}_0, E_t \in \mathbb{Z} \end{aligned} \tag{5.18}$$

The incoming signal value is multiplied by M_t and the result is then shifted by E_t bits to the left or right, depending on the sign.

In the last step, another MWD is performed with time constant τ_{sf} and window size $L_2 < L_1$ (window size of first MWD) leading to a function $F(t)$ (see Figure 5.5):

$$F(t) = \begin{cases} \frac{N_s}{\tau_s}\left(\frac{t}{\tau_{sf}} + 1\right) + \frac{N_f}{\tau_f} & , 0 \leq t < L_2 \\ \frac{N_s}{\tau_s}\frac{L_2}{\tau_{sf}} & , L_2 \leq t < L_1 \\ 0 & , \text{else} \end{cases} \tag{5.19}$$

As one can see, N_s can be determined by the slope of the straight line in the first area and the constant offset in the second area. In practice, the average of both delivers the best result. The intercept of the first straight line may be used to determine N_f.

The averages of the signal S_1, S_2 and S_3 are computed within three time windows $[t_1 - \frac{T}{2}, t_1 + \frac{T}{2}]$, $[t_2 - \frac{T}{2}, t_2 + \frac{T}{2}]$, $[t_3 - \frac{T}{2}, t_3 + \frac{T}{2}]$ of size T (see figure 5.5). The slope and intercept of the first straight lines are determined by S_1 and S_2, while the constant offset in the second area is determined by S_3.

With the two scintillation components N_f and N_s obtained by this algorithm, the incident particle is identified.

As an illustration, the Figure 5.6 was obtained by the pulse shape reconstruction (baseline and pile-ups should be eliminated) and analysis from the proton beam at the MLL facility (see Appendix A).

On this picture, one can clearly see three lines, corresponding (from the top) to the identified γ, protons and deuterons. The γ line shows the 4 MeV, single escape and double escape peaks from the carbon excitation, the 15MeV peaks appears as a large band. The protons line shows two large groups at high energy corresponding to the elastically and inelastically scattered protons on the carbon target. Finally the deuterons line shows essentially the elastically scattered deuterons.

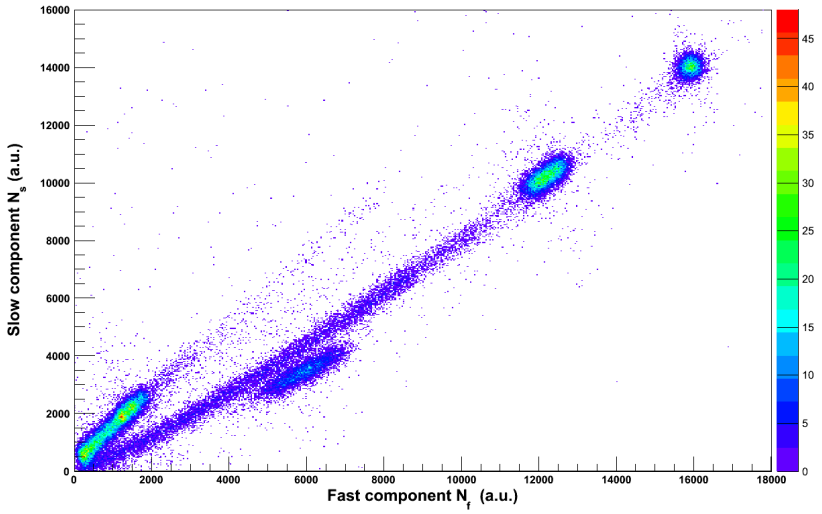

Figure 5.6.: Reconstructed slow component as a function of its corresponding fast component, both in arbitrary units.

5.6. Readout of CALIFA

CALIFA detector belongs to a general and versatile experimental setup of the R^{3}B experiment. Therefore its data have to be combined with the data from the other detectors. The complete setup is foreseen to be merged in two different ways: a so-called triggered mode, where most of the detectors send a signal indicating detected particles to a central trigger logic, which is then responsible to validate certain events, corresponding to interesting physics cases. This more traditional method allows for a quite strong reduction of data close to the detector and simplifies data transport processing and storage significantly. Older detector systems are usually based on this mode. The second mode is the so-called triggerless, where each detector individually validates the events, records the data and marks with a global time-stamp in order to synchronise the data afterwards in an event builder or by the analysis software.

The CALIFA DAQ system will allow for both options to be used in all the different experimental configuration in R^{3}B but also allows the combination with other experiments at FAIR.

In this section, we will first present the different triggers that can be generated in CALIFA before discussing the two integration schemes mentioned above.

5.6.1. Trigger Generation

The wide range of physics cases to be investigated as part of the R^{3}B program necessitates the development of triggers optimised for each case.

In order to avoid any confusion, the triggers mentioned in this section are logic signals generated by the FEE to indicate the possible detection of a particle. As previously mentioned, those signals will be combined into readout triggers (see section 5.6.2).

Depending on the reaction to be observed, it has been found for previous detection arrays utilised for a similar purpose that three different generated triggers can be usefully employed: a logical OR, multiplicity and analogue sum. A brief description of the operations of these three trigger types is outlined below.

When a single-photon is emitted, it is likely to be detected in one crystal, causing the generation of an electronic pulse. That pulse is discriminated (constant-fraction discriminator), meaning that a logic pulse is generated if the electronic pulse is larger than a certain threshold (typically 50 mV). All the logical pulses are ORed together, generating the so-called OR trigger. The physical meaning of that trigger is that at least one of the crystal had an electronic signal above the given threshold. That trigger is very useful for source calibration runs, or for single low-energy γ detection. However given the risk of false trigger on a single channel, the OR trigger can be very noisy (see section 5.6.1).

Due to different physics reactions, and in particular the Compton scattering, it is possible that a photon (or any particle) leaves the crystal. Hence not all its energy can be detected in that crystal. Often, the remaining energy can be determined in a neighbouring crystal. This effect can be so important that none of the crystals detect enough energy to pass above the threshold and hence the event would be lost. Therefore, another, less biased, trigger was defined: the energy sum. The electronic pulses from the different crystals are analogically summed and the resulting pulse is compared to a threshold. That trigger has the advantage that it offers the possibility to have a higher threshold hence lowering the total rate compared to the OR trigger and also it does not depend on the ratio between the main crystal and neighbours.

In case of higher energy photons, or in simultaneous events (like a decay cascade), more than one crystal passes the individual threshold (the difference can be determined by the Simulation, see section 4). It is possible to characterise such events by summing the logical signals from the individual crystals. The height obtained is proportional to the number of crystals above the threshold. A second threshold is set in order to define a minimum number of crystals that are expected to detect a sufficient amount of energy. This is the multiplicity trigger.

Depending on the physics of interest and the reaction rate, a trigger was chosen to signal the detection of a particle in the calorimeter. Previous detection arrays intended for a purpose similar to CALIFA utilised analogue FEE; consequently the generation of triggers was made analogically as well. For CALIFA, however, the digital FEE offers further possibilities.

Triggers Generated by CALIFA

Due to the structure of the FEE of CALIFA, the generation of logical signals that indicate the detection of a particle, or triggers, can be separated into four different levels.

As illustrated in Figure 5.7 and detailed in section 5.1, the electronic pulse from the APD is transmitted to the digital FEE. Firstly for each crystals, two branches are considered (marked in the 'crystal' part of the figure): a discrimination ($\sqcup\!\sqcap$), where the pulse is compared to a threshold as in the case of the Crystal-Ball, and an energy determination (see section 5.5.4).

The channels of 16 crystals are grouped together in the FEB ('cluster'). The discriminated signal from the 'crystal' can be ORed together (4 on the figure), but can also be summed. That sum can then be discriminated: this is the multiplicity trigger, on the cluster level

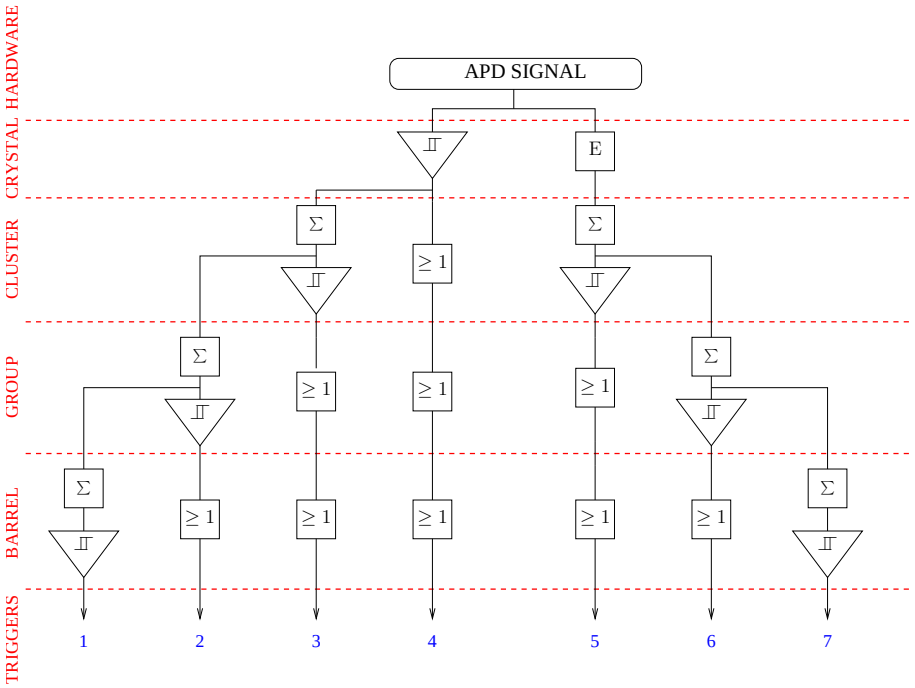

Figure 5.7.: Overview of the triggers generated from CALIFA: a pulse is generated by the APD and transmitted to the FEE. At first two branches are considered: one is a simple discrimination (marked with ⊥⊓) and the second is an energy determination (E). Those information from all the crystals are combined in the FEB ('group'), chain of FEB ('group') and the whole detector ('barrel') in order to provide so-called detector triggers. The combination is composed essentially of logical OR operation (≥ 1), analogue sums of either the energy or the multiplicity of triggers ($\sum$) and discrimination (is the sum above a threshold?).

(3). In parallel or instead, the energies determined on the 'crystal' level can be summed. That resulting sum can then be compared to a threshold: this is the energy sum trigger of the cluster level (5).

The FEB are chained together in a particular geometrical configuration: each chain defines a region of the detector. The combination of the signals from the different clusters, forms the groups. At the group level, a similar operation as on the cluster level can be employed. It is then possible to define new multiplicity (2) and energy sum (6) triggers on the group level.

Finally the chains are all combined into the electronics of the whole detector: the 'barrel' level. As before new triggers can be defined.

All the triggers defined in this section are summarised in Table 5.1.

Of course, other combinations can be defined in particular cases. However those triggers offer the most important possibilities to define a detected particle as the analogue sum, the multiplicity and the OR triggers (7, 1 and 4 respectively). The others offering then a way to limit the trigger decision and acquisition to a certain geometrical portion of the whole barrel.

Trigger	Name
1	Barrel multiplicity
2	Group multiplicity
3	Cluster multiplicity
4	OR
5	Cluster energy sum
6	Group energy sum
7	Barrel energy sum

Table 5.1.: Summary of different generated triggers. The trigger number refer to Figure 5.7.

Hardware Implementation of Triggers

The different triggers possibilities have been described and now the question of their implementation will be examined.

The implementation of both the energy determination and the discrimination within on crystal level are described in section 5.5 as they are fully implemented within the FPGA of the FEB. The cluster level is also implemented on the same hardware.

At the group level, the OR are implemented by pulled-down cables. As soon as one of the FEB on the chain gets a signal from the cluster level, the level on the cable (one per trigger) in changed from high to low, hence informing the other modules of the trigger, and propagating the information to the barrel level.

The implementation of the group energy sum and multiplicity triggers are more complex. Indeed, it is required to accumulate over a group of FEB, the energy and multiplicity delivered by each of the group. For that purpose, specific trigger modules are connected to the FEB. Those trigger modules are connected in a chain to sum on-the-fly the energy sum and multiplicity determined in the FEB (on cluster level). The organisation of that group trigger bus is summarised in Figure 5.8.

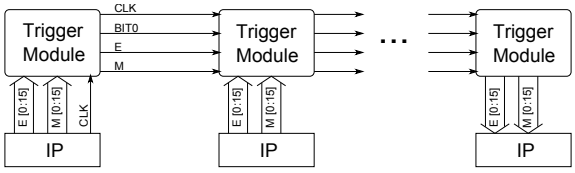

Figure 5.8.: Structure of the trigger bus used to generate group level energy sum and multiplicity triggers. Each IP represent the FEB used for the digitisation of the data, and the trigger module represents extra hardware connected to the board.

The first FEB in the chain generates a 40 MHz clock and a bit0 signal. Those are propagated throughout the chain and used to synchronised the actions of the different nodes on the chain. Each FEB sends the cluster energy and multiplicity to its corresponding trigger module. Those values are serialised and added on-the-fly by each module to the corresponding line. This method presents the advantages of a limited number of cables:

four lines are required between each module (clock, bit0, energy and multiplicity), additionally having an asynchronous behaviour, avoiding to block the whole line in order to wait for all the modules to have added their contribution. The trigger module is based on a Complex Programmable Logic Device (CPLD) which offers constant and predictable signal propagation delays, together with the versatile possibility of a (re)programmable device. The last module in the chain deserialises the values and compare them with given thresholds: a trigger signal is generated when those values crosses the threshold.

As the clock (operation synchronisation) and bit0 (event synchronisation) are directly propagated through the module and the energy and multiplicity signals have to pass through the combinatorial logic of summation, a delay of the data signal relative to the synchronisation signals will occur. This limits greatly the length of the chains that can be used with this method, for a given frequency (or limits the frequency for a given chain). The total propagation delay (from the generation of bit0 to the generation of a trigger signal) of 660-1060 ns has been observed for a chain of 24 modules at 40 MHz and 16 bits data, depending on the relative occurrence of an event to the sampling window.

Finally all the information is gathered in the readout PC, so that the barrel level operations could be done at this stage.

Trigger Rate Estimation

In order to determine the choice of the trigger, it is essential to have an idea about triggering rates.

In previous experiments, the OR trigger was connected to a scaler module. From there it was possible to determine that the increase of trigger rate due to the beam was of the order of 1kHz[4]. Of course the exact value depends on the beam intensity, the target type and thickness, etc.

In order to evaluate the noise rate that would act as a background, a measurement with a single crystal without any source of photons (no beam, no calibration source) was performed. A certain number of logic signals were obtained from a discriminator, depending on the threshold chosen. Assuming random coincidences, it is possible to evaluate different trigger rate. Those are summarised in Table 5.2.[5]

5.6.2. Readout

The data have been digitised, and a sensible trigger has been generated to inform the rest of the system that an event was recorded. The data then has to be collected and sent to a data stream in order to, eventually, be written into a file. In order to achieve that, two different approaches have to be considered: the readout is triggered externally or the readout is triggered by the system of CALIFA.

[4]The GSI experiment labelled S393 from August-September 2010 was chosen as an illustration.

[5]This values were obtained considering 1952 crystals. Discriminated signals from the crystal level have a width of 250 ns and the coincidence window for the multiplicity trigger is 2.5 μs. A measurement with a 18 cm-longed crystal with unoptimised electronics estimated the spontaneous trigger rate to be larger than 250 Hz. The value of 250 Hz was chosen for this calculation.

Trigger	Level	Rate (Hz)
OR		$4.8\text{x}10^{5}$
Mult-2	Cluster	24
	Group	$5.1\text{x}10^{3}$
	Barrel	$1.7\text{x}10^{5}$
Mult-4	Cluster	$2.0\text{x}10^{-4}$
	Group	9.7
	Barrel	$1.7\text{x}10^{4}$
Mult-8	Cluster	$1.2\text{x}10^{-15}$
	Group	$3.1\text{x}10^{-6}$
	Barrel	20

Table 5.2.: Calculated noise rate from different trigger. The OR and the different levels of multiplicity triggers correspond to the definition given in section 5.6.1. The digit of multiplicity indicates the minimum multiplicity requirement for the trigger.

External Triggering

In this configuration, the determined energy and time are stored in memory and marked in order to be associated with the corresponding trigger. The trigger generated as explained above, is sent to the trigger logic. This central system is responsible to combine the triggers from different detectors, and by using coincidences determine sensible physics events trigger, like an incoming ion is detected, an outgoing fragment is observed in the fragment branch and a proton was detected in CALIFA. This is likely to represent the reaction of the incoming ion in the target and emission of a proton at large angle while the remaining fragment follows in the beam-like branch.

Once the trigger logic emits a signal, the readout of all the individual sub-systems is triggered. In particular, the readout of the data in the FEE of CALIFA are collected. The collected data are then sent to an event stream and combined with the ones from the other detectors. Once the readout trigger is received, a deadtime is issued: no other events will be treated until that one is done, so no trigger should be sent to the trigger logic.

The synchronisation of the events, the combination of the data and the handling of the deadtime is made in this case using the MBS framework [KE10]. MBS provides a framework for the programming of the readout of the electronics associated with physics experiments. It is usually running on a machine (like the VME RIOs) and synchronising the triggers, trigger type and deadtime using a dedicated trigger module, like the TRIVA in VME standard, or in the case of CALIFA, the TRIXOR. The locally running readout is considered a slave system in the MBS framework, and the data are sent over the network using TCP/IP protocol to an event builder. This extra node in the network is responsible to collect the data from the different sub-systems, wrap them with some specific headers and write them into a file of the LMD format. Those files will be used in following analysis (near-line, off-line).

In the case of CALIFA, a PC is used to run the dedicated slave branch of MBS. The trigger and deadtime synchronisation is made via the trigger bus connected to the PCI

board TRIXOR[6]. The different FE boards are connected to the PC via another PCI board, the PEXOR[7]. That connection is made via glass fibres chaining the FE boards one after another. When the TRIXOR receives a readout trigger, a token is sent to the first board in the chain, the data are collected and sent along the chain. When all the data from that module have been read out, the token goes to the next board in the chain. And so on.

In order to minimise the delay of collecting the data within one chain, the FE boards are equally spread over 4 chains per PEXOR. Due to the requested modularity of CALIFA (see 10), the readout is divided in two independent subsystems, each for one half (left-right) of the detector. This lead to 15-16 FE boards per chain (using one PEXOR per side). The full collection on the PCs of all the channels of the detector takes then about 50 μs.

Self-Triggering

In the case of self-triggering, the readout follows essentially the same scheme, with the exception that the readout triggers are not coming from the trigger logic but are determined locally. As there is some freedom about how to do it, and it can be adjusted for every experiment, no general scheme will be provided within the range of this document. However as an illustration, one could imagine that the readout sequence is triggered every 20 global OR triggers received. In that way, the fibres chains have the time to perform the full read out before having issues with the next event. As all the events are time-stamped with a precise and synchronised time-stamping system,[8] they can be stored in the local memory and only read out at a later stage. The data read out are sent to some data stream or directly written on tape (possibly using the MBS framework, or using a dedicated one).

In order to be able to combine the information in the following analysis, the time-stamping system is of high importance in this mode. The time distribution scheme and modules follows the general NuSTAR standard.

5.7. Slow control

The control of the CALIFA Barrel involves the reading and setting of a given number of parameters for each of the individual acquisition channels[9], as well as some specific values[10] unrelated to any specific acquisition channel. The high number of crystals alone implies that a very high number of parameters shared among more than a hundred different modules. Additionally, the CALIFA Barrel slow-control must comply with the requirements of the R3B framework, be able to monitor over time all the changes made, send data to the data stream for offline monitoring, as well as support automation and scriptability (i.e, capability of invoking chains of commands automatically).

Detector system (slow-)control software must be adapted for two types of users. On the one hand the technical people highly acquainted with the setup, on the other hand, scientists familiar with the experiment but not necessarily with the details of the slow-control and/or the acquisition. The high segmentation of the detector would make extremely difficult for

[7] Electronic modules produced by the Experiment Electronic Department of GSI, Darmstadt.
[8] The standard NuSTAR time-stamping system will be used.
[9] For examples, the width of the different windows used in the RPID, the triggering scheme.
[10] E.g. the different temperature readings inside the detector and set points for the cooling system.

the later group to set and refine the global state, due to the high number of commands that should be issued to reach a desired configuration.

5.7.1. Detector Command Language

To solve this problem without giving up the power of a scriptable solution,[11] an interpreted language has been introduced and named Detector Command Language (DCL). The parameters can be read and set both for individual crystals as well as for groups using DCL. Incremental changes are also possible. The language offers complex commands to create, manage and delete groups of crystals, according to conditions on some of their parameters (such as reaction angle or alveoli number amongst others).

To provide this functionality, the language models a hierarchical set of elements arranged as a tree. Leaves on the tree are single crystals along with their electronics and acquisition chains, whereas internal branches describe the alveoli and plate grouping of detectors. Each branch or node in the tree contains the same set of parameters, e.g, all the parameters that can be read and/or written related to the electronic processing and digitalising. Additionally to the given groups, the language provides means to define new groups by giving a condition on the parameters of elements.

Some extra features have been introduced like an alarm setting to notify the user(s) that a parameter (typically the temperature) is drifting past some boundaries. In order to follow the historic of changes, all the manual and automatic changes are automatically saved in log files. In that way, one can *a posteriori* see what changes were made when, and whether they had an impact on the results. In order to improve the final resolution, some critical parameters read automatically by the slow-control system will be time-stamped and merged into the data stream. It would then be possible to correct the measurement depending on those values.

Even with those extra features brought in by DCL, in practical cases, no matter how flexible the slow-control setup can be done, the global state of a parameter among the different detectors in CALIFA can become very difficult to understand for inexperienced users or even hard to find and/or remember. In order to improve on it, a graphical user interface (GUI) have been developed. The GUI shows a clickable 3D representation of CALIFA (see Figure 5.9). All the parameters can be accessed, read and modified in a few clicks. As an illustration, upon clicking on one of the tile, a window with the list of parameters corresponding to that tile appear. This provides at the same time a general visual overview of the state of CALIFA and allows crystal picking and grouping using the mouse. Mouse interaction allows zooming, panning and rotating the model to display all the tiles. This second graphical window will be also remotely available, in the sense that no direct hardware access is used for the display and can be successfully SSH-tunnelled.

As illustrated in Figure 5.10, both the GUI and the command console are connected to the DCL interpreter. This allows for an easy development of different user interface if needed.

[11] A script is needed for the automation of tasks required by setups like R3B. Some parameters can be the shared by the different elements of the setup and thus the slow control should allow-but not restrict-the user to set them all at once and not each individually.

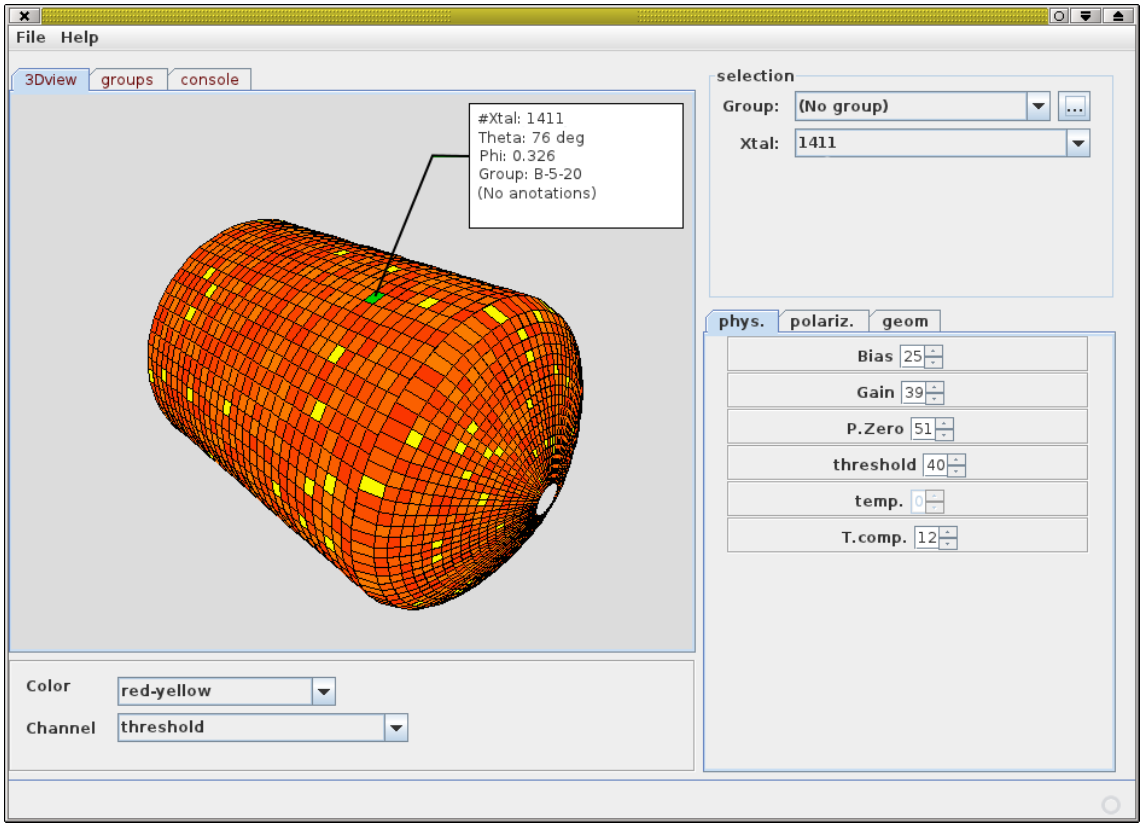

Figure 5.9.: Snapshot of the slow control GUI.

The DCL interpreter will translate the commands received on a set of instruction to be passed on to the controlling software. Different software could be used, but the NuSTAR set EPICS as a standard (though the DCL interpreter could replace EPICS as well).

Although DCL have been developed in the attempt to provide a modular way for slow-controlling CALIFA, it can be used for other applications as well.

5.7.2. Hardware

Although the GUI and console could be accessed remotely, the DCL interpreter and the EPICS server will be running on a dedicated machine in order to prevent undesired parallel control (e.g. in particular in case of voltage control). As shown in Figure 5.10, the communication between the slow-control computer and the different controller uses the local network (TCP/IP).

Preamplifiers and Amplifiers Control

Inside the hall, there are two controllers for the CALIFA Barrel, each one located in one half of the detector. Each controller runs in an VME crate. The controllers accept the intermediate level commands issued by EPICS and acts accordingly, setting the individual modules. The VME crate is further equipped with a serial controller module. This module groups 4 serial interfaces, accessible from the computer side via the VME bus.

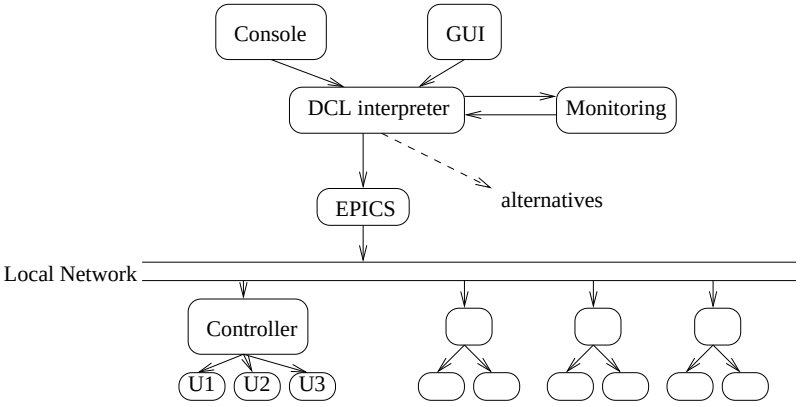

Figure 5.10.: Slow control structure: the user acts on the user interface of his choice (console or GUI). The DCL commands will then be interpreted into, e.g., EPICS commands and the information will be sent to the monitoring system (essentially log-files and data stream). The EPICS commands are transmitted to the different controllers via the local network, which, in turn, will access the modules and do the action requested by the user.

From each of the serial interfaces, a daisy-chain of up to 16 preamplifiers can be connected. Due to the LEMO daisy-chain structure, the control can only be achieved at a moderate speed (to avoid collisions on the chain). An addressing system is implemented to ensure that only one preamplifiers answers the call of the controller.

FPGA Control

All the parameters needed for the signal processing and digitisation of the electronics pulses on the FEBEX board can be directly controlled using the GOSIP interface. Therefore, the acquisition computer serves as a slow-control point for the FPGA, which then avoids the need of developing extra hardware material for that purpose.[12]

Acquisition Control

The acquisition runs on the PCs located in the experimental hall. Those are connected to the network and therefore the control of the acquisition can be easily done remotely, and the interface used will be the same as developed by the NuSTAR DAQ Working Group.

[12]It should be noted that if this feature is not implemented on the currently available FEBEX boards, a system of remote reprogramming of the FPGA is foreseen. Such a system has been implemented and extensively tested by the HADES collaboration, for example. This would allow an easy reprogramming of all the FEBEX boards at once, without having to access the modules physically.

6. Mechanical Structure

In order to place the crystals and related electronics in the positions described in the previous Chapters, as well as to sustain the weight of all the elements, a carefully designed mechanical structure has been developed. Its details are presented in this Chapter.

6.1. Concept

The mechanical solution for the arrangement of the individual crystals in the required array geometry will employ a carbon fibre alveolus structure. In addition to the dimensions of the alveoli, the method proposed to join the alveoli together and the solution for the support structure to be used in cave C to hold CALIFA in place for experiments will be detailed below. The calorimeter is, as previously explained, separated into two parts: the Barrel and the forward EndCap. Keeping the technical remit of this report this Chapter discusses the Barrel section of CALIFA.

The active volume of the Barrel, comprised of CsI(Tl) crystals, is segmented according to the required resolution and efficiency needed for the physics cases as described in previous Chapters. This segmentation results in almost two thousand scintillating crystals, with a combined weight in excess of 1200 kg. The challenge here lies in the suspension of such a weight with the required exact and stable positioning of all crystals, through the use of a minimum of 'dead' material; in order to reduce as far as possible the detrimental effect of non-active material on detector performance. An additional factor to be accounted for is the support of the very-front-end and front-end electronic modules and the cooling system.

The design conditions imposed by the project for the active region include:

i. A robust and safe weight support.

ii. A minimum of structural material.

iii. Full definition (within tolerance) of the static positioning and orientation of the active elements.

iv. Partition of the system in two autonomous (azimuthal) symmetric halves. A safe procedure for the operations of separation and integration of the halves for non highly-qualified operators.

v. Possibility to make a longitudinal shift between the halves to allow for a clearance of the forward angles. A safe procedure for the separation of the halves as required, suitable for non highly-qualified operators.

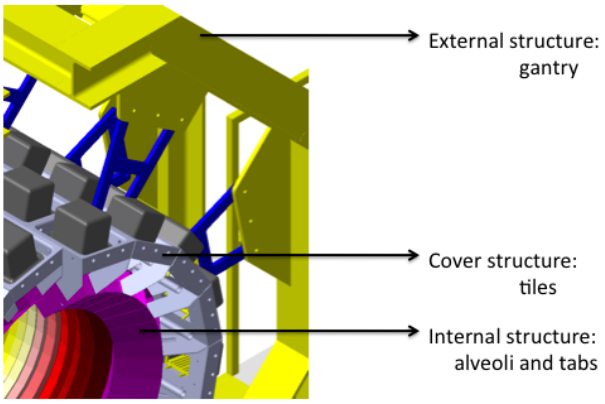

Figure 6.1.: View of a section of the Barrel where the different structural components can be observed. The internal layer consists of a carbon fibre structure which contains the crystals. The cover structure is composed of individual aluminium tiles. It connects the (inner) active region with the external support structure, and also supports the very-front-end electronics.

To achieve these criteria, a structure comprising of three main layers is proposed: **inner, cover,** and **external structures.** In Fig. 6.1 a view of the Barrel system displays the different layers that will be described in this Chapter, with details of the complete set of integral structural elements.

The **inner layer**, relating to the active region, provides the support and positioning for the crystals. The inner layer consists of an epoxy-carbon composite (or carbon fibre, *CF* in the following text), segmented into separate compartments, termed 'alveolus' (alveoli), which each hold 4 individual wrapped crystals (with the exception of the alveoli at the greatest polar angle, which contain a single crystal). The underlying motivation for this is detailed in Chapter 4. In Fig. 6.2 is shown a collection of custom-made CF pieces, sizes corresponding to prototype models of 0.25 mm wall thickness.

The active region is surrounded by a cylindrically shaped **cover** envelope. It is comprised of equally sized 'tiles'. This structure acts as an interface between the inner structure and the external support. The cover holds both the 'tabs', pieces which support the internal *CF* structure, and the 'arms' employed to suspend the whole system from the mobile external structure. The cover also supports the very-front-end electronics (vFEE) elements, with the corresponding connection passthroughs and the module support elements. The temperature and humidity control of the active region is achieved by a flow of dry nitrogen underneath the cover layer, and an air flow across the tiles; the necessary distribution pipes and passthroughs are attached to the cover. The cover also guarantees the light- and gas- tightness of the system. The overall geometrical parameters of the inner and cover structures for the Barrel are displayed in Table 6.1.

The **external** structure, which acts as an exoskeleton, has a robust design sufficient for the suspension of each half of the cover, in addition to the internal structures. In Fig. 6.3 is displayed the layout (from different vantage points) of the mechanical structure, with the corresponding dimensions indicated. Two independent blocks allow for the movements of the Barrel halves. Each block is composed of an upper structure ('gantry') which holds the cover; and a lower structure ('bench') that allows for the support and movement of the

outer radius	(min) 594.9 mm
inner radius	(min) 534.9 mm
length	990.0 mm
target (design) position	
from Barrel front face	461.5 mm
from Barrel back face	528.5 mm

Table 6.1.: Main dimensional parameters of the cover structure of the Barrel.

Figure 6.2.: Hand-made epoxy-carbon fibre alveoli, 0.25 mm thick walls, for the preliminary tests.

gantry. A relative displacement (shift) between the Barrel halves of maximum 165.0 mm is possible (82.5 mm in the picture, lateral view). The separation of the Barrel halves is possible at a defined opening angle along the rails on the floor (see Fig 6.3). Both movements are possible with the use of two sets of independent linear slides at the platform which hold the bench structure of each block.

Each block requires an overall volume defined by the lower platform surface and the total height (rails included). The platform additionally reserves a space for the associated electronics. The main dimensions are displayed in Table 6.2.

6.1.1. Inner structure: alveolus

The necessary robustness of the *CF* structure can be guaranteed by making a 'single' structure for each half of the Barrel. This is possible with alveoli designed to be glued face-to-face at each contact side, in both polar and azimuthal directions. The result is a hollow, 'honeycomb' structure, with resulting robust properties. For a Barrel shape this restriction results in pieces of prismatic shape with trapezoidal base, and lateral edges with opening (non right) angles, both in azimuthal and polar directions. These pieces are glued in the azimuthal direction to enable a ring structure, divided into two equal azimuthal parts. The pieces will also be glued at the surfaces in polar direction, thus forming the two halves of the *CF* inner Barrel structure of CALIFA. In Fig. 6.4, left, is shown an isometric view of the *CF* structures of the two halves of the Barrel.

The size of the pieces was designed with a view to meet several criteria:

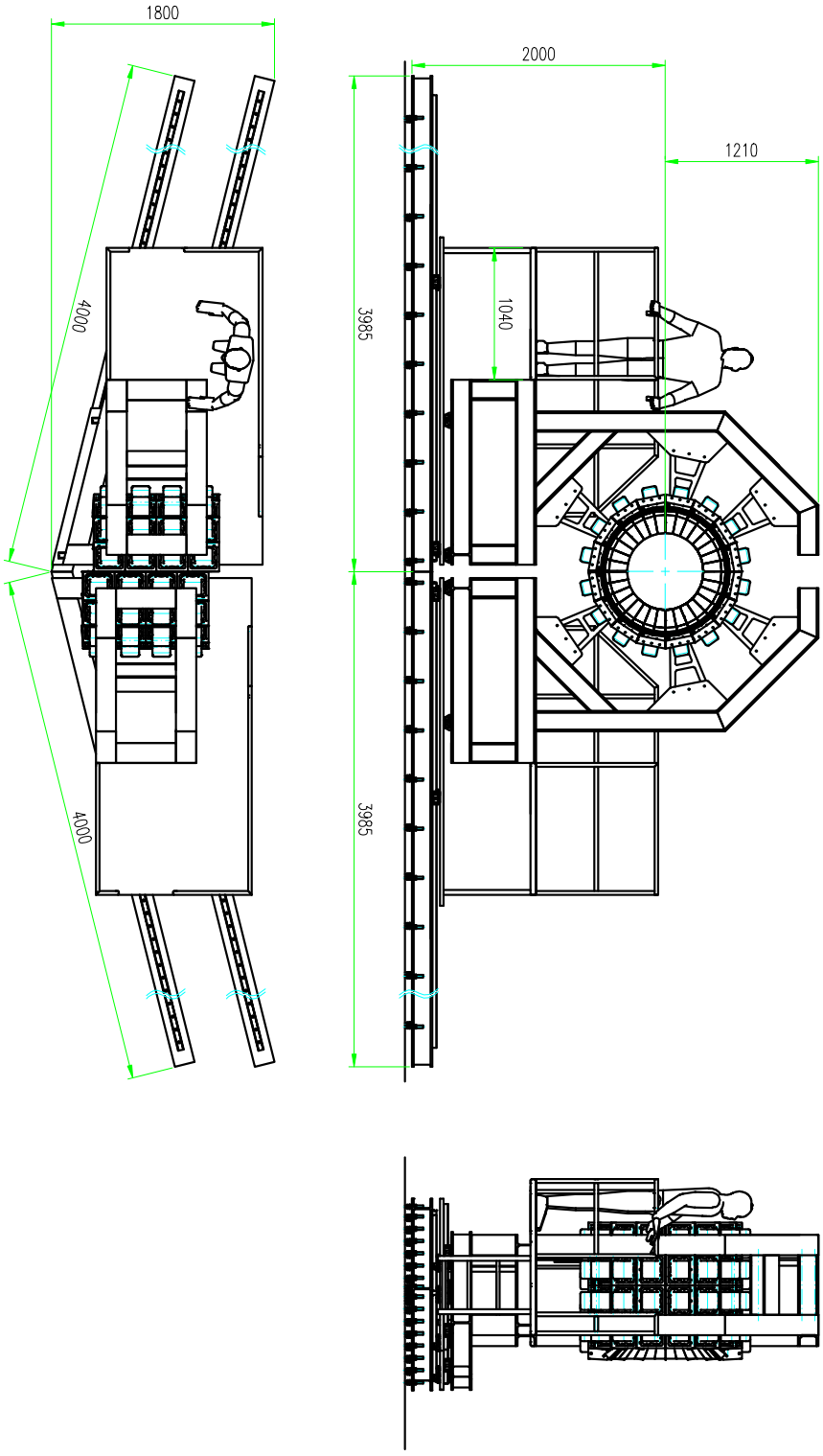

Figure 6.3.: Layout of the Barrel with the characteristic sizes indicated (in mm). In the top view the two halves are shifted in longitudinal direction by 82.5 mm. The two halves of CALIFA are able to slide apart on rails 4 m long, positioned at 15°.

block	
longitudinal length	1.8 m
transversal length	2.6 m
total transversal length	4.0 m
height	3.2 m
structure weight	3.3 tons
operational weight (1)	4.2 tons
contact surface	1.3 m^2
CALIFA	
opening angle	15°
sliding rails length	4 m
longitudinal length	1.8 m
transversal length	5.2 m
total transversal length	8.0 m
height	3.2 m
structure weight	6.6 tons
operational weight (1)	8.5 tons
support surface	2.6 m^2

Table 6.2.: Main dimensional parameters of the external structure of the Barrel. Note (1): operational refers to the structure plus the inner and cover structures, and active elements, plus all vFEE and FEE modules and connections.

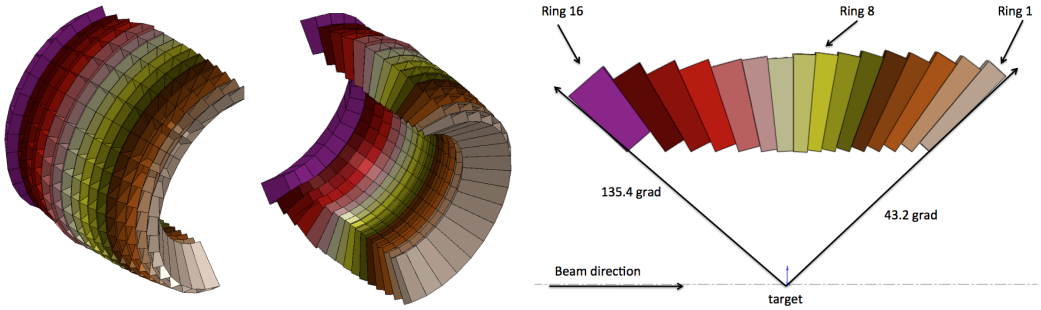

Figure 6.4.: Left: view of the honeycomb structure composed of *CF* alveoli. The two halves of the Barrel are set separately. Right: lateral view of a single line of *CF* alveoli along the polar direction. All the pieces are joined at the outer faces. The covering polar angles are indicated.

i. A maximum of 4 crystals per alveolus, to allow for an easy handling of the elements.

ii- An even number of elements in the azimuthal direction, to allow for a stable, equal azimuthal separation of the Barrel.

iii. The partition structure corresponds directly with the necessary geometrical restrictions pertaining to the resolution of the detector. Therefore, the partitioning both in polar and azimuthal directions was designed according to the resolution demanded, determined via dedicated simulations.

CF structure		
	wall thickness	(nominal) 0.23 mm
	outer radius	(max) 528.1 mm
	inner radius	(min) 298.7 mm
	length	(max) 982.4 mm
	polar angle coverage	43.2 to 135.4°
	weight	12.3 Kg
Alveoli		
	Polar direction	16
	Azimuthal direction	32
	TOTAL	16 x 32 = 512
Crystals		
	Polar direction	15 rings x 2
		1 ring x 1
	Azimuthal direction	32 x 2 (15 rings)
		32 x1 (1 ring)
	TOTAL	1952
	weight	1286 Kg

Table 6.3.: Dimensions of the CF structure, and number of alveoli and crystals of the Barrel.

The current design solution contains 16 different types of alveoli which span the polar angle region required, at each angular point, to maintain the resolution demanded by the R^3B physics program requirements. Typically each alveolus contains four crystals, this being the case from ring 1 (downstream) to 15. Only the 16th ring contains a single crystal in each alveolus. The half-rings in azimuthal direction are constructed with 16 alveoli in each half of the CALIFA Barrel. The number of the alveoli needed to contain all the crystals is displayed in Table 6.3.

The overall characteristics of the *CF* alveoli are as follows:

Material: One layer of epoxy-carbon fibre pre-impregnated ('pre-preg') plain-weave fabric.

Thickness: The face thickness of each alveolus corresponds to the layer of the pre-preg: i.e. 0.23 mm (N.B.; this is the nominal value of the fabric before curing. Small variations in this value are expected following the curing process). This thickness is sufficient for the support of the crystals inside each alveolus without significant deformation or load transmission among alveoli, according to the finite elements model (FEM) simulations performed.

Fabrication system: The pre-preg layer will be carefully laid inside the inner-outer casts prior to curing of the carbon fibre. The curing is achieved via the application of appropriate combined pressure and thermal cycle, as defined by the producer of the pre-preg.

Tolerances: The geometrical tolerances will be under $\pm$ 100 μm in any dimension of edges of the piece. The thickness tolerance, due to the fabrication process, is

expected to be below 30 μm. The total thickness-plus-gluing tolerance is expected to be well below 50 μm.

Mounting: The mounting of the pieces to construct the honeycomb structure will be made with the help of a 'negative' cast of the inner volume of the structure. The *CF* pieces will be placed over the cast, determining the correct positioning prior to adhesion.

Mounting tolerances: The mounting cast will have geometrical tolerances below 100 μm. This, together the individual tolerance of the *CF* pieces, will guarantee a reliable construction of the structure. This will also ensure the position tolerance of the crystals lay within the 100 micron limit.

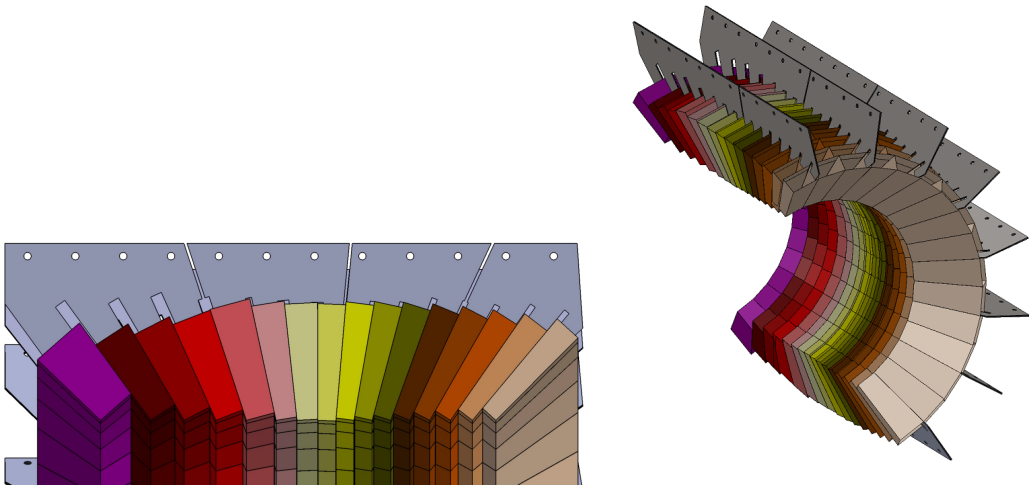

Figure 6.5.: Left panel: view of the components comprising a tab, positioned along the polar direction and inserted (the flaps) into the alveoli. Right panel: isometric view of the inner structure of half a Barrel, the *CF* structure and tabs.

In Fig. 6.4, right panel, is shown a two-dimensional section of a single line of alveoli along the polar direction. Each of the 16 elements (polar) are part of the 16 rings in an azimuthal direction around the beam axis. The complete set of design parameters of the *CF* pieces are detailed in table 6.4.

Holding system: tabs

In order to 'hang' the honeycomb *CF* structure to the cover, the inner structure includes **tabs**. The tabs are plates that hold the structure in polar direction, and are placed every two *CF* elements in the azimuthal direction, see Fig. 6.5, left and right. The stainless steel flat tabs are robustly glued to the CF structure with special adhesives, and fastened between two tiles of the cover, in the polar direction. In this way the tabs transfer all of the load to the cover structure.

The tabs do not interfere in the active region nor touch the crystals, since they are just above the rear face of the crystals (photo-electronics included). The flaps of the tabs extend into and adhere to the alveoli inner face (see a drawing of the design and a view in Fig. 6.6). Two equal pieces, glued together, and also tightening the *CF*, form the tab. This coupling of *CF* and tabs allows for the mounting of the structure in addition to an ease of

type or ring	azimuthal long mm	edge short mm	polar edge mm	polar up-stream grad	opening angles down-stream grad	azimuthal up-stream grad	opening angles down-stream grad	height mm
1	63.13	59.04	31.00	92.50	92.50	94.32	93.99	24.0
2	62.71	59.03	31.00	92.50	92.50	94.62	94.32	24.0
3	62.29	59.06	31.00	92.50	92.50	94.88	94.61	24.0
4	61.82	59.03	31.00	92.50	92.50	95.10	94.88	23.0
5	61.35	58.78	31.00	92.50	92.50	95.29	95.10	23.0
6	60.84	59.04	31.00	92.50	92.50	95.44	95.29	22.5
7	60.33	59.04	31.00	92.50	92.50	95.54	95.44	22.0
8	59.80	59.04	31.00	92.50	92.50	95.61	95.54	22.0
9	59.05	58.78	31.00	92.50	92.50	95.62	95.61	22.0
10	59.43	59.04	36.00	93.00	93.00	95.62	95.59	21.0
11	60.16	59.05	36.00	93.00	93.00	95.59	95.50	21.0
12	61.60	59.05	50.00	93.00	93.00	95.50	95.34	20.0
13	62.58	59.04	50.00	93.00	93.00	95.34	95.13	20.0
14	63.51	59.03	50.00	93.00	93.00	95.13	94.86	20.0
15	64.41	59.05	50.00	93.00	93.00	96.86	94.54	20.0
16	68.07	59.04	70.00	95.00	95.00	94.54	93.90	18.0

Table 6.4.: List of the design parameters of the *CF* pieces of the inner structure of CALIFA.

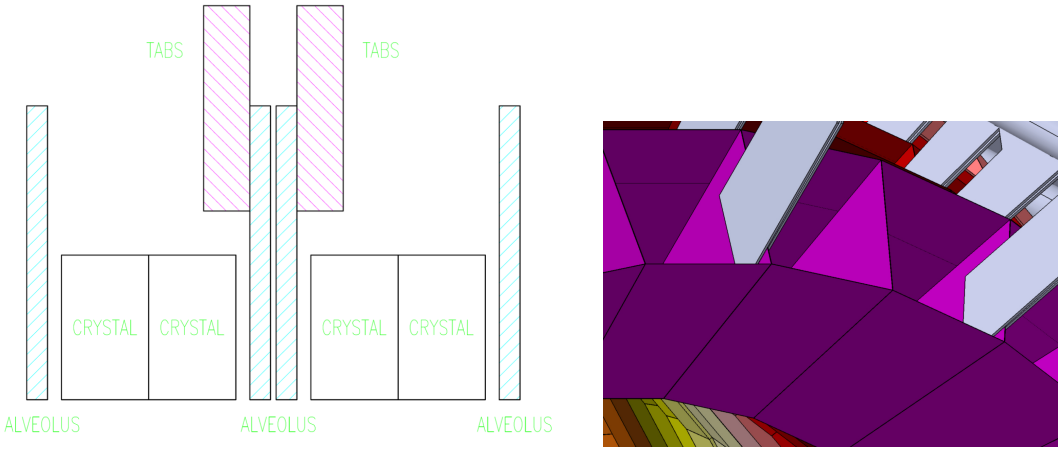

Figure 6.6.: Left panel: drawing of the positioning of the tabs. The two flaps are held between the faces of two alveoli. Note that the thickness are not to scale. Right panel: view of the inner structure. The flaps of the tabs are glued on the inner side of the alveoli.

handling of the crystals. Due to the profile of the *CF* structure in polar direction the tabs are divided into four pieces, see Fig. 6.5, left. This partition allows the insertion of the flaps at the right angles of the alveoli at the time of assembly. For the sake of simplicity, we give the term 'tab' to the pieces spanning the polar direction, even if it is truly made of 4 separate pieces.

The main characteristics of the tabs are:

- Material: stainless steel 316L.
- Double layer per tab, 1.5 mm thickness each layer.

- Four pieces to conform a tab along the whole polar direction.
- A set of 16 equal tabs to hold the whole *CF* structure.

It is worth to mention that the crystals inside any alveolus can be removed at any time with the condition of firstly removing the crystals on the side of the alveolus without the flap inserted. That is, the crystals corresponding to the external positions in Fig. 6.6, left panel.

Holding system: FEM simulations

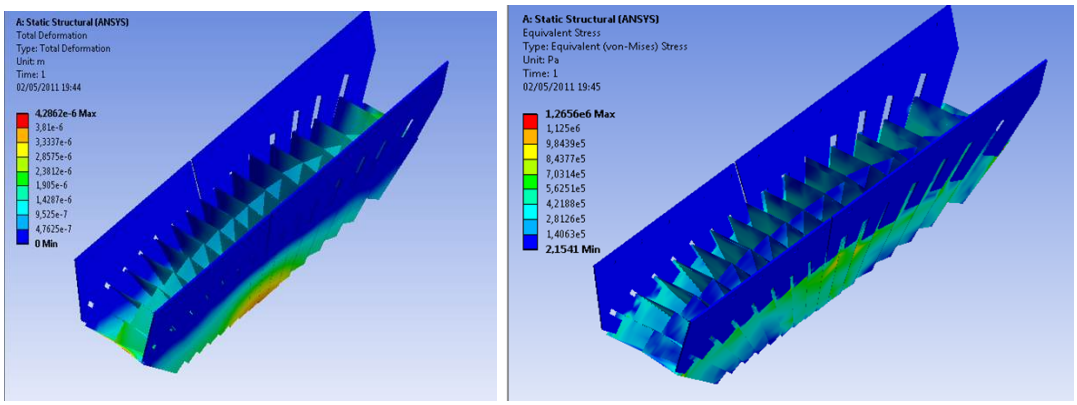

Figure 6.7.: Result of FEM analysis of the system of tabs and alveoli loaded as for the real conditions. See the text for details. Left: result of the deformation. The deformation scale has a maximum of 0.005 mm. Right: result of the stress (von-Misses criterion). The stress scale has a maximum of 1.3 MPa.

A systematic study of the deformation and stress of the components for the inner structure was done in order to ensure adequate performance of the materials. Finite elements models (FEM) were employed to undertake simulation tests with dedicated analysis tools. In this way, and using conservative parametrisation of the material properties, we could establish the thicknesses and geometries that guarantee the robustness and stability of the structure. The construction of the DEMONSTRATOR (in this Chapter) will require the production of an appreciable number of structural elements (namely CF alveoli). Therefore, this will enable systematic studies to fully validate the models results.

In Figs. 6.7 left and right, is shown the deformation and stress results provided by the model considering a single polar segment, with the total load applied as in real conditions. This is a realistic evaluation providing that the strength of the contact between *CF* and steel (tab) can be accurately ascertained. For this calculation a conservative value obtained with the available adhesives was selected.

The analysis concluded that no deformations above 90 μm are expected in the tabs. The deformation does not affect the actual position of the alveoli, and therefore neither of the crystals. The transition regions (potential weak points of the structure) do not suffer any significant stress. In general the system reveals only a safety factor 3 in the stress analysis.

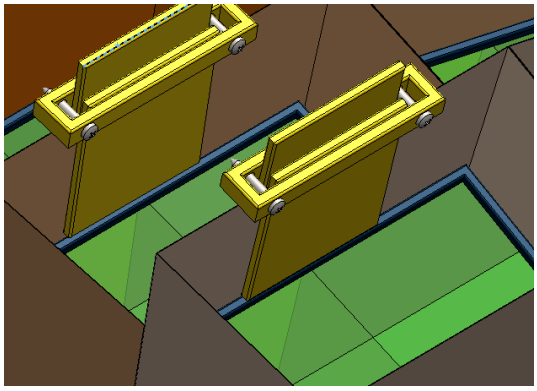

Figure 6.8.: View of the system used to hold the crystals in place within the *CF* alveoli. The retention-ring slides in, touching the top of the crystal-block. The clip, formed via two plates, fastens the faces of two alveoli, blocking the ring in the lower part. In the picture the tabs touching the azimuthal faces of the alveoli are not represented.

Holding of crystals

The crystals, individually wrapped, will be inserted into the alveoli. In order to maintain the position of each of the four crystals housed within each alveoli, a retention-ring and a clip system will be employed, see Fig. 6.8. The retention ring, plastic, slides into the *CF* alveolus, enclosing the top of the four crystal block. The ring, in one of the faces of the azimuthal direction, remains below the flap of the tab that hold the *CF* structure. In the opposite (polar) sides, the rings are held by clips. These clips consist of two plates, inserted and touching the inner sides of two alveoli, blocking the ring below them. The clip fastening is just an additional screwed ring around the plates.

This ring-and-clip system is robust and light. At the same time, the insertion procedure is easy and non aggressive with the delicate active elements.

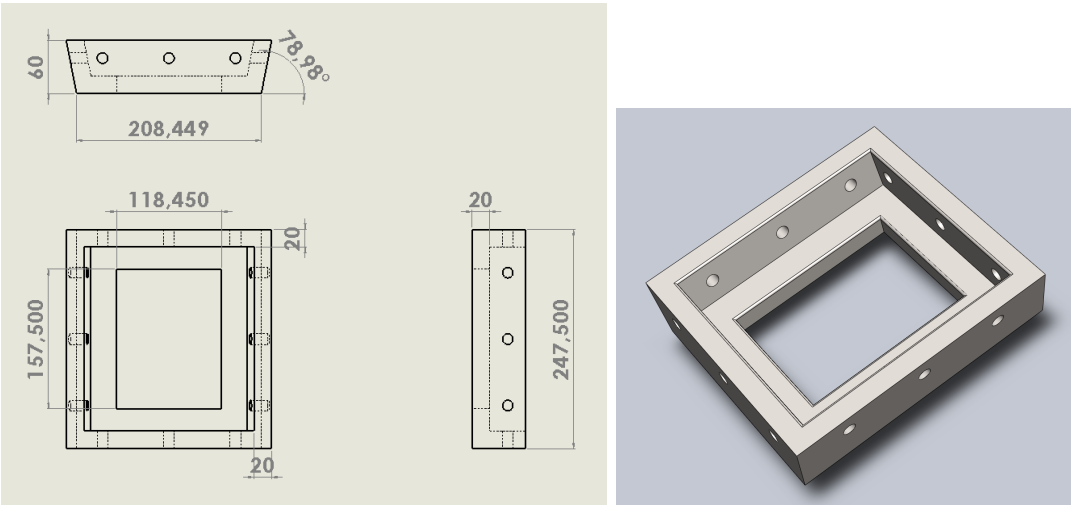

Figure 6.9.: Left panel: Design drawing of the tiles of the cover structure, with the main dimensions shown (mm). Right panel: 3D representation of one tile of the cover structure.

material	aluminium
fasteners	4 x 3 M12 bolts
tiles in polar direction	4
tiles in azimuthal direction	16
tiles, total	64
length (polar direction)	247.5 mm
width (azimuthal direction)	232.0 mm
height	60.0 mm
thickness	20.0 mm
weight	3.6 Kg
size tolerance	0.10 mm
inner opening length	157.5 mm
inner opening width	118.4 mm
bolt alignment tolerance (1)	0.20 mm
planarity	0.050 mm

Table 6.5.: Design parameters of the tiles of the cover structure of the Barrel. (1) The tolerance for the bolts of the positions between the two Barrel halves is 0.40 mm.

6.1.2. Cover structure: tiles

The cover is a hollow cylindrical structure surrounding the inner structure of the Barrel. It is composed of equal pieces called **tiles**. The tiles are fasten by interlocking bolts, three per side, in both polar and azimuthal directions. The longitudinal sides (polar direction) allow also to fasten the tabs of the inner structure. The tiles are frame shaped, with an opening to give access to the photo-electronics and help in the vFEE mounting phase. Each of these tiles can be independently removed, one per operation, to get full access to the crystals and corresponding electronics for diagnostic and replacement purposes. The principal structural aim of the cover is to absorb the entire static load of the inner structure, transferred through the tabs. In Figs. 6.9 shown left and right, is a schematic diagram and a 3D representation of one tile, respectively. In Table 6.5 we give the main dimensional parameters of the tiles.

The method used for the fabrication of the tiles is firstly sand casting, and then machining to fit the shapes and sizes corresponding to the design specifications. The azimuthal size (width) of the tiles is adapted to accommodate the adjacent positioning of the tabs.

Cover: FEM simulations

A systematic study of the deformation and stress of the components of the cover structure was done in order to ensure the performance of the materials. Finite element models (FEM) were used to perform simulation tests under ANSYS. FEM analysis was also performed for the case in which one tile was removed from the cover, as it can be during the assembly phase or for maintenance. Fig. 6.10 shows the deformation resulting from the analysis of the tiles under the nominal load, for the case in which one tile is removed. This analysis concluded that no deformations above 0.1 mm are expected in the tiles. The regions of the attachment of the arms that hold the cover structure (see the next section for details) are potential weak points of the structure. The analysis show that these regions do not suffer significantly high stress. The system shows a minimum safety factor of 5 in the stress analysis.

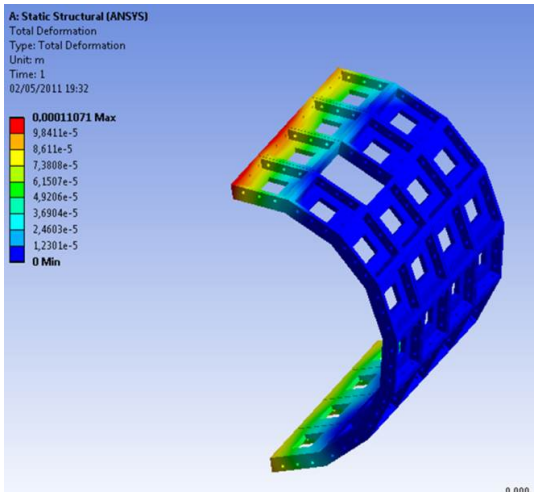

Figure 6.10.: Results of the FEM analysis of the cover and tiles loaded as in real conditions: Deformation for the situation for which one tile is removed. The deformation scale has a maximum of 0.1 mm.

6.1.3. External structure

The external structure should contain each half of the Barrel, allowing in a safe operation for opening and closing the Barrel, as well as the shift between the two halves of the Barrel as necessary. The external structure acts as an exoskeleton, constructed using standard HE steel beams. To allow for the necessary movements, the external support has two completely independent and equal structural blocks, one per half of the Barrel, as seen in the views of Fig. 6.3. Additionally, each block has two parts: the lower one (**bench**) and the upper one (**gantry**). The gantry will be fastened to the bench structure, and includes guiding pins to keep the position reference. This concept allows for the operation of moving half of the Barrel attached to the gantry by means of an appropriate crane.

A platform in the lower part of the bench and a double set of linear slides allows for the double movement of the blocks. The linear guides mounted below the platform, on top of HE beams placed on the basement, allow for moving the bench, thus a whole block, in order to separate or join the Barrel halves. Additionally, the linear guides mounted on top of the platform and below the bench beam structures allow for the shift movement between the two halves of the Barrel. Details of the bench platform and the double linear slide system are shown in the left panel of Fig. 6.11.

Between the basement and the HE beams that hold the lower linear guides of the bench platforms, there is a simple system of bolts. A double nut will allow the adjustment of the height of the Barrel by manual operation during the mounting phase. Details of the system are shown in the right panel of Fig. 6.11.

The main characteristics of the external structure are:

- HE steel structural beams.
- Linear slides to allow for the opening of the Barrel.
- Linear slides to allow for the shift, up 165.0 mm (maximum), between the Barrel halves.

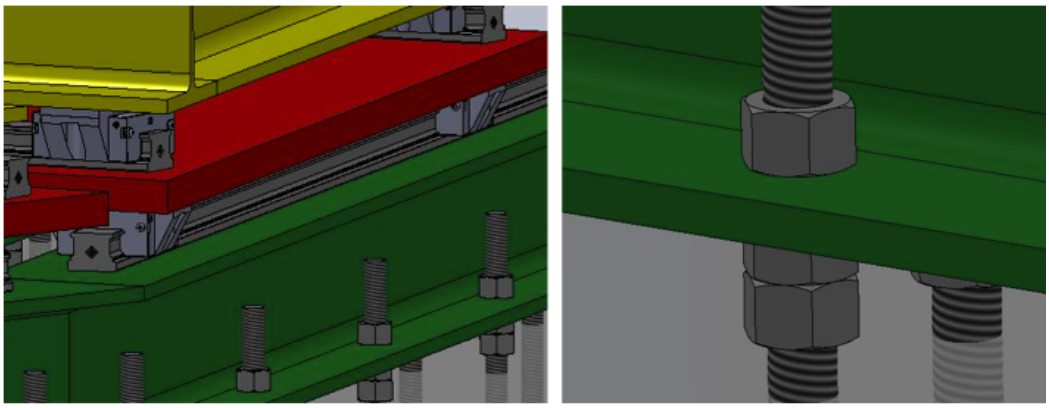

Figure 6.11.: Left panel: Details of the platform that holds the bench of the external structure, with the linear slides allowing for the separation and shifting of the two Barrel halves. The lower guides are mounted on HE beams fasten to the basement. The upper guides a mounted on top of the platform and below the beams of the bench structure. Right panel: Detail of the bolt system to fasten the HE beams to the basement. It allows for the height control of the structural blocks.

- Fine adjustment in height with a double nut system.

Holding system: arms

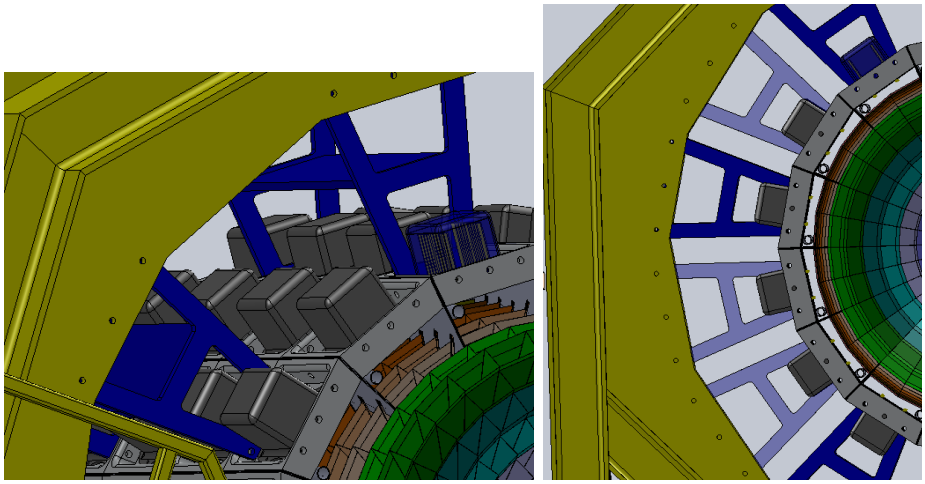

Figure 6.12.: Left panel: view of the arms attached to gantry and holding the cover. Right panel: The arms can be set between the gantry and any of the tiles of the cover below. This feature helps when removing any tile of the structure.

The cover structure of each half of the Barrel is supported by 6 **arms**, 3 in polar direction and 2 in azimuthal direction, that reach the external structure, as seen in the left panel of Fig. 6.12. An additional plate connecting each pair of arms in longitudinal direction will help to keep the stiffness of the arms system.

The shape and dimensions of these pieces are detailed in Fig. 6.13. The arms will be made of stainless steel 316L of 15 mm thickness. The fasteners will be three M12-bolts at the tile position, and three M12-bolts to link the arms at the flaps of the gantry.

The arms, six per half Barrel, can be set between the gantry and any of the tiles of the cover below, see right panel of Fig. 6.12. This feature helps when removing any tile of the structure. One arm-free tile can be taken out of the cover at any time, as demonstrated in the previous section with FEE calculations. To replace a tile with an arm, one or two arms should be placed in the neighbouring tiles (azimuthal direction). Then the first arm and tile can be safely removed.

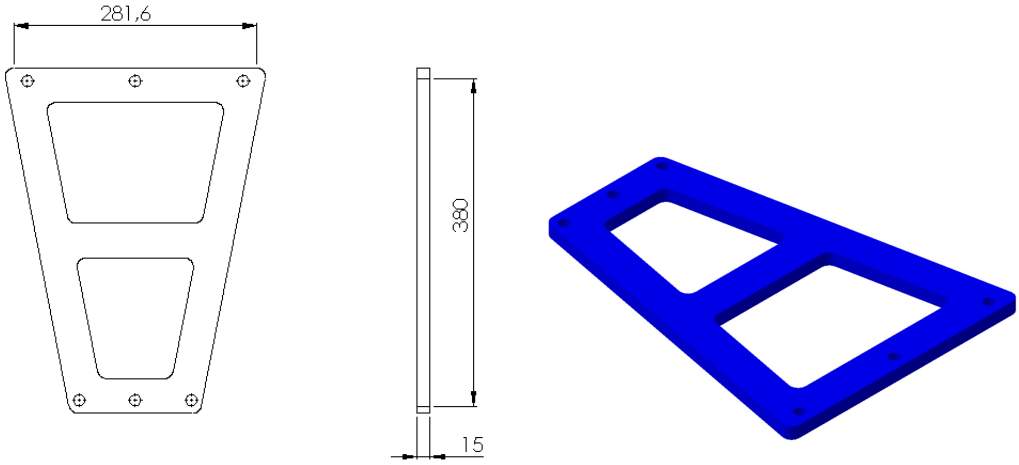

Figure 6.13.: Design drawing and 3D view of the arms to hold the cover at the external structure.

6.2. Technical requirements

The mechanical design must satisfy a list of technical requirements to ensure the correct integration of all the equipment of CALIFA. This section covers aspects such as electronics housing, assembly and maintenance operations, versatility of the geometry, minimisation of positional uncertainties and integration with other detectors.

6.2.1. Location of vFEE and FEE

The cover tiles will hold the vFEE. The two most forward angle tiles of the Barrel cover approx. 40 crystals each. The two remaining tiles cover only 24 crystals each. The distance between the top of the crystals and the outer face of the tile is in the range of 8 to 12 cm, depending on the crystal position. These values give an idea of the length of the cables between the APD electronics and the vFEE, as well as the vFEE density needed per tile.

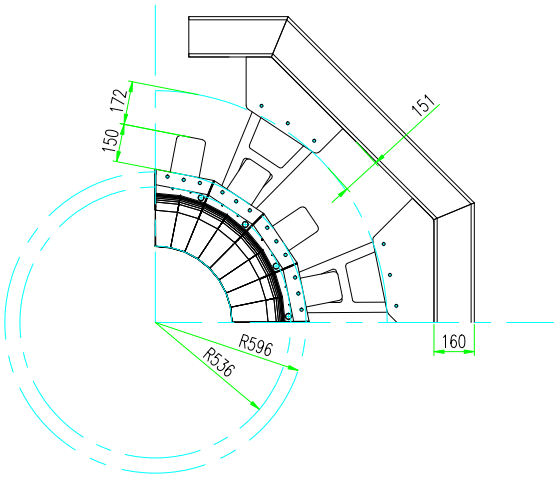

Figure 6.14.: Drawing of a section of the Barrel with the main dimensions of concern for the vFEE housing.

In Fig. 6.14 is shown a design indicating the available space in between the cover and the external structure.

In Figs. 6.15 we show a view of the vFEE modules mounted over the tiles with a dedicated support (left panel), as well as an exploded view of the elements of the mounting system (right panel). The dimensions over the tile surface are those of the 'hood' quoted in Fig. 6.14. The proposed mounting includes insulation elements. The tower-like support holds the VFFE module, and serve also as a guide to fit the paired connectors between the module and the passthroughs at the tile level.

Additional space for 19 inch racks is foreseen on the service platforms of the Barrel. These racks, not included in Fig. 6.15, will be moved together with each half of the detector and could be accessed from both sides.

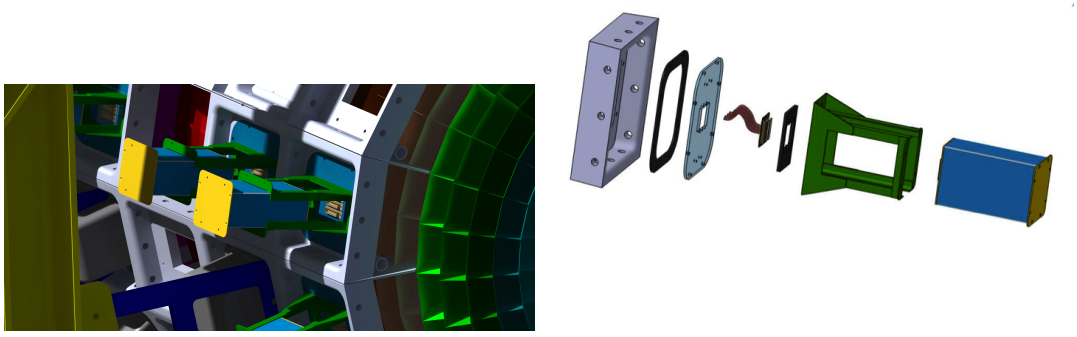

Figure 6.15.: Left panel: view of the vFEE modules mounted over the tiles. The modules appear not completely inserted in order to display the support structure. Right panel: An exploded view of the components of the vFEE system. The isolation elements, polymeric pads, are also visible.

6.2.2. Insulation of the inner region: temperature, humidity and light.

There are requirements for the working conditions of the active components in the inner structure of the system. That is the case of both the thermal stability and range temperature for the APDs, as well as the humidity and temperature of the crystals, and the light-tightness of the inner region. The refrigeration requirements for the inner structure elements are:

- Temperature operation of APDs: 18 ± 1°C.
- Safety operation temperature range: 15 to 30°C.
- Humidity control: values below 10% (relative humidity) for the crystals.

To deal with the temperature and humidity control there is a system of pipes running both under and above the cover structure, through which will flow dry nitrogen and air, respectively, with nozzles directed to the crystals and to the tiles. See the panels of Fig. 6.16.

To make the gas and light tightness of the cover structure effective it is foreseen to employ rubber pads, o-rings and sealing bands in the contact zones (tile-tile, tile-FEE, etc.), as in Fig. 6.15 right panel, as well as dedicated passthroughs for all connectors, wires and pipes. A set of thin aluminium panels (2 mm thick) placed at the front and back sides of the Barrel, and tightened between the tiles and the beam pipe, will act as a number of lids or a 'curtain' to enclose the inner structure. Additional curtains will allow the coverage of the medium plane of the Barrel halves, and operate each Barrel half autonomously.

The temperature control is made at the cover structure level. On the one side (internal) there will be APDs on each crystal, dissipating 0.012 W each, amounting to about 23.5 W in total. On the other side (external) there are the vFEE (pre-amplifiers) mounted on top of the tiles, dissipating 0.14 W/channel, including bias and temperature slow control systems, resulting in about 260 W in total. The forced convection will avoid a heat accumulation at the cover outer surface, and a strong temperature gradient along the vFEE modules fastened to the tiles.

Evaluation of the gas flux for temperature control.

The temperature can be controlled by using a flow of air at the outer surface of the cover. The air before the input inlet will be set at a temperature difference (dT) sufficient to drain the dissipated heat.

The dew point limits the temperature difference dT at which the gas can be introduced. Condensation at the outer surface will be avoided by the humidity limits guaranteed by the cave air conditioning system, and the fact that there will be always only a small temperature difference between the Barrel and the ambient temperature. In the table 6.6 we quote the safe dT values (last column) in the safety range of temperature, at different relative humidity (rH) and temperature values of the ambient air.

For a given amount of heat, the flow needed will only depend on the dT value. A special heat exchanger with flow regulation will decouple the cooling air temperature from the standard 12°C cooling water in the cave. Here the normal air will be filtered, dried during the heat exchange and then again reheated to provide a constant temperature air flow. A dT value of 8°C fits safely with the condition of avoiding condensation at room conditioned

air rH (%)	air temperature (°C)				dT (°C)
	15	20	25	30	
70	10	14	19	24	3
50	5	9	14	19	8
40	2	6	11	15	10
30	<0	3	6	10	15

Table 6.6.: Values of dew point (°C), for given ambient air relative humidity (rH) and temperature. The last column corresponds to the safe temperature differences (dT) to inject gas while avoiding condensation risks, at a given ambient air rH. The dew points were obtained according the Magnus-Tetens approximation.

ambient conditions (about 22°C, and less than 50% rH), and the cooling limit of 12°C, in the whole safety temperature range. We estimate the (total) air flux needed for cooling in 104 kL/h, distributed in 9 branches per Barrel half (basically, one arm per tile width) That value is easily sufficient to maintain a flux of 1.6 L/s per branch.

The nitrogen flux in the inner part of the cover will ensure the equilibrium of the temperature between the tiles and the crystals. We estimate that 10% of the (dry nitrogen) flux is needed for the total heat dissipation of the APDs power, satisfying this condition. Following the same evaluation as above, the resulting flux in 1 L/min, per branch.

The evaluations for cooling were taken considering that no additional heat sources exists. This is important specially with regards to the possible instruments placed inside CALIFA. Specific demands are listed in the dedicated section.

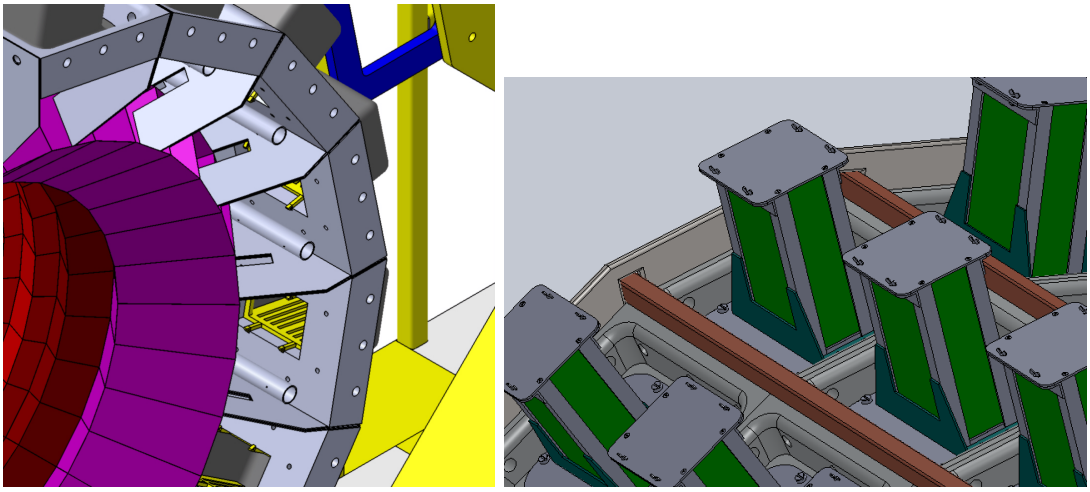

Figure 6.16.: Left panel: View of the pipes running under the tiles of the cover structure, to flow dry nitrogen into the active region and keep the humidity in that volume below the limit. Right panel: View of the pipes running on top of the tiles of the cover structure, to circulate cooled dry air and maintain a steady temperature of the system.

Evaluation of the flux for humidity control.

The CF structure, due to its thickness, is neither light- nor gas-tight. To control the humidity and equilibrating the temperature between tiles and crystals, we will use a flux of dry nitrogen distributed with pipes below the cover tiles. The cover structure, being significantly gas-tight, will be at an slight overpressure to guarantee the flow of gas in the volume of the cover, and to avoid ambient air to flow in.

The flux was set to 1 L/min per branch for temperature control purposes. This value equals to 32 renovation cycles/h of the volume in-between the crystals and the cover surface (about 27 L). Even if we take into consideration the entire empty volume generated by the forward and backward lids of the Barrel, and take the case of the central section being empty, the rate of renovation of the volume (about 315 L) is still 2.7 cycles/h. This large volume under the lids acts as a buffer to control both temperature and humidity of the active region. Therefore, the entire volume is renovated 2.7 times per hour with extremely dry gas. That renovation rate, the gas-tightness of the cover structure, and the slightly overpressure generated inside the cover structure, will maintain the humidity level at rather a low value, well below the required level of 10%. The gas can be driven from a connection to the low pressure Nitrogen line fed from the outside LN_2 tank.

For stand-by times and storage periods, a convenient flux to compensate the gas loss through the cover components has to be maintained in order to retain low humidity of the active volume. Special attention has to be paid to the temperature control at the starting operations, since the inner volume will not be drier than the ambient surroundings. Therefore the gas temperature difference dT has to be carefully set with respect to the dew point in order to avoid any water condensation inside the inner volume.

Light tightness.

The system has to be light-tight to shield the active elements of the detector from noise. As mentioned previously, the cover will be sealed so that no light can pass through. However the CF structure, due to its thickness, is neither light- nor gas-tight, as mentioned before. The forward and backward sides of the Barrel will be covered by aluminium panels acting as lids or curtains, fitted to the tiles and beam pipe. These layers of materials and thickness's will ensure the system is light-proof.

6.2.3. Geometrical versatility

In order to enable the assembly and maintenance operations, as well as to achieve the requirements of diverse experiments, some demands were introduced for the mechanical structure. A range of concepts related to versatility are discussed in this section.

Opening: It is necessary to have access to the inner target volume, both to change the reaction target and to install additional independent equipment, such as the tracking recoil detector, in the inner region. That is made possible by the design of the two halves of the Barrel. Special attention has been paid to the fast clamping system that should allow the operation of moving procedures with a minimal of intervention.

Half-Barrel operation: It is possible to manoeuvre separately each half of the Barrel. That is made possible by the design of the two halves being completely autonomous at every equipment level (gantry, cooling, electronics). Only an additional curtain is needed to make the half Barrel sufficiently gas- and light-tight.

Shifting: It is also possible to select a relative longitudinal movement of the two Barrel halves. This movement is limited to a maximum of two steps, of 82.5 mm each. This is due to the necessity of keeping the correct fastening of the tiles of the two halves. Additional curtains for gas- and light tightness are needed. The result is an angular clearance in the forward direction. The angular opening corresponding to one shift step, is 51.6° (8.4° difference, in respect to the nominal position of 43.2°), for details see Fig. 6.17, left panel.

Parking: The two Barrel halves can be set apart, via use of the floor rails. Two reserved volumes in the experimental room are foreseen to allow for safe parking of the Barrel halves for temporary stand-by, calibration or maintenance operations.

Crystal assembly: In order to assist in the assembly operations of hundreds of crystals into the *CF* structure, it is possible to move each half Barrel with just the gantry into a working room and back, on top of the bench structure. A dedicated support can hold the assembly in a position that exposes all tiles at a convenient angle, which should be of great benefit for the operation of crystal installation within the structure.

Crystals maintenance: The crystals are accessible after removing the corresponding tile of the cover. From the structural point of view the crystal units can be inserted or removed from the *CF* structure in any order. This is possible since the *CF* structure is designed to transfer the loads to the cover structure without significant deformations. Any tile can be removed, providing that it is a single tile per half Barrel and that the arms are set properly. The limitation to access of the crystals is imposed by the relative position of the tab. Only the pieces at the side without tab can be taken directly (after ring-and-clip retention removal). Following this operation, the adjacent pieces are accessible.

Crystals removing: Since the crystal units can be inserted or removed from the *CF* structure in any order, it is possible to remove a part of the crystals from the full-filled system to create 'holes' in the structure. The limitations are: (i) A reasonable load balance in the structure. (ii) It is not foreseen to have a holding system for individual crystal pieces, but for 4-pieces per alveolus; (iii) The *CF* structure is a single non-removable piece per half Barrel; (iv) Only one tile can be removed permanently from each half of the Barrel; (v) The arms should be re-located, if necessary, according to the structural needs.

6.2.4. Assembly operations of the Barrel halves

The operations for opening and closing, and shifting the Barrel halves, as well parking, etc. are based on the following concepts allowing for the autonomous operations of each Barrel half.

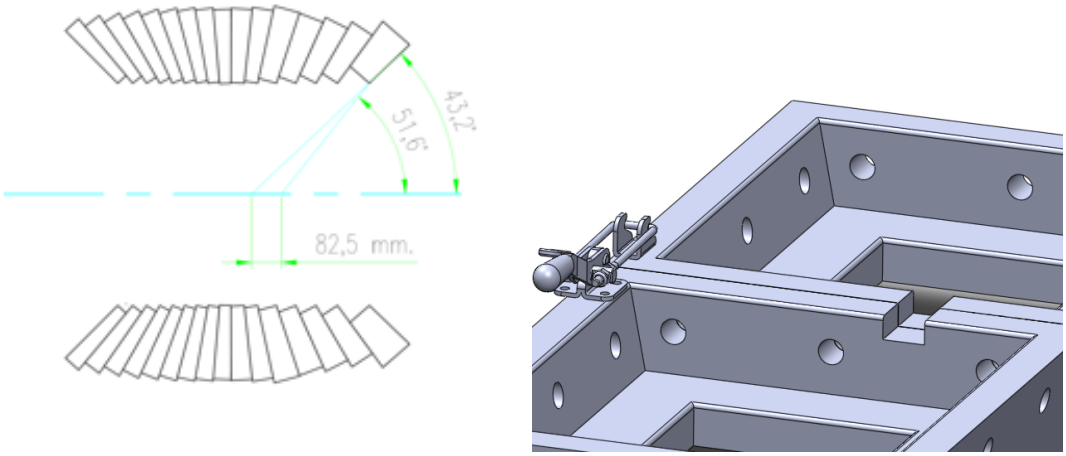

Figure 6.17.: Left panel: drawing of the *CF* structure after one step shifting (82.5 mm) between the two Barrel halves. The angular clearance is indicated in each case. Right panel: fast clamping system to tighten together the two halves of the Barrel at the cover level. The groove is designed to provide the correct alignment of the two halves of the Barrel.

Fast clamping: In order to allow for a safe and reliable procedure to join or separate the two halves of the Barrel, we include a fast clamping system, shown in the right panel of Fig. 6.17. Structurally it is not necessary to fasten the two cover halves with bolts. The interest in tightening this region is more due to alignment and gas- and light-control. The force provided by the small clamping devices is largely enough for those purposes. Additionally we avoid the use of bolts to fasten the tiles at these points, since it would mean dismounting the vFEE modules (and support structures) to allow for opening and closing operations.

Alignment: To ensure the alignment of the two halves of the Barrel when set together or shifted, we utilise grooves made at the top tiles, see the right panel of Fig. 6.17. A bolt fitting the groove will provide the mark to guaranty the correct alignment within tolerances. For the overall positioning of the block, we will use fixed points in the external structure ready for use with optical alignment methods, tolerances in positioning being of the order of 0.1 mm. A inner mould-fixture will allow for an easy alignment with the beam line, with tolerances within 0.2 mm.

General connections: To make possible both efficient and safe operations for each half of the Barrel we follow these general guidelines:

All cable connections passing through the cover elements will be made with adequate plug-and-play passthroughs.

vFEE: the modules can be inserted in the support attached to the tiles in a 'firmly-but-gently' operation with the help of the corresponding aligned passthroughs connectors.

Gas pipes (for temperature and humidity control) can be taken away at any moment from the system, being removable tubes with fast clipping connectors and fasteners.

The removal of the vFEE modules on top of any tile, provides a limited access to the crystals and APD electronics.

Any tile, but only one, after relocation of the arms if necessary, can be removed.

Independent front-end electronic modules will serve each Barrel half, moving together when shifted.

Cooling lines will serve each Barrel half independently.

Displacement: dimensions, control and clearance: The angle of aperture, 15°, and a length of the rail guides of 4 m, allows the movement of each block 3.9 m to each side, with a backwards displacement of 1 m. The movement will be operated and controlled via an automated system, driving the platforms along the linear slides with a minimum acceleration. The rails can be removed after service, including the finely calibrated section at the nominal position of CALIFA operation, in front of the magnet, as well as those dedicated to the parking of the CALIFA halves. This possibility will help to clear the space for other operations.

6.3. Demonstrator

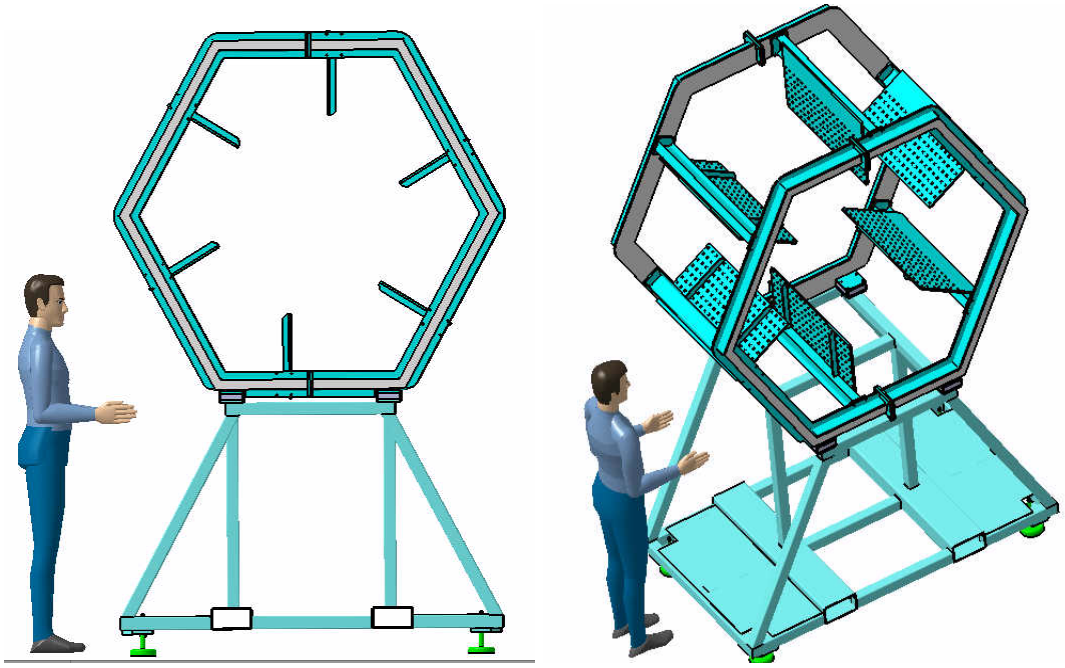

Figure 6.18.: Two views of the structure for the DEMONSTRATOR system. The two sub-structures, bench and gantry, are clearly identified. The plates around the gantry are the allocated panels in order to hold the active elements.

It is forseen to construct a DEMONSTRATOR array, based on a collection of grouped crystals, so called 'petals', with a geometry and dimensions corresponding to the furthest forward elements of the BARREL.
The DEMONSTRATOR is intended to serve as a reference for systematic studies of the elements and structures. This is specifically relevant in the case of the CF structures. In this way, the FEM models used to evaluate the entire CALIFA CF structure performance

can be validated and compared to real test results. While the array is intended to be a major step in the design and construction process of the structural elements, it will also be utilised to perform real physics experiments. In order to maximise the performance at this stage a range of geometrical configurations are forseen to adapt to the desired physics case. Finally, as a cost-effective measure, the components of DEMONSTRATOR will ultimately be incorporated into the CALIFA Barrel.

6.3.1. Petals

The petals are made with a CF structure with 2 (azimuthal) x 8 (polar) alveoli, so they can contain up to 64 crystals. The DEMONSTRATOR would be composed of eight petals. Each petal is held with a tab at each side (it actually requires two of the sub-pieces of each tab, to hold the 8 alveoli, see Fig. 6.5). Since the system is not 'closed' as for the Barrel, and the alveoli do not lean on the neighbouring pieces in azimuthal direction, the tabs will be extended till the bottom of the CF structure. Two (cover) tiles will hold the tabs, as well as the vFEE modules. The same concepts of insulation described for CALIFA can be used, just by closing the system with additional lids at the front and back sides.

This petal design, with the structural elements as an exoskeleton, forms a robust 'cell'. This is an interesting option as a test and transport unit, also planned for use in real physical experiments.

6.3.2. Mechanical structure

The petals will be held in place by the gantry of a dedicated structure. The structure is designed to be as versatile as possible, to better adapt to different experimental conditions. It is composed of two parts, the bench and the gantry, see Fig. 6.18. The gantry is aligned at the beam height, and can be split to be set around a beam pipe.

The gantry has six longitudinal beams which each hold one plate. This plates are the supports for the petals, with an 'arm' to suspend the tiles to the plates, see the left panel of Fig. 6.19. Because of the geometry this arm is completely different to that of the Barrel. A simple fastening procedure between the arm and the plate will allow reallocation of the petals in multiple positions and directions. The nominal position would be that of the corresponding CALIFA geometry.

6.3.3. Geometrical versatility

The petals can be positioned and oriented once fastened to a plate. There are six initial possibilities to position the petals. The petals can also be paired (at tile level), and two of then hung from one plate. Therefore, there are allocated spaces for up to 12 petals within the structure, that can be used in any combination, see Fig. 6.19.

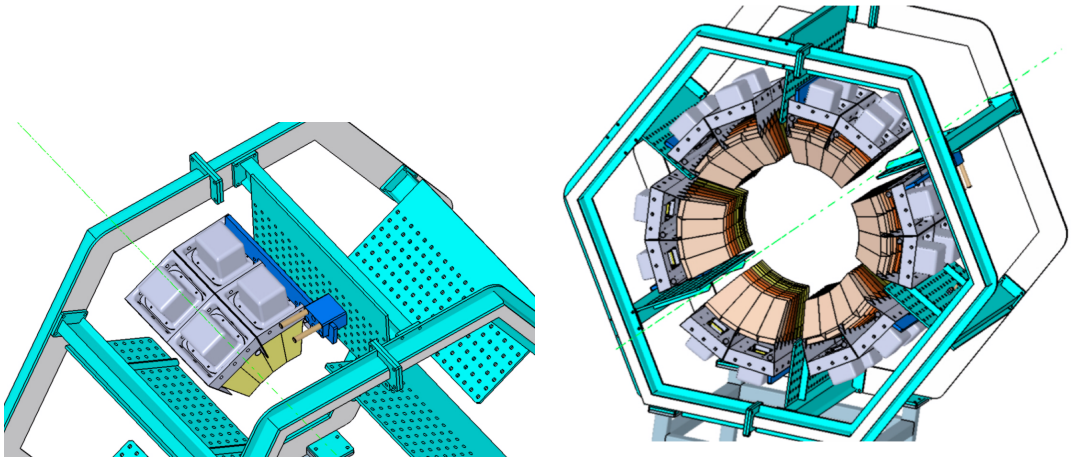

Figure 6.19.: Two views of the DEMONSTRATOR. In the left panel we can see two petals paired and placed into the same arm-plate structure. In the right panel, the twelve positions for petals in the DEMONSTRATOR are displayed to demonstrate its capacity.

6.4. Interface with the Forward EndCap

The Forward EndCap design is currently under discussion, but general guidelines are proposed for the integration with the Barrel.

- Full functional independence of the Barrel and EndCap systems.
- No dead angles or gaps in the transition.
- No major addition of matter in the transition.
- The possibility to fasten the covers of the Barrel and EndCap to help in the insulation of the system.
- The possibility to operate both Barrel and EndCap integrated within the same structure, as well as the EndCap alone, with a dedicated structure.

In Fig. 6.20 we show a proposal for the EndCap, the stand-alone structure, and the integration of the Barrel and EndCap into the whole CALIFA system.

6.5. Reserved space for additional equipment

We have followed the instruction to keep a reserved volume inside the Barrel dedicated for other purposes. The dimensions correspond to a diameter around the beam axis of at least 500 mm, 400 mm length from the target in forward direction, and 500 mm length from the target in backward direction, see Fig6.21.

At the same time the CALIFA-Barrel requirements towards other equipment are:

- No overlapping of the space assigned to CALIFA.

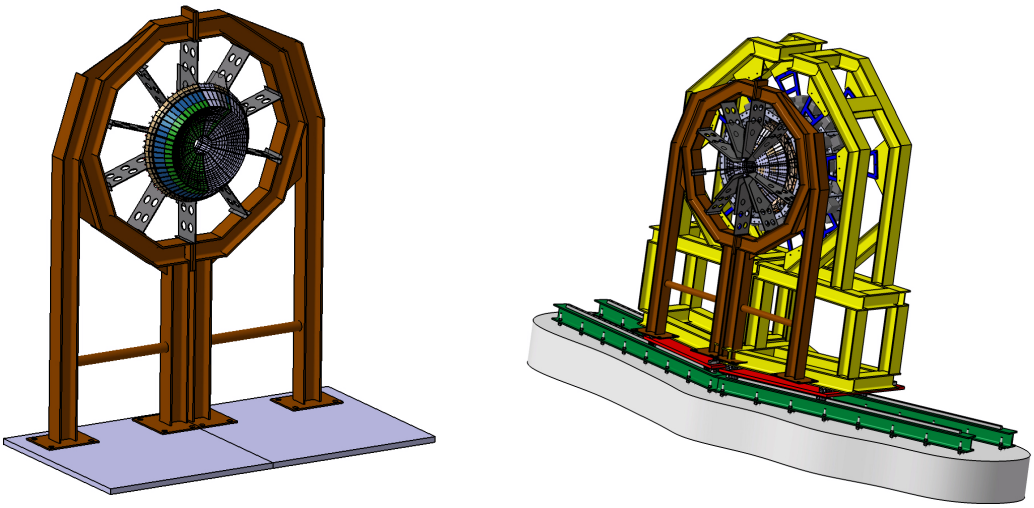

Figure 6.20.: Ad-hoc proposal for the EndCap, the stand-alone structure, and the integration of the Barrel and EndCap into the whole CALIFA system.

- No disturbance of the possibility to open or shift the Barrel.
- Any load transferred to CALIFA could eventually be done only at the external structure level and only after supervision and control of the effects of such loads.
- All heat dissipated inside the CALIFA volume has to be effectively drained in order to avoid any temperature gradient in the inner volume.

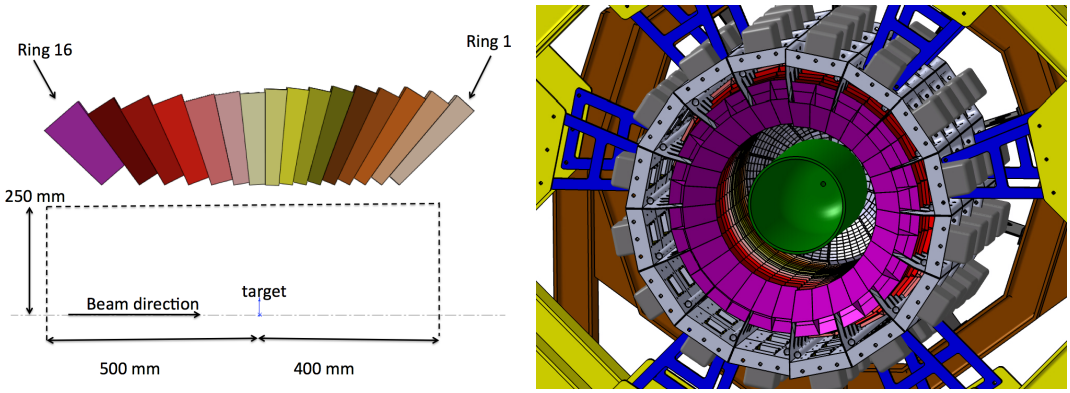

Figure 6.21.: Left panel: Drawing of the space reserved inside the Barrel for other purposes. Dimensions in mm. Right panel: view of a chamber with 250 mm radius located inside the Barrel.

7. Radiation Environment and Safety Issues

The radiation dose that CALIFA will be exposed to is comparably low, despite the detector surrounding the reaction target with quite a close geometry. The detector will be used for experiments with radioactive secondary beams with a maximum production rate of 10^8 particles/s. Assuming a target thickness corresponding to a 1% interaction probability, a maximum flux of neutrons and light charged particles of 10^7 particles/s from the target is expected. While the vast majority of projectile-like fragments will leave the target chamber in a forward direction, a maximum rate of approximately 2×10^6 particles/s target-like reaction products will be emitted within the acceptance of the CALIFA Barrel.

Many of the experiments will deal with very rare ions (down to 100 particles/s), therefore for the estimation of the overall dose on the calorimeter, a mean value of 10^6 beam ions/s and equivalent 10^5 particles/s are taken into account to be emitted within the acceptance of the CALIFA Barrel. With an operation time of 2 months per year, 5×10^7 particles/cm^2 and year pass the detector volume, neglecting duty cycle. While a large fraction of the low energy charged particles are already stopped in the target chamber, the emitted neutrons will not be thermalised and pass through the detector with a very low activation of the material. Other more abundant radiation such as X-rays and delta electrons have much lower impact on the material used in CALIFA. Radiation damages can therefore be excluded (see also section 3.2.5).
With respect to ageing the dose appears similarly irrelevant. A direct exposure of CALIFA to the ion beam is avoided already due to the geometrical layout. During operation the activation will be continuously monitored with the detector itself.

The APDs used for CALIFA require a high-voltage supply, up to 500 V. Each channel is individually protected with a current limit of 10 μA. Standard operation procedures according to VDE[1] will be followed to guarantee the safety. The CALIFA operation requires the use of dry Nitrogen at a maximum rate of 1000 l/h as a flushing gas to protect the detector against humidity. This will not significantly affect the Oxygen concentrations in both large volume and non hermetically closed experimental halls. Therefore, no required connection to the exhaust system is foreseen.

CALIFA, including the contributions from the frame and electronics, has a total weight of about 8.4 tons. With a contact area of about 2.6×2 m^2 for the CALIFA detector frame, a floor load of about 3.3 tons/m^2 is obtained, which is far below the foreseen floor loads for the experimental hall. The detector is basically split into two independent (left and right) parts which can be moved in the target area on a rail system mounted on the floor

[1] VDE, the Association for Electrical, Electronic & Information Technologies, German: Verband der Elektrotechnik Elektronik Informationstechnik e.V.

preventing any tilting of the rather highly placed objects. For transport and storage off-rails, additional bars are required to be mounted on floor level; expanding the base area to 3×2 m^2. The CALIFA Barrel opening procedure has been designed following security standards as detailed in Chapter 6. The mounting platform stands at approximately 1 m high around the Barrel, enclosed with outer handrails and an anti-slip floor to safeguard people during setup and maintenance.

8. Production, Quality Assurance and Acceptance Tests

The construction of the CALIFA Barrel necessitates a careful survey of the production process, including a quality assurance of the different elements. In order to guarantee that the final detector complies with the specifications detailed in this document the performance of acceptance tests corresponding to certain CALIFA components, addressed to cross-check the quality of the product delivered by the producers, will be necessary.

We will briefly describe in the following sections the actions planned to perform this task.

8.1. CsI(Tl) crystals

Results yielded from the tests described in Chapter 3 enable extraction of requirements to be met for CsI(Tl) crystals to fulfil the demands of the R^3B physics programme.

The average activator concentration will be 0.08 mol%. This concentration was used in some of the supplied test detectors and minimises the effect of non-uniformity in the Tl doping, allowing for an optimum light output [KSS+05, Gra84].
The heterogeneity in activator distribution along the single crystal in the primary boule needs to be better than 2.4% and the azimuth heterogeneity less than 1%. This will ensure that light yield variations between different parts of the crystal are acceptable.
All surfaces will be polished to mirror reflectivity using ZrO_2 powder with 1 μm grain size combined with ethylene glycol ($C_2H_6O_2$) as the solvent. The variation in absolute light output, defined relative to a reference crystal of size 25x25x25 mm^3, needs to be smaller than 15% between crystals.
Samples need to have a smooth exponential decrease in light output, LO, in the direction of the photo sensor. The maximum non-uniformity, defined as $\Delta LO = (LO_{max} - LO_{min})/LO_{average}$ needs to be better than 7% (from the growing process).
Those starting values will allow for a final light output non-uniformity smaller than 3%[1] after lapping (see section 3.1.1 for details). A sorting of the samples based on the final quality of the different crystals provided will be requested of the manufacturer.

The lapping procedure is foreseen to be provided by the crystal suppliers.

The quality of the polishing/lapping will be tested by members of CALIFA working group[2] by measuring before acceptance, and for all the received samples, the light output along

[1] That is the absolute variation allowed.
[2] Crystals will be distributed along different participating institutes.

the crystal at 3 points (close to entrance, middle and close to APD) starting from the front face using standard γ-ray sources of ^{22}Na, ^{137}Cs or ^{60}Co. Those tests will be completed following the wrapping and coupling to the LAAPD, and will also perform as a quality test of the complete detection units.

The crystals, in a set of 4, must fit correctly inside the rigid pockets defined by the CF alveoli. To ensure the correct insertion is achievable, the crystals must comply to a geometrical tolerance of (+0.03 mm, -0.20 mm) in their X and Y dimensions, a high tolerance in crystal length, dimension Z, being less critical in this respect.

8.2. Large Area APD

Standard and double Hamamatsu S8664-1010 have been investigated through the course of this work. They were found to have a specified gain of, M=50 at T=23 °C. The dark currents for the APDs given at their respective nominal voltage, V_{nom}, ranged from 10 to 50 nA, with an average dark current of about 30 nA when no special requirement was asked of the producers. When a low I_d selection requirement was made, a dark current of approximately 18 nA with a very small spread was achieved. This lower value of the dark current translates to a rather small dispersion. This selection is important as a spread in current corresponds directly to the spread in APD electronic noise and so affects the energy resolution. We have fixed $I_d < 20$ nA ($\pm$ 10nA) as the limit accepted for CALIFA Barrel APDs. Additionally, differences lower than 5V between the V_{nom} of a pair of APDs mounted on the same frame will similarly be requested.

Parameters such as the quantum efficiency (QE) and gain uniformity throughout the active surface will be checked by members of our collaboration, but only for a few control samples per delivery from the manufacturer.
The integral response of each APD will be calibrated as described below.

The gain of APDs is highly dependent on the applied reverse bias and the temperature. The latter will be actively compensated for by the electronics presented in section 6.2.2. Prior to this, every APD must be characterised, hence the change of the gain as a function of temperature and bias (see section 3.2.2) has to be measured and the optimal correction parameter has to be deduced. Additionally, the bias for the nominal gain ($M = 50$) at the nominal temperature ($T = 18$ °C[3]), the noise level, and the slopes ($\delta M/\delta V$ and $\delta M/\delta T$) at different gain, bias, and temperature values will be stored in a database for later comparison.

The characterisation will be done employing the set-up built by the PANDA collaboration at GSI which allows routine tests under well-controlled conditions, reinforcing in this way synergies between different FAIR collaborations. It is worthwhile mentioning that these synergies have been already established during the R&D period, particularly with members of PANDA collaboration.

[3]That is to say the corresponding value slightly below the room temperature.

Indeed, during our preliminary investigations the measurement of temperature dependence often turned out to be unreliable, with non-reproducible results. It is however clear that larger effort has to be undertaken in order to assure a constant temperature at a selectable value. The "clima box" built by PANDA offers such reliable conditions [The08, Wil].

A useful modification is planned with the installation of a light emitting diode (LED) which has a maximum emission point at a wavelength of 550 nm, representing well the fluorescence spectrum of CsI(Tl).

The reproducibility of the results, including the stability of the LED, can be cross-checked via X-rays detection, emitted from a ^{55}Fe source as previously detailed in Chapter 3.

8.3. Mechanical support

As presented in Chapter 6, different FEM calculations have been undertaken for the supporting structure of CALIFA. The ideal situation will of course follow validation of the simulations with real measurements. The assembly of the Demonstrator with the construction of the same carbon fibre alveoli structure to be implemented throughout the CALIFA barrel will serve as an excellent test bench in this respect.

An exhaustive plan of load and deformation measurements are foreseen for the carbon fibre alveoli during the Demonstrator phase. The possibility of a further reduction of the final alveoli thickness is still undergoing investigation.

The collaboration will guarantee the evaluation of a certain amount (of the order of 5%) of the delivered subsets to cross-check the quality provided by manufacturers.

Mechanical and dimensional tolerances concerning the main components of the main CALIFA mechanical structure components are provided through various sections of Chapter 6.

9. Calibrations

A precise calibration of CALIFA is essential to the success of the project. Major challenges are posed by the large number of channels due to the high granularity and the fundamentally different response of the CsI crystals to γ rays and protons (see section 5.5.5). Hence, individual calibration procedures for both species and a particle identification are foreseen. The procedures have to calibrate the system and to monitor the stability of the calibration throughout the entire operational running time. The success of these procedures is a major factor in the final performance of CALIFA. The aim of the calibration procedures described in this Section is to minimise the contribution from the calibration to the total energy resolution.

The check of the performance of individual detectors consisting of the crystal and the APD is discussed in Chapter 3 as well as in Chapter 8 as part of the quality control procedures. These detectors are grouped in larger units, i.e. the alveoli (Chapter 6), which comprise the whole instrument. However, smaller arrangements of detectors have already been used for proof-of-principle experiments.

In the first part of this Chapter we discuss reference experiments to be performed before or immediately after the mounting of parts or the whole array in Cave C at GSI or in the HEB cave accommodating the R^3B set-up at FAIR. These will be done with larger assemblies of CALIFA detectors, e.g. the petals. Physics events created via simple reactions will be used. It is foreseen that it is not necessary to repeat these kind of experiments regularly, though repeating some occasionally would be helpful to assure a stable performance. As mentioned above, since the light output of the crystals is different for γ rays and particles, calibrations cannot be extrapolated from one species to the other and, hence, different calibration experiments have to be performed. The second part describes calibration procedures which will be regularly performed with CALIFA situated at the experimental site, in particular the monitoring during the experiments.

9.1. Reference experiments

The experiments described in this section aim to check the performance of larger detector assemblies rather than individual detector modules. They are and will be performed at different laboratories. A final check will be performed with these modules mounted in Cave C or at the R^3B site. A main task is also to verify the results obtained in simulations (see Chapter 4). The programme comprises the determination of the response to high-energy γ rays not reachable by sources as well as particles like protons and neutrons. Beside the response of single detectors, effects like the cross scattering between detectors and the applied add-back procedure are of importance as they contribute to the efficiency of CALIFA.

9.1.1. γ rays

For the detection of high energetic γ rays of several MeV the interaction of photons with matter causes a rather complex response function of CALIFA. Thus, beside an energy calibration, the simulation of these response functions needs to be verified for several photon energies in the energy region of interest. For a reliable test, monoenergetic γ ray sources are needed in order to investigate the dependence of the response function on the γ-ray energy. In addition this also allows to verify the linearity of the entire system of crystal, photo-sensor and electronics for γ-ray energies up to 20 MeV.

γ-ray sources

For energies up to a few MeV radioactive sources are, of course, the ideal choice to investigate the response function of γ-ray detectors. Corresponding studies and comparisons to simulations have been done in recent years for individual crystals as well as small assemblies (Section 4.3). Similar tests will be also the first step in the calibration of larger detector assemblies, such as the petals.

NEPTUN

To extend such investigations to higher photon energies up to 20 MeV the NEPTUN tagger at the superconducting electron accelerator S-DALINAC operated at the TU Darmstadt is an ideal facility [SLG+10]. The tagging technique provides the possibility to select single photons with well defined energies ($\Delta E \leq 50$ keV) out of a continuous Bremsstrahlung spectrum. By changing the tagging conditions the energy can be freely tuned in the region between 2 MeV and 20 MeV.

NEPTUN has been already used to test the ProtoZero assembly which consisted of 15 crystals arranged in a 3×5 configuration by the time of the experiment. Figure 9.1 shows reconstructed energy spectra at three different selected incident γ-ray energies. The typical response function including the escape peaks and Compton regions to a monoenergetic photon beam defines the shape of the spectra. A small contribution from uncorrelated background can be even further suppressed by subtracting random coincidences with dedicated cuts in the timing spectra between the crystals and the focal plane of the tagging system. In this way the response function can be studied quantitatively and compared to simulations. This includes the investigation of single crystals, but especially also the multiplicity and add-back capabilities of even larger parts of CALIFA. This verification of the simulated response (of singles and in add-back mode) is an important step towards a detailed understanding of the response function of the entire CALIFA Barrel.

Reactions at the R^{3}B set-up

After the installation at the R^{3}B set-up high energy photons need to be generated in reactions, since tests at external facilities with the full set-up are then less profitable.[1] A suitable example is the ^{12}C(p,p'γ) reaction, where the deexcitation of the high-lying $T = 1$ state at about 15 MeV provides high energy γ rays of a single energy. This reaction has

[1] Though the transport of the setup may be possible, it requires a lot of logistics and some risk of damage to the components.

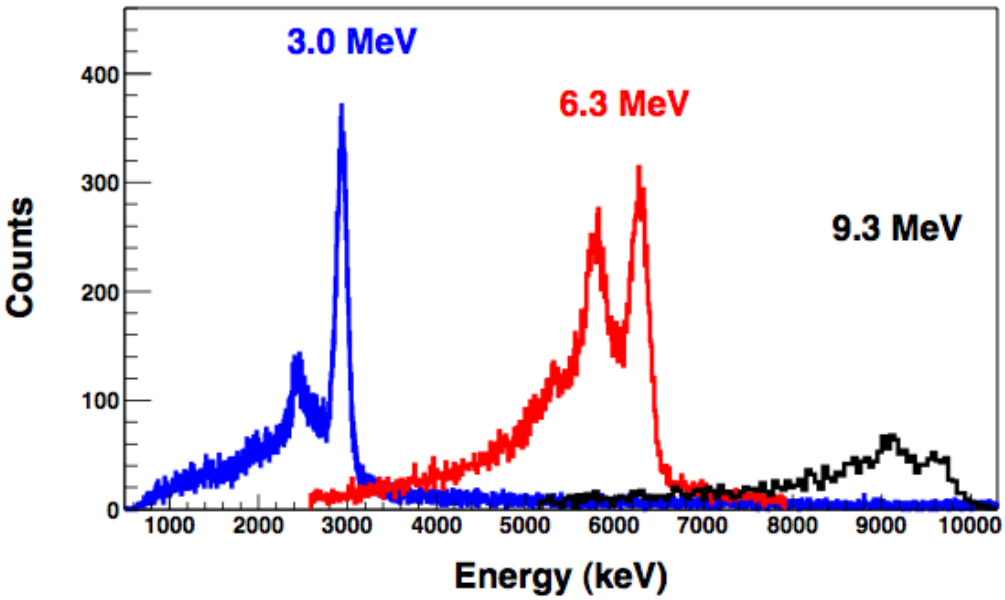

Figure 9.1.: Reconstructed energy spectra for three selected incident photon energies using the NEPTUN photon tagger [Gas10].

been used also during the most recent CALIFA test performed at the tandem accelerator in München allowing to directly compare the response to γ rays and particles at comparable energies (see Appendix A). Since the detector response of sub-part had been studied in detail at NEPTUN this single energy will be sufficient in order to adapt the results obtained to the full CALIFA array.

9.1.2. Protons

Individual crystals or small assemblies have already been tested with proton beams [vS12, BBG+09, DAC+09] (see Appendix A). They will also be tested at high-energy beam facilities. Active or passive degraders in front of the crystals allow for a variation of the energy. Fig. 9.2 shows the response of an assembly of two CsI crystals (at this time, read out by photomultipliers) illuminated at KVI directly by a 135 MeV proton beam or after inserting passive and/or active degrader. High-energy protons are also needed to calibrate the time-over-threshold method described in Section 5.3.5. Such calibration runs are necessary also for larger units of CALIFA detectors, e.g. the petals.

Additionally, the elastic scattering of a high-energy proton beam by a heavy target, e.g. ^{208}Pb, provides high-energy protons. The region of interest can be well covered with energies available at Cave C of GSI or in the R^{3}B cave at FAIR. Cross sections and angular distributions are well understood over a wide range of energies (200-800 MeV) relevant for R^{3}B, e.g. Ref. [MSA+86, OWT88]). The laboratory energy as function of the laboratory scattering angle of protons scattered by a Pb target is rather flat with values similar to the initial beam energy. Different beam energies even allow for a control of the linearity. Assuming a beam energy of 200 MeV, an intensity of 10^{10}/s and a target thickness of 500 mg/cm^2 (energy loss in the target below 1%), the most forward crystals will have a

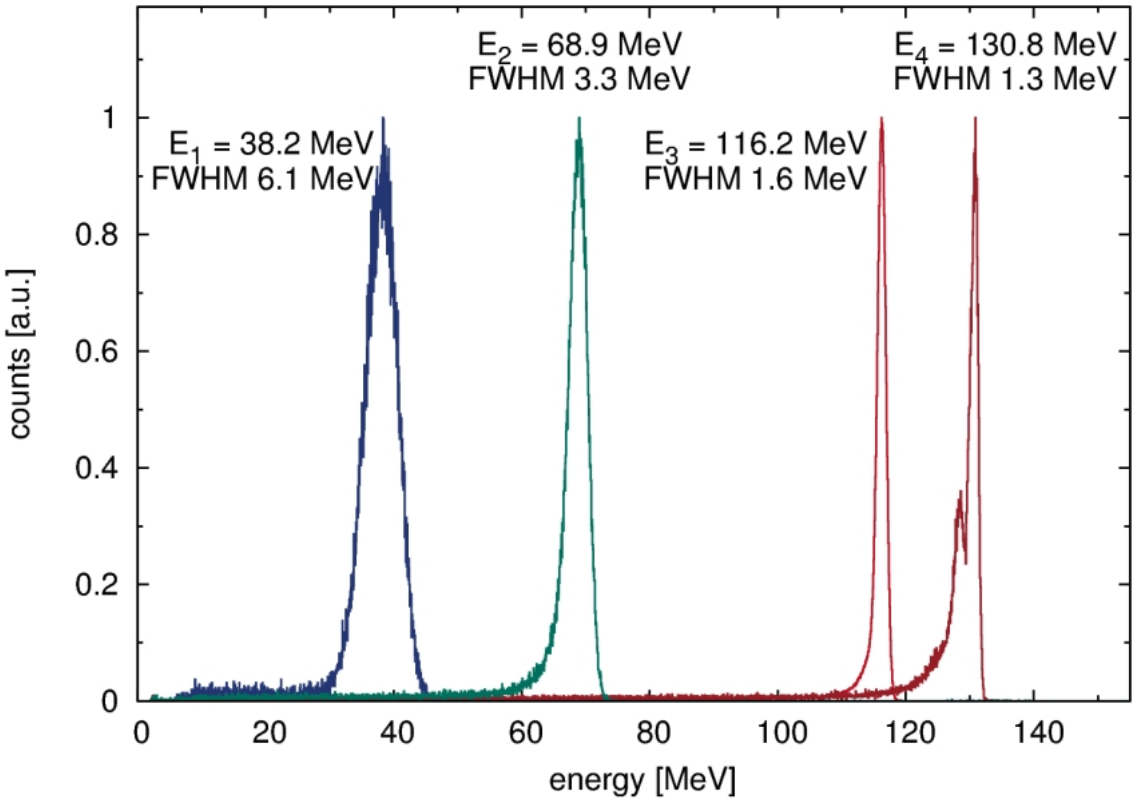

Figure 9.2.: Two CsI crystals with protons at different energies [vS12].

counting rate of 50 ions/s. Hence, this calibration can be done in a rather short-timed measurement. As the cross section exponentially decreases as function of the scattering angle, the more backward crystals have to be calibrated by moving the target upstream. The most forward crystals will then detect rates of some 10 kHz, hence rates easily to handle. Since the protons, in this configuration, cross through different crystals, in most cases several energy loss signals will be measured. However, the precise scattering angle can be determined by introducing a silicon tracker inside CALIFA. From this scattering angle the effective track length in the crystal can be calculated. As background only neutrons and γ rays are expected, which deposit much smaller amounts of energy.

A parallel calibration for both γ rays and protons can be done e.g. employing again the ^{12}C(p,p'γ)^{12}C reaction also at higher energies. The γ rays, e.g. at 4.44 MeV and 15.11 MeV, are emitted in coincidence with the protons [HAC+88].

A distinction between 'low-energy' protons and γ rays can be done either by requiring a signal from the silicon tracker inside of CALIFA (not always present even in physics experiments) or by pulse shape analysis (see Section 5.5.5). The latter has to be calibrated e.g. with the ^{12}C(p,p'γ)^{12}C at low proton energies as it has been done during the recent test in München.

9.2. Calibration of CALIFA before and after experiments

From the experience obtained in several test campaigns, it can be concluded that the response to γ rays and particles, although different, is very linear [Gas10] (see Fig. 3.13 and Fig. 9.2). Calibrations have to be done only at a few energies, separate for γ rays and particles, and then can be extrapolated. Therefore, the reference reactions described in the previous Section will be performed once and need not to be repeated on a regular base.

For a γ-ray calibration, standard calibration sources will be used before and after the experiments.

The response to light charged particles can be checked using cosmic rays passing through CALIFA. The muons have a relatively broad angular and energy distribution, peaking at polar angles around 90° and with a mean energy of 4 GeV [A+08]. Typically, they will leave as minimum ionising particles a relatively small energy loss deposit of around 1-2 MeV/(g/cm^2) in the crystals. Requiring two or more crystals on opposite sides of CALIFA having fired allows to determine approximately the track and, hence, the effective path length through the crystals. A similar method has been applied already for the Crystal Ball (CB) at Cave C [Wam11]. The higher granularity of CALIFA allows for such a tracking with better precision compared to the CB. In cases when the Si tracker is mounted inside CALIFA, a complete tracking through the array can be performed and the paths are determined with excellent precision. These analysis can be accompanied by simulations to refine the results. However, the rate is small (approximately 1 per cm^2 and minute) and such a calibration requires a rather long time of measurement.

9.3. Gain monitoring during experiments

The main task during an experiment is the continuous monitoring of the gain stability. The gain change of the APDs due to variations in temperature is compensated by the electronics described in Section 5.3.4. The stability of the electronics is monitored by injecting regularly electronic pulses.Although predicted to be within safe limits (see Chapter 7), it is possible that ageing and radiation damages may affect the crystal, the optical coupling to the APDs and the APD themselves even during the run of an experiment. Radiation damages in the crystals may affect the transparency and/or the light yield of the crystals. As a precaution, in order to monitor such effects two methods will be applied: light pulses from a LED system and γ rays from sources.

Both types of pulser systems are standard for calorimeters based on scintillation detectors as they are used in hadron or particle physics, e.g. CMS at LHC [CMS97] or PANDA at FAIR [The08], will be described in detail below. The combination of both pulser systems allows for a comprehensive monitoring of all elements of the detector: crystal - APD readout - electronics.

9.3.1. γ-ray sources

A degradation of the light yield cannot be monitored by the LED pulser and has to be checked by 'real' γ rays. Except for the few muons originating from cosmic rays, there are usually no charged particles with defined properties during experiments which can be

used for calibration or gain monitoring. Therefore, the calibration points obtained with γ rays have to be considered as being representative for the light production properties of the crystal. Different solutions have been considered.

One obvious solution seemed to be the monitoring of the 1460 keV transition following the ^{40}K decay during the intervals between the beam pulses. However, the experience with the CB in Cave C has shown that the rates are very small and the peak is hardly seen in the background originating from activation. As the granularity of CALIFA is an order of magnitude higher, this will not allow to collect sufficient statistics for each crystal.

The BaBar calorimeter has implemented a system of small tubes through which flows a radioactive liquid activated by a neutron source in the reaction $^{19}\mathrm{F} + \mathrm{n} \rightarrow {}^{16}\mathrm{N} + \alpha$ [Lew00]. ^{16}N decays emitting a γ ray of 6.13 MeV. Because of the short half-life of 7 s, the source can be "switched" on and off. However, we decided having only one single γ-ray energy does not justify the considerable effort concerning mechanics and radiation protection for such a system.

Thus we foresee to use small sources located within or outside of the calorimeter for the monitoring of the light yield in the intervals between beam pulses. Standard sources will be distributed in order to provide a reasonable count rate in each single crystal, which is on the one hand not too high to disturb the measurements during the beam pulse and on the other hand high enough in order to yield sufficient statistics collected between the beam pulses within a reasonable time, i.e. a rate a few events per second in each crystal.

A problem of this approach is the fact that there is no dedicated γ-ray trigger for this calibration and the spectrum thus suffers from contamination produced by activation due to the beam. A solution of this is to provide a trigger for the emission of the γ rays in the decay of the source. Such a trigger can be provided by detecting the electron/positron of the β decay of sources such as ^{22,24}Na or ^{207}Bi, since the γ-ray radiation is following in coincidence. There are two ways to achieve this. Either a small detector is attached to the source or a scintillation detector is activated in order to be detector and source simultaneously. For the latter a standard NaI detector can be used, i.e. activating a NaI crystal using high energy photons via the $^{23}\mathrm{Na}(\gamma, n)^{22}\mathrm{Na}$ reaction. The ^{22}Na beta-decay will be detected by the crystal providing the trigger for the emitted γ rays which will used for the monitoring of the CALIFA detectors.

It has to be pointed out, that for both the electronic pulses from the pulser and the light pulses from the LED a dedicated trigger active only between the beam pulses can be provided to the DAQ system. This is, of course, not possible for the γ rays emitted from radioactive sources, which will be measured either by a free off-beam trigger or by triggering on an active detector as described above.

9.3.2. Electronic pulser

The signal coming out of the APDs can be approximated by a sum of three Gaussians in the following form

$$V(t) = V_0 \left(n_s e^{-t/\tau_s} + n_f e^{-t/\tau_f} - (n_s + n_f) e^{-t/\tau_r} \right) \tag{9.1}$$

where τ_r, τ_s and τ_f are the rising, the slow decay and the fast decay constants respectively, while n_s and n_f are the relative weight of the slow and the fast components (see 5.5.5).[2] The energy for a given particle is then given by the amplitude V_0.

In order to convert the measured amplitude to the energy of a particle, two relations have to be established: between the measured amplitude and V_0 and between V_0 and the deposit energy. The latter is internal to the combination of the crystal and the APD, and hence, its calibration requires particles sources with known characteristics and/or LED pulses. The former, however requires the calibration for the chain composed of the pre-amplifier, the fast sampling ADC and the FPGA. That could be achieved by sending a pulse of known amplitude to the input of the pre-amplifier[3] and comparing the amplitude to the ultimately measured one.

Generation of an Electronic Pulse

In order to study the response of the FEE in conditions as close as possible to the real signals, a pulse must be generated as a sum of three exponentials distributions as shown in (9.1), where all the parameters are fully controlled, and in particular the amplitude. Due to the relative complexity of the shape of the pulse, a solution based on a FPGA together with digital-to-analog converter (DAC) has been adopted. This is summarised in Figure 9.3.

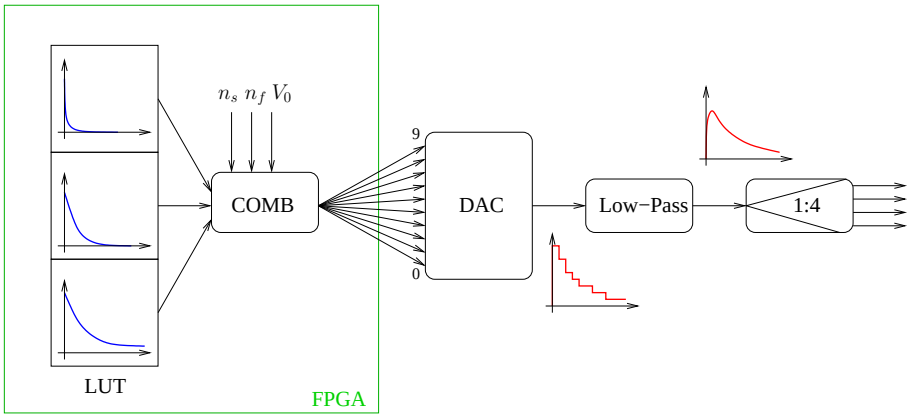

Figure 9.3.: Scheme of the pulse generator used for the calibration: three look-up tables (LUT) each containing the distribution of three exponentials with different time constants are used. The values from the LUT are weighted (by n_s, n_f) and combined in order to generate a signal similar to the one coming out of the APDs. Finally the whole signal is multipled by a value V_0. At the clock frequency, the amplitude of the signal is decomposed in 10 bits and each bit value is emitted by the FPGA individually. The 10-bits signal is then converted to an analog signal in the DAC, filtered and de-multiplexed (e.g. 1:4).

The three exponential distributions are encoded individually in look-up tables (LUT) in the FPGA. They are weighted individually (using the factors n_s and n_f) and summed. The result is then amplified by a factor V_0 and encoded in 10 bits. And each bit is then sent

[2] In practice, however, the rising time constant τ_r is neglected compared to the decay constants as has been done in Section5.3.

[3] The preamplifier of Mesytec has a test input that is used for that purpose, see 5.3.

individually on each clock. The 10 signals are collected by the DAC which then generates an analog signal. Since the generated signal has been recomposed from a clocked signal, it needs to be filtered in order to be continuous. For that purpose, a low-pass filter is used. And its output corresponds to the generated pulse that will be sent to the pre-amplifier.

In order to minimise the electronics, a demultiplexor is used and the generated pulse can be switched to up to, e.g., four different pre-amplifiers.

Integration in the Read-Out Scheme

A pulse similar to the signal from the APD is generated and sent to all the channels of one pre-amplifier. The result will be sampled and analysed in the FPGA of the FEBEX, and the maximum of the peak will be determined.

In order to calibrate the whole range, the amplitude V_0 chosen in the FPGA of the pulse-generator varies. Hence, the linearity of the response of the FEE can be verified over the whole range. Considering the technique used to determined the amplitude of the input signal, non-local linearities can be neglected. Therefore a certain set of amplitude is considered. The pulse generator looping over that set of amplitude. The value chosen is reccorded into the data stream in order to be used for off-line calibration.

The response of the electronics may vary during an experiment (temperature, etc.) therefore the pulses are sent during the operation of the detector at a lower rate so as not to overload the converting electronics with not physics-related data. The events, refered to as calibration events can be then off-line studied as a function of the time of the experiment and the variations can then be evalutated. In a trigger mode, those events will match calibration triggers such as the time calibration trigger (as the timing is not a precise measurement for the CsI(Tl)). And in triggerless mode, the system spontaneously generates such pulse at a given frequency (up to a few Hz).

The relative weights of the two decay constants depends strongly on the particle as was shown previously. There is then the possibilty to generate a pulse representing one or another particle. This choice can be modified for each experiment, and the ideal would be to calibrate the PID as well as the amplitude determination, however that would require a rather high rate of non-physics data to provide a good time dependence. By default, it is then preferable to choose $n_s = n_f = 1$, which corresponds to the detection of a photon.

9.3.3. LED light calibration system

CALIFA will be equipped with a light monitoring and calibration system. The task of this system is to evaluate continuously the functionality of almost all components of the CALIFA module: crystal, APD and the readout. During an experiment the gain and the linearity of each detector module is monitored and possible changes or degradations can be corrected in the analysis. The combination with the electronic pulser even allows to distinguish between effects occurring in the crystal and the APD or the subsequent electronics. The system will also permit a rapid survey of the full calorimeter during the installation or after long shutdowns.

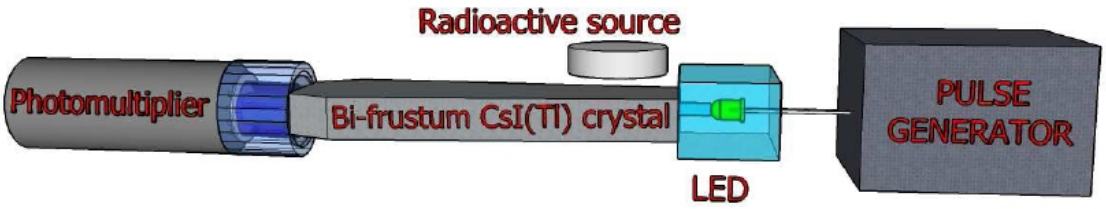

Figure 9.4.: Principle concept of the LED reference system [Gas10]

Concept

The concept of the system is similar to systems of other calorimeters, e.g. the EMCs of BaBar [Lew00] or PANDA [The08]. As in PANDA and contrary to the Xe flash lamps used in BaBar, a LED will be used as light source. CsI(Tl) has a comparatively slow light signal, therefore a laser as used in CMS is not required.

A well defined light signal from a pulsed LED will be periodically, e.g. at a fixed frequency or during the intervals between the beam pulses, sent into the crystal via an optical fibre. A bunch of fibres is illuminated by one LED and distributes the light to several crystals. Initially, for every crystal the amount of light arriving through the respective fibre is calibrated relatively to a source once.

The main components of the LED system are

- a LED as light source whose light resembles the scintillation light from the CsI(Tl) crystals;
- a control to vary of the length of the light pulses;
- a bunch of optical fibres to distribute the light to the crystals;
- a reference system to monitor the stability of the LED light source.

The subsequent readout and the analysis procedure for the light from the LED system coupled to the crystal is identical to the readout of "real" scintillation light. No particular trigger is required.

Technical implementation

The LED light calibration system will use standard components benefiting from the technological progress made in this field.

Nowadays, high power LEDs are widely available with a brightness of several 100 lm (1 lm = 1 cd·sr). At the nominal wave length of 555 nm 1 lm corresponds to about $4 \cdot 10^9$ photons/μs. Hence, a LED with 100 lm can provide the photons to calibrate about 800 crystals emulating an energy deposit of 100 MeV per crystal. Here, being very conservative it is assumed that only around 1% of the initial photons are coupled into the crystal. Such LEDs can simply be arranged in arrays to increase the power and even LEDs with different colours to better model the scintillation light of CsI(Tl) can be used. However, standard green LEDs ($\lambda_{\text{Peak}} = 525$ nm) are already near to the peak wave length of CsI(Tl). The power consumption of such LEDs is in the order of several Watts and

a passive cooling is foreseen. The amount of photons per pulse can be controlled by the length of the signal generated by the pulse generator.

Although industrial suppliers offer custom made bundles containing more than 1500 optical fibres, e.g. for imaging applications, we foresee the use of standard cables containing a smaller amount of fibres, such as 12, 24, or 48. The light from the LED will be focused by a lens on such a cable. The cable, e.g. containing 48 fibres, is then split in a passive split box and the light of each fibre focused on the next cable with e.g. 12 or 24 fibres. In a second split box this cable is then split to single fibres connected to the crystals. The use of lenses decreases the light losses in the split boxes. Standard optical cables with SC connectors will be used. Compared to a single custom made bundle containing many fibres this modular solution offers several advantages:

- lower price because of the use of standard parts;
- stepwise construction and adaptation to the geometry of the Demonstrator and the final CALIFA array;
- easy and inexpensive replacement of broken fibres;
- easy extension to the CALIFA EndCap if also CsI(Tl) crystals will be used.

The split boxes will be equipped with optical switches allowing to send the light signals only to groups of crystals in order not to generate a readout of the whole CALIFA array in one event.

An essential element of the light monitoring system is a stable reference photodetector with good sensitivity. In order to assure such a stable reference, the electronics circuit controlling the LED can be stabilised to compensate e.g. effects from a variation in temperature. However, in our concept the final reference will be a reference detector. A small CsI(Tl) crystal will be irradiated by both a radioactive source and one fibre illuminated by the LED. The crystal is then readout by a small standard photomultiplier. The signals will be fed into the DAQ as one additional channel. In this way, the light emission from the LED is continuously monitored by detecting its light as well as radiation with well-known properties, i.e. γ rays and/or α-particles, with the same detector at the same time. CMS monitors the amount of light emitted by the light distribution system simply by photo diodes. However, photo diodes are, to a small amount, sensitive to external conditions, e.g. temperature, this is considered as not precise enough for CALIFA. Fig. 9.4 demonstrates the principal concept of the LED reference for CALIFA. In the final version, as described above one fibre will illuminate the reference crystal. For practical reasons, in this first implementation a CALIFA prototype is used as crystal.

One reference system will be sufficient to monitor all crystals of CALIFA. Only one longer optical cable connecting both halves of the array is needed allowing to open the array without uncabling any of the devices.

As the whole system sits outside of CALIFA no requirements for the components concerning radiation hardness are necessary.

10. Infrastructure

Different mounting procedures have been foreseen for the Demonstrator and for the CALIFA Barrel. The Demonstrator is equipped with a flexible structure that can be mounted directly in the final detector position (Cave C). The size and weight of this structure allows its installation allowing for the main entrance of the cave. The different petals (previously mounted with the corresponding detector units) could be mechanically installed in the final detector position. Thus, no specific mounting infrastructure is needed for the demonstrator.

As was previously presented in Chapter 6, a dedicated support structure is foreseen for CALIFA Barrel. This structure includes rails for a linear slide system, mounted on the cave floor that allows the detector to be split into two halves. The crystals will be assembled together with the inner and cover structures, held by the gantry in a dedicated area located close to Cave C. This area covered with a tent is currently used as an R^3B detector room. It will be equipped with an additional dry air and filter system to provide a sufficiently clean environment. This additional infrastructure will be contributed by the collaboration. The individual halves mentioned above have a maximum weight of 4200 kg and a volume of 1.8 m (length) x 2.6 m (width) x 3.2 m(height).

A parking position close to the cave wall is foreseen for larger modifications at the target area. For an easy transport of the detector inside the cave, four wheels could be temporarily attached to each of the support frames as discussed in Chapter 11.

The CALIFA detectors are sensitive to temperature changes and excessive humidity. As described in Chapter 6 the preamplifier modules will be directly connected to the detector part of the CALIFA Barrel. Due to the temperature sensitivity of the APD sensors used, the temperature has to be stabilized slightly below room temperature; at around 18 - 23° C. The low power front-end electronics have an average power consumption of 100mW per channel. Including the slow control this leads to a total power dissipation of 260 W close to the detectors. Even though this is a small number, special care is taken to ensure that the massive aluminium outer shell of the Barrel is maintained at a constant temperature by a dedicated air cooling system. Removable tubes will guide pre-cooled dry air close to the separation lines of the tiles of which the outer shell of the detector is comprised. A special heat exchanger with flow regulation will decouple the cooling air temperature from fluctuation with the standard 12° C cooling water in the cave. Here the normal air will be filtered, dried during the heat exchange and than again reheated to provide a constant temperature air flow. The residual amounts of condensation water are returned to the hall air space via a small heater. To keep the inner part of the detector Barrel below the recommended humidity level of 10% a small flow of less than 1000 litre per hour of dry nitrogen will be used. Here a connection to the low pressure Nitrogen line fed by the outside LN_2 tank is needed in the target area.

The power consumption, and thus the heat dissipation, of the digital electronics mounted at a distance of 2 meters on the CALIFA support will be about 2 W/ch. Together with

the 2 kW from the data acquisition computers and another 1 kW from the slow control PCs, this amounts to 7 kW in total for the full CALIFA Barrel. Standard air cooling of the cave will be used for this part.

Data acquisition for the CALIFA Barrel in total will need 5 kW of installed electric power on each side of the target area. For the data transport the use of eight lines of standard glass fibre GBit Ethernet connections and 8 lines of Cat5 Ethernet connections are foreseen. For monitoring also 20 x RG-58 cables with BNC connectors should be installed. In addition, a connection to the BuTiS/White Rabbit time stamping system, developed in the NUSTAR-DAQ common working group, must be installed in close proximity.

11. Installation procedure

Crystals and APDs are delivered to the institutes of the CALIFA collaboration and individually tested as described in Chapter 8. The crystals and APD with sufficient quality will be mounted together in detector modules: the crystals will be wrapped and APDs connected and cabled in order to form independent single detector modules. The quality of those modules will be checked, in particular the light uniformity and absolute light output will be measured for each module.

The CALIFA demonstrator consists of 8 petals which are a fraction of the forward part of the Barrel of CALIFA (see Chapter 6). The detector modules are then gathered to form the petals. A final test is performed in the institutes using sources.

Those petals will be transported from the institutes to the site of GSI/FAIR. The petals will be tested upon arrival to check for any damage that may have occurred during transportation. Using the available petals, the CALIFA demonstrator (see section 6.3) will be assembled and tested in the detector room adjacent to the Cave C. The transport of this light weight device into cave C will be performed on small wheels mounted to the four corners of the support through the single-level experimental hall.

Further crystals and APDs will follow a similar procedure before being transported to the GSI/FAIR site as petals. After the first experiment campaign, the demonstrator will be moved back to the detector room and the petals will be removed. Those petals, together with those newly available, will be assembled to complete the first half of the CALIFA Barrel. When this is achieved, it will be tested first in the detector room, already mounted complete with readout electronics on the support frame. This complete unit will be moved to the experimental area and used in first experiments with already good efficiency for low- and medium energy γ-rays as well as proton detection. An option to avoid an extra opening of the roof of Cave C is floor transport via the standard hall crane. Here the support will be equipped with additional 2 m long extender bars close to floor level to form a square shaped foot print with the detector mass centred. At the four corners heavy load wheels (2 tons each) are mounted to ensure a smooth ride on the plane floor of the experimental hall. This method will be also used later for optional transports inside the cave. A thread based levelling system between the wheel bars and the support frame will be used to pass the support frame to the rail sockets where it will be tightly fixed.

The same procedure will be used for the second half of the Barrel. After individual testing with sources and other calibration procedures (as described in section 9), the detector will be commissioned with beam.

The precise position of the CALIFA Barrel within the cave and relative to the beam line is checked using fixed points on the mounting structure (see section 6.2).

12. Time schedule and organisation

We summarize in this Chapter the present organisation of the CALIFA Working Group (CWG) and the time schedule for the CALIFA project. For simplicity, we show here only names of participant institutes with the coordinates of a contact person.

12.1. Time schedule and Milestones

The construction of the CALIFA calorimeter plans to follow different phases. Firstly, we differentiate between the forward angular section or Forward EndCap and the most backward angular section or Barrel. This documents addresses uniquely the construction of the CALIFA Barrel. Different construction phases are also foreseen for the Barrel. The most important one consists on the construction of a CALIFA Barrel Demonstrator that will represent 20% of the final detector. The approximately 500 detection units (CsI(Tl), LAAPD and associated electronics) that will form the Demonstrator will be also incorporated into the final CALIFA Barrel.

The CALIFA Barrel production plan is done under the assumption of about 16 alveoli (64 detection units) per month. As the Barrel amounts to 512 alveoli, a total of 32 months will be necessary. Considering that a certain time (3 months) will be necessary for the startup of production lines by the different producers and also for the final detector installation at the FAIR site (4 months) we can conclude that 3 years and 3 months will be necessary for the full installation of CALIFA Barrel. The starting point for the construction will only be possible after the green light of the financing commitments[1] by the different funding agencies involved and the corresponding invitation to tender and order placing.

Assuming that the first financing commitments will be for Q3/2012 we can define the following milestones.

1. Demonstrator (20% of detector) ready for Q1/2014
2. Physics experiment with the Barrel Demonstrator in 2014 in Cave C at GSI
3. Full CALIFA Barrel ready for Q1/2016
4. Physics experiment with full CALIFA Barrel in 2016 in Cave C at GSI

In a longer time schedule we can define the milestones that would complete the full CALIFA detector

1. CALIFA Forward EndCap TDR approved by Q1/2014, start construction of Forward EndCap section
2. Final detector moved to R^3B Hall in Q4/2016

[1] At least partially.

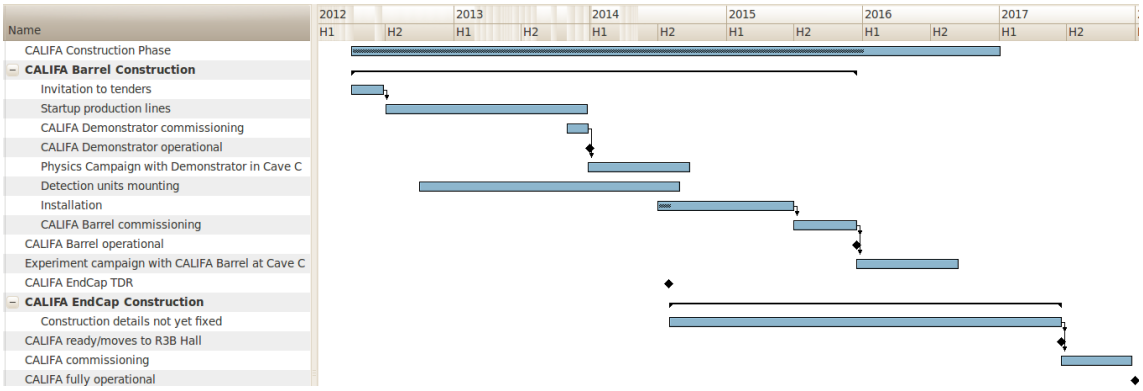

Figure 12.1.: Time schedule of CALIFA calorimeter

3. CALIFA fully operational for physics experiments in 2018

Fig. 12.1 summarises the time schedule of CALIFA Barrel including the most important milestones mentioned above.

12.2. Organisation and responsibilities

The R&D work summarised in this document has been shared between several institutions in five different countries. The R^{3}B participants in this working group are:

USC Universidad de Santiago de Compostela
H. Alvarez-Pol, J. Benlliure, D. Cortina-Gil, I. Duran, M. Gascón, D. González, N. Montes, B. Pietras, P. Cabanelas

IEM Instituto Estructura de la Materia, CSIC Madrid
M.J.G. Borge, O. Tengblad, E.Nacher, A. Perea, M. Carmona Gallardo, JA. Briz, J. Sanchez, J. Sanchez del Rio.

Chalmers Chalmers University of Technology, Göteborg
A. Heinz, H.T. Johansson, T. Nilsson and R. Thies

Lund Lund University
V. Avdeichikov, J. Cederkäll, P. Golubev, B. Jakobsson, D. Di Julio

GSI Helmholtzzentrum für Schwerionenforschung, Darmstadt
D. Bertini, J. Gerl, M. Heil, G. Ickert, H. Simon

Frankfurt Goethe University Frankfurt am Main
R. Reifarth

TUM Technische Universität München
M. Bendel, M. Boehmer, M. Dierigl, R. Gernhäuser, W. Henning, R. Kruecken [2], F. Kurz, T. Le Bleis, M.Winkel, S.Winkler

UVigo Universidad de Vigo
E. Casarejos, C. Parrilla, P. Yañez, J.A. Vilán

CFNUL Centro de Física Nuclear da Universidade de Lisboa
D. Galaviz, P. Teubig

[2] Also affiliated to TRIUMF.

EMMI Extreme Matter Institute and Research Division, GSI
E. Fiori, B. Löher, D. Savran
JINR Joint Institute for Nuclear Research, Dubna
V. Avdeichikov, A. Bezbakh, A. Fomichev, M. Golovkov, A. Gorshkov, S. Krupko, S. Sidorchuk
NRC Nuclear Reseach Center, Kurchatov Institute Moscow
L. Chulkov
TUD Technische Universität Darmstadt
T. Aumann, N. Pietralla, T. Bloch, A. Ignatov, Th. Kröll, M. von Schmid, F. Wamers, L. Schnorrenberger

The responsibilites of design and construction of the CALIFA Barrel detector have been shared among the active Working group members. The following diagram summarises the present situation.

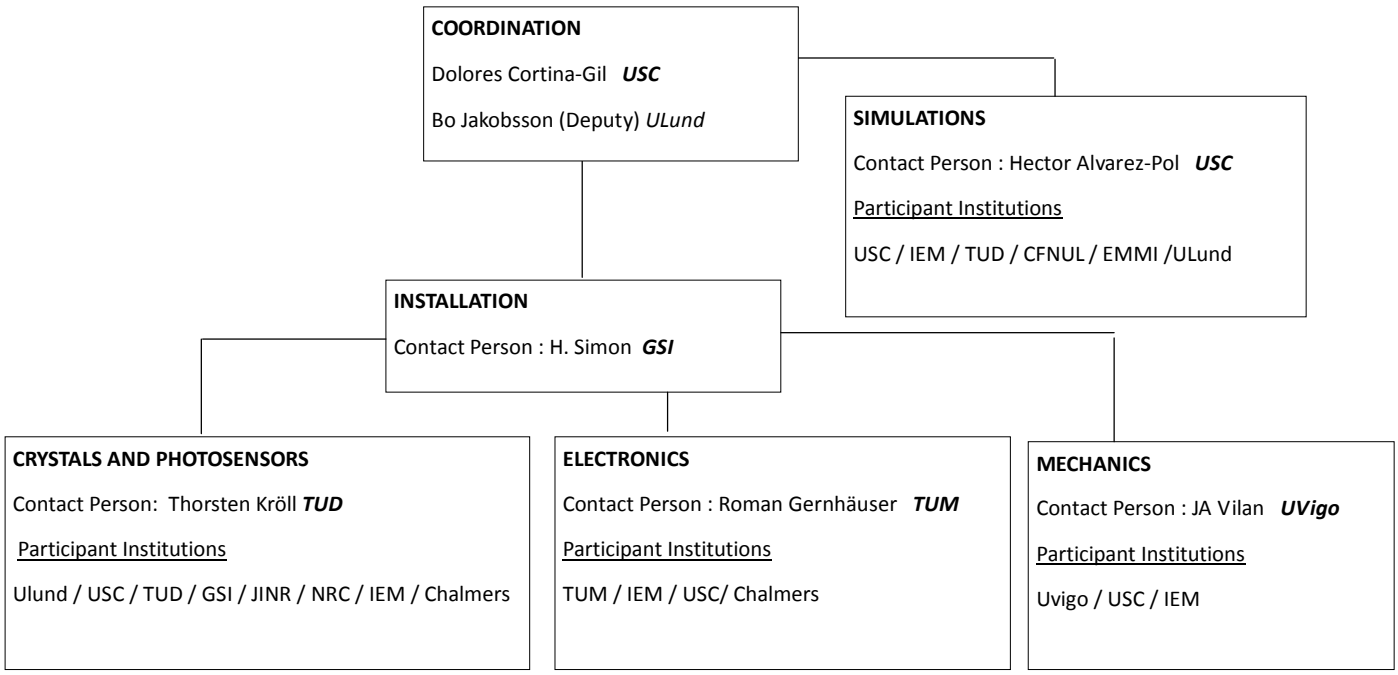

A. List of Experiments

This appendix briefly describes a set of experiments performed in different European facilities, and making use of different prototypes (introduced in Appendix B).
Those tests have been of extreme help to validate the technical viability of the requirements imposed to the detector, particularly in terms of final energy resolution.

- High energy γ rays at CMAM. Centro de Microanálisis de Materiales (CMAM) in Madrid (Spain), consisting of a 5 MV Cockroft-Walton accelerator where protons at 1 MeV were used to produce the reactions ^{19}F(p,γ)^{16}O and ^{7}Li(p,γ)^{8}Be, using a Teflon target (containing LiF). In these reactions, 6.1 and 17.6 MeV γ rays (the first excited states of ^{16}O and ^{8}Be) were produced.
- High energy γ rays at NEPTUN: To extend the investigations to higher photon energies up to 20 MeV the NEPTUN tagger at the superconducting electron accelerator S-DALINAC operated at the TU Darmstadt is an ideal facility [SLG+10]. For the Technische Universität Darmstadt (TUD) in Darmstadt (Germany), in the NEPTUN facility, the electrons collide against a thin target (radiator), producing γ rays by Bremsstrahlung radiation The tagging technique provides the possibility to select single well defined photon energies ($\Delta E \leq 50$ keV) out of a continuous Bremsstrahlung spectrum. By changing the tagging conditions the energy can be freely tuned in the region between 2 MeV and 20 MeV.
- High energy protons at Uppsala: The Svedberg-laboratoriet (TSL) in Uppsala (Sweden), proton accelerator can reach energies up to 200 MeV. Two different proton energies: about 180 and 120 MeV were explored. In this particular setup, a rather thick Double Sided Silicon Strip detector (2 mm) was located prior to the prototype.
- High energy protons at KVI: Two CsI(Tl) crystals have been irradiated by protons with an initial energy of 135 MeV. The energy has been attenuated stepwise by introducing an active degrader (two thin DSSSDs and two thick Si(Li) detectors) or a passive degrader (Al block). Aim was to determine the linearity of the light output as function of the energy of the impinging protons. The DSSSDs allowed for a tracking of the impinging protons for two energies. A study of protons scattered between the CsI(Tl) crystals and the add-back properties was possible.
- High energy γ rays and low energy protons in Munich: The Tandem accelerator at Technische Universität München was also used to produce high-energy γ rays and low energy protons. A $\sim$ 24 MeV high-intensity proton beam was used on a range of ^{12}C, plastic and deuterated plastic targets. Aims of the experiment included the observation of high energy γ rays scattering throughout adjacent crystals, for example the 4.44 and 15.11 MeV γ rays released during the de-excitation of the 2^+ and 1^+ excited states of ^{12}C. Data on the interaction of elastically scattered protons (with energies around 15 MeV) impinging on the prototypes were also recorded.

B. Tests of photosensors

Rather thorough investigations have been conducted during the evaluation of the different photosensors systems, as mentioned in Chapter 3. Results obtained in the tests of photomultiplers and photodiodes are presented here.

B.1. Photomultipliers

Photomultipliers are the most commonly used photosensors in experimental nuclear physics. It was consequently the first type to be evaluated.

B.1.1. Magnetic Field Sensitivity

A PMT shielded with multiple layers of μ-metal can keep the detector operational in magnetic fields up to 30-50 mT. To be effective the shield has to extend to 1-1.5 times the diameter of the PMT beyond the photocathode plane. For the GLAD magnet the fringe field will be below 20 mT at 30 cm distance from the magnet entrance. PMTs could therefore be a valid option for the central and backward angle section of the Barrel if a proper mechanical design could be applied.

B.1.2. Photomultiplier Tests

Three types of PMTs were tested that fit the geometry of the CALIFA CsI(Tl) element [A$^+$c] (see Table B.1). The only difference between the two PMTs of the R7400 type in Table B.1 is their QE, which is 7.5% and 16.5%, respectively. A higher QE results in an improved energy resolution. The energy resolution measured using the PMTs given in Table B.1 is shown in Fig. B.1. The end surface of the crystal light guide was 10x10 mm^2. ESR film was applied to cover the part of the light guide not covered by the PMT's sensitive area. At 662 keV the resolution is close to 10% for the three cases.

Table B.1.: Characteristics of tested PMTs.

	$R7400U-03$	$R7400U-20$	$R4124$
Active diameter (mm)	8	8	10
Dark current (nA)	0.2	2-5	1-5
QE (% at 560 nm)	4.5	16.5	7.5
Immunity to magnetic field	no	no	yes

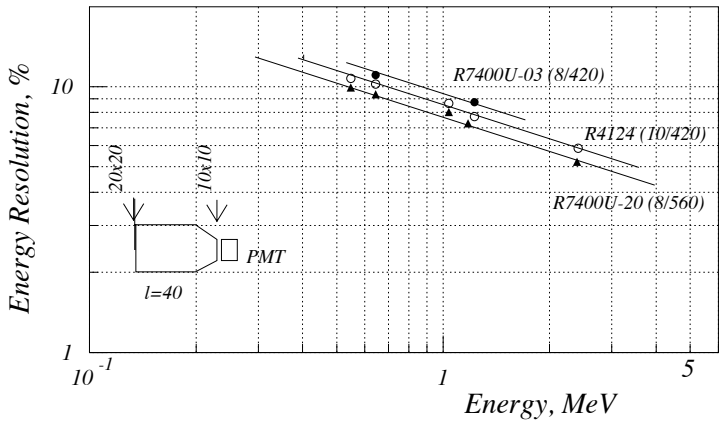

Figure B.1.: The energy resolution of a CsI(Tl) element measured by the PMTs.Numbers in brackets denote the photocathode diameter (mm)/peak wavelength (nm).

Photosensor type	PD S3590
Active area (mm^2)	10x10
C (pF)	35
QE (560 nm,%)	85
I_d (nA at 25^o)	1-10
Gain	1

Table B.2.: Summary of properties of the PD S3590 by Hamamatsu Co.

Recently Hamamatsu Co. has developed a Hybrid Photon Detector [SBB+09] with a 18 mm GaAsP photocathode with a peak QE $> 50\%$ at 560 nm. Extended magnetic field insensitive photo-triodes and photo-tetrodes are also under development by Electron Co. [NRI]. Application of a hybrid photon detector for a magnetic field insensitive PMT could be of interest for future long-term developments of the CALIFA system.

B.2. Photodiodes

Due to photomultiplier sensitivity to magnetic field, photodiodes were also investigated.

B.2.1. Background

PIN photodiodes (PDs) are insensitive to magnetic field and they are well matched to the spectral response of CsI(Tl). They have low operation voltage and are stable to voltage and temperature variations. Their disadvantage is that the electronic noise of the

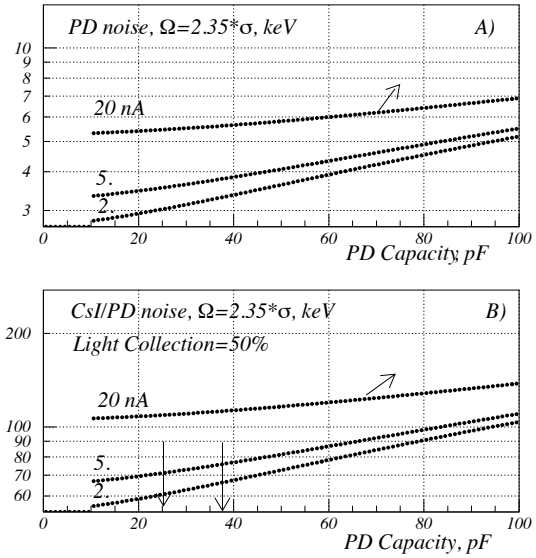

Figure B.2.: (A): The PD preamplifier noise as a function of the PD capacity and dark current for the time constant, $\tau = 2$ μs. (B): CsI(Tl)/PD effective noise FWHM when the light collection from the CALIFA element is about 50%.

PD/preamplifier system defines the energy resolution for low energy γ-rays [A+d]. Table B.2 summarizes some of the important characteristics for the PD S3590 made by Hamamatsu Co. The typical dark current for this PD is 1-10 nA at 25° and the capacitance, 35 pF.

B.2.2. Electronic Noise

The Equivalent Noise Charge (ENC) gives the number of electrons that has to be collected from a Si-sensor in order for the signal to be equal to the noise level. For the PD/preamplifier system the ENC can be expressed as:

$$ENC^2 = 43(C_d + 15)^2/\tau + 8\tau(I_d + 800) + 50000$$

where ENC is in eV, C_d is the PD capacity in pF, τ the shaping constant of the main amplifier in μs, and I_d is the detector current in pA. The PD noise is shown in the upper panel of Fig. B.2 as a function of PD capacity.

The energy of a detected γ-ray, that creates a charge equal to the ENC, can be calculated in the following way. If the number of light quanta produced per MeV of deposited energy is taken to be $60 \cdot 10^3$, the light collection efficiency to be 80% and the QE of the PD to be 75%, then a 1 MeV γ-ray, that deposits its full energy in the crystal, will create $36 \cdot 10^3$ photons that are registered by the PD [MSKB02]. With an e-h creation energy of 3.5 eV for Si, the equivalent detected energy is 130 keV. This calculation can be used to correlate a noise level given by ENC to the energy of an incoming photon that deposits its full energy in the crystal, i.e. to the effective noise level. For a CALIFA element using a photosensor with an active area of 10x10 mm^2, 44-50% of the primary light can be collected. This

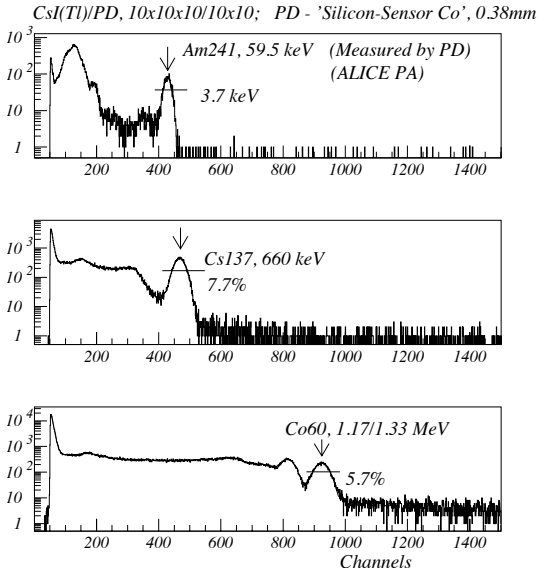

Figure B.3.: PH4: The ^{241}Am X-ray spectrum measured by the PD (the energy scale is 0.14 keV/channel) and γ-ray spectra of ^{137}Cs and ^{60}Co sources measured by a 1 cm^3 CsI(Tl)/PD detector.

results in an effective noise (FWHM) of ∼60 keV. The graph for a 50% collection efficiency is given in the lower panel of Fig. B.2.

Measurements were made using a 1 cm^3 CsI(Tl)/PD detector. The energy scale was calibrated using a ^{241}Am X-source (see Fig. B.3). The energy resolution obtained for the PD detector, 3.7 keV, is completely defined by the detector/preamplifier noise for a shaping time constant of 2.0 μs (1.0 nA dark current). The noise input to the energy resolution can be approximated as 3.7 keV/59.5 keV=6.2% when 80% of the light is collected by the PD. As seen from Fig. B.2 the electronic noise arising from the PD capacitance and leakage current dominates the energy resolution at low γ-ray energy.

The electronic noise measured for the CsI(Tl)/PD element restricts its application as photosensor for CALIFA for the following reasons. The energy resolution of a single element is low, especially for low-energy γ-rays. The low-energy threshold for γ-ray energy registration in a single element, given by $E_{th} = 2 \cdot \Omega$, with Ω the FWHM noise, would be on the level of about 120 keV. The electronic noise for a number, n, of fired elements is, Ω_n=$\Omega \cdot \sqrt{n}$. For $E_\gamma = 1$ MeV the average number of fired elements is equal to 2.6. The noise level, after add-back, would be $60 \cdot \sqrt{2.6} \simeq 100$ keV and the threshold near 200 keV.

References

[3M] 3M. Display films. http://vikuiti.com.

[A+a] V. Avdeichikov et al. CALIFA CWG Meeting, 30.09.2009. http://fpsalmon.usc.es/r3b/videoConf160408/presents/CWG080416VA.pdf.

[A+b] V. Avdeichikov et al. R3B/EXL CWG Meeting, Milano, 2007. http://fpsalmon.usc.es/r3b/internal00001.shtml.

[A+c] V. Avdeichikov et al. CALIFA CWG Meeting, GSI, 30.01.2008. http://fpsalmon.usc.es/r3b/videoConf220908/download.shtml.

[A+d] V. Avdeichikov et al. CALIFA CWG Meeting, GSI, 16.10.2007. http://fpsalmon.usc.es/r3b/videoConfGSI0907/presentations.shtml.

[A+08] C. Amsler et al. Review of Particle Physics. *Phys. Lett.*, B667:1–1340, 2008.

[AAA+03] S. Agostinelli, J. Allison, K. Amako, J. Apostolakis, H. Araujo, P. Arce, M. Asai, D. Axen, S. Banerjee, G. Barrand, F. Behner, L. Bellagamba, J. Boudreau, L. Broglia, A. Brunengo, H. Burkhardt, S. Chauvie, J. Chuma, R. Chytracek, G. Cooperman, G. Cosmo, P. Degtyarenko, A. Dell'Acqua, G. Depaola, D. Dietrich, R. Enami, A. Feliciello, C. Ferguson, H. Fesefeldt, G. Folger, F. Foppiano, A. Forti, S. Garelli, S. Giani, R. Giannitrapani, D. Gibin, J. J. Gómez Cadenas, I. González, G. Gracia Abril, G. Greeniaus, W. Greiner, V. Grichine, A. Grossheim, S. Guatelli, P. Gumplinger, R. Hamatsu, K. Hashimoto, H. Hasui, A. Heikkinen, A. Howard, V. Ivanchenko, A. Johnson, F. W. Jones, J. Kallenbach, N. Kanaya, M. Kawabata, Y. Kawabata, M. Kawaguti, S. Kelner, P. Kent, A. Kimura, T. Kodama, R. Kokoulin, M. Kossov, H. Kurashige, E. Lamanna, T. Lampén, V. Lara, V. Lefebure, F. Lei, M. Liendl, W. Lockman, F. Longo, S. Magni, M. Maire, E. Medernach, K. Minamimoto, P. Mora de Freitas, Y. Morita, K. Murakami, M. Nagamatu, R. Nartallo, P. Nieminen, T. Nishimura, K. Ohtsubo, M. Okamura, S. O'Neale, Y. Oohata, K. Paech, J. Perl, A. Pfeiffer, M. G. Pia, F. Ranjard, A. Rybin, S. Sadilov, E. D. Salvo, G. Santin, T. Sasaki, N. Savvas, Y. Sawada, S. Scherer, S. Sei, V. Sirotenko, D. Smith, N. Starkov, H. Stoecker, J. Sulkimo, M. Takahata, S. Tanaka, E. Tcherniaev, E. S. Tehrani, M. Tropeano, P. Truscott, H. Uno, L. Urban, P. Urban, M. Verderi, A. Walkden, W. Wander, H. Weber, J. P. Wellisch, T. Wenaus, D. C. Williams, D. Wright, T. Yamada, H. Yoshida, and D. Zschiesche. G4–a simulation toolkit. *Nuclear Instruments and Methods in Physics Research Section A: Accelerators, Spectrometers, Detectors and Associated Equipment*, 506(3):250 – 303, 2003.

[ABI+05] D. Aleksandrov, S. Burachas, M. Ippolitov, V. Lebedev, V. Manko, S. Nikulin, A. Nyanin, I. Sibiriak, A. Tsvetkov, A. Vasiliev, A. Vinogradov, M. Bogolyubsky, Y. Kharlov, S. Konstantinov, V. Petrov, B. Polishchuk, S. Sadovsky, V. Senko, A. Soloviev, V. Victorov, A. Vodopianov, P. Nomokonov, V. Basmanov, D. Budnikov, R. Ilkaev, A. Kuryakin, S. Nazarenko, V. Punin, Y. Vinogradov, H. Delagrange, Y. Schutz, G. Balbestre, J. Diaz, A. Klovning, O. Mæland, O. Odland, B. Pommersche, D. Röhrich, Z. Yin, B. Skaali, D. Wormald, J. Mares, K. Polak, A. Deloff, T. Dobrowolski, K. Karpio, M. Kozlowski, K. Redlich, T. Siemiarczuk, G. Stefanek, L. Tykarski, G. Wilk, T. Sugitate, K. Shigaki, and R. Kohara. A high resolution electromagnetic calorimeter based on lead-tungstate crystals. *Nuclear Instruments and Methods in Physics Research Section A: Accelerators, Spectrometers, Detectors and Associated Equipment*, 550(1-2):169 – 184, 2005.

[ACD+06] V. Andreev, J. Cvach, M. Danilov, E. Devitsin, V. Dodonov, G. Eigen, E. Garutti, Y. Gilitzky, M. Groll, R.-D. Heuer, M. Janata, I. Kacl, V. Korbel, V. Kozlov, H. Meyer, V. Morgunov, S. Němeček, R. Pöschl, I. Polák, A. Raspereza, S. Reiche, V. Rusinov, F. Sefkow, P. Smirnov, A. Terkulov, Š. Valkár, J. Weichert, and J. Zálešák. A high-granularity plastic scintillator tile hadronic calorimeter with APD readout for a linear collider detector. *Nuclear Instruments and Methods in Physics Research Section A: Accelerators, Spectrometers, Detectors and Associated Equipment*, 564(1):144 – 154, 2006.

[Aea] V. Avdeichikov et al. GSI Sci. Report 2008, p.218.

[AJ05] T. Aumann and B. Jonson. Technical Proposal for the design, construction, commissioning and operation of R3B, a universal setup for kinematical complete measurements of Reactions with Relativistic Radioactive Beams. Technical report, The R3B collaboration, 2005.

[AJN+01] V. Avdeichikov, B. Jakobsson, V. A. Nikitin, P. V. Nomokonov, and E. J. van Veldhuizen. On-beam calibration of the ΔE(Si)-Sci/PD charged particle telescope. *Nuclear Instruments and Methods in Physics Research Section A: Accelerators, Spectrometers, Detectors and Associated Equipment*, 466(3):427 – 435, 2001.

[AKF+05] P. Adrich, A. Klimkiewicz, M. Fallot, K. Boretzky, T. Aumann, D. Cortina-Gil, U. D. Pramanik, T. W. Elze, H. Emling, H. Geissel, M. Hellström, K. L. Jones, J. V. Kratz, R. Kulessa, Y. Leifels, C. Nociforo, R. Palit, H. Simon, G. Surówka, K. Sümmerer, and W. Waluś. Evidence for Pygmy and Giant Dipole Resonances in ^{130}Sn and ^{132}Sn. *Phys. Rev. Lett.*, 95:132501, Sep 2005.

[APBC+08] H. Alvarez-Pol, J. Benlliure, E. Casarejos, D. Cortina, I. Durán, and M. Gascón. Design studies and first crystal tests for the R3B calorimeter: Proceedings of the XVth International Conference on Electromagnetic Isotope Separators and Techniques Related to their Applications. *Nuclear Instruments and Methods in Physics Research Section B: Beam Interactions with Materials and Atoms*, 266(19-20):4616–4620, 2008.

[BBB+04] D. Bédéréde, E. Bougamont, P. Bourgeois, F. X. Gentit, Y. Piret, and G. Tauzin. Performances of the CsI(Tl) detector element of the GLAST calorimeter. *Nuclear Instruments and Methods in Physics Research Section A: Accelerators, Spectrometers, Detectors and Associated Equipment*, 518(1-2):15 – 18, 2004. Frontier Detectors for Frontier Physics: Proceedings.

[BBG+09] J. Bergtröm, E. Blomberg, E. Gallneby, J. Hagdahl, M. Nordström, and H. Wittler. BSc. thesis, 2009.

[BBL+09] A. Badalá, F. Blanco, P. La Rocca, F. Librizzi, G. S. Pappalardo, C. Petta, A. Pulvirenti, and F. Riggi. Prototype and mass production tests of avalanche photodiodes for the electromagnetic calorimeter in the alice experiment at lhc. *Nuclear Instruments and Methods in Physics Research Section A: Accelerators, Spectrometers, Detectors and Associated Equipment*, 610(1):200 – 203, 2009. New Developments In Photodetection NDIP08, Proceedings of the Fifth International Conference on New Developments in Photodetection.

[BCHM] R. Brun, F. Carminati, I. Hrivnacova, and A. Morsch. The Virtual Monte Carlo Computing in High Energy and Nuclear Physics, 2003, 24-28 March 2003, La Jolla, California.

[Ben10] M. Bendel. Entwicklung und Test einer digitalen Auslese für das CALIFA-Kalorimeter. diploma thesis, Technische Universität München, 2010.

[Ber09] D. Bertini for the R3B Collaboration. R3BRoot: a ROOT based Simulation and Analysis framework for R3B, 2009.

[BFL+94] M. Bosetti, C. Furetta, C. Leroy, S. Pensotti, P. G. Rancoita, M. Rattaggi, M. Redaelli, M. Rizzatti, A. Seidman, and G. Terzi. Effect on charge collection and structure of n-type silicon detectors irradiated with large fluences of fast neutrons. *Nuclear Instruments and Methods in Physics Research Section A: Accelerators, Spectrometers, Detectors and Associated Equipment*, 343(2-3):435 – 440, 1994.

[BG71] H. W. Bertini and M. P. Guthrie. News item results from medium-energy intranuclear-cascade calculation. *Nuclear Physics A*, 169(3):670 – 672, 1971.

[BGGR+94] J. Bea, A. Gadea, L. M. Garcia-Raffi, J. Rico, B. Rubio, and J. L. Tain. Simulation of light collection in scintillators with rough surfaces. *Nuclear Instruments and Methods in Physics Research Section A: Accelerators, Spectrometers, Detectors and Associated Equipment*, 350(1-2):184 – 191, 1994.

[BMTKU08] D. Bertini, M.A.-Turany, I. Koenig, and F. Uhlig. The FAIR simulation and analysis framework. *Journal of Physics: Conference Series*, 119(3):032011, 2008.

[BRQ05] D. Britton, M. Ryan, and X. Qu. Light collection uniformity of lead tungstate crystals for the cms electromagnetic calorimeter. *Nuclear Instruments and Methods in Physics Research Section A: Accelerators, Spectrometers, Detectors and Associated Equipment*, 540(2-3):273 – 284, 2005.

[BY-] BY-ND. CMake - Cross Platform Make. http://www.cmake.org/.

[CGFVA+04] D. Cortina-Gil, J. Fernandez-Vazquez, T. Aumann, T. Baumann, J. Benlliure, M. J. G. Borge, L. V. Chulkov, U. Datta Pramanik, C. Forssén, L. M. Fraile, H. Geissel, J. Gerl, F. Hammache, K. Itahashi, R. Janik, B. Jonson, S. Mandal, K. Markenroth, M. Meister, M. Mocko, G. Münzenberg, T. Ohtsubo, A. Ozawa, Y. Prezado, V. Pribora, K. Riisager, H. Scheit, R. Schneider, G. Schrieder, H. Simon, B. Sitar, A. Stolz, P. Strmen, K. Sümmerer, I. Szarka, and H. Weick. Shell Structure of the Near-Dripline Nucleus ^{23}O. *Phys. Rev. Lett.*, 93:062501, Aug 2004.

[CMS97] CMS. - ECAL, Technical Design Report, CERN/LHCC 97-33, 1997.

[col01] T. F. collaboration. FAIR CDR - An International Accelerator Facility for Beams of Ions and Antiprotons, Conceptual Design Report. Technical report, GSI, 2001.

[DAC+09] D. D. DiJulio, V. Avdeichikov, J. Cederkall, P. Golubev, B. Jakobsson, H. Johansson, and C. Tintori. Proton in-beam tests of the Lund calorimeter prototype. *Nuclear Instruments and Methods in Physics Research Section A: Accelerators, Spectrometers, Detectors and Associated Equipment*, 612(1):127 – 132, 2009.

[DGI+00] D. V. Dementyev, M. P. Grigoriev, A. P. Ivashkin, M. M. Khabibullin, A. N. Khotyantsev, Y. G. Kudenko, O. V. Mineev, M. Aoki, J. Imazato, Y. Kuno, T. Baker, M. Blecher, P. Depommier, M. Hasinoff, Y. Igarashi, T. Ikeda, J. A. Macdonald, C. R. Mindas, C. Rangacharyulu, S. Shimizu, and T. Yokoi. CsI(Tl) photon detector with PIN photodiode readout for a kμ3 t-violation experiment. *Nuclear Instruments and Methods in Physics Research Section A: Accelerators, Spectrometers, Detectors and Associated Equipment*, 440(1):151 – 171, 2000.

[EPT+01] J. Eberth, G. Pascovici, H. G. Thomas, N. Warr, D. Weisshaar, D. Habs, P. Reiter, P. Thirolf, D. Schwalm, C. Gund, H. Scheit, M. Lauer, P. van Duppen, S. Franchoo, M. Huyse, R. Lieder, W. Gast, J. Gerl, and K. Lieb. MINIBALL A Ge detector array for radioactive ion beam facilities. *Progress in Particle and Nuclear Physics*, 46(1):389 – 398, 2001.

[FIW04] G. Folger, V. N. Ivanchenko, and J. P. Wellisch. The binary cascade. *The European Physical Journal A - Hadrons and Nuclei*, 21:407–417, 2004. 10.1140/epja/i2003-10219-7.

[GAPB+08a] M. Gascón, H. Alvarez-Pol, J. Benlliure, E. Casarejos, D. Cortina-Gil, and I. Duran. Characterization of large frustum CsI(Tl) crystals for the R3B calorimeter. In *Nuclear Science Symposium Conference Record, 2008. NSS '08. IEEE*, pages 1649 –1654, oct. 2008.

[GAPB+08b] M. Gascón, H. Alvarez-Pol, J. Benlliure, E. Casarejos, D. Cortina-Gil, and I. Duran. Optimization of Energy Resolution Obtained with CsI(Tl) Crystals for the R3B Calorimeter. *Nuclear Science, IEEE Transactions on*, 55(3):1259 –1262, june 2008.

[Gas10] M. Gascón. *Prototype of a new calorimeter for the studies of nuclear reactions with relativistic radioactive beams.* PhD thesis, Universidade de Santiago de Compostela, 2010.

[GG93] A. Georgiev and W. Gast. Digital pulse processing in high resolution, high throughput, gamma-ray spectroscopy: Nuclear Science, IEEE Transactions on. *Nuclear Science, IEEE Transactions on DOI - 10.1109/23.256659*, 40(4):770–779, 1993.

[GGL94] A. Georgiev, W. Gast, and R. M. Lieder. An analog-to-digital conversion based on a moving window deconvolution: Nuclear Science, IEEE Transactions on. *Nuclear Science, IEEE Transactions on DOI - 10.1109/23.322868*, 41(4):1116–1124, 1994.

[GM62] R. Gwin and R. B. Murray. Studies of the scintillation process in CsI(Tl). *IRE Transactions on Nuclear Science*, 9(3):38–32, 1962.

[Gol74] A. S. Goldhaber. Statistical models of fragmentation processes. *Physics Letters B*, 53(4):306 – 308, 1974.

[Gra84] B. C. Grabmaier. Crystal scintillators. *Nuclear Science, IEEE Transactions on*, 31(1):372 –376, feb. 1984.

[Gra08] S. Grape. *PWO Crystal Measurements and Simulation Studies of Lambdabar Hyperon Polarisation for PANDA*. PhD thesis, Department for Physics and Astronomy, Uppsala University, 2008.

[GWW+03] H. Geissel, H. Weick, M. Winkler, G. Münzenberg, V. Chichkine, M. Yavor, T. Aumann, K. Behr, M. Böhmer, A. Brünle, K. Burkard, J. Benlliure, D. Cortina-Gil, L. V. Chulkov, A. Dael, J.-E. Ducret, H. Emling, B. Franczak, J. Friese, B. Gastineau, J. Gerl, R. Gernhäuser, M. Hellström, B. Jonson, J. Kojouharova, R. Kulessa, B. Kindler, N. Kurz, B. Lommel, W. Mittig, G. Moritz, C. Mühle, J. Nolen, G. Nyman, P. Roussell-Chomaz, C. Scheidenberger, K.-H. Schmidt, G. Schrieder, B. Sherrill, H. Simon, K. Sümmerer, N. Tahir, V. Vysotsky, H. Wollnik, and A. Zeller. The Super-FRS project at GSI. *Nuclear Instruments and Methods in Physics Research Section B: Beam Interactions with Materials and Atoms*, 204(0):71 – 85, 2003. 14th International Conference on Electromagnetic Isotope Separators and Techniques Related to their Applications.

[HAC+88] K. H. Hicks, R. Abegg, A. Celler, O. Häusser, R. S. Henderson, N. W. Hill, K. P. Jackson, R. G. Jeppesen, N. S. P. King, M. A. Kovash, R. Liljestrand, C. A. Miller, G. L. Morgan, J. R. Shepard, A. Trudel, M. Vetterli, and S. Yen. Spin-dependent observables for the $^{12}C(p, p'\gamma)$ reaction at 400 mev. *Phys. Rev. Lett.*, 61:1174–1177, Sep 1988.

[Ham] Hamamatsu Photonics. Optical Technology & Opto Electronics - Hamamatsu Photonics. http://jp.hamamatsu.com/products.

[HLN+95] I. Holl, E. Lorenz, S. Natkaniez, D. Renker, C. Schmelz, and B. Schwartz. Some studies of avalanche photodiode readout of fast scintillators. *Nuclear Science, IEEE Transactions on*, 42(4):351 –356, aug 1995.

[Hof11a] J. Hoffmann. *FEBEX 2, preliminary specification.* preliminary specification, 2011.

[Hof11b] J. Hoffmann. *FEBEX 3/16, preliminary specification.* preliminary specification, 2011.

[IKY+03] T. Ikagawa, J. Kataoka, Y. Yatsu, N. Kawai, K. Mori, T. Kamae, H. Tajima, T. Mizuno, Y. Fukazawa, Y. Ishikawa, N. Kawabata, and T. Inutsuka. Performance of large-area avalanche photodiode for low-energy X-rays and [gamma]-rays scintillation detection. *Nuclear Instruments and Methods in Physics Research Section A: Accelerators, Spectrometers, Detectors and Associated Equipment*, 515(3):671–679, 2003.

[IKY+05] T. Ikagawa, J. Kataoka, Y. Yatsu, T. Saito, Y. Kuramoto, N. Kawai, M. Kokubun, T. Kamae, Y. Ishikawa, and N. Kawabata. Study of large area hamamatsu avalanche photodiode in a γ-ray scintillation detector. *Nuclear Instruments and Methods in Physics Research Section A: Accelerators, Spectrometers, Detectors and Associated Equipment*, 538(1-3):640 – 650, 2005.

[IMN] V. Innocente, M. Maire, and E. Nagy. GEANE: Average Tracking and Error Propagation Package.

[KCI+02] R. Kanungo, M. Chiba, N. Iwasa, S. Nishimura, A. Ozawa, C. Samanta, T. Suda, T. Suzuki, T. Yamaguchi, T. Zheng, and I. Tanihata. Experimental Evidence of Core Modification in the Near Drip-Line Nucleus ^{23}o. *Phys. Rev. Lett.*, 88:142502, Mar 2002.

[KE10] N. Kurz and H. Essel. Welcome to MBS. http://www-win.gsi.de/daq/. 2010, http://www-win.gsi.de/daq/.

[Kno10] G. F. Knoll. *Radiation detection and measurement*. John Wiley, Hoboken, N.J, 4 edition, 2010.

[KSI+06] J. Kataoka, R. Sato, T. Ikagawa, J. Kotoku, Y. Kuramoto, Y. Tsubuku, T. Saito, Y. Yatsu, N. Kawai, Y. Ishikawa, and N. Kawabata. An active gain-control system for Avalanche photo-diodes under moderate temperature variations. *Nuclear Instruments and Methods in Physics Research Section A: Accelerators, Spectrometers, Detectors and Associated Equipment*, 564(1):300–307, 2006.

[KSS+05] A. Kudin, E. Sysoeva, E. Sysoeva, L. Trefilova, and D. Zosim. Factors which define the α/γ ratio in CsI:Tl crystals. *Nuclear Instruments and Methods in Physics Research Section A: Accelerators, Spectrometers, Detectors and Associated Equipment*, 537:105 – 112, 2005.

[LAN] LAND Collaboration. The Large Area Neutron Detector. http://www.gsi.de/forschung/kp/kp2/collaborations/land/indexe.html.

[Lew00] B. Lewandowski. Ph.D. thesis, 2000.

[MBKP10] J. Michel, M. Böhmer, G. Korcyl, and M. Palka. *A Users Guide to the HADES DAQ Network*. In house, 2010.

[MCS+02] M. Moszynski, W. Czarnacki, M. Szawlowski, B. L. Zhou, M. Kapusta, D. Wolski, and P. Schotanus. Performance of large-area avalanche photodiodes at liquid nitrogen temperature. *Nuclear Science*, 49(3):971–976, 2002.

[Mes11] Mesytec GmbH & Co. KG. *MPR-16/L datasheet*, v6.4 edition, 2011.

[MGK+09] P. Maierbeck, R. Gernhäuser, R. Krücken, T. Kröll, H. Alvarez-Pol, F. Aksouh, T. Aumann, K. Behr, E. A. Benjamim, J. Benlliure, V. Bildstein, M. Böhmer, K. Boretzky, M. J. G. Borge, A. Brünle, A. Bürger, M. Caamaño, E. Casarejos, A. Chatillon, L. Chulkov, D. Cortina-Gil, J. Enders, K. Eppinger, T. Faestermann, J. Friese, L. Fabbietti, M. Gascón, H. Geissel, J. Gerl, M. Gorska, P. G. Hansen, B. Jonson, R. Kanungo, O. Kiselev, I. Kojouharov, A. Klimkiewicz, T. Kurtukian, N. Kurz, K. Larsson, T. Le Bleis, K. Mahata, L. Maier, T. Nilsson, C. Nociforo, G. Nyman, C. Pascual-Izarra, A. Perea, D. Perez, A. Prochazka, C. Rodriguez-Tajes, D. Rossi, H. Schaffner, G. Schrieder, S. Schwertel, H. Simon, B. Sitar, M. Stanoiu, K. Sümmerer, O. Tengblad, H. Weick, S. Winkler, B. Brown, T. Otsuka, J. Tostevin, and W. Rae. Structure of 55Ti from relativistic one-neutron knockout. *Physics Letters B*, 675(1):22 – 27, 2009.

[MSA+86] C. Miller, A. Scott, R. Abegg, R. Helmer, K. Jackson, M. Whiten, S. Yen, L. Lee, T. Drake, D. Frekers, S. Wong, R. Azuma, L. Buchmann, A. Galindo-Uribarri, J. King, R. Schubank, R. Dymarz, H. V. Geramb, and C. Horowitz. Large angle elastic scattering of 200 Mev protons from 208Pb. *Physics Letters B*, 169(2-3):166 – 170, 1986.

[MSKB02] M. Moszyński, M. Szawlowski, M. Kapusta, and M. Balcerzyk. Large area avalanche photodiodes in scintillation and X-rays detection. *Nuclear Instruments and Methods in Physics Research Section A: Accelerators, Spectrometers, Detectors and Associated Equipment*, 485(3):504 – 521, 2002.

[NRI] NRI Electron. OJSC NRI Electron/Home Page. http://www.electron.spb.ru.

[OWT88] N. Ottenstein, S. J. Wallace, and J. A. Tjon. Elastic scattering of protons by ^{16}O, ^{40}Ca, and ^{208}Pb at 200, 500, and 800 mev: Effects of vacuum polarization and pauli-blocking corrections. *Phys. Rev. C*, 38:2289–2295, Nov 1988.

[RTV] RTV. 681 from Scionix Netherlands.

[SAB+07] C. Sgró, W. B. Atwood, L. Baldini, G. Barbiellini, R. Bellazzini, F. Belli, E. Bonamente, T. Borden, J. Bregeon, A. Brez, M. Brigida, G. Caliandro, C. Cecchi, J. Cohen-Tanugi, A. D. Angelis, P. Drell, C. Favuzzi, Y. Fukazawa, P. Fusco, F. Gargano, S. Germani, N. Giglietto, F. Giordano, T. Himel, M. Hirayama, R. P. Johnson, H. Katagiri, J. Kataoka, N. Kawai, W. Kroeger, M. Kuss, L. Latronico, F. Longo, F. Loparco, P. Lubrano, M. Massai, M. Mazziotta, M. Minuti, T. Mizuno, A. Morselli, D. Nelson, M. Nordby, T. Ohsugi, N. Omodei, M. Ozaki, M. Pepe, S. Rainó, R. Rando, M. Razzano, D. Rich, H. F.-W. Sadrozinski, G. Scolieri, G. Spandre, P. Spinelli, M. Sugizaki, H. Tajima, H. Takahashi, T. Takahashi, S. Yoshida, C. Young, and M. Ziegler. Construction, test and calibration of the glast silicon tracker. *Nuclear Instruments and Methods in Physics Research Section A: Accelerators, Spectrometers, Detectors and Associated Equipment*, 583(1):9 – 13, 2007. Proceedings of the 6th International Conference on Radiation Effects on Semiconductor Materials, Detectors and Devices, RESMDD 2006.

[SAD+04] M. Stanoiu, F. Azaiez, Z. Dombrádi, O. Sorlin, B. A. Brown, M. Belleguic, D. Sohler, M. G. Saint Laurent, M. J. Lopez-Jimenez, Y. E. Penionzhkevich, G. Sletten, N. L. Achouri, J. C. Angélique, F. Becker, C. Borcea, C. Bourgeois, A. Bracco, J. M. Daugas, Z. Dlouhý, C. Donzaud, J. Duprat, Z. Fülöp, D. Guillemaud-Mueller, S. Grévy, F. Ibrahim, A. Kerek, and A. Krasznahorkay. $N = 14$ and 16 shell gaps in neutron-rich oxygen isotopes. *Phys. Rev. C*, 69(3):034312, Mar 2004.

[SBB+09] T. Y. Saito, E. Bernardini, D. Bose, M. V. Fonseca, E. Lorenz, K. Mannheim, R. Mirzoyan, R. Orito, T. Schweizer, M. Shayduk, and M. Teshima. Very high QE HPDs with a GaAsP photocathode for the MAGIC telescope project. *Nuclear Instruments and Methods in Physics Research Section A: Accelerators, Spectrometers, Detectors and Associated Equipment*, 610(1):258 – 261, 2009. New Developments In Photodetection NDIP08, Proceedings of the Fifth International Conference on New Developments in Photodetection.

[SCO+00] E. Sauvan, F. Carstoiu, N. A. Orr, J. C. Angélique, W. N. Catford, N. M. Clarke, M. Mac Cormick, N. Curtis, M. Freer, S. Grévy, C. L. Brun, M. Lewitowicz, E. Liégard, F. M. Marqués, P. Roussel-Chomaz, M. G. S. Laurent, M. Shawcross, and J. S. Winfield. One-neutron removal reactions on neutron-rich psd-shell nuclei. *Physics Letters B*, 491(1-2):1 – 7, 2000.

[SGNB05] V. P. Semynozhenko, B. V. Grinyov, V. V. Nekrasov, and Y. A. Borodenko. Recent progress in the development of CsI(Tl) crystal – Si-photodiode spectrometric detection assemblies. *Nuclear Instruments and Methods in Physics Research Section A: Accelerators, Spectrometers, Detectors and Associated Equipment*, 537(1-2):383 – 388, 2005. Proceedings of the 7th International Conference on Inorganic Scintillators and their Use in Scientific adn Industrial Applications.

[SJW58] R. S. Storey, W. Jack, and A. Ward. The Fluorescent Decay of CsI(Tl) for Particles of Different Ionization Density. *Proceedings of the Physical Society*, 72(1), 1958.

[SLG+10] D. Savran, K. Lindenberg, J. Glorius, B. Löher, S. Müller, N. Pietralla, L. Schnorrenberger, V. Simon, K. Sonnabend, C. Wälzlein, M. Elvers, J. Endres, J. Hasper, and A. Zilges. The low-energy photon tagger NEPTUN. *Nuclear Instruments and Methods in Physics Research Section A: Accelerators, Spectrometers, Detectors and Associated Equipment*, 613(2):232 – 239, 2010.

[Smi03] S. W. Smith. *Digital signal processing: A practical guide for engineers and scientists*. Newnes, Amsterdam and Boston, 2003.

[The02] The BABAR collaboration. The BABAR detector. *Nuclear Instruments and Methods in Physics Research Section A: Accelerators, Spectrometers, Detectors and Associated Equipment*, 479(1):1 – 116, 2002. Detectors for Asymmetric B-factories.

[The08] The PANDA Collaboration. Technical Design Report for PANDA Electromagnetic Calorimeter (EMC), 2008.

[vS12] M. von Schmid. *TBA*. PhD thesis, Technische Universität Darmstadt, Expected 2012.

[Wam11] F. Wamers. *Quasi-Free-Scattering and One-Proton-Removal Reactions with the Proton-Dripline Nucleus 17Ne at Relativistic Beam Energies*. PhD thesis, Technische Universität Darmstadt, Germany, 2011.

[Wil] A. Wilms. Private communication.

[Zhu94] R.-Y. Zhu. On quality requirements to the barium fluoride crystals. *Nuclear Instruments and Methods in Physics Research Section A: Accelerators, Spectrometers, Detectors and Associated Equipment*, 340(3):442 – 457, 1994.